Optical measurements of injection and fuel mixing in a dual-fuel internal combustion engine and a constant volume chamber

A Thesis Submitted for the Degree of Doctor of Philosophy

By

Alexander Michael Lauterkorn

Department of Mechanical and Aerospace Engineering,
Brunel University London

2026

Abstract

Due to the need to reduce greenhouse gases and prevent global warming, alternative solutions for internal combustion engines are being developed. Since electric engines cannot fully replace internal combustion engines in certain transportation sectors, this thesis explores dual-fuel combustion as a promising alternative. Two experimental investigations were conducted:

Dual-Fuel Combustion Experiments at Brunel University A single-cylinder optical dual-fuel engine was used to study the effects of injection timing and fuel quantity on combustion. High-speed imaging captured flame area, ignition delay, and cycle-to-cycle variations. Results showed that a split pilot fuel injection creates an initial flame front, which efficiently ignites the subsequent pilot and main fuel injections, thereby reducing the required Diesel quantity. However, this approach exhibited significant variability in the initial flame formation, attributed to random flame locations, while variations in swirl speeds affected the later combustion stages.

Pilot Spray Characteristics and TWIN Nozzle Geometry at Woodward L'Orange Spray experiments in a Constant Volume Chamber examined how TWIN nozzle geometry influences spray penetration, angle, and area. The results indicated that spray hole diameter and distance are the primary factors affecting spray characteristics, while the relative spray hole angle plays a role mainly under low-pressure, short-duration conditions. By comparing the experimental data to established spray penetration formulas, modifications were recommended to better predict the behavior of TWIN nozzles.

The findings contribute to a deeper understanding of dual-fuel combustion and nozzle design, paving the way for future studies on optimizing initial flame front formation with premixed main fuel and minimal pilot fuel, as well as exploring additional geometric parameters of TWIN nozzles.

This project has received funding from the European Union Horizon 2020 Research and Innovation programme. Grant Agreement No 861002

Foreword

After finishing this work, I would like to thank Prof. Hua Zhao, Dr. Xinyan Wang, Dr. Ilona Ruoff and Martin Maierhofer for the incredible opportunity and support within this research project for which I will be forever grateful.

Furthermore, I would like to thank my family, that has always supported me during the last years, my friends who were always by my side and of course my fiancée Gabi, who was patiently with me during this process and supported me in every possible way.

This project has received funding from the European Union Horizon 2020 Research and Innovation programme. Grant Agreement No 861002

Contents

Abstract II

Contents IV

List of Tables VIII

List of Figures X

Abbreviations XV

1 Introduction 1
- 1.1 Motivation . . . 1
- 1.2 Thesis structure . . . 3

2 Literature Review 4
- 2.1 Reviewed Literature . . . 4
- 2.2 Engine Technologies . . . 5
  - 2.2.1 Heat engine classification . . . 6
  - 2.2.2 Idealized Diesel and dual-fuel cycle . . . 9
- 2.3 Engine emissions . . . 15
  - 2.3.1 Emission composition and their effects on humans and the environment . . . 15
  - 2.3.2 Emission reduction technologies . . . 18
- 2.4 Dual-Fuel engines . . . 21
  - 2.4.1 Dual-fuel engine and operation mode distinction . . . 21
  - 2.4.2 Challenges . . . 23
  - 2.4.3 Fuel mixtures . . . 26
- 2.5 Combustion & Spray Observation . . . 29
  - 2.5.1 Optical Engines . . . 29
  - 2.5.2 Constant Volume Chambers . . . 30
  - 2.5.3 High Speed Imaging . . . 31

This project has received funding from the European Union Horizon 2020 Research and Innovation programme. Grant Agreement No 861002

2.6 Optical measurement methods 32
2.6.1 Schlieren photography 32
2.6.2 Side/Back illumination 34
2.6.3 Shadowgraphy 34
2.6.4 Mie-scattering 35
2.6.5 Laser Induced Fluorescence 37
2.7 Direct injection studies 40
2.7.1 Pilot fuel injectors for dual-fuel engines 40
2.7.2 Dual-fuel injectors 41
2.8 Summary and gaps in current research 42

3 Investigation of the dual-fuel combustion 44
3.1 Dual-Fuel combustion experiments 44
3.1.1 Single cylinder optical engine 44
3.1.2 High speed recording equipment 46
3.1.3 Experimental setup 47
3.2 IMEP, NetHRR & combustion speed calc 55
3.3 Dual-fuel combustion analysis 59
3.3.1 Combustion image analysis 59
3.3.2 Analysis of dual-fuel combustion processes 63
3.4 Summary 124

4 Study of the fuel injection process 126
4.1 Pilot fuel injection measurements 126
4.1.1 Constant Volume Chamber and the TWIN nozzle injector 127
4.1.2 High speed recording equipment 132
4.1.3 Experimental setup 132
4.2 Spray analysis 133
4.3 Results of the geometric investigation 200
4.4 Summary 205

5 Adjustment of the spray penetration calculations for TWIN Nozzles 206
5.1 Based on Hiroyasu and Arai 206
5.1.1 Single hole nozzle adjustment 207
5.1.2 TWIN nozzle adjustments 211
5.2 Based on Naber and Siebers 222
5.2.1 Single hole nozzle adjustment 223
5.2.2 TWIN nozzle adjustments 225

This project has received funding from the European Union Horizon 2020 Research and Innovation programme. Grant Agreement No 861002

5.3 Summary 236

6 Summary and recommendation for future studies 237

6.1 Summary 237

6.2 Recommendations for future work 239

References XVI

This project has received funding from the European Union Horizon 2020 Research and Innovation programme. Grant Agreement No 861002

List of Tables

2.1 Heat engine classifications 9
2.2 Engine exhaust gases 17
2.3 Global warming potential of selected exhaust gases 17
2.4 Emission Factors for Greenhouse Gas Inventories 18
2.5 Dual-fuel engine distinctions 24
2.6 Main fuels for dual-fuel combustion 28
2.7 Tracers used in LIF measurements 38

3.1 Properties of the optical equipment and engine used in this study 47
3.2 Dual-fuel test cases injection duration, mass and timing 51
3.2 Dual-fuel test cases injection duration, mass and timing 52
3.2 Dual-fuel test cases injection duration, mass and timing 53
3.2 Dual-fuel test cases injection duration, mass and timing 54
3.3 Summarized IMEP and NetHRR for cases A1-G5 57
3.4 CA10, CA50, CA90 and combustion duration for cases A1-G5 58

4.1 Tested nozzles 130
4.1 Tested nozzles 131
4.2 Test pressures with tested energization durations 132

5.1 Coefficients for the single hole nozzles manufactured with SAC hole A . 209
5.2 Coefficients for the single hole nozzles manufactured with SAC hole B . 209
5.3 Root Mean Squared Error for the adjusted Hiroyasu calculations for single hole nozzles 210
5.4 Coefficients for the TWIN nozzles manufactured with SAC hole A 212
5.5 Coefficients for the TWIN nozzles manufactured with SAC hole B 213
5.6 Root Mean Squared Error for the adjusted Hiroyasu calculations for TWIN nozzles 214
5.7 Coefficients for the TWIN nozzles manufactured with SAC hole A, with first term reduction 215

This project has received funding from the European Union Horizon 2020 Research and Innovation programme. Grant Agreement No 861002

5.8 Coefficients for the TWIN nozzles manufactured with SAC hole B, with first term reduction 215
5.9 Root Mean Squared Error for the adjusted Hiroyasu calculations for TWIN nozzles, with first term reduction 216
5.10 Coefficients for the TWIN nozzles manufactured with SAC hole A, with second term reduction 217
5.11 Coefficients for the TWIN nozzles manufactured with SAC hole B, with second term reduction 218
5.12 Root Mean Squared Error for the adjusted Hiroyasu calculations for TWIN nozzles, with second term reduction 218
5.13 Coefficients for the TWIN nozzles manufactured with SAC hole A, with third term reduction 220
5.14 Coefficients for the TWIN nozzles manufactured with SAC hole B, with third term reduction 220
5.15 Root Mean Squared Error for the adjusted Hiroyasu calculations for TWIN nozzles, with third term reduction 221
5.16 Difference between the Root Mean Squared Error without term reduction to reduced terms 222
5.17 Coefficients for the single hole nozzles manufactured with SAC hole A . 223
5.18 Coefficients for the single hole nozzles manufactured with SAC hole B . 224
5.19 Root Mean Squared Error for the adjusted Naber calculations for single hole nozzles 224
5.20 Coefficients for the TWIN nozzles manufactured with SAC hole A 226
5.21 Coefficients for the TWIN nozzles manufactured with SAC hole B 227
5.22 Root Mean Squared Error for the adjusted Naber and Siebers calculations for TWIN nozzles 228
5.23 Coefficients for the TWIN nozzles manufactured with SAC hole A, with first term reduction 229
5.24 Coefficients for the TWIN nozzles manufactured with SAC hole B, with first term reduction 229
5.25 Root Mean Squared Error for the adjusted Hiroyasu calculations for TWIN nozzles, with first term reduction 230
5.26 Coefficients for the TWIN nozzles manufactured with SAC hole A, with second term reduction 231
5.27 Coefficients for the TWIN nozzles manufactured with SAC hole B, with second term reduction 232

This project has received funding from the European Union Horizon 2020 Research and Innovation programme. Grant Agreement No 861002

5.28 Root Mean Squared Error for the adjusted Naber and Siebers calculations for TWIN nozzles, with second term reduction 232
5.29 Coefficients for the TWIN nozzles manufactured with SAC hole A, with third term reduction 232
5.30 Coefficients for the TWIN nozzles manufactured with SAC hole B, with third term reduction 233
5.31 Root Mean Squared Error for the adjusted Naber and Siebers calculations for TWIN nozzles, with third term reduction 234
5.32 Difference between the Root Mean Squared Error without term reduction to reduced terms 235

This project has received funding from the European Union Horizon 2020 Research and Innovation programme. Grant Agreement No 861002

List of Figures

2.1 Idealized Diesel cycle 10
2.2 Idealized dual-fuel cycle 11
2.3 Actual Diesel cycle 12
2.4 Actual dual-fuel cycle 13
2.5 Greenhouse effect 16
2.6 Schlieren schematics 33
2.7 Side/Back illumination schematics 34
2.8 Shadowgraphy schematics 35
2.9 Mie-scattering schematics 36

3.1 Schematics of the optical single cylinder engine 45
3.2 Gas Injector (left) and Diesel injector (right) 46
3.3 Schematics of the optical test bay 48
3.4 Data acquisition system in Labview with A, frontend and B, backend as block diagram 49
3.5 Image processing via Masking and Binarization 60
3.6 Image processing via Scikit-Image and Scipy 61
3.7 Image stacking to show flame probability distribution 62
3.8 Complete and Thresholded average Flame images 63
3.9 Pixel count & Deviation for A1&A2 65
3.10 Pixel count & Deviation for A3&A4 66
3.11 Pixel count & Deviation for B1&B2 69
3.12 Pixel count & Deviation for B3&B4 70
3.13 Pixel count & Deviation for B5&B6 71
3.14 Pixel count & Deviation for B7&B8 72
3.15 Pixel count & Deviation for B9&B10 73
3.16 Pixel count & Deviation for B11&B12 74
3.17 Pixel count & Deviation for B13 75
3.18 Pixel count & Deviation for C1&C2 78

This project has received funding from the European Union Horizon 2020 Research and Innovation programme. Grant Agreement No 861002

3.19 Pixel count & Deviation for C3&C4 79
3.20 Pixel count & Deviation for C5&C6 80
3.21 Pixel count & Deviation for C7 81
3.22 Pixel count & Deviation for D1&D2 85
3.23 Pixel count & Deviation for D3&D4 86
3.24 Pixel count & Deviation for D5&D6 87
3.25 Pixel count & Deviation for D7&D8 88
3.26 Pixel count & Deviation for D9&D10 89
3.27 Pixel count & Deviation for D11&D12 90
3.28 Pixel count & Deviation for E1&E2 92
3.29 Pixel count & Deviation for E3&E4 93
3.30 Pixel count & Deviation for E5&E6 94
3.31 Pixel count & Deviation for F1&F2 97
3.32 Pixel count & Deviation for F3&F4 98
3.33 Pixel count & Deviation for F5&F6 99
3.34 Pixel count & Deviation for F7 100
3.35 Flame formation comparison for F1 and F7 102
3.36 Pixel count & Deviation for G1&G2 104
3.37 Pixel count & Deviation for G3&G4 105
3.38 Pixel count & Deviation for G5 106
3.39 Comparison of the average combustion images A1-B10 108
3.40 Comparison of the average combustion images B11-D3 109
3.41 Comparison of the average combustion images D4-E5 110
3.42 Comparison of the average combustion images E6-G5 111
3.43 HRR & NetHRR for cases A1-A4 and B1-B5 113
3.44 HRR & NetHRR for cases B6-B13 114
3.45 HRR & NetHRR for cases C1-C7 117
3.46 HRR & NetHRR for cases D1-D8 118
3.47 HRR & NetHRR for cases D9-D12 119
3.48 HRR & NetHRR for cases E1-E6 120
3.49 HRR & NetHRR for cases F1-F7 122
3.50 HRR & NetHRR for cases G1-G5 123

4.1 Schematics of the back illumination measurements at the CVC 127
4.2 Schematics of the TWIN nozzle 128
4.3 TWIN nozzle illustration 129
4.4 SAC holes illustration 130
4.5 spray recording example 134

This project has received funding from the European Union Horizon 2020 Research and Innovation programme. Grant Agreement No 861002

4.6 spray characteristics schematic 135
4.7 Relative spray angle influence N5&N6 1400 bar & 300 µs 138
4.8 Relative spray angle influence N5&N6 1400 bar & 1000 µs 139
4.9 Relative spray angle influence N5&N6 1400 bar &300 µs 142
4.10 Relative spray angle influence N5&N6 1400 bar &1000 µs 143
4.11 Relative spray angle influence N21&N22 1400 bar & 300 µs 146
4.12 Relative spray angle influence N21&N22 1400 bar & 1000 µs 147
4.13 Relative spray angle influence N5&N6 2200 bar & 300 µs 150
4.14 Relative spray angle influence N5&N6 2200 bar & 1000 µs 151
4.15 Relative spray angle influence N15&N16 2200 bar & 300 µs 154
4.16 Relative spray angle influence N15&N16 2200 bar & 1000 µs 155
4.17 Relative spray angle influence N21&N22 2200 bar & 300 µs 158
4.18 Relative spray angle influence N21&N22 2200 bar & 1000 µs 159
4.19 Relative spray hole distance influence N1-N25 stand. 1400 bar & 300 µs 162
4.20 Relative spray hole distance influence N1-N25 stand. 1400 bar & 1000 µs 163
4.21 Relative spray hole distance influence N1-N25 180° rot. 1400 bar & 300 µs 165
4.22 Relative spray hole distance influence N1-N25 180° rot. 1400 bar & 1000 µs 166
4.23 Relative spray hole distance influence N1-N25 stand. 2200 bar & 300 µs 168
4.24 Relative spray hole distance influence N1-N25 stand. 2200 bar & 1000 µs 169
4.25 Relative spray hole distance influence N1-N25 180° rot. 2200 bar & 300 µs 172
4.26 Relative spray hole distance influence N1-N25 180° rot. 2200 bar & 1000 µs 173
4.27 Relative spray hole distance influence N12-N26 stand. 1400 bar & 300 µs 176
4.28 Relative spray hole distance influence N12-N26 stand. 1400 bar & 1000 µs 177
4.29 Relative spray hole distance influence N12-N26 180° rot. 1400 bar & 300 µs 179
4.30 Relative spray hole distance influence N12-N26 180° rot. 1400 bar & 1000 µs 180
4.31 Relative spray hole distance influence N12-N26 stand. 2200 bar & 300 µs 182
4.32 Relative spray hole distance influence N12-N26 stand. 2200 bar & 1000 µs 183
4.33 Relative spray hole distance influence N12-N26 180° rot. 2200 bar & 300 µs 185

This project has received funding from the European Union Horizon 2020 Research and Innovation programme. Grant Agreement No 861002

4.34 Relative spray hole distance influence N12-N26 180° rot. 2200 bar & 1000 µs 186
4.35 Relative spray hole diameter influence N1-N27 stand. 1400 bar & 300 µs 189
4.36 Relative spray hole diameter influence N1-N27 stand. 1400 bar & 1000 µs190
4.37 Relative spray hole diameter influence N1-N27 180° rot. 1400 bar & 300 µs 192
4.38 Relative spray hole diameter influence N1-N27 180° rot. 1400 bar & 1000 µs 193
4.39 Relative spray hole diameter influence N1-N27 stand. 2200 bar & 300 µs 195
4.40 Relative spray hole diameter influence N1-N27 stand. 2200 bar & 1000 µs196
4.41 Relative spray hole diameter influence N1-N27 180° rot. 2200 bar & 300 µs 198
4.42 Relative spray hole diameter influence N1-N27 180° rot. 2200 bar & 1000 µs 199
4.43 N1 contour diagram for 80 mm penetration timing 202
4.44 N16 contour diagram for 80 mm penetration timing 203
4.45 N23 contour diagram for 80 mm penetration timing 204

5.1 Comparison of the measured single hole nozzle penetration with the calculation after Hiroyasu and Arai 208
5.2 Comparison single hole nozzle penetration with Hiroyasu and Arai . . . 211
5.3 TWIN nozzle adjustment for Hiroyasu and Arai 214
5.4 TWIN nozzle adjustment for Hiroyasu and Arai, first iteration 216
5.5 TWIN nozzle adjustment for Hiroyasu and Arai, second iteration 219
5.6 TWIN nozzle adjustment for Hiroyasu and Arai, third iteration 221
5.7 Comparison single hole nozzle penetration with Naber & Siebers 225
5.8 TWIN nozzle adjustment for Naber and Siebers 228
5.9 TWIN nozzle adjustment for Naber and Siebers, first iteration 230
5.10 TWIN nozzle adjustment for Naber and Siebers, second iteration 233
5.11 TWIN nozzle adjustment for Naber and Siebers, third iteration 234

This project has received funding from the European Union Horizon 2020 Research and Innovation programme. Grant Agreement No 861002

Abbreviations

ATDC	After Top-Dead-Center
BTDC	Before Top-Dead-Center
CA	Crank Angle
CDFO	Conventional Dual-Fuel Operation
CFD	Computational Fluid Dynamics
CI	Compression Ignition
CNG	Compressed Natural Gas
CVC	Constant Volume Chamber
DI	Direct Injector
ECE	External Combustion Engine
EDEM	**E**xperimentally validated **D**NS and L**E**S approaches for fuel injection, **m**ixing and combustion of dual-fuel engines
GWP	Global Warming Potential
HPDF	High Pressure Dual-Fuel
HRR	Heat Release Rate
ICE	Internal Combustion Engine
IMEP	Indicated Mean Effective Pressure
ISFC	Indicated Specific Fuel Consumption
LIF	Laser Induced Fluorescence
LPG	Liquefied Petroleum Gas
NG	Natural Gas
PDFO	Pilot Ignited Dual-Fuel Operation
PFI	Port Fuel Injector
PIV	Particle Image Velocimetry
PLIF	Planar Laser Induced Fluorescence
PM	Particulate Matter
RCCI	Reactivity Controlled Compression Ignition
SCR	Selective Catalytic Reduction
TDC	Top-Dead-Center

This project has received funding from the European Union Horizon 2020 Research and Innovation programme. Grant Agreement No 861002

Chapter 1

Introduction

1.1 Motivation

In order to tackle the rising demand for higher efficiency engines with simultaneously lower engine emissions, the processes within a Internal Combustion Engine (ICE) need to be further investigated to improve their understanding. One way to achieve this is by combining Computational Fluid Dynamics (CFD)-Simulations and experiments with optical engines in order to visualize the combustion events like ignition delay, combustion duration and flame propagation within the four-stroke cycle. Another one are experiments concentrating on testing new fuels because of their potentially higher efficiency and/or lower emissions. One of the approaches to reduce engine emissions is dual-fuel combustion, where a main fuel, which could not be compression ignited or only with very high compression ratios, is ignited by a pilot fuel, which auto ignites under the given conditions and therefore initiates the combustion of the main fuel. The main advantage of dual-fuel engines is that existing Compression Ignition (CI) engines can be easily modified by adding a Port Fuel Injector (PFI). However, this adjustment faces difficulties like unstable combustion in low load applications and the Direct Injector (DI) often is oversized for small injection quantities, so the maximum substitution rate can often not be reached. A typical dual-fuel mixture is Diesel-Natural Gas (NG). The main component of NG is Methane, which has potentially lower emissions than Diesel. However, this is only the case for burning the NG completely, because the Global Warming Potential (GWP) of the unburnt CH_4 is 28 times the GWP of CO_2 and therefore it is critical to ensure a complete combustion in order to reduce the emissions.

Especially in the transportation industry, where some engines can not be replaced by electric engines, dual-fuel engines are a promising approach to reduce the emissions. For example the marine sector can not completely substitute all ICEs with batteries, as shown by Kistner, Bensmann and Hanke-Rauschenbach [1] who calculated

This project has received funding from the European Union Horizon 2020 Research and Innovation programme. Grant Agreement No 861002

the theoretical achievable distances for different container ships, reaching the conclusion that the maximum for battery powered vessels is at 10000 km and economically the maximum is 2500 km. Since many shipping routes exceed these distances it is expected that combustion engines remain necessary. This motivated the investigation of heavy-duty dual-fuel combustion in this thesis. With the advancement of marine engine legislations around the world, a review for the current regulations of marine Diesel engines is shown by Ni, Wang and Li [2]. Furthermore, the researchers examined environmental impacts and emission reduction efforts. LNG is considered to remain a major fuel for the shipping industry for the next few decades due to their lower carbon and cleaner exhaust, which is why Natural Gas is investigated as main fuel for dual-fuel combustion in this thesis. The European Union decided to release an action to reduce Greenhouse gases by including them in the EU Emissions Trading System starting by reporting 40% of emissions in 2025, rising by 30% each following year [3], making it even more necessary to explore transition technologies to reduce them. Therefore, this thesis focuses on improving the efficiency and sustainability of heavy-duty combustion engines through dual-fuel combustion and pilot fuel spray investigations.

Because of the complications and the potential of dual-fuel engines, optical measurements are necessary in order to further understand their combustion and fuel mixing mechanisms. Various methods have already been used to investigate the combustion processes like for example Mie-scattering, Laser Induced Fluorescence (LIF), Schlieren and Shadowgraphy. Each of these methods provides their own advantage and insight of the processes but unfortunately optical engines are always combined with limitations in comparison to production engines. For example, the engine speed is very often limited to only a fraction of the average engines and the optical components limit the runtime duration in order to prevent them from getting damaged. When translating the results from optical engines to production engines it has to also be kept in mind that the surface temperatures, heat transfer and compression ratio differ from conventional combustion engines. This study focusses on investigating the dual-fuel combustion with Diesel as pilot and NG as main fuel as well as the spray characteristics of the TWIN nozzles. The combustion experiments are carried out in a low load optical engine with a Diesel DI and NG PFI. The spray investigations were carried out within a Constant Volume Chamber (CVC). The research within this study was split in these two parts in accordance with the EDEM project and relates in the influence of the pilot spray on the dual-fuel engines as it is often desired to run these in dual-fuel and pure Diesel mode. This still faces challenges since common Diesel injectors can not support minimum injection quantities with good spray characteristics and the influence of these non symmetrical sprays on the combustion has to be investigated as well as

This project has received funding from the European Union Horizon 2020 Research and Innovation programme. Grant Agreement No 861002

methods on improving the injectors.

1.2 Thesis structure

This thesis is structured into six chapters, beginning with an overview of the motivation for the research and the potential of dual-fuel engines to fill the niche market of transitioning marine engines towards lower emissions.

Chapter two provides a literature review of the research that has been done up until now within the engine technologies, engine emissions and the optical research for dual-fuel engines. This is followed by spray investigations and the methods proposed by researchers in predicting them. The end of the review shows gaps in the current research and how the experiments carried out within this thesis aim for filling some of these.

Chapter three describes the dual-fuel combustion experiments that were carried out within Brunel University at an optical single cylinder engine and the results of the experiments. The analysis of the flame locations is used to investigate the cycle-to-cycle variation of different dual-fuel combustions with varying injection timings and amounts for the pilot and main fuel. These experiments are aiming to further improve the understanding of the dual-fuel combustion and how to improve their efficiency.

Chapter four shows the research carried out within Woodward L'Orange where different TWIN nozzles are investigated to analyse the influence of the geometrical parameters on the spray characteristics. The aim is to further improve the TWIN nozzle design, which has the capability to run dual-fuel engines in pure Diesel and dual-fuel mode with minimum pilot fuel quantity, while maintaining good spray characteristics for both cases.

Chapter five analyses the current most commonly used spray penetration calculations and proposes an adjustment to them, depending on the geometric parameters which were varied within the TWIN nozzle experiments as well as the commonly used parameters. The main influence on the calculations is from the parameters pressure difference, spray hole diameter, time after energization and spray hole distance which is in accordance with the experimental data.

Finally, chapter 6 provides a short summary of the main results and a recommendation for further research.

This project has received funding from the European Union Horizon 2020 Research and Innovation programme. Grant Agreement No 861002

Chapter 2

Literature Review

2.1 Reviewed Literature

In order to summarize the state of the art engine and spray technologies, emissions and research methods, literature from books on combustion engines and spray as well as technical papers and online sources have been reviewed. The focus was set on technologies used in the transportation sector, since there are still many possibilities to improve the engines used within it at the moment, in terms of efficiency and/or engine emissions, especially in the area of dual-fuel engines. The research in the improvement of dual-fuel compression ignition engine technologies is part of the EDEM Project, which stands for "**E**xperimentally validated **D**NS and L**E**S approaches for fuel injection, **m**ixing and combustion of dual-fuel engines" [4], which is part of the European Union Horizon 2020 Initiative, see [5]. To understand these possible improvements, the focus was directed towards dual-fuel compression ignition engines and their injectors, which have seen a spike of interest in recent years due to their potential of transitioning the marine transportation sector towards lower emissions. Furthermore, the different current spray calculations are reviewed in order to compare these for newly designed nozzles.

This project has received funding from the European Union Horizon 2020 Research and Innovation programme. Grant Agreement No 861002

2.2 Engine Technologies

This chapter is aiming to give a review of the state of the art engine technologies and give an overview of their classification as well as the theory behind the efficiency of combustion engines. This decision was made in order to be able to understand which further improvements for modern engines are necessary in terms of efficiency and emissions. Therefore, at first the different heat engine classifications are reviewed. Afterwards, the idealized Diesel cycle is shown as well as other indicators to calculate engine efficiency. For example critical parameters for Internal Combustion Engine (ICE) to observe and improve the efficiency and emissions are the flame propagation, swirl of the injection and cycle-to-cycle variation. Spicher, Velji and Kruse [6] investigated the flame propagation and fluid flow in an optical engine, observing how the injection start and swirl impact the ignition delay. Flame propagation defines from where the ignition in the combustion chamber starts and afterwards advances. Their work demonstrates the importance of optical investigation methods for studying combustion processes. Their research is a foundation for the flame propagation and cycle-to-cycle variation analyses performed in this thesis. Bravo, Ripplinger and Samimi [7] carried out numerical simulations on Diesel jets, showing the influence of the injection pressure on the flame propagation. These findings are relevant to the present work because the injection pressure is one of the key parameters that is affecting spray development and combustion behaviour. Therefore, it was influencing the spray investigation that was carried out in this thesis. Swirl is a flow parameter of the injection which describes the turbulence of it and therefore determines how well the fuel and air are mixed. Li et al. [8] investigated the influence of a swirl control valve on the discharge coefficient and the swirl ratio, as well as visualizing the swirl and simulating it. Furthermore, the effect of swirl on dual-fuel combustion is shown by Lim et al. [9] , who showed that a reduction in swirl can lead to a similar gross IMEP with a lower total fuel amount in low load conditions. These findings are especially relevant to the research carried out in this thesis because many of the investigated dual-fuel combustion cases were strongly influenced by Diesel dominated combustion behaviour. For these the swirl significantly affects fuel-air mixing and flame propagation. At the moment this thesis is written, there are two most common engine types used in the transportation industry. The first one are Internal Combustion Engines, which are heat engines and defined by the Cambridge Dictionary as “an engine that produces energy by burning fuel within itself” [10]. Heat engines are all types of engines which convert thermal energy into mechanical energy. The other commonly used type are electric engines, currently used for example in the automotive industry. As the name indicates, electric engines convert electrical energy

This project has received funding from the European Union Horizon 2020 Research and Innovation programme. Grant Agreement No 861002

into mechanical energy. Electric engines have the capability of being used in the transport sector without producing emissions directly, however they are not suitable to be used in all types of transport sectors, because the batteries required to drive engines powerful enough for the heavy duty transportation sector would put too much additional weight on the vehicle and therefore make it impractical. Çabukoglu et al. [11] showed that currently there is no option to replace the Diesel engines of heavy-duty-vehicles with electric ones. The researchers based this conclusion on three conditions that have to be met for trucks to be powered by battery systems: (1) increased permissible vehicle weight (2) high-capacity charging access and (3) intra-day energy support. All of these conditions are, at the moment this thesis is written, rarely available. The engine technologies studied in this review are therefore kept to combustion engines, since there are fields in the industry where it is not practicable to use electric engines and therefore liquid fuels are still necessary. These sectors include for example the marine transport sector, the rail transport sector and heavy duty trucks. In order to reduce the emissions of these transport forms, while maintaining equal levels of efficiency compared to momentary technologies, new engine modifications and types are investigated.

2.2.1 Heat engine classification

The first overall classification of heat engines has already been mentioned, as they can be set apart by whether the combustion of the engine is external or internal. In External Combustion Engine (ECE) the work produced is created by an external combustion and converted to work within the engine, as for example in a Stirling engine. These engines use an external heat source to expand a working fluid within them, which is then used to drive a piston and therefore create mechanical work. Thombare and Verma [12] showed in their study the development of Stirling engines and suggested future usages with renewable energies. According to the researchers a low temperature Stirling engine that uses helium as a working fluid and is powered by solar energy is a promising approach. However, at the moment this thesis is written nearly all heavy-duty engines used in the transport sector use internal combustion engines because the ICE offers much higher performance and greater power density. Therefore, this study focuses on their improvement. In ICE, the combustion happens within the engine and produces work. As for example in Diesel engines, where the combustion of Diesel produces heat energy and drives a piston, which converts it to mechanical energy. A review for Internal Combustion Engines was created by Taylor [13], which also shows new concept in order to improve the efficiency of the engines. These concepts

This project has received funding from the European Union Horizon 2020 Research and Innovation programme. Grant Agreement No 861002

show four advanced approaches that are all capable of recovering energy from waste heat, making them a promising approach in the reduction of energy losses. For this literature review the focus was kept on Internal Combustion Engines because of their more common utilization within the transportation industry. In order to understand why the different approaches of engine technologies are investigated and used in the modern industry it is necessary to understand the chemical reactions within the combustion chamber. The chemical theory of combustion is that fuels react with the oxygen of the inlet air stream and release thermal energy during the reaction. The global reaction for fuel with oxygen is shown in Equation 2.1, compare [14].

$$C_x H_y + \left(x + \frac{y}{4}\right) O_2 = xCO_2 + \frac{y}{2} H_2O \tag{2.1}$$

With this Equation the amount of oxygen necessary for the fuel to completely burn can be calculated and is known as the oxygen-fuel ratio, as shown in [14]. When this conditions is met, the proportion of fuel and air is described as stoichiometric proportion with the ratio described as stoichiometric air-fuel ratio. Depending on whether this ratio is met or the mixtures or regions have more air or fuel than at the stoichiometric ratio, the regions can be described as lean or rich. The regions and mixtures within the combustion chamber can be described as rich, when the fuel within it excesses the amount of air. Vice versa are the regions and mixtures within the combustion chamber described as lean, when the air within it excesses the amount of fuel. In rich mixtures the shortage of oxygen can lead to unburnt fuel or just partially reactions, forming Hydrocarbons HC or Carbon Monoxide CO. Both of these components are capable of causing harm to humans, which is why it is necessary to post-process the engine exhaust gases in this case. The composition of engine exhaust gases and their affects to humans and nature will be reviewed in the following section. In leaner regions the excessive amount of oxygen should lead to a complete burn of the fuel in theory, however research showed, that the low reactivity due to the small amount of fuel present in these regions can lead to no reaction and therefore leaving part of the fuel unburnt. The calculation of the air fuel ratios and their influence on the combustion is more deeply described in [14]. There are multiple ways to distinguish Internal Combustion Engines. For example the type of injector used differentiates the engines. Most commonly are Direct Injectors, where the injector is mounted in the cylinder head and directly injects the fuel into the combustion chamber. Another injection system, which is similar to Direct Injection, is a prechamber system, where the fuel is injected into a prechamber system, which is often also mounted in the cylinder head and directly injects into the combustion chamber. Prechamber systems differ from Direct Injectors, because the fuel is ignited in the prechamber and then a turbulent flame stream is injected into the

This project has received funding from the European Union Horizon 2020 Research and Innovation programme. Grant Agreement No 861002

combustion chamber. Another approach to inject the fuel is by mounting the injector into the inlet air stream of the engine to receive a premixed charge, which then enters the combustion chamber during the inlet stroke. Direct injection leads to higher power and better fuel efficiency but can produce more PM. Port fuel injection produces lower PM but results mostly in lower power and fuel efficiency. This type of injection is often used within modified Diesel engines for dual-fuel operation, where the main fuel is injected into the inlet air stream due to its low modification costs. This will be described in more detail in the later section. Also the fuel is injected into the inlet air stream in Port fuel injection design engines. The type and geometry of the used injector also influences the previously mentioned swirl level of the fuel. Gleis et al. [15] showed, that the swirl level has a high influence on the Flame propagation. Again, this means how the flames advance in the combustion chamber after the first ignition of the fuel. The researchers showed that a higher swirl level leads to a slower radial propagation and to a more efficient burn. Furthermore, the engine operation modes can be distinguished by, whether the fuel is injected into the combustion chamber within one single injection or with split injections. Often, split injections tend to achieve higher efficiencies, while keeping the pressure rise rate of the engine lower and therefore, preventing damage to the engine. On the other hand, the adjustment for single injection to achieve optimal engine efficiency and emissions is easier. Their research laid the foundation for the dual-fuel combustion experiments carried out in this thesis. Also, heat engines can be subdivided by their ignition type into spark ignition engines and compression ignition engines. In spark ignition engines, the fuel injected into the combustion chamber is afterwards ignited by a spark plug because it is mostly not capable to auto ignite, for example Petrol. In compression ignition engines on the other hand, the fuel is auto or self ignited after the injection due to the pressure and temperature rise in the combustion chamber during the compression stroke, for example Diesel. Both the compression ignition engine and the spark ignition engine can be built as two-stroke or four-stroke engine, which is another criteria to classify ICE. In two-stroke engines the combustion events from the inlet of the air, to the injection of the fuel and its combustion and afterwards to the outlet of the resulting mixture happen in one crankshaft rotation. In four-stroke engines, the described serial of events takes two crankshaft rotations. The last classification criteria reviewed in this paper is the number of different fuels used in the Internal Combustion Engines. Mostly it is common to use one main fuel but as will be shown more in detail in the following section, it is also possible to use two main fuels in dual-fuel engines in order to improve the emissions from engines while maintaining an equal efficiency compared to engines running on one main fuel. For the studies in this literature, four-stroke compression ignition engines are investigated, since most

This project has received funding from the European Union Horizon 2020 Research and Innovation programme. Grant Agreement No 861002

dual-fuel engines are modified four-stroke Diesel engines due to its low adjustment costs. Furthermore, four-stroke engines tend to have higher efficiency compared to two-stroke engines and often also have lower emissions. The heat engine classifications are summarized in the Table 2.1.

Table 2.1: Heat engine classifications

Heat engine classification	Example
Combustion location	Internal combustion e.g. Diesel engine or external combustion e.g. Stirling engine
Injector type	Direct injector or inlet air stream injection or prechamber system
Ignition type	Spark ignition or compression ignition
Number of strokes	Two stroke or four stroke
Number of fuels	One main fuel or pilot and main fuel combination

To understand the theory of combustion and therefore the correlating engine designs within compression ignition engines, the idealized Diesel cycle is reviewed in the following section.

2.2.2 Idealized Diesel and dual-fuel cycle

The theoretical efficiency of compression ignition engines can be described with the idealized Diesel cycle. The Idealized Diesel cycle is a thermodynamic cycle for a heat engine showing the theoretically maximum amount of heat work generated by a compression ignition engine. The cycle is idealized by assuming that the system is adiabatic, meaning that there is no heat or mass transfer through the system boundaries. Also, the system obeys the ideal gas law, which is shown in Equation 2.2, where the product of the pressure P and volume V is equal to the product of the gas amount n, ideal gas constant R and the temperature T. The ideal gas law is a simplification, because it ignores the temperature change of the gas during expansion or compression. However, it is still a good approach to calculate the effects of changes in the temperature, pressure or volume on the relating properties of the gas.

$$PV = nRT \tag{2.2}$$

When the idealized Diesel cycle is displayed in a Pressure-Volume diagram, as can be seen in Figure 2.1, the graph between point 1 and point 2 in the cycle indicates the isentropic compression, simplifying the process by idealizing that there is no ex-

This project has received funding from the European Union Horizon 2020 Research and Innovation programme. Grant Agreement No 861002

change of heat or matter through the system. In a four-stroke Diesel engine, this would correlate to the compression stroke. The graph from point 2 to point 3 indicates the reversible isobar heating. Relating to the four-stroke engine, this would happen during the combustion of the fuel. This is followed by the isentropic expansion, which is shown through the graph between the points 3 and 4. In the four-stroke engine, this would be correlating to the expansion stroke. At last the graph between the points 4 and 1 shows the reversible isochoric cooling, which would be the exhaust stroke in the four-stroke engine. Again, the idealized Diesel cycle differs here from reality, since it assumes the simplification, that there is no heat or mass exchange through the system boundaries. In a realistic Pressure-Volume diagram for a four-stroke Diesel engine the extraction of volume through the exhaust stroke and the inlet of volume during the inlet stroke is also taken into account and depicted.

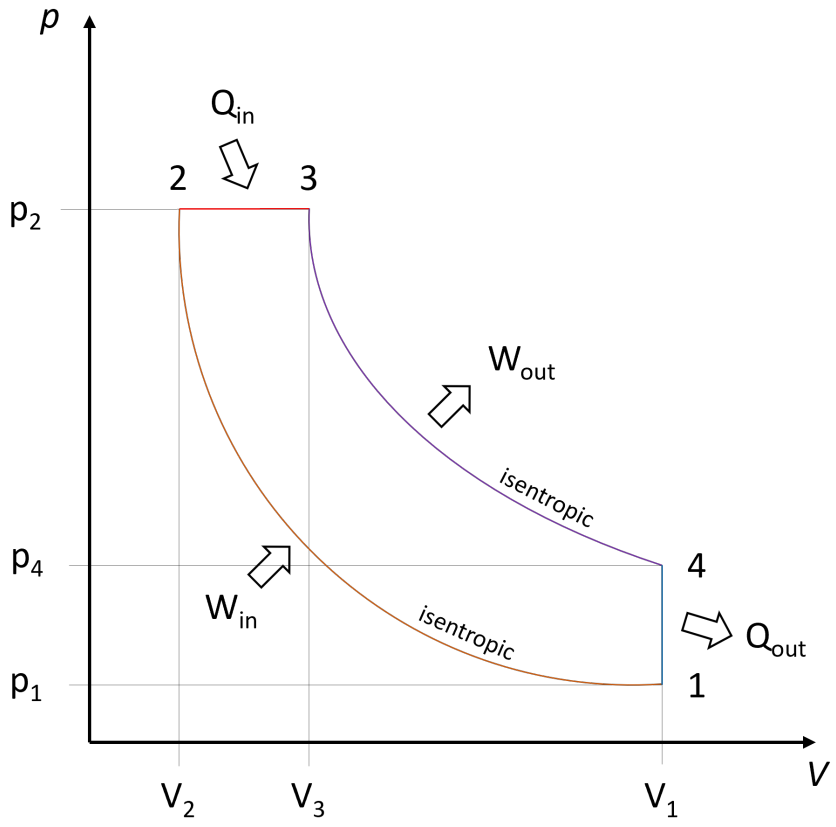


Figure 2.1: Idealized Diesel cycle

The ideal Diesel cycle differs from the ideal dual-fuel cycle because two fuels are added and therefore a second Q_{in} is added between step 2 and 3. This is raising the pressure to a higher maximum compared to the idealized Diesel cycle. The idealized dual-fuel cycle can be seen in Figure 2.2.

The actual Diesel cycle differs from the ideal Diesel cycle because there are no

This project has received funding from the European Union Horizon 2020 Research and Innovation programme. Grant Agreement No 861002

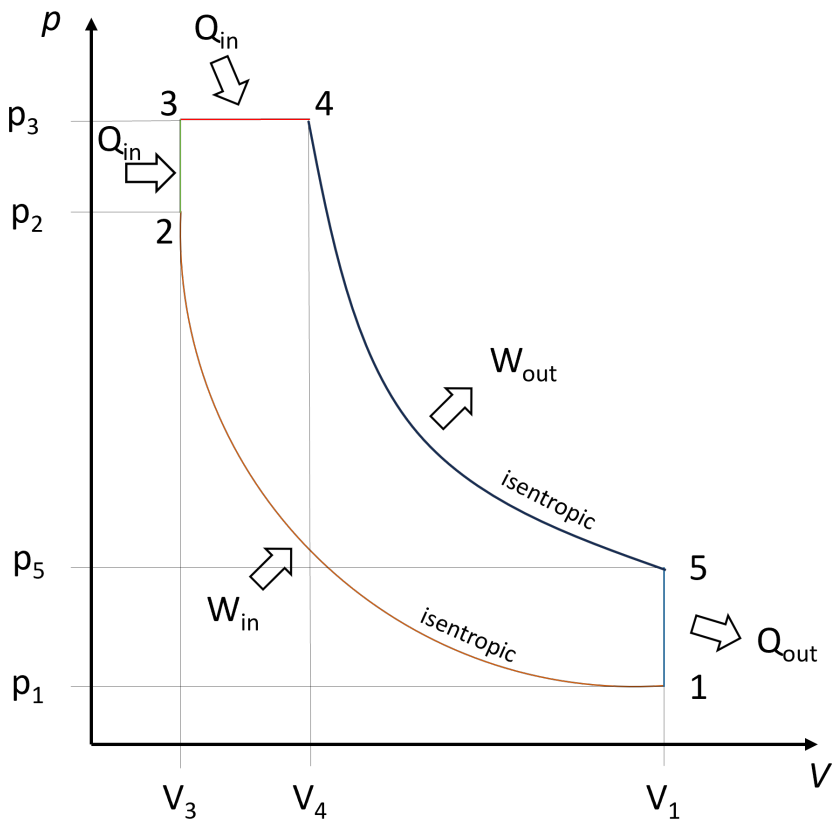


Figure 2.2: Idealized dual-fuel cycle

reversible isentropic compression and expansion or instant heat changes in a real engine. The combustion occurs over a designated time period while heat is transferred through the combustion chamber and partly lost through the cylinder walls. Therefore, the peak cylinder pressure is lower and the enclosed area of the p-V diagram is smaller in comparison to the ideal Diesel cycle. The actual Diesel cycle can be seen in Figure 2.3.

The actual dual-fuel cycle differs from the ideal dual-fuel cycle because of the same conditions as named for the Diesel cycle. Compared to the actual Diesel cycle, the actual dual-fuel cycle has a higher peak pressure due to the addition of the second fuel. This also results in a steeper expansion curve which is representing the increased energy release during combustion. The actual dual-fuel cycle can be seen in Figure 2.4.

W_{in} describes the work put into the system during the compression stroke from the piston. W_{out} describes the work leaving the system from the fuel pushing the piston. Q_{in} describes the heat put into the system from the fuel combustion and Q_{out} describes the Heat leaving the system through the exhaust stream. By calculating the subtraction of Q_{in} minus Q_{out}, the net work produced is calculated. The thermal efficiency of a

This project has received funding from the European Union Horizon 2020 Research and Innovation programme. Grant Agreement No 861002

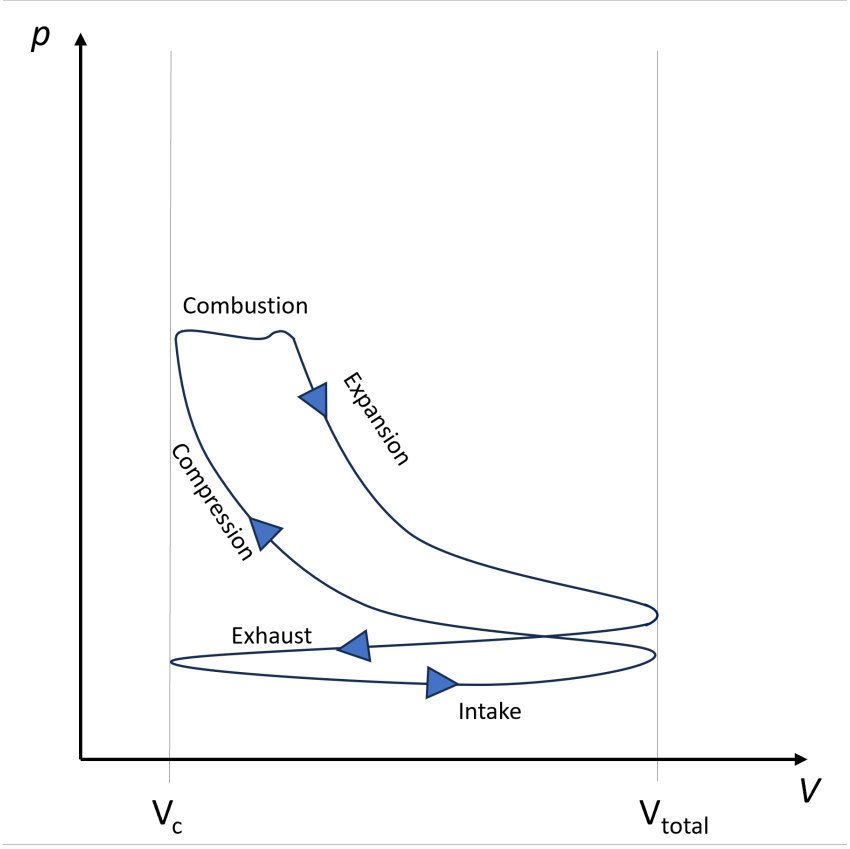


Figure 2.3: Actual Diesel cycle

idealized Diesel engine is calculated as shown in Equation 2.3 with the ratio α, which is the ratio of V_3/V_2 as shown in Equation 2.4, the compression ratio of the engine, calculated by the division of V_1/V_2 as shown in Equation 2.5 and γ, which is calculated by the ratio of the specific heats C_p/C_v as shown in Equation 2.6.

$$\eta_{th} = 1 - \frac{1}{r^{\gamma-1}} \left(\frac{\alpha^{\gamma} - 1}{\gamma(\alpha - 1)} \right) \tag{2.3}$$

$$\alpha = \frac{V_3}{V_2} \tag{2.4}$$

$$r = \frac{V_1}{V_2} \tag{2.5}$$

$$\gamma = \frac{C_p}{C_v} \tag{2.6}$$

The specific heat constants are properties of the fuel where C_p is the specific heat capacity under the assumption that the fuel is isobaric, meaning it was measured at a constant pressure. C_v on the other hand, describes the specific heat capacity for

This project has received funding from the European Union Horizon 2020 Research and Innovation programme. Grant Agreement No 861002

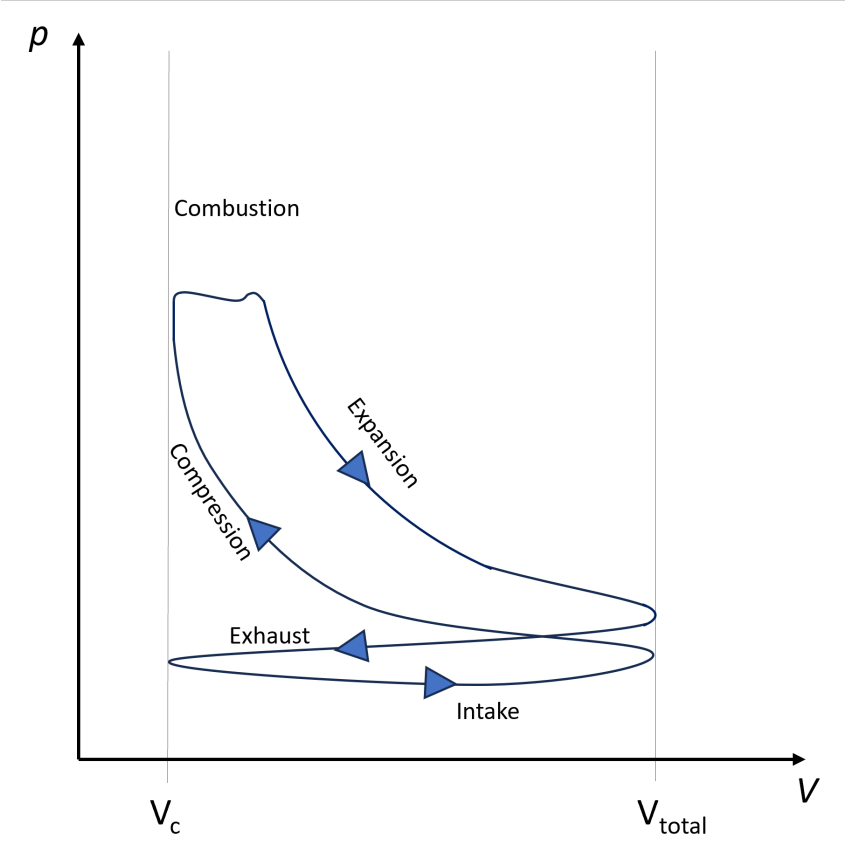


Figure 2.4: Actual dual-fuel cycle

the assumption that the fuel is isochoric, meaning it was measured at a constant volume. Another way to examine the engine efficiency is by calculating the Indicated Mean Effective Pressure (IMEP) or the Indicated Specific Fuel Consumption (ISFC). Both these values are theoretical combustion characteristics which make it possible to compare the engine efficiencies. The Indicated Mean Effective Pressure is calculated as a numerical approximation of the area beneath the graph in the Pressure-Volume diagram of the engine with consideration of the Displacement Volume V_d, as shown in Equation 2.7.

$$IMEP = \frac{1}{V_d} \int_y^x p \cdot dV \tag{2.7}$$

The ISFC takes the amount of fuel into the consideration when comparing different combustions and is therefore calculated with the fuel mass flow $\dot{m}_f$ and the engine speed rpm, as shown in Equation 2.8.

$$ISFC = \frac{\dot{m}_f \cdot rpm}{IMEP \cdot V_d} \tag{2.8}$$

For example injecting 20 mm^3 of Diesel within a injection duration time of 694 mi-

This project has received funding from the European Union Horizon 2020 Research and Innovation programme. Grant Agreement No 861002

croseconds, considering the injector pull in time of 278 microseconds and the fuel density of 0,832 mg/mm^3, the mass flow of Diesel can be calculated as shown in Equation 2.9.

$$\dot{m_f} = \frac{20mm^3 \cdot 0,832\frac{mg}{mm^3}}{694\mu s - 278\mu s} = 0,04\frac{kg}{s} \tag{2.9}$$

If the IMEP of this combustion has a value of 5 bar and the Displacement Volume is 500 cm^3, while the engine is running at 1200 rpm, the Indicated Specific Fuel Consumption can be calculated as shown in Equation 2.10.

$$ISFC = \frac{0,04\frac{kg}{s} \cdot 1200rpm}{5bar \cdot 500cm^3} = 192\frac{g}{kWh} \tag{2.10}$$

The IMEP is used to compare different operation conditions, for example different injection timing, when the same amount of fuel is used. Otherwise, the ISFC gives a better comparison. Due to their high pressure ratio, compression ignition engines have a higher efficiency than spark ignition engines, since the pressure ratio of these is limited by knocking. This phenomenon occurs when the flame propagation of the combustion is not uniformly initiated by the spark plug but also by small areas within the combustion chamber being preignited. This causes the combustion to be shifted in the four-stroke cycle and can lead to damage on the piston and cylinder walls. However, the amount of Particulate Matter (PM) emissions produced by Diesel engines is about six to ten times higher than those from Otto engines, see [16]. This is one of the motivations for the dual-fuel combustion cases investigated in this thesis in order to reduce the PM emissions. Therefore, new approaches to modify Diesel engines in order to reduce these exhaust gases are investigated. One of these approaches are dual-fuel engines which will be evaluated in a later section of this review. In the following section, the emissions of existing Diesel engines will be examined and new approaches to reduce these will be introduced.

This project has received funding from the European Union Horizon 2020 Research and Innovation programme. Grant Agreement No 861002

2.3 Engine emissions

In this section, the composition of engine exhaust gases is reviewed as well as their effect on humans and the environment and at the moment this thesis is written state of the art technologies to reduce these.

2.3.1 Emission composition and their effects on humans and the environment

Global warming is one of the main threats to the environment and mostly driven by the greenhouse effect, which means that gases in the atmosphere reflect the sunrays which would otherwise travel through the atmosphere, similar to the characteristic of the ozone in the atmosphere but with higher intensity and by that causing a "trap" of heat in the atmosphere. A part of these globally emitted greenhouse gases is produced by engines running on fossil fuels. Therefore, one of the main aims in the development of ICE is to reduce the emissions while maintaining the efficiency in order to reduce global warming. At the moment this paper is written, many experiments focus on reducing the exhaust gases of engines used in the automobile industry. However, other transportation industry sectors also rely on fossil fuels and as mentioned in the previous chapter it is often not practical to exchange these with electrical engines. In order to be able to understand how these engines can be altered in order to maintain equal levels of efficiency while reducing the harm to the environment as well as humans, the composition of their exhaust gases needs to be reviewed. Afterwards, the effects of each component of these engine emissions is examined whether it affects humans or the environment or both. The effect of gases contributing to the greenhouse effect is measured as their Global Warming Potential (GWP), which relates their effect to the greenhouse effect of CO_2. The direct greenhouse gases from engine exhaust are Carbon Dioxide CO_2, Methane CH_4 and Nitrous Oxide N_2O, compare [17]. According to definition, direct greenhouse gases contribute directly to global warming by reflecting the heat radiation from the earth and thereby causing a "trap" of heat, whereas indirect greenhouse gases react with other chemicals and therefore create direct greenhouse gases, see [17]. At the moment this thesis is written, most engines running on fossil fuels either use Diesel or Petrol. As previously mentioned the engine technology in this review is kept to compression ignition. Therefore the exhaust gases from Diesel are compared to methane in Table 2.4, since Methane has the capability to lower the emissions from engines when used as main fuel, under the assumption of it burning completely.

This project has received funding from the European Union Horizon 2020 Research and Innovation programme. Grant Agreement No 861002

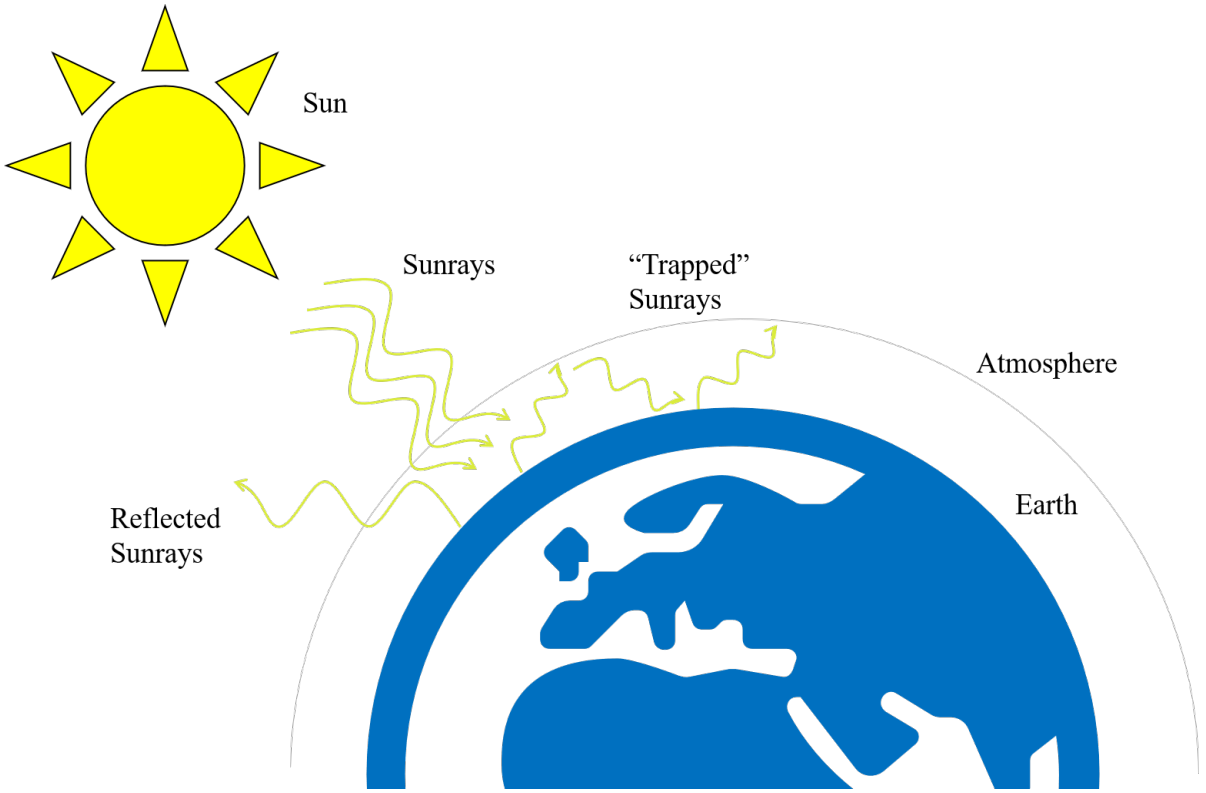


Figure 2.5: Greenhouse effect

Figure 2.5 shows a sketch of the greenhouse effect, where the reflected sunrays of the surface of earth get reflected on the atmosphere again and are therefore "trapped", causing a rise in earths temperature. Exhaust gases from engines relying on fossil fuels consist of the mixtures of the gases shown in Table 2.2 with their chemical formula and environmental and/or individual harmful effects, see [14].

Table 2.2 shows that the exhaust gases Nitrogen, Oxygen cause no harmful effects, whereas Carbon Dioxide, Sulphur Dioxide, Water vapour and Hydrocarbons are causing environmental harm. Moreover, the gases Carbon Monoxide, Nitrogen Oxides, Hydrocarbons, Benzene and PM or soot are capable of causing direct health issues. The percentage composition of the engine exhaust gases from Diesel engines consists about 67% from N_2, about 12 % from CO_2, about 11 % from H_2O, about 9% from O_2 and about 1% from the remaining pollutant emissions, compare [16]. The exhaust gases which cause health related harmful effects can often be reduced with different engine designs as well as particle filters. The reduction of the exhaust gases causing environmental issues is often investigated and different approaches to reduce these are part of modern experiments and research. The greenhouse gases with the highest GWP produced from Diesel engines are Nitrous Oxide, Methane and Carbon Dioxide. Their GWP as well as their emission factors are shown in Tables 2.3 and 2.4 compare

This project has received funding from the European Union Horizon 2020 Research and Innovation programme. Grant Agreement No 861002

Table 2.2: Engine exhaust gases

Exhaust gas	Chemical formula	Harmful effects
Nitrogen	N_2	No harmful effects
Oxygen	O_2	No harmful effects
Water	H_2O	No harmful effects for health, but vapour can negatively impact ozone
Carbon Dioxide	CO_2	No harmful effects for health, but causes greenhouse effect
Carbon Monoxide	CO	Causes health issues, e.g. headaches and respiratory problems
Nitrogen Oxides	NO_x	Causes respiratory health issues
Sulphur Dioxide	SO_2	Causes acid rain
Hydrocarbons	HC	Causes respiratory health issues and greenhouse effect
Benzene	C_6H_6	Carcinogen
Particulate matter (PM) or soot	$PM_{2.5}$ & PM_{10}	Causes respiratory health issues

[18].

Table 2.3: Global warming potential of selected exhaust gases

Greenhouse gas	GWP
CO_2	1
CH_4	28
N_2O	265

Table 2.3 shows the GWP of different exhaust gases from the fifth assessment report of Greenhouse Gas Protocol [19]. The global warming potential of Carbon Dioxide is set to one, because the potential of other greenhouse gases is measured in relation to it. The potential of Methane is at 28 and the potential of Nitrous Oxide is at 265. Therefore, the exhaust of these gases should be prevented or minimized as much as possible. When Methane is used as main fuel in engines, it is therefore necessary to ensure that no unburnt fuel is leaving the exhaust or otherwise the global warming potential of these engines exhaust gases will be worse when compared to engines running on Diesel or Petrol. Due to the high global warming potential of methane the prevention of methane slip as part of the dual-fuel engine emissions is part of the mo-

This project has received funding from the European Union Horizon 2020 Research and Innovation programme. Grant Agreement No 861002

tivation for the dual-fuel combustion investigation in this thesis.

Table 2.4: Emission Factors for Greenhouse Gas Inventories

Fuel	CO2 Factor (g CO2 per short ton)	CH4 Factor (g CH4 per short ton)	N2O Factor (g N2O per short ton)
Natural gas	54.44	0.00103	0.00010
Biodiesel (100)	9450	140	10

Table 2.4 shows the emissions for all the exhaust gases shown in Table 2.3 as listed by the United States Environmental Protection Agency [20]. It can be seen that the emissions from Natural Gas are significantly lower than from Biodiesel, which is why there is a high potential in reducing engine emissions by modifying existing Diesel engines for dual-fuel operation, which is investigated in this thesis. Under the assumption that Methane as fuel will burn completely, without releasing unburnt CH_4 into the exhaust stream, since Table 2.3 shows that its GWP is 28 times higher compared to CO_2.

2.3.2 Emission reduction technologies

Modern engines use different technologies to reduce engine emissions. For example F. Ahmad, S. u. R. Shah and M. S. Siddiqui [21] tried to reduce emissions by creating a mathematical model based on the chamber geometry, compression ratio, heat loss through walls, turbo-charging and weight optimization. They showed that the efficiency of the engine and its emissions can be improved through the use of alternative materials for weight optimization. Furthermore, they analysed the key parameters that influence the engine performance which are the engine bore and stroke. Another approach to reduce the emissions from unburnt or partially burnt fuel reactions as well as reducing Nitrous Oxide emissions from high combustion temperatures is the engine recirculation systems. C. L. Dumitrache et al. [22] show how these are designed and simulated using Computational Fluid Dynamics in order to investigate the fluid flow. They showed that EGR can reduce NOx emissions by an average of 46% under the right conditions. This motivated them to investigate the recirculated exhaust gases using CFD simulations, which revealed that the gases are not cooled consistently. Since this may lead to fluctuations in combustion conditions and NOx emissions, their research provides an insightful foundation for further improvements of EGR systems. While the approach proposed by the researchers represents a valid strategy for reducing emissions the further investigation of this method is beyond the scope of this thesis. Instead, the present work focuses on dual-fuel engine operation in

This project has received funding from the European Union Horizon 2020 Research and Innovation programme. Grant Agreement No 861002

order to reduce engine emissions. These engine exhaust gases can be redirected to the combustion chamber through the inlet air stream in order to ensure the full chemical reaction of the unburnt fuels and also ensuring lower combustion temperatures due to the reduced amount of Oxygen present. However, this is often linked with a rise of the remaining engine exhaust gases. Another approach to reduce engine emissions is to use catalysts and particle filters as previously mentioned. In the catalysts the amount of Nitrogen monoxide NO and Carbon Monoxide CO is reacting with Oxygen O_2 to form Nitrogen Dioxide NO_2 and Carbon Dioxide CO_2. The chemical Equation for this process is shown in Equation 2.11 and Equation 2.12.

$$2NO + O_2 = 2NO_2 \tag{2.11}$$

$$2CO + O_2 = 2CO_2 \tag{2.12}$$

The second approach to reduce exhaust gases, which are capable to cause harm on humans, through exhaust gas postprocessing, are particle filters. In the particle filter, Soot/PM is reacting with Oxygen to also form CO_2. The chemical Equation for this process is shown in Equation 2.13.

$$C + O_2 = CO_2 \tag{2.13}$$

While these filter systems aim to reduce the harm of engine exhaust gases on humans, the amount of Carbon Dioxide CO_2 is higher and further research is necessary to improve their effectivity. For example, Pong, Wallace and Sullivan [23] modeled different geometries to improve a stationary Diesel after treatment. Their results indicated that Selective Catalytic Reduction (SCR) performance is most sensitive to the catalyst height to inlet diameter ratio. Although this research identifies a promising opportunity for reducing emissions the after-treatment system optimization is not considered further in this thesis. The focus of this research was instead concentrated on the investigation of dual-fuel engines as a emissions reduction opportunity. Dohle and Eimers-Klose [24] showed trends in the development of the fuel injection and exhaust after treatment with the usage of electronic controls. The researchers concluded that further emission reductions will require even further advances in fuel injection systems and exhaust after treatment. While these approaches remain important, the present thesis focuses on dual-fuel engine operation as an alternative strategy for reducing emissions from existing Diesel engines. Further after treatment research is shown in [25] [26] [27], where Xiaoguang et al. [25] evaluated PM filtration technologies, Shu et al. [26] analysed the thermal behavior of Diesel after treatment systems and Rossi et al. [27] studied

This project has received funding from the European Union Horizon 2020 Research and Innovation programme. Grant Agreement No 861002

catalyst preheating to improve cold start performance. While these studies demonstrate the potential of after-treatment technologies for emission reduction, their further investigation is beyond the scope of this thesis. Instead, the present work focuses on dual-fuel engine operation. Joshi [28] published a review on the vehicle efficiencies and emissions. The researcher highlighted recent regulation changes and different exhaust treatment methods to reduce heavy-duty vehicle emissions. These aim to meet the 2027 California low-NOx and Euro VII standards. Due to the challenges and limitations of modern exhaust treatments, alternative ways to reduce the GWP of modern engines are investigated, such as the scope of this thesis, which focuses on dual-fuel engines. However there are challenges in using dual-fuel operation mode for existing Diesel engines, in terms of the operating conditions, scavenging and commissioning the injections as well as the valve timings. This means, that some operating conditions need to be further investigated, in order to be able to make dual-fuel engines completely competitive with comparable Diesel engines. In the following Chapter the technology behind dual-fuel engines and their current technological challenges will be evaluated.

This project has received funding from the European Union Horizon 2020 Research and Innovation programme. Grant Agreement No 861002

2.4 Dual-Fuel engines

The following sections are aiming to give an insight of dual-fuel engines and the challenges which researcher and developer are currently facing in order to develop and improve them. Afterwards, a short summarization of the fuel mixtures most commonly used is shown. As previously mentioned, dual-fuel engines differ by their combustion process as well as by the fuels used in these. In the literature reviewed in this chapter the engine technology is kept to compression ignition. This decision was made, because as previously mentioned many transport sectors at the moment this thesis is written, rely on Diesel engines and they could be modified for dual-fuel operation in order to reduce their emissions. For the distinction of these engines, there are different ways to distinguish the engines as well as the operation modes. Dual-fuel engines, which use compression ignition need a pilot injection of a fuel which is capable to auto-ignite due to the pressure and temperature rise in the combustion chamber during the compression stroke, for example Diesel. The ignition of the pilot fuel then ignites the main fuel which is not capable to auto ignite but similar to a spark plug engine, gets ignited from a external source, in this case the auto ignition of the pilot fuel. An example for a main fuel in dual-fuel engines is Methane, due to its potentially low emissions as mentioned in the previous chapter, but other fuels are also investigated by researchers, as will be shown later in this section.

2.4.1 Dual-fuel engine and operation mode distinction

First of all, different ways to distinct dual-fuel engines are reviewed. The first criteria of distinction for dual-fuel engines is the injection of the fuel. Most commonly Direct injection is used for the pilot fuel, since as previously mentioned, dual-fuel engines are often modified Diesel engines, which use Direct injection systems, due to economic reasons. Selim and Saleh [29] have shown that unconventional fuels like Cottonseed and Soybean Oils can also be used as pilot fuels and match the characteristics of Diesel. For this study the following research was nevertheless kept to engines with Diesel as pilot fuel in order to investigate the properties of more common dual-fuel engines used in the industry. For the injection of the main fuel Sahoo, Sahoo and Saha [30] showed that the main fuel can be injected into the air stream if the priority is to keep the modification costs of the engines for dual-fuel operation as low as possible. The researchers concluded that in low load conditions the negative effects of higher HC and CO emissions can be countered by adjusting and further investigating the effects of the pilot fuel injection timing. Part of this thesis further investigates the effect of pilot fuel injection timings on the low load dual-fuel combustion comparably

This project has received funding from the European Union Horizon 2020 Research and Innovation programme. Grant Agreement No 861002

to their research. Depending on how and when the pilot fuel is injected into the combustion chamber, the efficiencies and combustion events of the engines differ. Again, most engines use conventional Diesel direct injection for their dual-fuel operation, but Mancaruso,Todino and Vaglieco [31] showed, that the emissions can be significantly reduced in lean operation conditions by using a smaller injection system or a Diesel prechamber system. These injection systems make it possible to reduce the proportion of pilot fuel to as small as necessary to ignite the main fuel without producing work and therefore effectively only using the main fuel, which has potentially lower emissions, as convertible energy source. A similar approach is taken in this thesis through the investigation of the TWIN nozzle spray characteristics. The TWIN nozzles can potentially reduce the fuel amount needed for a stable minimum Diesel injection with stable spray characteristics. This would allow a better dual-fuel combustion with minimum amount of pilot fuel. Depending on how much of the charge or power output the pilot fuel consumes, the engine operation modes can be distinguished. According to Papagiannakis et al. [32] the Conventional Dual-Fuel Operation (CDFO) describes a operation condition, where a desired power output of the engine is achieved by creating up to 50 percent of it with the pilot fuel and the rest with the main fuel. The other operation condition is Pilot Ignited Dual-Fuel Operation (PDFO), in which the pilot injection is used to cover the mechanical losses from the engine and to start the ignition of the main fuel, but not to create a power output. The comparison between CDFO and PDFO shows the importance of minimum amount pilot fuel injection with stable spray characteristics in order to achieve stable combustion and low emissions. Therefore, this thesis investigates the influence of geomertci parameters on the TWIN nozzle pilot fuel injection to potentially improve dual-fuel engine performance. Furthermore, dual-fuel engines can be differentiated by the main fuel used for the combustion. There are many different main fuels investigated in the literature in order to study their effects on the engine emissions and power output. Most commonly investigated is Natural Gas, because of its comparable low emissions when compared to Diesel, as shown in the previous chapter. Other main fuels can also be used as shown by Wagemakers and Leermakers [33], where the effects of using Natural Gas as main fuel are compared to using Liquefied Petroleum Gas, Synthesis Gas and Hydrogen. The paper showed that these main fuels are capable to match the efficiencies of Methane and the use of Natural Gas or Liquefied Petroleum gas combined with Diesel leads to lower emissions of Nitrous Oxide. They also showed, that the use of Hydrogen or Synthesis gas combined with Diesel can lead to higher Nitrous Oxide emissions due to increased flame temperature. Mustafi and Raine [34] researched the use of Natural Gas as well as Biogas as main fuels. The different combinations of pilot and main fuels for dual-fuel

This project has received funding from the European Union Horizon 2020 Research and Innovation programme. Grant Agreement No 861002

compression ignition combustion are summarized later in this chapter. The wide range of fuels available for dual-fuel operation demonstrates the potential of this technology to reduce engine emissions. Therefore, the present thesis focuses on Diesel-Natural Gas and Diesel-Hythane combustion, as both fuel combinations can potentially lower engine emissions while creating a comparable engine power. Depending on how and when the main fuel is injected, dual-fuel engines can be distinguished. In modified Diesel engines, the main fuel is often injected into the inlet air stream, due to the comparably low modification costs. However, the main fuel can also be directly injected into the combustion chamber, if it is possible to add another injector in the cylinder head, but this is often linked with comparably higher modification costs. Moreover, the timing of the injections can also be used to distinguish the dual-fuel combustion. For example in a High Pressure Dual-Fuel (HPDF) combustion process, also called Reactivity Controlled Compression Ignition (RCCI) according to Gleis et al. [15], the main fuel is directly injected into the combustion chamber and the pilot fuel is injected in order to start the auto-ignition in the RCCI process, after the main fuel and oxidizer are compressed. The researcher in the reviewed technical papers mostly used Natural Gas as the main fuel and Diesel as the pilot fuel. This decision was made, as previously mentioned, because of the aim to reduce the emission of greenhouse gases and particles from the engines. Therefore, Methane (CH4) was chosen as main fuel because of its low C/H-ratio, which leads to low Carbon Dioxide emissions, if it reacts completely, compare [35]. In the experiments performed by Rochussen, McTaggart-Cowan and Kirchen [36], different equivalence ratios between the main fuel and the pilot fuel where used in order to study the impact of it on the performance and emissions of the engines. Also, the impact of different timing of the intake valve was studied. Depending on the parameters of the combustion, they identified five processes, creating a base study for further dual-fuel experiments.

The dual-fuel engine distinctions are summarized in the Table 2.5.

From most of the reviewed literature it can be concluded that further investigation on dual-fuel engines is necessary to investigate the effects of the parameters of the premixed charge on the combustion and therefore, also on the efficiency of the engine. The following chapter shows the challenges for the further improvement and development of dual-fuel engines.

2.4.2 Challenges

As previously mentioned, dual-fuel engines still face multiple challenges compared to conventional internal combustion engines. These include combustion instability due

This project has received funding from the European Union Horizon 2020 Research and Innovation programme. Grant Agreement No 861002

Table 2.5: Dual-fuel engine distinctions

Dual-fuel engine distinction	Example
Pilot fuel injection	Direct injection or prechamber system
Main fuel injection	Direct injection or inlet air stream injection
Operation mode	Conventional dual-Fuel Operation (CDFO) or Pilot Ignited dual-Fuel Operation (PDFO)
Pilot fuel	Diesel or cottonseed oil or soybean oil
Main fuel	Natural Gas or Hydrogen or Liquefied Petroleum Gas or Biogas

to the interaction of the two fuels, knocking or misfiring caused by improper fuel mixing, increased emissions from unburnt fuel, calibration difficulties resulting from the higher complexity of the dual-fuel system and lower efficiency at some of the operation conditions. A review of these challenges, as well as the opportunities offered by dual-fuel engines, was presented by Karimi et al. [37]. Typically, dual-fuel engines tend to have better emissions than comparable Diesel engines in operating conditions with high loads. However, for low loads, these engines tend to have higher emissions due to unburnt fuel in the combustion chamber, compare [32] [38] [39]. Liu et al. [38] investigated the effect of premixing duration in a Diesel-Ammonia dual-fuel engine at low load. The researcher found that longer premixing times resulted in visible changes of the recorded flames. These changes indicated a higher amount of Ammonia combustion and therefore a reduction in ammonia slip. Ulshney et al. [39] investigated different gas compositions in a dual-fuel engine at low loads. The researcher discovered that the CO2 and NOx emissions can be reduced up to 20% compared to conventional Diesel engines. However, most of their results led to a rise in CO and HC emissions. Therefore, this thesis focuses on low load dual-fuel combustion and also investigates pilot fuel injection strategies. These investigations aim to improve combustion stability and reduce emissions. Abd Alla et al. [40] investigated the effect of the pilot fuel injection timing on the dual-fuel low load combustion and were able to improve the efficiency by advancing the injection timing up to 30° BTDC. Similarly, Zhang et al. [41] studied the effect of the pilot fuel injection in a range of 8° to 2° BTDC. This studies were a foundation for the experiments carried out in this thesis. As previously mentioned, depending on the main fuel used for dual-fuel combustion, NOx emissions may be higher than those of conventional Diesel combustion engines. Also the amount of Natural Gas to gain the same amount of power when using Diesel leads to more fuel consumption, due to the lower combustion temperatures and increased ignition delays resulting from

This project has received funding from the European Union Horizon 2020 Research and Innovation programme. Grant Agreement No 861002

the lower energy density of Natural Gas, compare [33]. Furthermore, Papagiannakis et al. [32] mention, that modified Diesel engines for dual-fuel combustion often need to have their valve timing adjusted to avoid scavenging which can cause methane slip and therefore increase the engines emissions. The effect of scavenging on the combustion of a two-stroke marine dual-fuel engine was also investigated by Yu et al. [42], who showed that an increase in scavenging pressure can reduce NOx and HC emissions. Furthermore, methane slip is practically non-existent in a two-stroke dual-fuel engine. Felayati et al. [43] investigated the effect of scavenging on the emissions of the engines. In Diesel engines, valve overlapping is used to completely remove combustion residues with the resulting air stream as well as to cool the combustion chamber. For modified Diesel engines for dual-fuel operation, where the main fuel is injected into the air inlet before entering the combustion chamber, in order to receive a premixed charge, this valve overlapping can lead to unburnt main fuel directly exiting the combustion chamber and therefore, increasing the emissions. This phenomena is called scavenging which can be prevented by adjusting the valve timing or the injection timing of the main fuel injector. However, altering the valve timing can lead to a worse cooling of the combustion chamber and therefore to a worse combustion efficiency. Therefore, it is recommended by Papagiannakis et al. [32] to try alternative injection methods or timings for the main fuel injection before solving the scavenging by using different valve timings. These findings are part of the motivation for this thesis to investigate different dual-fuel injection timings in order to reduce the pilot fuel amount while achieving a low emissions combustion. Another challenge for modified Diesel engines for dual-fuel combustion is the Direct Diesel injector, since it was designed for pure Diesel combustion, it can often not be reduced to low Diesel quantities. Papagiannakis et al. [32] suggests exchanging the existing injector with a smaller Diesel injector or Diesel prechamber system in order to be able to only inject the minimum amount of Diesel required as previously mentioned. However this eliminates the possibility of switching to pure Diesel combustion, for example in low power requirements, where lean main fuel mixtures would lead to higher emissions and therefore, a pure Diesel combustion has to be preferred. On this behalf Papagiannakis et al. [32] argues that the change of the injector still is legitimate, since the purpose of modifying Diesel engines for dual-fuel combustion is to reduce the engine emissions with the use of a different main fuel than Diesel and therefore pure Diesel combustion should be completely avoided. The challenge of injecting very small pilot fuel quantities while maintaining operation flexibility motivates the investigation of alternative nozzle concepts. Since the TWIN nozzle investigated in this thesis has the potential to achieve stable injection with good spray penetration at low fuel quantities and can potentially achieve the same

This project has received funding from the European Union Horizon 2020 Research and Innovation programme. Grant Agreement No 861002

characteristics as conventional Diesel injectors, it was a vital part of the studies in this thesis to investigate which geometric parameters influence their spray behaviour as well as adopting conventional spray calculations to their novel design. Another challenge which dual-fuel compression ignition engines face is the occurring of knocking. As previously mentioned, knocking is a phenomena and limitation which mostly Spark ignition engines face, however it can also occur in dual-fuel engines with small pilot fuel injections, since the flame propagation is not fast enough in this case to burn the main fuel completely. Instead, small regions within the combustion chamber can get auto ignited and therefore cause knocking, see [44]. Therefore, it is important to reach minimum pilot fuel injection quantities with stable and optimal spray characteristics. As a conclusion, this thesis investigates the influence pilot fuel injection timing and amount for dual-fuel combustion and the geometric influences of TWIN nozzles on the spray behaviour as two potential measures to prevent knock. Furthermore, the effect of the premixed fuel on the dual-fuel combustion has to be further investigated to improve the understanding of these. Nemati et al. [45] simulated this effect in order to improve the understanding of the effect on the auto-ignition delay. The researchers showed that they were able to predict the ignition delay with a deviation of up to 7%. Park, Shim and Bae [46] further investigated the effect of the premixed fuel with different injection strategies, ranging from 70° to 0° BTDC. The researchers showed that a double injection strategy of the Diesel pilot led to a lower fuel consumption as well as the reduction of the CO and HC emissions. Furthermore, Choi and Park [47] investigated the effect of premixed gas composition on micro pilot dual-fuel combustion in a heavy-duty engine. in their experiments they varied the methane mixture by adding hydrogen, propane and carbon dioxide. The researcher showed that the addition of propane led to knocking, while Hydrogen and carbon dioxide suppressed it. Their results highlight the importance of investigating different main fuels for dual-fuel combustion. Therefore, this thesis investigates Diesel-Natural Gas and Diesel-Hythane dual-fuel combustion. Even though considerable research has been carried out within the last decades in order to understand the dual-fuel combustion, especially the effect of the injection timings and quantities on the combustion, there is still room for improvement and for each engine the optimum combination has to be found through experiments and/or simulations.

2.4.3 Fuel mixtures

This section aims to give a short summarization of the fuel mixtures mostly used in the dual-fuel engine experiments. As previously mentioned, most engines use Methane

This project has received funding from the European Union Horizon 2020 Research and Innovation programme. Grant Agreement No 861002

as main fuel and Diesel as pilot fuel due to their potentially low emissions. There has been also a rise of the investigations in using Liquefied Petroleum Gas (LPG) as main fuel [48][49][50], as well as Ammonia [51][52] and Hydrogen [53][54] [55]. While LPG has the lowest carbon reduction potential the researcher Ogawa et al. [48] showed that it can still lead to lower NOx emissions than conventional Diesel combustion. In comparison, Ammonia and Hydrogen are carbon free fuels, but they introduce other challenges when used in dual-fuel combustion. For example Ammonia causes low combustion efficiency at low loads and has higher NOx emissions at high loads due to higher combustion temperatures as shown by Hegab et al. [51]. For Hydrogen, these challenges include storage and transport difficulties as well as a tendency to cause knock and backfire and potentially higher NOx emissions from higher combustion temperatures as shown by Vavra et al. [53]. In another experiment by Florea et al. [56] the main fuel has been Ethanol and the pilot fuel was n-Heptane in order to use it for low temperature combustion. The researchers analysed the dual-fuel combustion using formaldehyde PLIF. They found that increasing the ethanol content led to lower local temperatures which were promoting formaldehyde formation. Furthermore, Jiang, Wang and Shuai [57] used Gasoline as main fuel and Diesel as pilot fuel in order to achieve a lean burn compared to normal Gasoline engines. It is also possible to use Compressed Natural Gas (CNG) or Hydrogen as main fuels if the aim is to reduce the emissions. Also, the possibility to use Synthesis Gas as main fuel has already been mentioned in this chapter. The wide variety of fuel combinations shows the potential of dual-fuel combustion in reducing engine emissions and paving a way for a cleaner future. While the alternative fuels reviewed in this section show promising results it was decided for this thesis to investigate Natural Gas and Hythane due to their low costs and potentially low emissions. As previously mentioned, there are also possible substitutions for the pilot fuel, as shown in [29] like Cottonseed and Soybean Oils which match the characteristics of Diesel. Chauhan et al. [58] reviewed the different pilot fuel blends used by the researchers and compares there effect on the emissions, mostly the fuel blends reduce the Carbon related emissions, while increasing the Nitrogen based emissions . For the commonly used dual-fuel compression engines especially modified Diesel engines for dual-fuel combustion, mostly Diesel is used as pilot fuel. Table 2.6 shows a summarization of the mentioned main fuels and pilot fuels.

Other pilot and main fuels can also be used for dual-fuel combustion, in order to improve the engine emissions. However, the prioritized combination for the reviewed literature was kept to Diesel as pilot fuel and Methane as main fuel, in order to represent the most common type of dual-fuel engines. Dronniou et al. [35] studied the equivalence ratio between the amount of fuels and the amount of air in the combus-

This project has received funding from the European Union Horizon 2020 Research and Innovation programme. Grant Agreement No 861002

Table 2.6: Main fuels for dual-fuel combustion

Main fuel	Pilot fuel
Natural Gas	Diesel
Hydrogen	Soybean Oil
Compressed Natural Gas	Cottonseed Oil
Synthesis Gas	n-Heptane
Ethanol	
Gasoline	

tion chamber. The researcher observed that the equivalence ratio does not impact the ignition location which starts at near wall regions. However, low equivalence ratios can lead to high levels of unburnt Hydrocarbons from the main fuel and therefore are not able to improve the engine emissions. With high equivalence ratios they observed near wall flame propagation. Therefore, this thesis further investigates pilot fuel injection timing and durationin order to improve combustion characteristics under low load dual-fuel operation conditions. To be able to study the combustion events and fuel distribution, the next chapter gives an introduction on optical test facilities.

This project has received funding from the European Union Horizon 2020 Research and Innovation programme. Grant Agreement No 861002

2.5 Observation of Combustion events and Injection fuel distribution

This chapter is aiming to give a short introduction to optical test facilities commonly used to carry out research on Internal Combustion Engines. In order to observe the combustion events within engines as well as the fuel distribution during injection, optical measurement methods are used. These can be performed in Constant Volume Chambers to investigate the fuel injection and in optical engines to observe the fuel injection and/or combustion events. For the observation of these events, high speed imaging is required, since most of the desired observation happen within the time frames of Milli - or Microseconds.

2.5.1 Optical Engines

In order to observe the combustion events, optical access to the combustion chamber is required. In this section the different types of optical engines and their benefits as well as limitations are reviewed. According to Zhao [59], optical engines can be distinguished by the number and position of windows used to investigate the combustion and fuel distribution. For example, the window to investigate the combustion events can be placed in the cylinder head to gain view of the combustion events from above, compare[59]. For example, Merola et al. [60] used a Diesel engine which was modified with a steel crown to gain optical access to the combustion chamber. This configuration is used for two-stroke engines, as shown in [59], since four-stroke engines use overhead valves and therefore, the window would require repositioning the valves. Another approach was shown by Hult, Matlok and Mayer [61] who used a special designed custom made optical cover to gain access to a large two-stroke engine for marine applications. If this configuration is not possible, because it would mean changing the properties of the intake or outtake valves, an optical window in the piston head can be used. Therefore, the piston is extended, so that a 45° angled mirror is placed below it, to observe the events in the combustion chamber. However, this limits the view to a 2D plane of the events. This configuration is often used in optical engine research, some examples are shown in [62][63][64][65][66]. For example, Liu et al. [63] used it to investigate the flame propagation of Natural Gas, whereas Zha et al. [64] investigated the in-cylinder flow during the compression stroke. This highlights the versatility of this optical engine configuration. A similar experimental approach is taken in this thesis, where optical access through the piston is used to investigate the dual-fuel combustion processes. In order to extend the observation, windows in the cylinder walls can be

This project has received funding from the European Union Horizon 2020 Research and Innovation programme. Grant Agreement No 861002

an additional extension so that the events can be better observed. However there are limitations when using optical engines and comparing them to common Internal Combustion Engines. For example, optical engines are often limited in their running time, since the thermal robustness of the optical accessible parts is less than that of common engines. Furthermore, the lubrication of engines with windows in the piston head often tends to be less efficient which leads to running breaks in order to relubricate the piston and to clean the mirror below it. Also, the soot from the combustion may cause a regular cleaning of the optical accessible parts to be required, regardless of their position. Therefore, the book [59] shows that it is also possible to gain optical access to the combustion chamber through an endoscope. Since the other configurations often limit the test set up to an optical engine with one piston and lower engine speed, endoscopic access to the combustion chamber can be used to get a more realistic imaging of the combustion events. The endoscope is placed in the cylinder head to observe the combustion chamber. For example, Larrson [67] carried out a study on an optical Diesel engine using an endoscope to observe the fuel injection and combustion.

2.5.2 Constant Volume Chambers

In this section, the structure and function of Constant Volume Chambers is reviewed. Cold Constant Volume Chamber, as the name indicates, consist of a optical accessible Chamber with constant volume to investigate the spray distribution and fuel evaporation without combusting the fuel, while Hot Constant Volume Chambers allow combustion. The optical measurement methods, which can be used in these chambers are for example Mie-Diffused Light, Shadowgraphy and Schlieren. The aim of these investigations is often to get a better understanding of how the fuel injector geometries influence the fuel distribution in combustion chambers, in order to be able to improve the combustion and therefore, lower the emissions of existing and new engines while maintaining the same levels of efficiency. These chambers are mostly constructed of stainless steel and windows mounted on the sides, so that they can withstand the pressure rise, compare [68]. To extend the portrayal of the fuel distribution it is sometimes also possible to add windows on the top and/or bottom of the chamber. Constant Volume chambers are quite commonly used in the automotive research. For example Kang et al. [69] investigated the combustion of Hydrogen mixed with Compressed Natural Gas. The researchers demonstrated how added Hydrogen increases the combustion pressure and temperature. While this leads to more optimal combustion conditions it also can lead to an increase in NOx emissions due to higher combustion temperatures. In order to further investigate this behaviour, this thesis investigates Diesel-Hythane dual-fuel

This project has received funding from the European Union Horizon 2020 Research and Innovation programme. Grant Agreement No 861002

combustion in an optical engine. Whereas Shimizu et al. [70] used a Constant Volume Chamber to investigate the spray distribution of synthetic fuels and compared them to Diesel and afterwards numerical simulations. Similarly, this thesis investigates the influence of geometric parameters on the TWIN nozzle pilot fuel spray characteristics. Baik et al. [71] investigated premixed and direct injected Compressed Natural Gas in a CVC with a swirling motor, showing that direct injection leads to a more rapid combustion. Sureshkumar et al. [72] investigated the effect of the chamber pressure on the spray and compared it to their numerical model. The researchers were able to develop a model that predicted the experimental results with a deviation of less than 4%. Their study influenced the preparation on the pilot fuel investigation carried out in this thesis.The optical measurement methods used in Constant Volume Chambers are more deeply explained in the following sections.

2.5.3 High Speed Imaging

As previously mentioned, the observation of combustion events as well as fuel distribution requires high speed imaging. Depending on the events desired to be observed and the engine speed, the requirements for high speed imaging differ. For example, observing an engine running at 1200 rpm results in one crankshaft rotation within 0.05 seconds. If the desired events are to be depicted within 1 degree crank angle steps, each crank angle step results in a time step of about 13.89 Milliseconds. Therefore, at least one picture has to be taken at this time step, resulting in a minimum required imaging frequency of 7200 frames per second. Modern high speed cameras are capable of filming with up to 200 000 frames per second, making it possible to observe the events within the optical engines and CVC in time steps of 5 Microseconds. However, this is often linked to a reduction of the resolution, which is why it is often more practical to choose the frame rate of the camera depending on the minimum time resolution desired. Depending on which type of optical measurements are carried out to observe the engines it may also be necessary to use an image intensifier. This optical tool converts the incoming photons into electrons, which are then amplified within it and converts them afterwards back to photons. This process intensifies the imaging of events such as Laser induced fluorescence. For example, Zhao and Kaiser [73] used high speed imaging to observe the knock in an compression engine. The researchers were able to predict knock based on the velocity fields which they calculated from the recorded images. In accordance, high-speed imaging is employed in the present thesis to investigate dual-fuel combustion processes. The different optical measurement methods are explained in the following section.

This project has received funding from the European Union Horizon 2020 Research and Innovation programme. Grant Agreement No 861002

2.6 Optical measurement methods

This chapter aims to give a introduction of the main optical measurement methods used in the reviewed literature for studying combustion events. Four main, optical measurement methods are investigated and used in the reviewed literature. Schlieren, Shadowgraphy and Mie-scattering are used to investigate the fuel distribution, whereas Laser Induced Fluorescence can be used to investigate the combustion process as well as the fuel distribution, depending on the use of suitable tracers. Another optical measurement to investigate the combustion process is the recording of OH* chemiluminescence and soot luminescence. OH* are emerging radicals from the combustion of fuels like Methane and can be used to indicate the quantity of fuel burnt and therefore indicate the richer and leaner regions within the combustion chamber. OH* radicals emit light in a bandwidth of 280-350 nm. In this measurement method the light emitted from the combustion chamber is divided, mostly by a dichroic mirror, in order to separate the different light sources depending on the wavelength of the light they have emitted. The wavelength of OH* emitted light lies at about 308 nm and the soot luminescence above 340 nm. Therefore, the dichroic mirror separates light at 340 nm wavelength. The OH* emissions originate from the combustion and are an indicator for the quantity of the local heat. The soot luminescence was used to trace the position and the influence on the combustion, see [35] and [36]. Similarly, this thesis uses optical diagnostics to analyse combustion behaviour by using flame pixel detection and comparison of the deviations from the average cycle to calculate the cycle-to-cycle variation. Since the chemiluminescence appears as a result of the combustion process, it can be combined with other measurement methods, which will be shown later in this section.

2.6.1 Schlieren photography

The first optical measurement method to be reviewed is Schlieren photography. Schlieren photography is a optical measurement technique used in Constant Volume Chambers as well as optical engines for spray diagnostics. In this optical measurement method, a light source is used to illuminate the test area through the previously mentioned windows or lenses and then captured with a high speed camera or screen through another window or lens with the usage of a knife edge. This makes it possible to capture high speed 2-D records of the fuel injection, with which the properties of the fuel distribution can be calculated. The penetration of the chamber can be observed, as well as the spray cone angle, the spray elevation angle, the spray area and the spray circumference. With the observation of these values the fuel injection can be adjusted as desired in order to improve the efficiency of the engine for example by

This project has received funding from the European Union Horizon 2020 Research and Innovation programme. Grant Agreement No 861002

modifying the angle of the injector or the fuel injection pressure to ensure homogenous fuel distribution within the combustion chamber.

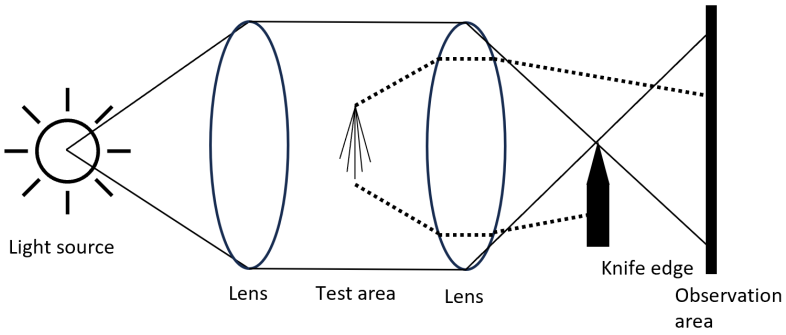


Figure 2.6: Schlieren schematics

Figure 2.6 shows the schematic structure of Schlieren, where the test area is surrounded by lenses and illuminated by a light source. The resulting light beam is then partially cut of by a knife edge and projected on a screen or a capturing camera. For test subjects with density variations, the knife edge helps prevent image distortion and makes it possible to see the density variations in the recording. This helps identifying for example turbulent or laminar regions within the fuel injection which can then be modified according to the desired effects, compare [74]. Schlieren is therefore often used to investigate the fuel sprays and their evaporation. Fujikawa, Ozasa and Kozuka [75] show an example of developing an optical engine for Schlieren applications. The researchers were able to visualize the flame kernel formation, flame propagation and distribution of unburnt gases within the combustion chamber. This demonstrates the potential of optical diagnostics for investigating in-cylinder combustion processes. Lee et al. [76] show how the penetration of the vaporous phase of a Diesel injection was measured with Schlieren. The researches visualized how higher injection pressures lead to a higher injection vapor phase penetration. Their work represents an alternative approach to many spray investigations, which primarily focus on the liquid-phase spray penetration. Ouchi, Chikahisa and Murayama [77] showed that Schlieren can be used in internal combustion engines to determine the fuel vapour and density distribution. Their results demonstrated that the method can be used as an effective diagnostic for internal combustion engine research. Whereas Pastor et al. [78] used Schlieren to analyse the flame propagation of Diesel, showing how different injection pressures infuence the flame evolution. While Schlieren imaging provides valuable information on the vapor phase fuel distribution, the present thesis primarily focuses on the liquid spray characteristics since they mainly influence the dual-fuel combustion behaviour.

This project has received funding from the European Union Horizon 2020 Research and Innovation programme. Grant Agreement No 861002

2.6.2 Side/Back illumination

The second optical measurement method to be reviewed is Side/Back illumination, which is similar to Schlieren, as it also uses a light source to illuminate a chamber in order to investigate the fuel distribution. However compared to Schlieren, Side/Back illumination is a simpler technique, since it functions without the use of the previously mentioned knife edge or lenses in the Schlieren experimental setup. Therefore, Side/Back illumination is not capable to observe the density variations and image distortions may occur, especially in non-uniform test subjects. This means that Side/Back illumination is only capable of observing the geometric values of the fuel injection as spray cone angle, the spray elevation angle, the spray area and the spray circumference.

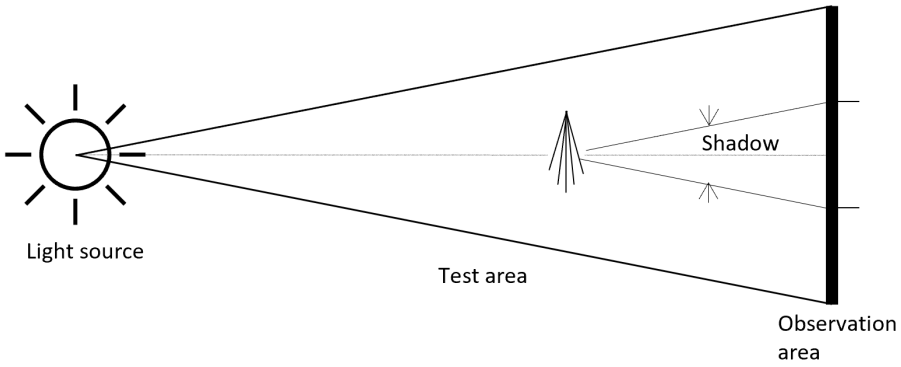


Figure 2.7: Side/Back illumination schematics

Figure 2.7 shows the schematic structure of Side/Back illumination, where the test area is also illuminated by a light source and the non uniformity in the test area, e.g. temperature differences or different gases, cause a light diversion which is then captured on screen or by a camera, compare [74]. In this study, the spray was investigated using Side/Back illumination since the focus was on analysing the liquid phase, particularly the spray penetration,spray angle and spray area, for which this technique is better suited than Schlieren imaging.

2.6.3 Shadowgraphy

The third optical measurement method to be reviewed is Shadowgraphy, which is also similar to Schlieren, as it also uses a light source to illuminate a chamber in order to investigate the fuel distribution. Again, this technique does not use the knife edge and

This project has received funding from the European Union Horizon 2020 Research and Innovation programme. Grant Agreement No 861002

therefore is not capable to observe the density variations and image distortions may occur, especially in non-uniform test subjects, similar to Side/Back illumination.

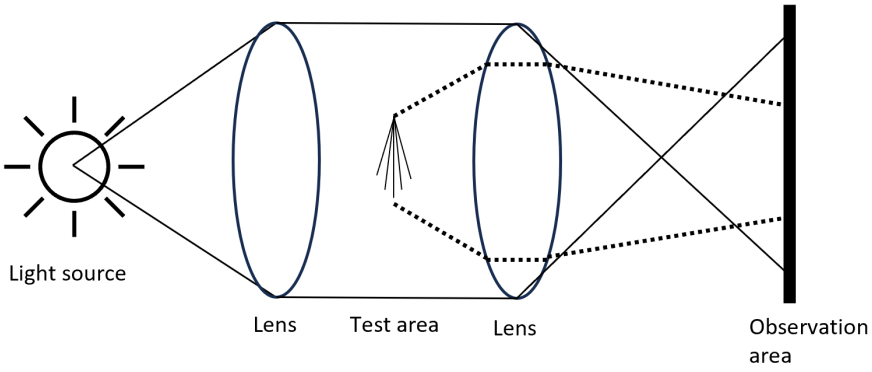


Figure 2.8: Shadowgraphy schematics

Figure 2.8 shows the schematic structure of Shadowgraphy similar to Figure 2.6 and 2.7.

Kunkulagunta [79] investigated the spray characteristics of a Diesel spray within an optical engine, showing how it can also be used to analyse the shot-to-shot variation. They utilized Shadowgraphy to analyse the variation of the spray characteristics for different fuel pressures, similarly to the apporach taken in this thesis for the TWIN nozzle spray investigations. Furthermore, Daly et al. [80] used Shadowgraphy to analyse the impact of the injector temperature on the spray characteristics. Afterwards they modelled the injectors in comparison to their experiments and discovered, that early spreading angle transients have a impact on penetration and mixture formation. Guerrassi and Champoussin [81] validated their computational model on the wall impingement of Diesel Sprays by using Shadowgraphy, showing how it can be easily used to validate models. Shimoda, Suzuki, and Shigemori [82] investigated the particle formation process using Laser Shadowgraphy, displaying how it can also be used to analyse engine emissions . The studies demonstrate the suitability of Shadowgraphy for visualizing in-cylinder flow and combustion phenomena. Although Shadowgraphy was not used in this thesis, similar investigations have been carried out in this thesis, where Side illumination was employed to investigate the spray characteristics of the TWIN nozzles.

2.6.4 Mie-scattering

The fourth optical measurement method to be reviewed is Mie scattering, which can also be used in Constant Volume Chambers as well as in optical engines, as for ex-

This project has received funding from the European Union Horizon 2020 Research and Innovation programme. Grant Agreement No 861002

ample shown by Kim, Park and Bae [83]. The researchers demonstrated that Diesel exhibits greater liquid phase penetration than gasoline under identical operating conditions, while vapor phase penetration remained largely unaffected by the fuel properties. In this optical measurement technique, the scattering of the electromagnetic waves from a light source is observed in order to measure or observe particles. The electromagnetic waves from the light source are elastically scattered by particles with a similar or larger diameter than the wavelength of the used illumination source. Therefore, most light sources used for Mie-scattering are Lasers, with Wavelengths suitable for the diameter of the desired particles to be observed.

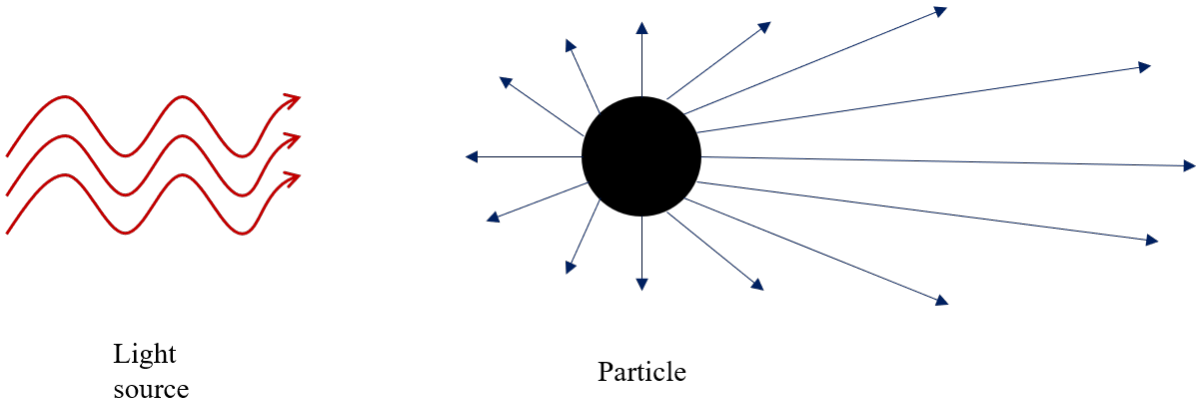


Figure 2.9: Mie-scattering schematics

Figure 2.9 shows a schematic sketch of Mie-scattering. The electromagnetic waves from the light source get scattered by the particle and make it possible to observe the divergence of the electromagnetic waves. Xu, Myers, and Uyehara [84] used Mie-scattering to measure the PM that forms during combustion in an optical engine and it was comparable to the data from a smoke meter. Atalaş et al. [85] carried out a similar study and measured the amount of Soot in a DI Diesel engine. The researchers showed that for a combustion thatt starts at TDC the soot formation began to increase at approximately 20° CA ATDC. In contrast, the NOx formation began at the early combustion phase until 40° CA ATDC.. Montanaro et al. [86] used Mie-scattering in combination with Schlieren to simultaneously investigate the liquid and vapour phase of Diesel injections. Whereas Münch and Leipertz [87] illuminated an optical engine in a sheet plane to observe injection in a fixed plane for comparison.

Mie-scattering can also be used for Particle Image Velocimetry (PIV), where a seeding material with known particle size is added to the flow of interest and a associated light source with the correlating wavelength lead to Mie-scattering at these particles, making it possible to observe the flow. The use of Particle Image Velocimetry (PIV) to investigate the injection and combustion with a optical piston which is brightened by a

This project has received funding from the European Union Horizon 2020 Research and Innovation programme. Grant Agreement No 861002

light source makes it possible for a high speed camera to frame the actions within the combustion chamber. Mostly these pistons have a Bowditch design, which means the window is in the upper part of the piston as mentioned in the previous chapter. For the tracking of gaseous fuels the PIV measurement method is used for example by Gleis et al. [15]. This method adds seeding particles to make the movement of the fluid visible as mentioned. The seeding the researchers at the Technical University Munich choose were Titanium dioxide particles because of their high thermal stability and their low hardness, which makes testing possible without scratching the surface of the windows, compare [15]. With the frames from the camera it is possible to track the movement of the particles after the injection and to trace the ignition. The occurring of the studied events is linked to the crank angles in order to make the different processes comparable. The studies demonstrate the suitability of Mie scattering for visualizing in-cylinder flow and combustion phenomena. Although Mie scattering was not used in this thesis, similar investigations have been carried out in this thesis, where Side illumination was employed to investigate the spray characteristics of the TWIN nozzles.

2.6.5 Laser Induced Fluorescence

The last optical measurement method to be reviewed is Laser Induced Fluorescence, which is an optical measurement method where a fuel tracer mixture is shine on with a light source, mostly Lasers, which have a wavelength and intensity capable of stimulating the tracer to emit fluorescence, which is then captured with the use of an image intensifier and a high speed camera. This makes it possible to investigate the fuel distribution and it can also be used to investigate the emerging radicals of the combustion process. Depending on the wavelength of the light source, a suitable tracer has to be used in order to achieve fluorescence. The selection of a tracer has to be based on the different conditions of the experiments. First of all the fuel used in the experiments influences the choice of the tracer, since it should be having similar properties to the fuel in order not to falsify the experiments, especially when investigating the fuel distribution. Second, the tracer needs to be suitable for the purpose of the experiments, meaning that the investigation of liquid fuels and gaseous fuels need different approaches. Third the tracer used for investigating combustion events and resulting regimes need to be suitable for combustion. As previously mentioned, it is sometimes also possible to use OH* chemiluminescence to observe the resulting regimes of combustion. This can be combined with Laser Induced Fluorescence experiments in order to receive better results, but attention to the choice of tracer and light source has to be paid in order not to interfere with the from the OH* chemiluminescence emitted electro-

This project has received funding from the European Union Horizon 2020 Research and Innovation programme. Grant Agreement No 861002

magnetic waves. The Table 2.7 shows a selection suitable tracers with their correlating wavelengths taken from the book written by Zhao [59]:

Table 2.7: Tracers used in LIF measurements

Tracer and Fuel	Absorption Band (nm)
$C_6H_5N(CH_3)_2$, N,N-dimethylaniline (0.2 vol. % in iso-octane)	200-320
$C_{16}H_{10}$, fluoranthene,(1,2-benzene) (<1.0 mass. % in iso-octane)	200-400
C_2H_5CHO, propionaldehyde (9.1 vol. % in iso-octane)	220-340
C_3H_7CHO butyraldehyde (9.1 vol. % in iso-octane)	220-340
C_5H_9CHO N-valerdehyde (9.1 vol. % in iso-octane)	220-340
$C_6H_{13}CHO$ heptaldehyde (9.1 vol. % in iso-octane)	220-340
C_6H_5CHO bensaldehyde (9.1 vol. % in iso-octane)	220-340
CH_3COCH_3 acetone	200-330
$C_2H_5COCH_3$, 2-butanone, (ethylmethylketone, EMK) (100 %)	210-310
$C_2H_5COC_2H_5$, 3-pentanone (diethylketone)(2.0-25.0 vol.% in isooctane)	220-340
$CH_3COCOCH_3$, biacetyl, (2,3-butanedione) (2.0-6.0 vol.% in isooctane)	200-480
NO_2, nitrogen dioxide (0.2 vol % in nitrogen)	UV-Visible

Dronniou et al. [35] used Planar Laser Induced Fluorescence (PLIF) to show the distribution of the fuel. In this method, the air has been replaced by nitrogen and the tracer naphthalene $C_{10}H_8$ has been added to the pilot fuel to make tracking via a fourth harmonic Nd:Yag laser with a wavelength of 266nm possible. As previously mentioned, the technology investigated in this review is mostly kept to dual-fuel compression ignition engines, which use Diesel as pilot fuel and Methane as main fuel. In order to perform Laser Induced Fluorescence measurements on these engines, a suitable tracer to observe the distribution of the pilot fuel would be naphthalene $C_{10}H_8$ with a Laser stimulation bandwidth of around 270 nm, compare [88]. Therefore, a Nd:YAG Laser with frequency quadrupling would be suitable. Also, a combination of using biacetyl $CH_3COCOCH_3$ with a Nd:Yag Laser with frequency tripling is possible, as shown in Table 2.7. A suitable tracer to observe Natural gas would be Nitrogen Dioxide NO_2, with a absorption band from UV until visible light. Therefore, a suitable Laser would also be a Nd:Yag Laser with frequency doubling to 532 nm, in order to avoid Diesel flourescence as shown in Table 2.7. Laser Induced fluorescence is used for many applications to investigate the combustion events or spray distribution. Willman et al. [89] used it in combination with Laser Induced Grating Spectroscopy in order to observe the temperature in 2 dimensions. Similar measurements have been carried out by Scott et al.

This project has received funding from the European Union Horizon 2020 Research and Innovation programme. Grant Agreement No 861002

[90]. The researchers were able to measure the temperatures with a deviation of only 1% throughout the entire engine cycle. Brands et al. [91] used it to observe the first two stages of the ignition in a split injection Diesel combustion. The researchers were able to demonstrate that the ignition delay of the main injection was up to five times longer than that of the pilot injection. Whereas Rothamer et al. [92] used two different wavelengths to simultaneously investigate the temperature and composition, carrying out two laser Induced fluorescence measurements. In this experiment, the researchers were able to measure temperatures with a deviation of up to 5% while simultaneously determining the EGR mole fraction. Florea et al. [93] investigated the dual-fuel combustion of Ethanol and N-Heptane by using formaldehyde as tracer. In their study they focused on partially premixed combustion and were able to show through PLIF that the tracer was in highest concentration close to the combustion chamber walls. However, LIF faces challenges when investigating combustion in engines due to the presence of soot particles, which can absorb or scatter the incoming laser light and thereby reduce or even prevent fluorescence. Furthermore, soot particles may also absorb the emitted fluorescence before it can be detected. Therefore, in this study, the results from previous LIF investigations were considered, but LIF itself was not used to analyse the combustion events.

This project has received funding from the European Union Horizon 2020 Research and Innovation programme. Grant Agreement No 861002

2.7 Direct injection studies

Another possibility to optimize the dual-fuel combustion is the improvement of the pilot fuel distribution in the combustion chamber, in order to operate correctly with minimum injection amounts and in all engine conditions. In the past, many studies have been conducted in order to investigate the different parameters that influence the spray. For the transportation sector, the most accurate equations to calculate the penetration of large injectors for the transportation sector are from Hiroyasu and Arai or Naber and Siebers. Hiroyasu and Arai [94] calculated the spray penetration depending on the pressure difference, fuel density, spray hole diameter and ambient density of the spray chambers. Naber and Siebers [95] evaluated the proposed calculations from Hiroyasu and Arai and further developed them by adding the velocity coefficient, contraction coefficient and spray angle. Further models were created in order to fit the constantly increasing variety of injectors, a review of these was created by Liu et al. [96]. A comparison with the calculations of Hiroyasu as well as Naber and Siebers was carried out in this thesis. This decision was made because these models represent the most fitting calculations for predicting the spray behaviour of the conventional heavy-duty injector used in this pilot fuel study.

2.7.1 Pilot fuel injectors for dual-fuel engines

Due to the fact, that dual-fuel engines are often retrofitted Diesel engines, the pilot fuel injector is often not suited for all dual-fuel operations. Therefore, numerous studies were carried out to investigate the injection influence on the combustion in order to improve the dual-fuel operation. Liu et al. [97] investigated the effect of the pilot fuel quantity on the engine emissions, discovering at which quantities the NO_x and PM can be reduced. The researchers discovered that NOx emissions from dual-fuel combustion are generally lower than those from pure Diesel combustion with an average reduction of 30%, while particulate matter (PM) emissions are significantly lower overall but show greater variability. Also the influence of the nozzle geometry has often been investigated as shown by Payri et al. [98], who linked the nozzle geometries to cavitation and discovered that the velocity and mass flow rate were highly influenced by it, while the momentum flux was not. Motivated by these observations, the present thesis investigates a TWIN nozzle concept, which has the potential to provide stable spray penetration and ignition characteristics while operating with reduced pilot fuel quantities.

This project has received funding from the European Union Horizon 2020 Research and Innovation programme. Grant Agreement No 861002

2.7.2 Dual-fuel injectors

Since the common Diesel direct injectors are not optimized for dual-fuel combustion, dual-fuel injectors have been created by different manufacturers to solve this issue. These injectors normally combine two fluid in one injector, but face the challenge, that injection will be off center in the combustion chamber. Many studies have been carried out using dual-fuel injectors, in order to optimize their usage. Golo and Kontani [99] show the design of a dual-fuel injector example, which used a throttle type nozzle in combination with a hole type. Another example dual-fuel injector is produced by Woodward L'Orange [100] [101] which offer different technologies of delivering both fuels to the combustion chamber, either via a decentralized second needle or a nozzle that has an extra outlet to inject gaseous fuels. Furthermore, Woodward L'Orange started investigating and offering the first prototypes of a Diesel injector with a TWIN nozzle which is capable of delivering low fuel quantities with a stable and optimized spray penetration. However, the influence of the geometric parameters on the spray characteristics is still widely unknown since the only research that has been carried out at the moment this thesis is written was in the bachelor thesis of Bose [102]. However, his investigation still leaves gaps for improvement and the geometrical nozzle influences on the spray behaviour have not been deeply analysed, so that the nozzle can not be adapted to specific engine geometries.

Since neither the dual-fuel injectors nor the Diesel injectors can fully support the dual-fuel engines in all operating conditions, further studies have to be conducted in order to find a solution for these challenges.

This project has received funding from the European Union Horizon 2020 Research and Innovation programme. Grant Agreement No 861002

2.8 Summary and gaps in current research

This last section within this literature review chapter aims to give a short summarization of the current state of the art engine and dual-fuel research. The different heat engine and dual-fuel engines classifications are reviewed. Heat engines can be classified by their combustion location, injector type, ignition type, number of strokes and number of fuels. For the theoretical calculation of the efficiency of compression ignition engines, the idealized Diesel cycle can be used. Dual-fuel engines can be classified by their pilot fuel injection, main fuel injection, operation mode and by the fuels used as pilot and main fuel. As well as the engine emissions from compression ignition engines and the capability of Natural Gas as main fuel to lower the emissions compared to Diesel engines. For the study of the dual-fuel compression ignition combustion events and the fuel distribution, optical engines and Constant Volume Chambers can be used. The optical measurement methods used in in these include Schlieren, Shadowgraphy, Mie-scattering and Laser Induced Fluorescence, captured with high speed imaging. Existing research on dual-fuel combustion has mainly focused on improving combustion efficiency and reducing emissions through variations in pilot injection strategy, fuel substitution ratio and operating conditions mostly through engine testing. However, the interaction between low-load dual-fuel combustion stability, cycle-to-cycle flame development, and the spray characteristics of injectors specifically designed for heavy-duty dual-fuel applications is still not fully understood. Therefore, the author of this thesis identified three gaps which this thesis aims to fill. A first research gap is the limited understanding of how pilot Diesel injection duration and timing affect affect the in-cylinder mixing, ignion and comustion processes, and hence the achievable load and dual-fuel combustion behaviour under low-load dual-fuel operation. This is particularly relevant because low-load operation is often associated with poor combustion stability and reduced Main fuel combustion. Therefore, this thesis investigates different dual-fuel combustion cases in an optical engine to identify operating strategies that achieve high IMEP while minimizing the required Diesel pilot fuel amount. A second research gap concerns the evaluation of flame cycle-to-cycle variation. Conventional analysis methods often focus on global combustion parameters, while spatial flame development is less frequently analysed. To address this, a pixel count based method was developed to evaluate flame development in each cycle relative to the average flame images. A third research gap is related to injector nozzle design for heavy-duty dual-fuel combustion. While conventional nozzle geometries and established spray penetration correlations are well documented, their applicability to novel TWIN nozzle concepts is limited. Therefore, this thesis investigates the influence of different geo-

This project has received funding from the European Union Horizon 2020 Research and Innovation programme. Grant Agreement No 861002

metric parameters of a heavy-duty injector with a TWIN nozzle on the resulting spray characteristics. Finally, existing spray penetration correlations, such as the Hiroyasu and Naber and Siebers approaches, were originally developed for conventional nozzle geometries. Their direct application to the investigated TWIN nozzle can therefore lead to reduced prediction accuracy. To address this limitation, this thesis modifies these calculations by adding a second order linear regression model based on the TWIN geometric parameters. In this way, existing knowledge is applied to a new nozzle concept and extended for improved prediction of the TWIN nozzle spray penetration. Overall, this thesis contributes to improving heavy-duty dual-fuel combustion by linking combustion optimization, optical flame analysis, TWIN nozzle spray characterization, and the adaptation of established spray penetration models to novel nozzle geometries.

This project has received funding from the European Union Horizon 2020 Research and Innovation programme. Grant Agreement No 861002

Chapter 3

Investigation of the dual-fuel combustion

In this chapter the experiments carried out within Burnel University will be described and afterwards the results of the experiments will be discussed and the data analysed. The first section shows the experimental setup for the dual-fuel combustion studies and the approaches to analyse the flame area and cycle-to-cycle variation by analysing the pixel of the average combustion cycle. Parts of the study in this chapter have been previously published in [103].

3.1 Dual-Fuel combustion experiments

In order to observe the dual-fuel combustion, a single cylinder optical compression ignition engine was retrofitted with a gas injector and Natural Gas/Hythane were chosen as main fuels, ignited by a Diesel pilot injection. The pilot fuel was chosen mainly because most engines that are or can be converted for dual-fuel combustion are Diesel engines and need further investigation in order to improve their combustion efficiency and lower their emissions. The main fuels were chosen to be Natural Gas due to its potentially low emissions if it combusts completely and Hythane with a blend of 20% Hydrogen and 80% Natural Gas since it has a potentially faster combustion than Natural Gas, which is one of the set backs of converting Diesel engines for dual-fuel combustion.

3.1.1 Single cylinder optical engine

The experiments to study the Diesel-NG and Diesel-Hythane combustion were carried out at an optical single cylinder engine from Ricardo. The engine was originally designed to observe Diesel compression ignition combustion with focus on the spray

This project has received funding from the European Union Horizon 2020 Research and Innovation programme. Grant Agreement No 861002

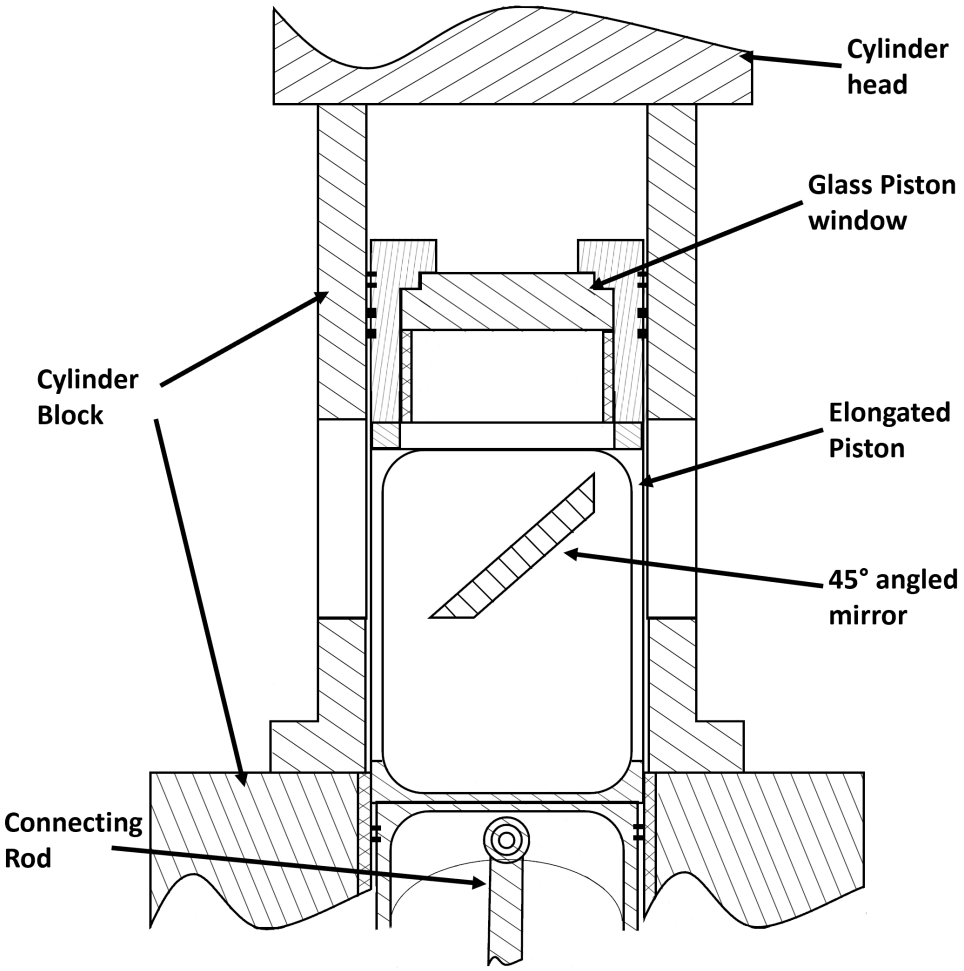


Figure 3.1: Schematics of the optical single cylinder engine

penetration and distribution. For this study it was equipped with a Natural Gas injector in the intake manifold. The Diesel injector remained the original, which was designed for pure Diesel combustion. The engine is built in a Bowditch extended piston design with an optical window in the piston top of 56 mm diameter and also has the possibility to install side view windows for a planar observation of the chamber or access for illumination sources. For the observation of the dual-fuel combustion only the bottom access to the combustion chamber via the piston window was used. A Diesel direct injector from Delphi is mounted in the cylinder head in the middle of the combustion chamber and the gas injector from Bosch was retrofitted into the air intake manifold. The cylinder head is from a Ford 2.0 liter ZSD 420 Duratorq turbocharged DI Diesel engine. The schematics of the engine are shown in Figure 3.1 and the injectors can be seen Figure 3.2.

The water and oil circuits of the engine were preheated before each test, to ensure operation conditions as close as possible to a constantly running commercial engine.

This project has received funding from the European Union Horizon 2020 Research and Innovation programme. Grant Agreement No 861002

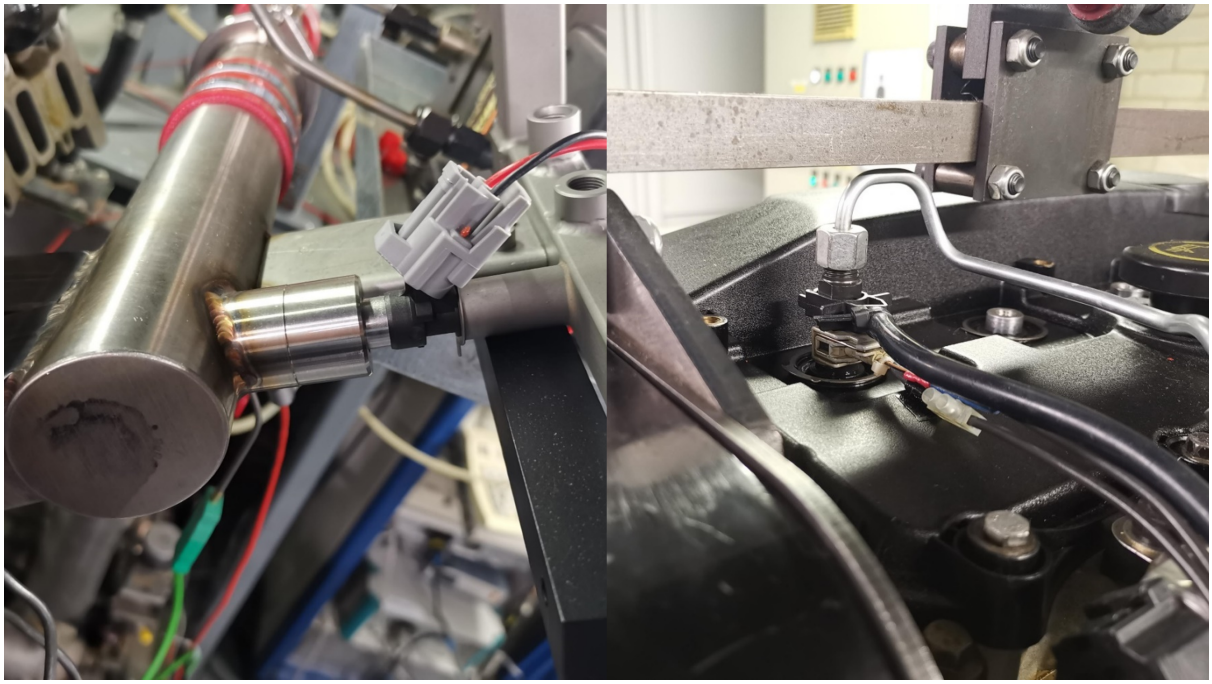


Figure 3.2: Gas Injector (left) and Diesel injector (right)

Since it is an optical engine, the operation conditions had to be different from conventional engines. The runtime had to be limited to a minimum in order to prevent the optical parts from being damaged. Also the pressure rise rate was kept to a maximum of 10 bar/CA to avoid damaging the engine windows. Furthermore, a maximum of 22 image cycles of combustion were recorded for each case, since the window in the piston top was getting polluted during testing and had to be cleaned. In parallel 50 cycles of the pressure were measured, but could not be exactly overlapped with the image recordings due to restrictions from the control system. For the images a power analysis was carried out to assess the whether 22 cycles would suffice. For all investigated operating conditions, statistical power values greater than 90% were obtained, confirming that the recorded image samples were sufficient to capture the relevant cycle-to-cycle behaviour. In parallel, convergence analyses of the cycle-averaged pressure and HRR traces demonstrated convergence within 40-50 cycles for all test cases. These results indicate that the selected sample sizes were adequate to ensure representative and statistically reliable combustion and imaging analyses.

3.1.2 High speed recording equipment

The external illumination of the combustion chamber was implemented with a copper vapor Laser from Oxford Lasers. The Laser repetition rate was 10 000 Hz with a pulse duration of 10-40 ns and a wavelength of 512 nm. This ensured recording the injection

This project has received funding from the European Union Horizon 2020 Research and Innovation programme. Grant Agreement No 861002

Table 3.1: Properties of the optical equipment and engine used in this study

Equipment	Parameters	Values
Ricardo Optical single cylinder engine	Bore	86 mm
	Stroke	86 mm
	Swept Volume	499 cm^3
	Compression Ratio	16:1
	Piston Window Diameter	56 mm
Oxford Lasers copper vapour Laser	Wavelength	512 nm
	Pulse duration	10-40 ns
	Repetition rate	10 000 Hz
Photron Fastcam Mini AX 100	Framerate	10 000 fps
	Shutter Speed	950 000 1/s
	Resolution	512 x 512 Pixel
Nikon UV Nikkor Lens	Focal length	105 mm
	Aperature	f 4.5

and combustion events with a minimum motion blur. The images were recorded with a PHOTRON Fastcam Mini AX 100 with a matching framerate of also 10 000 fps and a shutter speed of 950 000 1/s respectively with a shutter opening duration of approximately 1.05 µs per frame, which was the minimum duration possible for the camera in order to reduce motion blur to a minimum. The image resolution was set to the highest possible square resolution for recording with the selected framerate of 512 x 512 pixels to record images through the window in the piston top. The lens used to capture the images was a Nikon UV Nikkor 105mm f/4.5s. The details of the experimental set up are summarized in Table 3.1.

3.1.3 Experimental setup

The Laser was connected to a beam expander at the end of a optical fiber to illuminate the combustion chamber through the 45° angled mirror below the window in the extended piston top. The Laser radiation was then reflected in the combustion chamber, back to the mirror and from there it was recorded by the camera. The camera and Laser were synchronized via TTL signals from the Laser to trigger the camera frames. The schematics of the optical test bay are shown in Figure 3.3.

Simultaneous to the optical recordings, the pressure data was recorded with a Kistler In-Cylinder pressure sensor and National Instruments cRIO 9066 Data acquisition system using a code written in LabView. The data was recorded with steps of 0.2 ° CA with a encoder attached to the crankshaft. The pressure curves were used to calculate the IMEP of each combustion case and therefore evaluate the released

This project has received funding from the European Union Horizon 2020 Research and Innovation programme. Grant Agreement No 861002

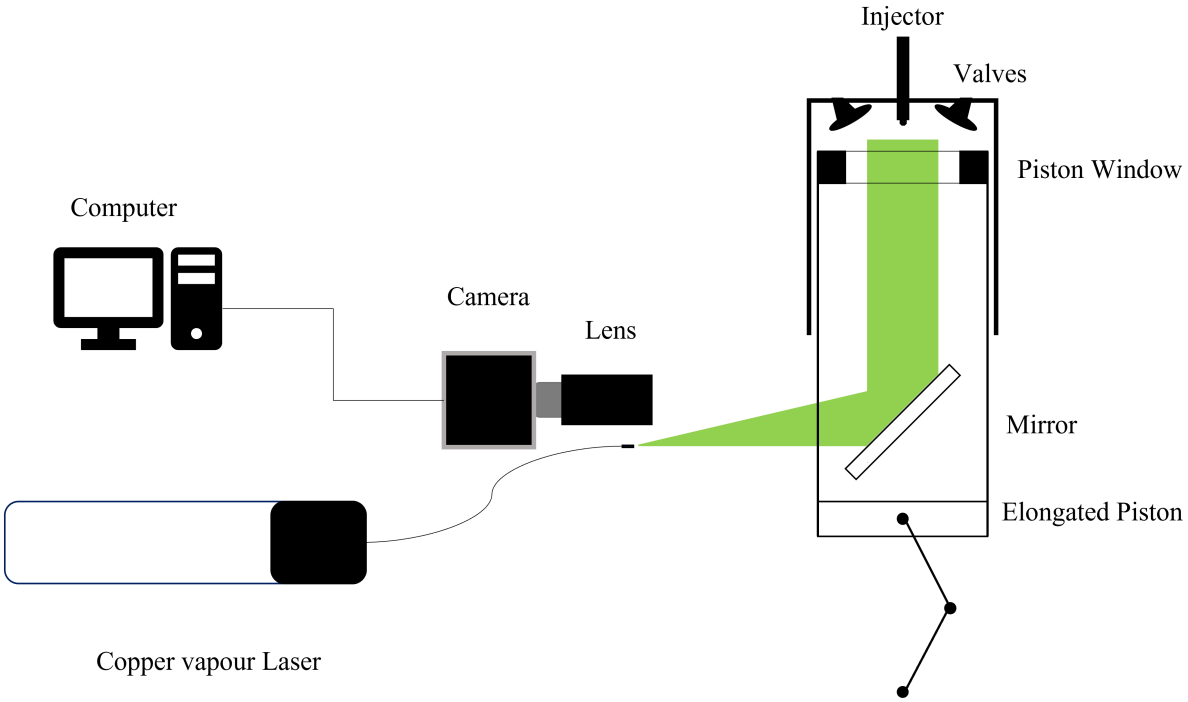


Figure 3.3: Schematics of the optical test bay

energy of each. Various injection timings and durations were combined to observe the flame propagation and area within the combustion chamber. The injectors were triggered via a National instruments DIDS system with the recommended energization curves from the manufacturers. For all the experiments in this study the engine speed was constantly kept to 1200 rpm to reduce the stress on the optical parts and prevent damage to the engine. The injection pressure for the Diesel was kept to 500 bar in order to be able to observe dual-fuel combustion with a low load. For the NG injector it was kept to 5 bar, since this was the minimum recommended pressure from the manufacturer for a stable mass flow. Backflow was prevented by a reed valve in the intake air pipe since it could also be heated and therefore it needed to be avoided that the air fuel mixture reaches the thermoelement. Furthermore, the Bosch gas injector was mounted in close proximity to the intake valves, resulting in a very short flow path. In combination with the non-return valve used to prevent backflow and the very early injection timings employed in this study, it was assumed that the fuel-air mixture was fully premixed before entering the combustion chamber upon intake valve opening. Therefore, the transport time between the commanded injection event and the arrival of the fuel at the intake valves was considered negligible in this study. The system to control the injector as well as to have a synchronized pressure and crank angle acquisition system, was set up by this author for these experiments. Figure 3.4 shows the code in Labview where A is the frontend and B is the code as block diagram.

This project has received funding from the European Union Horizon 2020 Research and Innovation programme. Grant Agreement No 861002

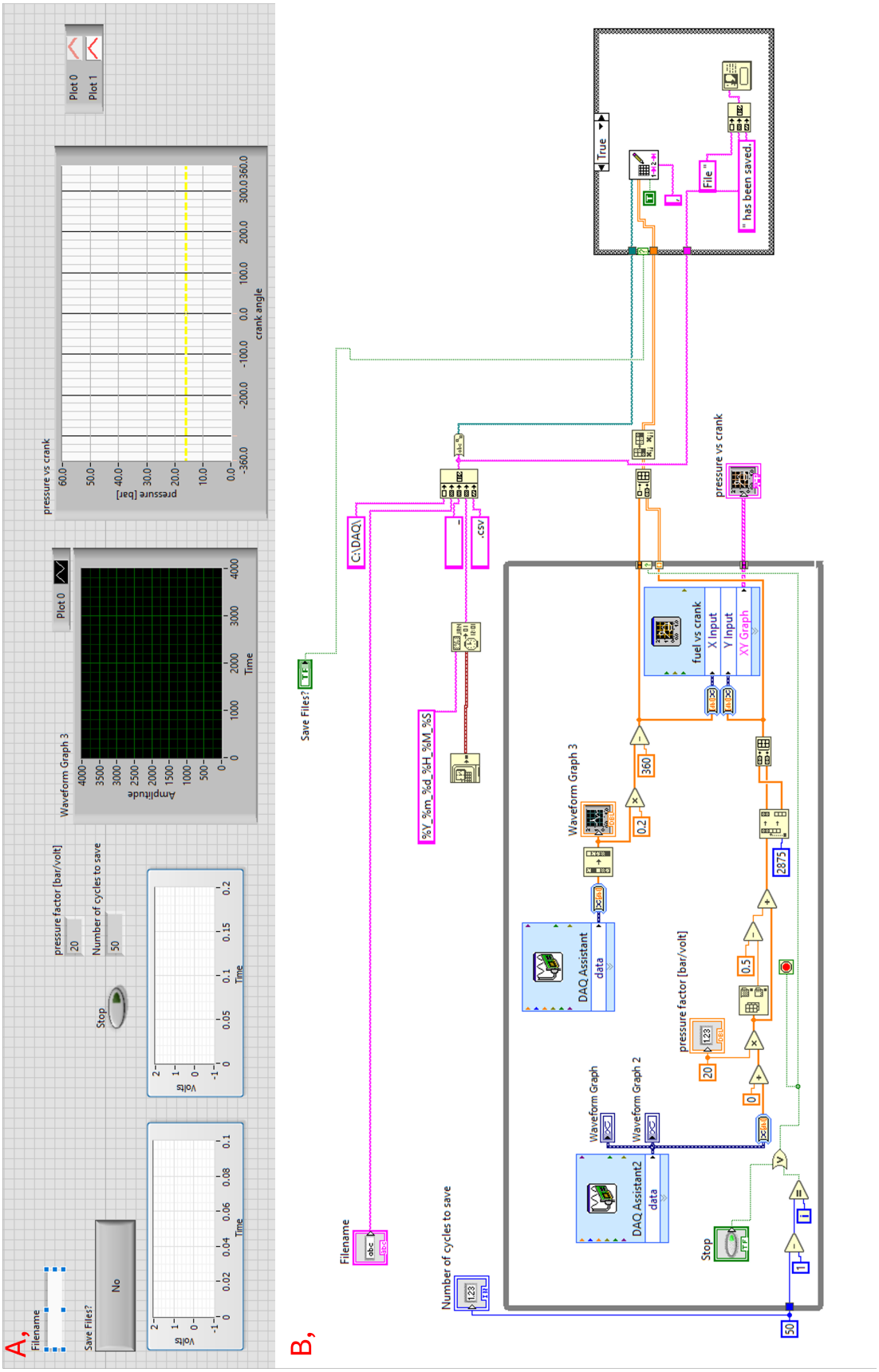


Figure 3.4: Data acquisition system in Labview with A, frontend and B, backend as block diagram

This project has received funding from the European Union Horizon 2020 Research and Innovation programme. Grant Agreement No 861002

A total of 54 test cases were selected for presentation in this thesis. The study aimed to improve the understanding of how pilot Diesel injection timing, injection duration, and fuel substitution influence combustion stability, flame development, and Diesel fuel demand during low-load dual-fuel operation. The individual test cases were therefore not intended to represent isolated operating points, but rather a systematic variation of key combustion parameters. This approach enabled the investigation of the conditions required to achieve stable dual-fuel combustion with high Natural Gas/Hythane substitution rates while minimizing the required Diesel pilot fuel quantity. Furthermore, the optical measurements allowed the influence of these parameters on cycle-to-cycle flame development to be assessed, providing insight beyond conventional pressure-based combustion analysis. Cases A1 - A4 represent the pure Diesel combustion with different injection durations and timings with split injection. The optimal timing for these was determined before the optical experiments by optimizing the IMEP of the combustion with a pure metal piston. Cases B1 - B13 represent dual-fuel combustion with a single Diesel pilot injection and Natural Gas as main fuel. Cases C1 - C7 represent dual-fuel combustion with split Diesel injection and 1.5 ms Natural Gas injection. Similar to this, cases D1 - D12 represent the dual-fuel combustion with 2 ms Natural Gas injection and minimum Diesel split injection. Cases E1 - E7 are similar to cases D1 - D12 but with a higher Diesel amount. Cases F1 - F7 have a minimum amount first Diesel injection with minimum 10 ° CA before TDC and a second minimum amount Diesel injection after TDC. The remaining cases G1 - G5 were dual-fuel combustion cases similar to F1 - F7 but with Hythane as main fuel. For easier readability the injection durations of the Diesel will be represented as t_{D} and the injection durations for Natural Gas as t_{NG} . Accordingly, the Diesel injection timings will be represented as θ_{D} and the Natural Gas injection timings as θ_{NG}. The Diesel injection timings were based on previous experiments conducted to determine injection settings that resulted in stable Diesel combustion while maintaining a pressure rise rate below 10 bar/CA. The Natural Gas injection timings were selected using an injection duration of 1.5 ms as the minimum injection duration, as the objective of this study was to investigate dual-fuel combustion at a meaningful substitution rate. From this baseline, the Natural Gas injection duration was increased in 0.5 ms steps. The summarization of the injection durations, fuel masses and injection timings Before Top-Dead-Center (BTDC) for all cases are shown in Table 3.2. For the Diesel the fuel amount was measured for each injection timing by injecting into a container 100 times and then measuring the average amount per injection. For the Main fuel the mass flow rate was measured in a coriolis measurement pipe and then calculated depending on the injection duration.

This project has received funding from the European Union Horizon 2020 Research and Innovation programme. Grant Agreement No 861002

Table 3.2: Dual-fuel test cases injection duration, mass and timing

Case	Diesel injec. duration [ms] t_{D}	NG injec. duration [ms] t_{NG}	Diesel mass approximation [mg]	NG mass approximation [mg]	Diesel injec. timing [°CA before TDC] θ_{D}	NG injec. timing [°CA before TDC] θ_{NG}
A1	0.468 + 0.468	-	2 x 3.62	-	10+5	-
A2	0.4 + 0.4	-	2 x 1.83	-	10+5	-
A3	0.45 + 0.45	-	2 x 2.87	-	10+5	-
A4	0.45 + 0.45	-	2 x 2.87	-	14+5	-
B1	0.35	2	0.79	1.77	25	300
B2	0.35	2	0.79	1.77	20	300
B3	0.486	1.5	3.62	1.29	5	300
B4	0.486	1.5	3.62	1.29	10	300
B5	0.486	1.5	3.62	1.29	12	300
B6	0.486	2	3.62	1.77	5	300
B7	0.486	2	3.62	1.77	12	300
B8	0.486	2	3.62	1.77	14	300
B9	0.486	2	3.62	1.77	16	300
B10	0.486	2	3.62	1.77	18	300

This project has received funding from the European Union Horizon 2020 Research and Innovation programme. Grant Agreement No 861002

Table 3.2: Dual-fuel test cases injection duration, mass and timing

Case	Diesel injec. duration [ms] t_{D}	NG injec. duration [ms] t_{NG}	Diesel mass approximation [mg]	NG mass approximation [mg]	Diesel injec. timing [°CA before TDC] θ_{D}	NG injec. timing [°CA before TDC] θ_{NG}
B11	0.486	2.5	3.62	2.25	12	300
B12	0.486	2.5	3.62	2.25	14	300
B13	0.55	1.5	4.51	1.29	12	300
C1	0.3 + 0.4	1.5	0.3 + 1.83	1.29	17+0	300
C2	0.35 + 0.4	1.5	0.79 + 1.83	1.29	10+(-3)	300
C3	0.35 + 0.4	1.5	0.79 + 1.83	1.29	12+(-3)	300
C4	0.35 + 0.4	1.5	0.79 + 1.83	1.29	14+(-3)	300
C5	0.35 + 0.4	1.5	0.79 + 1.83	1.29	15+(-2)	300
C6	0.4 + 0.4	1.5	2 x 1.83	1.29	5+0	300
C7	0.44 + 0.44	1.5	2 x 2.72	1.29	5+0	300
D1	0.4 + 0.35	2	1.83 + 0.79	1.77	12+(-2)	300
D2	0.35 + 0.4	2	0.79 + 1.83	1.77	12+(-3)	300
D3	0.35 + 0.4	2	0.79 + 1.83	1.77	12+(-2)	300
D4	0.35 + 0.4	2	0.79 + 1.83	1.77	20+0	300

This project has received funding from the European Union Horizon 2020 Research and Innovation programme. Grant Agreement No 861002

Table 3.2: Dual-fuel test cases injection duration, mass and timing

Case	Diesel injec. duration [ms] t_{D}	NG injec. duration [ms] t_{NG}	Diesel mass approximation [mg]	NG mass approximation [mg]	Diesel injec. timing [°CA before TDC] θ_{D}	NG injec. timing [°CA before TDC] θ_{NG}
D5	0.35 + 0.4	2	0.79 + 1.83	1.77	15+0	300
D6	0.35 + 0.4	2	0.79 + 1.83	1.77	30+0	300
D7	0.35 + 0.4	2	0.79 + 1.83	1.77	30+2	300
D8	0.35 + 0.4	2	0.79 + 1.83	1.77	35+0	300
D9	0.38 + 0.38	2	2 x 1.05	1.77	12+(-2)	300
D10	0.35 + 0.35	2	2 x 0.79	1.77	16+5	300
D11	0.35 + 0.35	2	2 x 0.79	1.77	10+5	300
D12	0.35 + 0.35	2	2 x 0.79	1.77	25+10	300
E1	0.4 + 0.4	2	2 x 1.83	1.77	10+6	300
E2	0.4 + 0.4	2	2 x 1.83	1.77	10+5	300
E3	0.4 + 0.4	2	2 x 1.83	1.77	11+7	300
E4	0.4 + 0.4	2	2 x 1.83	1.77	15+5	300
E5	0.4 + 0.4	2	2 x 1.83	1.77	16+5	300
E6	0.486 + 0.486	2	2 x 3.62	1.77	10+5	300

This project has received funding from the European Union Horizon 2020 Research and Innovation programme. Grant Agreement No 861002

Table 3.2: Dual-fuel test cases injection duration, mass and timing

Case	Diesel injec. duration [ms] t_{D}	NG injec. duration [ms] t_{NG}	Diesel mass approximation [mg]	NG mass approximation [mg]	Diesel injec. timing [°CA before TDC] θ_{D}	NG injec. timing [°CA before TDC] θ_{NG}
F1	0.33 + 0.33	2	2 x 0.37	1.77	15+(-2)	300
F2	0.3 + 0.3	2	2 x 0.3	1.77	15+(-2)	300
F3	0.3 + 0.33	2	0.3 + 0.37	1.77	13+(-2)	300
F4	0.3 + 0.33	2	0.3 + 0.37	1.77	12+(-2)	300
F5	0.3 + 0.33	2	0.3 + 0.37	1.77	12+(-1)	300
F6	0.3 + 0.33	2.5	0.3 + 0.37	2.25	12+(-1)	300
F7	0.3 + 0.33	4 + 4	0.3 + 0.37	2 x 3.7	15+(-1)	360+320
G1	0.3 + 0.33	4	0.3 + 0.37	3.7	15+(-1)	360
G2	0.3 + 0.33	2	0.3 + 0.37	1.77	15+(-1)	360
G3	0.3 + 0.33	4 + 2	0.3 + 0.37	3.7 + 1.77	13+(-1)	360+320
G4	0.3 + 0.33	3 + 3	0.3 + 0.37	2 x 2.7	12+(-1)	360+320
G5	0.3 + 0.33	4 + 4	0.3 + 0.37	2 x 3.7	12+(-1)	360+320

This project has received funding from the European Union Horizon 2020 Research and Innovation programme. Grant Agreement No 861002

During the tests, the aim was to improve the IMEP of each dual-fuel combustion while simultaneously using a high substitution rate of the main fuel. Furthermore, Hythane was used in the cases G1 - G5 to have a comparison between the NG and Hythane in its combustion duration, ignition delay and resulting IMEP. The relative air/-fuel ratio λ was not measured during the present study. As a result, conclusions regarding the degree of premixing were based on the selected injection timings and durations, together with the combustion behaviour observed from the cylinder pressure traces and high-speed imaging recordings. The early injection timings provided a substantial premixing period, while the pressure and imaging data offered further insight into the resulting combustion process. Therefore, the discussion of mixture formation and premixing is based on the available experimental observations rather than direct measurements of the mixture composition. After investigating the dual-fuel combustion, different nozzles for the injection of the pilot fuel were investigated at Woodward L'Orange.

3.2 IMEP, NetHRR and combustion speed calculations

The dual-fuel combustion and pure Diesel combustion cases were compared by their IMEP and Net Heat Release Rate (HRR). In order to calculate the IMEP, the cylinder volume/° CA has to be calculated first. Equation 3.1 shows how it is calculated. Where

V is the cylinder volume

V_c is the clearance volume

B is the cylinder bore

l is the connection rod length

a is the crank radius

s is the distance between the crankshaft and the piston pin axes

$$V = V_c + \frac{\pi B^2}{4}(l + a - s) \tag{3.1}$$

The distance between the crankshaft and the piston pin axes is calculated by the crank radius, the crank angle and the connection rod length. Equation 3.2 shows how it is calculated. Where

θ is the crank angle

This project has received funding from the European Union Horizon 2020 Research and Innovation programme. Grant Agreement No 861002

$$s = a\cos\theta + \sqrt{(l^2 - a^2\sin^2\theta)} \tag{3.2}$$

The compression ratio can be calculated by the clearance volume and the displacement volume. Equation 3.3 shows how it is calculated. Where

r_c is the compression ratio

V_c is the displacement volume

$$r_c = \frac{V_d + V_c}{V_c} \tag{3.3}$$

The displacement volume can be calculated by the Bore and the stroke, which is the half of the crank radius. Equation 3.4 shows how it is calculated. Where

$$V_d = \frac{\pi B^2}{4\frac{a}{2}} \tag{3.4}$$

With these, the Equation 3.1 can be changed to Equation 3.5.

$$V = V_c\{1 + \frac{1}{2}[r_c - 1][\frac{l}{a} + 1 - \cos\theta - \sqrt{\frac{l^2}{a^2} - \sin^2\theta}]\} \tag{3.5}$$

With the volume, displace volume and pressure, the IMEP can be calculated, as shown in Equation 3.6.

$$IMEP = V_d \int p\,dV \tag{3.6}$$

After the IMEP was calculated, the Heat Release Rate was calculated as shown in Equation 3.7, where

γ is the ratio of specific heats, in this calculations it was assumed to be 1.4

$$HRR = \frac{\gamma}{\gamma - 1} P\frac{dV}{d\theta} + \frac{1}{\gamma - 1} V\frac{dP}{d\theta} \tag{3.7}$$

The summarized $IMEP_{sum}$ and NetHRR for each case are listed in Table 3.3.

This project has received funding from the European Union Horizon 2020 Research and Innovation programme. Grant Agreement No 861002

Table 3.3: Summarized IMEP and NetHRR for cases A1-G5

Case	$IMEP_{sum}$ [bar]	$NetHRR$ [kJ]	**Case**	$IMEP_{sum}$ [bar]	$NetHRR$ [kJ]
A1	3.63	2.42	**D4**	2.08	1.81
A2	2.55	1.92	**D5**	2.67	2.01
A3	4.59	2.84	**D6**	3.65	2.57
A4	2.18	1.64	**D7**	2.76	2.11
B1	-0.18	0.67	**D8**	2.85	2.18
B2	0.04	0.67	**D9**	3.11	2.31
B3	0.73	1.03	**D10**	0.66	0.96
B4	-0.05	0.70	**D11**	0.94	1.09
B5	-0.04	0.68	**D12**	0.73	0.95
B6	0.26	0.77	**E1**	2.60	1.88
B7	0.90	1.09	**E2**	2.11	1.59
B8	0.77	1.01	**E3**	2.25	1.59
B9	0.70	1.00	**E4**	0.51	0.9
B10	0.62	0.96	**E5**	0.97	1.06
B11	0.67	0.94	**E6**	4.31	2.71
B12	0.60	0.90	**F1**	1.84	1.56
B13	1.11	1.14	**F2**	1.74	1.54
C1	1.81	1.52	**F3**	2.95	2.04
C2	3.02	2.09	**F4**	3.10	2.11
C3	3.08	2.28	**F5**	2.82	1.99
C4	1.70	1.51	**F6**	2.99	2.08
C5	1.73	1.47	**F7**	6.53	3.68
C6	0.93	1.17	**G1**	4.68	2.91
C7	1.42	1.34	**G2**	3.72	2.40
D1	3.06	2.13	**G3**	4.35	2.75
D2	2.96	2.24	**G4**	2.73	2.14
D3	2.97	2.19	**G5**	7.88	4.42

After the IMEP, the mass fraction burned was calculated to evaluate the combustion speed. It is calculated by the pressure difference due to the combustion of each step in relation to the overall pressure difference created by the combustion. The mass fraction burned CA10, CA50, CA90 After Top-Dead-Center (ATDC) and combustion duration CA90-CA10 in °CA for each case are listed in Table 3.4.

This project has received funding from the European Union Horizon 2020 Research and Innovation programme. Grant Agreement No 861002

Table 3.4: CA10, CA50, CA90 and combustion duration for cases A1-G5

Case	CA10 ° CA ATDC	CA50 ° CA ATDC	CA90 ° CA ATDC	Combustion duration ° CA	**Case**	CA10 ° CA ATDC	CA50 ° CA ATDC	CA90 ° CA ATDC	Combustion duration ° CA
A1	5.70	12.19	32.37	26.67	**D4**	-0.65	13.67	27.15	27.80
A2	4.74	10.74	21.11	16.37	**D5**	1.82	13.18	30.86	29.04
A3	7.93	13.21	45.34	37.41	**D6**	-4.51	13.59	27.40	31.91
A4	0.30	5.79	19.32	19.02	**D7**	-5.17	12.00	24.16	29.33
B1	-3.84	7.52	18.21	22.05	**D8**	-3.15	14.66	25.68	28.83
B2	-2.41	5.66	18.11	20.52	**D9**	2.33	14.59	36.76	34.43
B3	-0.66	14.41	21.63	22.29	**D10**	2.76	11.20	20.10	17.34
B4	4.41	11.31	17.96	13.55	**D11**	6.32	12.78	20.09	13.77
B5	3.10	9.78	17.41	14.31	**D12**	1.32	8.83	18.54	17.22
B6	3.51	13.98	21.89	18.38	**E1**	6.18	11.29	22.63	16.45
B7	-1.03	8.45	18.33	19.36	**E2**	6.34	11.58	20.38	14.04
B8	-0.53	6.81	17.75	18.28	**E3**	5.42	10.11	18.99	13.57
B9	-2.74	5.81	17.68	20.42	**E4**	1.41	9.13	18.79	17.38
B10	-3.35	5.25	17.93	21.28	**E5**	1.95	10.65	20.19	18.24
B11	2.93	9.59	18.98	16.05	**E6**	15.08	29.42	65.66	50.58
B12	1.44	8.04	18.51	17.07	**F1**	-3.77	4.40	17.97	21.74
B13	-3.40	7.06	16.34	19.74	**F2**	-4.21	4.70	17.42	21.63
C1	-2.67	11.04	20.38	23.05	**F3**	-2.11	11.03	19.31	21.42
C2	5.13	15.36	32.29	27.16	**F4**	-1.22	11.88	19.95	21.17
C3	3.43	16.18	37.81	34.38	**F5**	-0.96	11.70	20.33	21.29
C4	0.54	13.11	21.51	20.97	**F6**	-1.50	11.64	20.45	21.95
C5	-0.81	11.99	20.53	21.34	**F7**	0.58	7.36	20.42	19.84
C6	8.33	19.76	29.02	20.69	**G1**	0.06	9.63	21.57	21.51
C7	8.89	21.52	31.02	22.13	**G2**	-0.59	9.89	19.51	20.10
D1	2.98	12.87	29.83	26.85	**G3**	-0.23	9.21	21.62	21.85
D2	2.33	15.56	36.20	33.87	**G4**	5.07	14.80	28.87	23.80
D3	2.51	14.81	35.26	32.75	**G5**	1.13	7.68	19.94	18.81

This project has received funding from the European Union Horizon 2020 Research and Innovation programme. Grant Agreement No 861002

3.3 Dual-fuel combustion analysis

3.3.1 Combustion image analysis

After carrying out the dual-fuel experiments and recording the images, the different test case recordings were analysed. The captured images were processed with a code written in Python 3.8 using the packages Scikit-Image 0.18.3, OpenCV 4.0.1, ImageIo 2.9.0, Numpy 1.21.2, Matplotlib 3.4.3, Scipy 1.7.1, and PILLOW 8.4.0. For the Python distribution platform Anaconda 4.12.0 was chosen and Spyder 5.1.5 was used as Python Integrated Development Environment. The code is used to firstly identify the region of the piston window as shown by image [A] to image [B] in Figure 3.5. The images are masked and cropped as shown by image [B] to image [C] in Figure 3.5. These steps exclude all the unnecessary information and unwanted laser reflections in the recordings. Afterwards, the cropped and masked images are binarized with a threshold, with a minimum pixel value of 75, set to show only the flame contours as shown in image [C] to image [D] in Figure 3.5. This change was implemented since this study aims to analyse the flame area and not the intensity of individual regions.

Similar to the approach to the combustion images reported in [36] after these processing steps, the binarized images are filtered with an area closing function to fill the holes within the flames below a threshold area of 25 pixels to make the image uniformly as shown by image [E] to image [F] in Figure 3.6. Furthermore, the area opening function is applied to eliminate small islands below a threshold area of 10 pixels as depicted in Figure 3.6 [F] to image [G]. Afterwards a gaussian filter is applied to smooth the contours of the flame, where the sigma of the filter was chosen to be 0.2. The image processing parameters were determined empirically. The chosen values provided effective noise reduction and contour smoothing while preserving the overall flame shape and size. The effects of the filter would be minor to not falsify the original outlines as shown in image [G] to [H] in Figure 3.6.

Multiple cycles need to be recorded in order to build images for the average flame structure. The maximum number of recordings per test case for the Mini AX 100 at 512 x 512 pixels are 21829 images. This amount was taken for each case and it captured about 22 combustion cycles at 1200 rpm +- 10 rpm. The program starts with the first image of the pilot injection and saves the following 100 pictures to a new folder for each cycle. With these images the average per test case is built by stacking the images and it is visualized with the Matplotlib.pyplot "turbo" colormap, where the regions with the highest concentration of flames present are shown in red (100 % overlap of the pixels) and the lowest in blue (0 % overlap). Figure 3.7 shows the schematics for building the average pictures.

This project has received funding from the European Union Horizon 2020 Research and Innovation programme. Grant Agreement No 861002

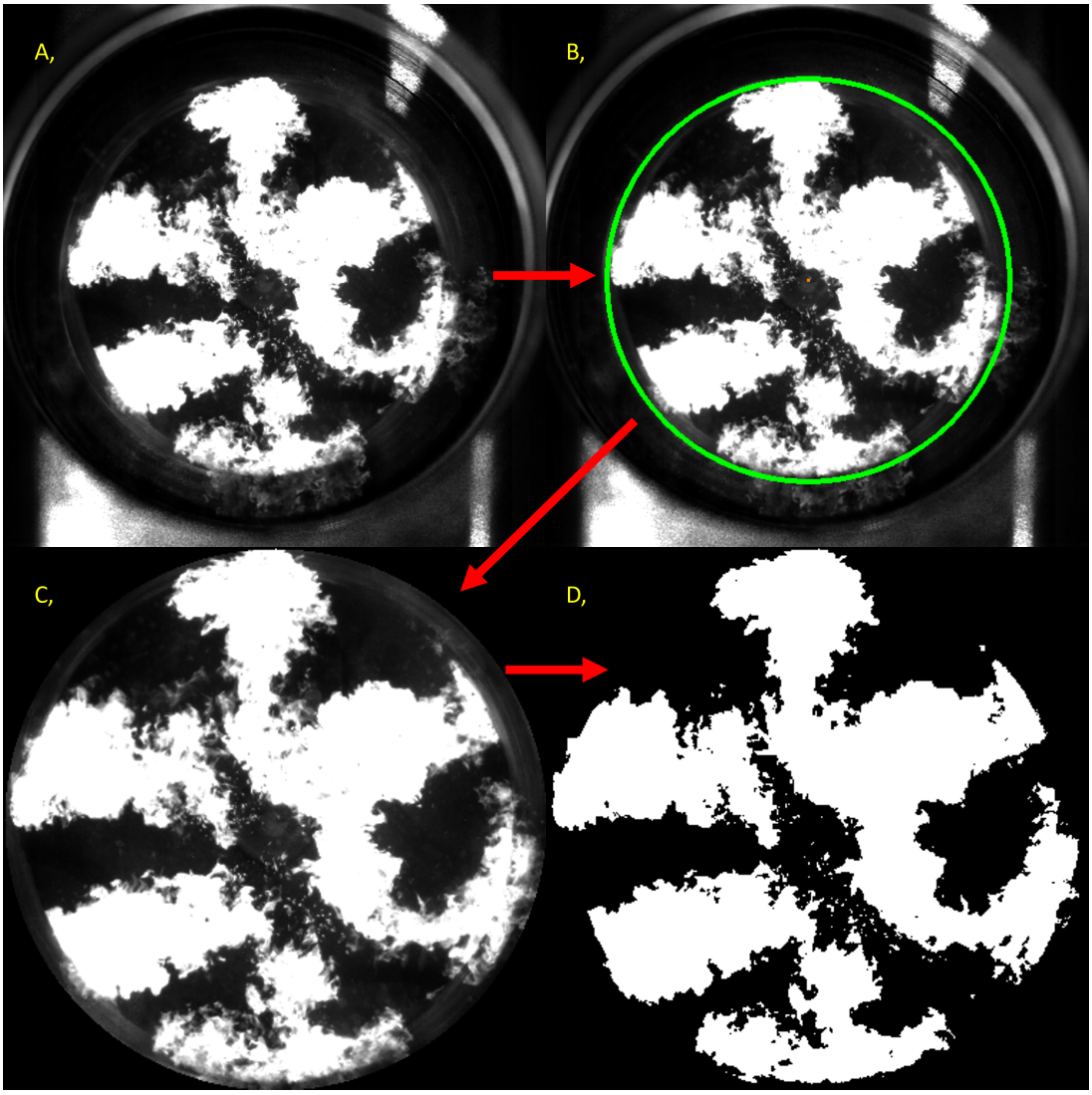


Figure 3.5: Image processing via Masking and Binarization

The last step is to analyse the flame area pixel distribution and its change during the combustion process. This was realized by counting the number of the non-zero pixels of the overlap areas and dividing them by the total number of pixels in the average image, to create the curve called "overlap". Since the average images were created by stacking 22 images which can either have a pixel value of 255 (flame present) or 0 (no flame observed), the maximum value of the overlap pixels is also 255. As a result, any pixel in the average image can only take a fixed value, for example a pixel where 13 cycles overlap would take the value shown in Equation 3.8.

$$PixelValue = \frac{13}{22} \times 255 \approx 150.68 \tag{3.8}$$

In order to analyse the cycle-to-cycle variation in the combustion sites and identify

This project has received funding from the European Union Horizon 2020 Research and Innovation programme. Grant Agreement No 861002

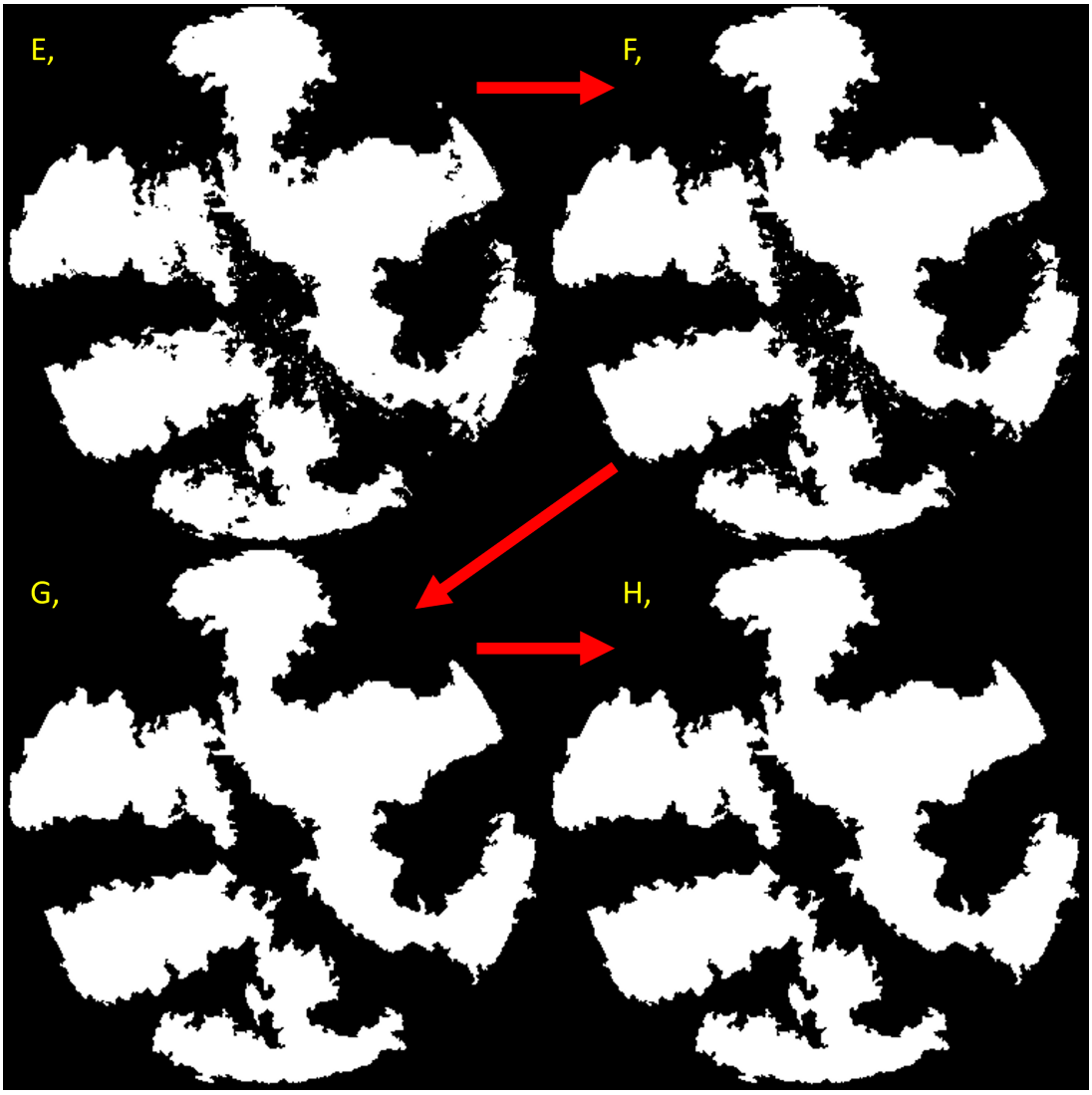


Figure 3.6: Image processing via Scikit-Image and Scipy

the location of most combustion taking place, the level of overlap was then applied to the average images. Firstly, when the threshold is set to 35 for pixels of the averaged images, pixels with combustion in 3 or more cycles will be included. As the threshold is increased to 82, pixels with combustion in 7 or more cycles are shown. In turn, the minimum number of cycles with overlap combustion pixels will increase to 11, 15 and 18, as the threshold is raised to 128, 175 and 210. The overlap thresholds were selected to represent different levels of cycle-to-cycle repeatability. Since the average images were generated from 22 combustion cycles, the chosen threshold levels correspond to combustion occurring in an increasing number of overlaps, which allows the identification of combustion regions which developed flames in most combustion cycles. The schematics of this step are illustrated in Figure 3.8.

In the last step, the deviation of threshold images at a given crank angle from the

This project has received funding from the European Union Horizon 2020 Research and Innovation programme. Grant Agreement No 861002

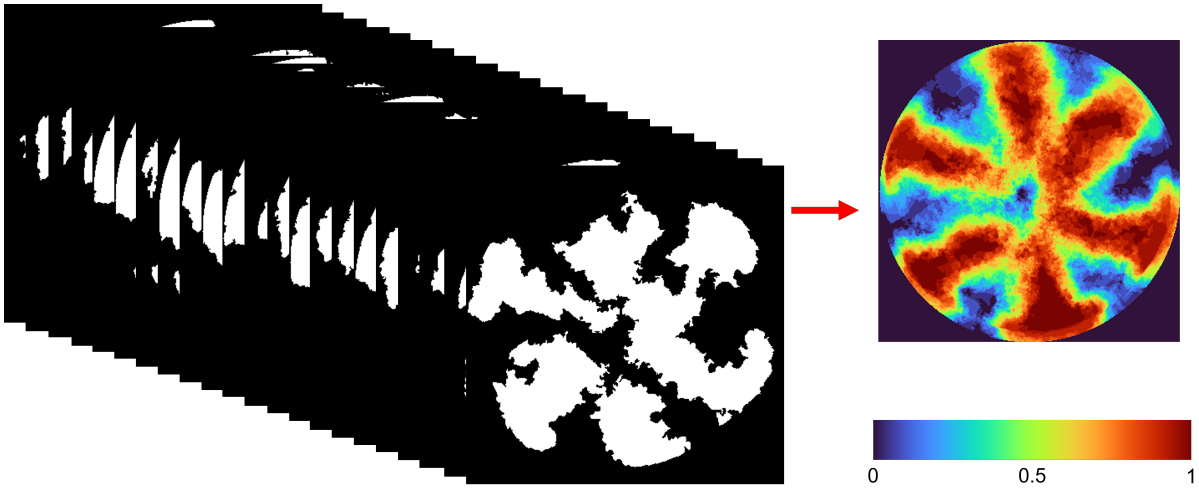


Figure 3.7: Image stacking to show flame probability distribution

complete overlap images was determined by dividing the number of images of a given threshold (for example 150 so that minimum 13 cycles have to overlap) to the amount of the complete overlap pictures (no threshold, all overlapping pixels are counted) and then subtracting it from 1, as shown in the Equation 3.9:

$$Deviation = 1 - \frac{Pixelcount_{thresholded}}{Pixelcount_{completeOverlap}} \tag{3.9}$$

This was done to show the cycle-to-cycle variation in more comprehensible way, since non variant cycles would be overlapping as much as possible and nearly never reach the maximum deviation of 1. For cases with stronger combustion the pixel analysis is deteriorated since the residues pollute the piston window and limit the camera view. Therefore, the deviation of the threshold curves to the complete overlap serves as comprehensive comparison.

This project has received funding from the European Union Horizon 2020 Research and Innovation programme. Grant Agreement No 861002

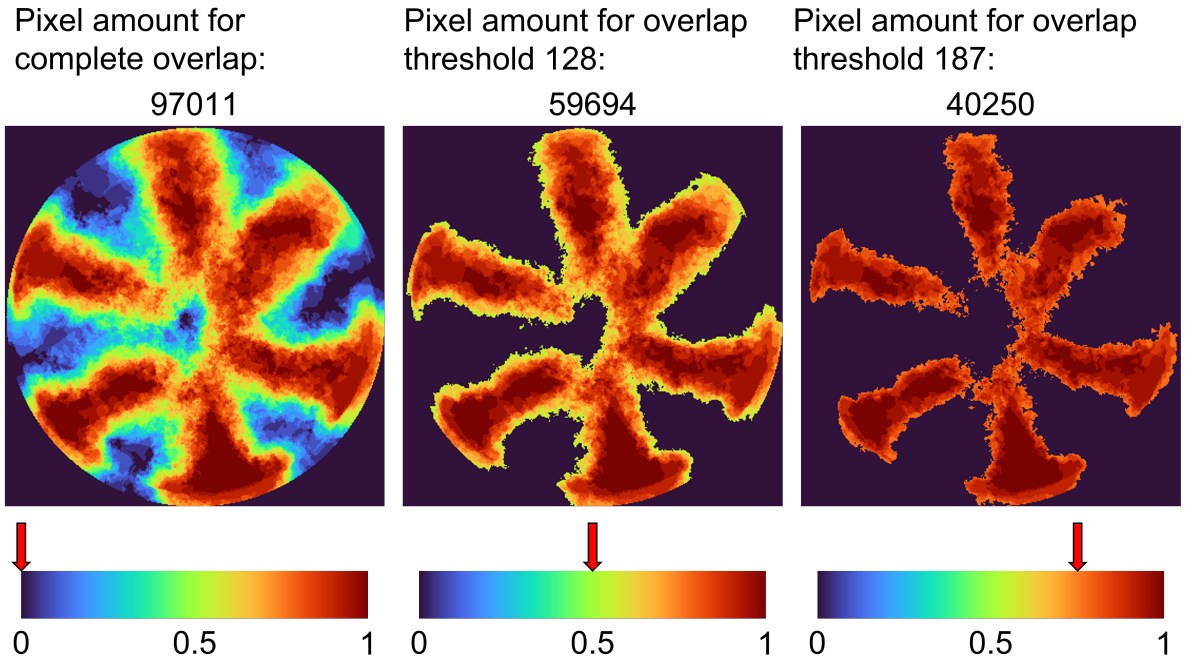


Figure 3.8: Complete and Thresholded average Flame images

3.3.2 Analysis of dual-fuel combustion processes

Based on the above analysis, the results for the cases A1 until G5 are shown in Figure 3.9 to Figure 3.38. In each Figure, the left graph shows the complete overlap pixels curve (overlap) together with the in-cylinder pressure (Cylinder pressure) and the thresholded overlap curves for 3, 7, 11, 15 and 18 cycles overlapping (indicated by their thresholds in the curve descriptions) and the right one showing the deviation curves for the different thresholds with similar description. To aid the analysis, the graphs also include markers for the injection timings, the Crank Angles where 10%, 50% and 90% of mass fractions were burnt (CA10, CA50 and CA90). For improved readability, the optical combustion images are presented in groups of four cases. This grouping is solely intended to reduce the amount of information displayed in a single figure and does not represent a separate categorization of the investigated operating conditions. The scientific discussion is always based on the complete set of cases within a given series (e.g., Series A, B, or C), and conclusions are drawn from the comparison of all cases belonging to that series rather than from the individual figure groups. Cases A1-A4, which represent the pure Diesel combustion, are shown in Figure 3.9 and Figure 3.10. Case A1 ($t_{\mathrm{D}} = 0.468 + 0.468$, $\theta_{\mathrm{D}} = 10 + 5$) shows a pressure peak close to CA50 with the minimum deviation occurring around 8° CA ATDC. This is mainly caused by the Diesel injection starting the combustion close to the spray and the cycle-to-cycle variation being introduced by varying swirl speeds. With a combustion duration of 26.67°

This project has received funding from the European Union Horizon 2020 Research and Innovation programme. Grant Agreement No 861002

CA and a CA10 at 5.70° CA ATDC as well as a CA50 at 12.19° CA ATDC this combustion is probably dominated by a fast burn in the beginning and afterwards followed by an extended late diffusion combustion caused by the split injections close to TDC in combination with the high amount of Diesel. The injection strategy leading to this was chosen to reduce the pressure rise rate per crank angle and have a smoother combustion but unfortunately this also leads to extended combustion into the expansion stroke and therefore lower produced work. Case A2 ($t_{\mathrm{D}} = 0.4 + 0.4$, $\theta_{\mathrm{D}} = 10 + 5$) shows similar behavior to case A1 with an overall higher amount of flame area. With a duration of only 16.37° CA but the same injection timings as A1 it can be observed that the reduced Diesel amount leads to a faster combustion. This is probably caused by the the lower Diesel quantity, which leads to enhanced fuel evaporation and mixture formation due to the smaller amount of fuel that needs to vaporize and mix with the surrounding air. Improved mixture preparation can promote a faster combustion process and thus shorten the combustion duration. Case A3 ($t_{\mathrm{D}} = 0.45 + 0.45$, $\theta_{\mathrm{D}} = 10 + 5$) has a higher pressure peak due to the more rapid combustion, seemingly due to the higher amount of fuel compared to A2 but a better mixing than compared to A1, but also results in a longer combustion of 37.41° CA. The combustion from case A3 shows a higher cycle-to-cycle variation, indicating that it is less stable. The longer ignition delay increases the influence of cycle-to-cycle variations in fuel-air mixing and local thermodynamic conditions, resulting in a less repeatable combustion process. Case A4 ($t_{\mathrm{D}} = 0.45 + 0.45$, $\theta_{\mathrm{D}} = 14 + 5$) combusts closer to TDC and therefore generates more positive work compared to the other cases, but the too rich mixture prevents the fuel-air mixture from combusting rapidly, leading to a low peak pressure. The deviation minimum is also caused by the pilot fuel spray influence with the small amount of disturbance being introduced by varying swirl speeds. The combustion of these cases and the maximum IMEP will be used for comparison in order to judge the dual-fuel combustions.

This project has received funding from the European Union Horizon 2020 Research and Innovation programme. Grant Agreement No 861002

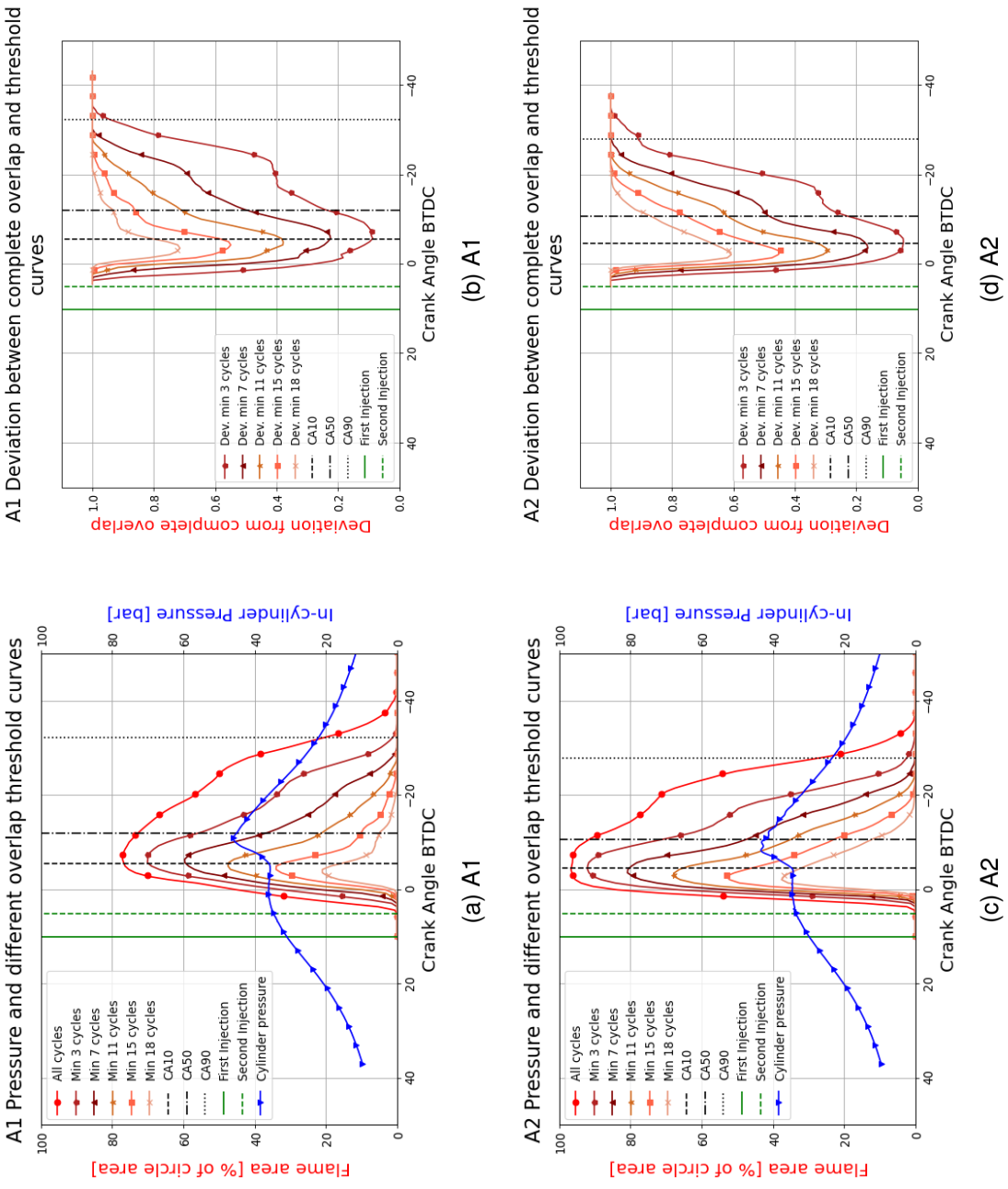


Figure 3.9: Pixel count (left) & Deviation (right) for thresholds and pressure curve case A1&A2

This project has received funding from the European Union Horizon 2020 Research and Innovation programme. Grant Agreement No 861002

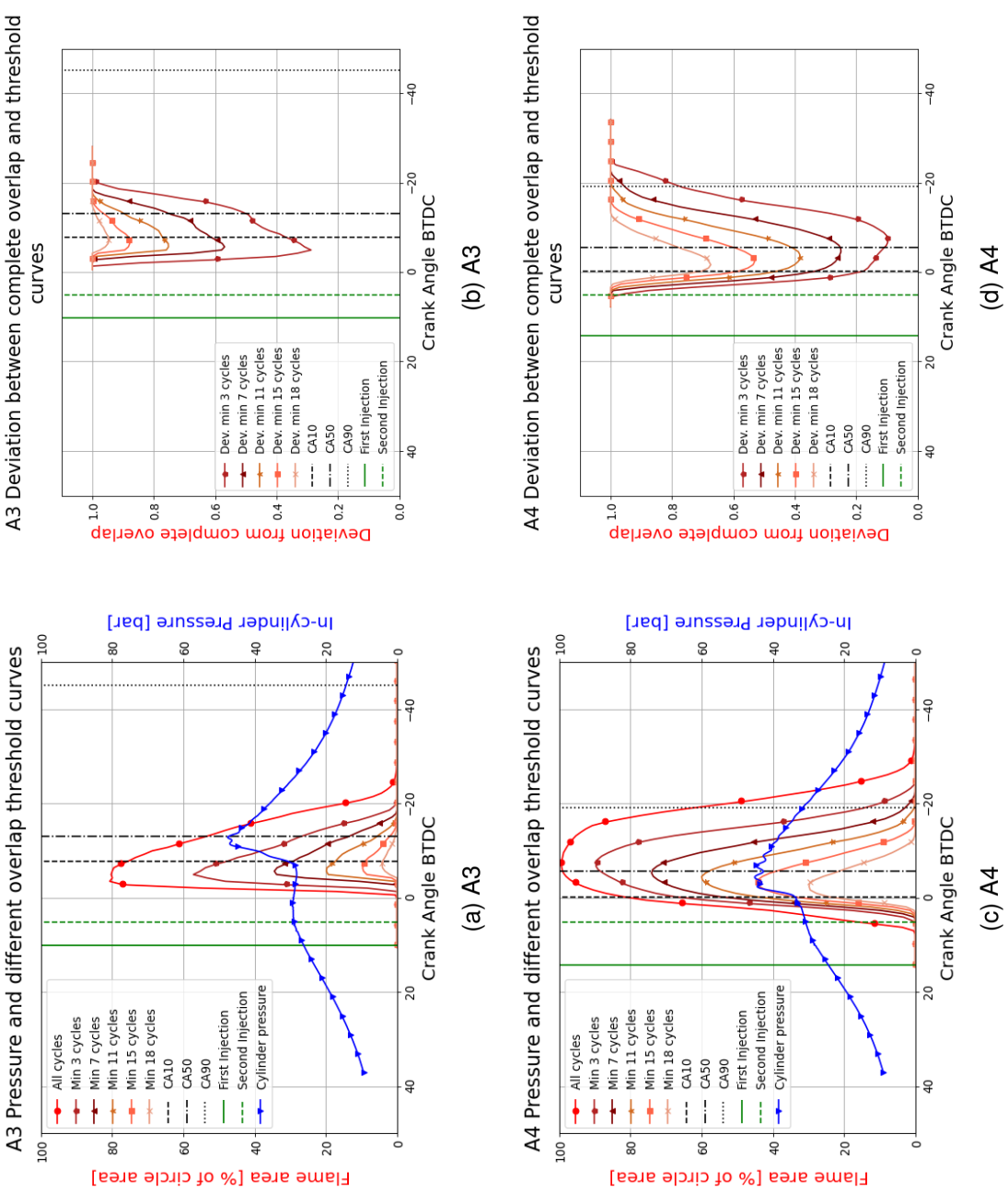


Figure 3.10: Pixel count (left) & Deviation (right) for thresholds and pressure curve case A3&A4

This project has received funding from the European Union Horizon 2020 Research and Innovation programme. Grant Agreement No 861002

Cases B1-B13 represent the dual-fuel combustion with a single pilot fuel injection. The main fuel is port fuel injected before the valves open, creating a fuel air mixture that enters the combustion chamber with the valve opening time. Cases B1-B4 are shown in Figure 3.11 and Figure 3.12. Case B1 ($t_{\mathrm{D}} = 0.35$, $t_{\mathrm{NG}} = 2$, $\theta_{\mathrm{D}} = 25$, $\theta_{\mathrm{NG}} = 300$) shows nearly no signs of combustion with only very small amounts of flame areas randomly forming in the combustion chamber. This is caused by the advanced injection timing as well as a low amount of pilot fuel, creating a very lean mixture, which reduces the reactivity of the fuels. The combustion reaches CA10 at 3.84° CA BTDC which results in negative work being produced. This indicates that the mixture is premixed but unfortunately this leads to a combustion start BTDc as well as a lower thermal efficiency and low pressure rise. Case B2 ($t_{\mathrm{D}} = 0.35$, $t_{\mathrm{NG}} = 2$, $\theta_{\mathrm{D}} = 20$, $\theta_{\mathrm{NG}} = 300$) is similar with a small flame front accumulating BTDC, which extinguishes shortly afterwards. Since only a single Diesel injection is applied in this case, there is no separate main Diesel spray that could initiate combustion. Instead, the injected Diesel serves as the ignition source for the dual-fuel mixture after its ignition delay. Following autoignition, the combustion develops from the Diesel ignition sites and propagates into the surrounding premixed Natural Gas-air mixture. This shows that advancing the pilot fuel injection to 20° CA also leads to a premixed fuel-air mixture that starts the combustion before TDC with nearly the same combustion duration. It was therefore determined, that a dual-fuel combustion case with small amount of pilot fuel injection should inject closer to TDC, as seemingly both injection cases with 20° CA BTDC or earlier in combination with low pilot fuel amounts, lead to weak combustions. Case B3 ($t_{\mathrm{D}} = 0.486$, $t_{\mathrm{NG}} = 1.5$, $\theta_{\mathrm{D}} = 5$, $\theta_{\mathrm{NG}} = 300$) shows the first visible dual-fuel combustion, which behavior and cycle-to-cycle variation is dominated by the influence of the pilot fuel injection, since its fuel amount was increased to 3.62mg of pilot fuel and the injection timing was delayed to 5° CA BTDC. The fact that the CA10 is at 0.66° CA BTDC indicates that the Natural Gas-air mixture is already well mixed at the time the Diesel is introduced into the combustion chamber and therefore ignites shortly afterwards. However, the overall pressure rise from the mixture is still very low, indicating that the combustion is slowed due to the properties of the Natural Gas. Case B4 ($t_{\mathrm{D}} = 0.486$, $t_{\mathrm{NG}} = 1.5$, $\theta_{\mathrm{D}} = 10$, $\theta_{\mathrm{NG}} = 300$) is the first stable dual-fuel combustion with a peak close to TDC caused by the pilot fuel. The pressure peak is closer to TDC since the pilot fuel injection was advanced to 10° CA BTDC to counter the effect that the main fuel burns slower than Diesel. Since the combustion duration is only 13.55° CA this suggests that the combustion process is strongly influenced by the pilot fuel combustion. Cases B5-B8 are shown in Figure 3.13 and Figure 3.14. Case B5 ($t_{\mathrm{D}} = 0.486$, $t_{\mathrm{NG}} = 1.5$, $\theta_{\mathrm{D}} = 12$, $\theta_{\mathrm{NG}} = 300$) behaves similar to case B4 but has a peak closer to TDC, due to

This project has received funding from the European Union Horizon 2020 Research and Innovation programme. Grant Agreement No 861002

the pilot fuel injection being advanced by 2° CA. Case B6 ($t_{\mathrm{D}} = 0.486$, $t_{\mathrm{NG}} = 2$, $\theta_{\mathrm{D}} = 5$, $\theta_{\mathrm{NG}} = 300$) is similar to case B3 and has a combustion peak around 10° CA ATDC, which is too delayed for the combustion to be able to produce significant positive work. However, B6 has a longer ignition delay and a shorter combustion duration, indicating that the fuel-air mixture is better premixed. Furthermore, case B7 ($t_{\mathrm{D}} = 0.486$, $t_{\mathrm{NG}} = 2$, $\theta_{\mathrm{D}} = 12$, $\theta_{\mathrm{NG}} = 300$) combusts even earlier than case B5, which has the same pilot injection but a lower amount of Natural Gas injected„ producing negative work. However, this is the first dual-fuel case where a second peak after TDC is visible in the pressure curve, indicating that the slower combustion of the main fuel dominates in this combustion phase. Case B8 ($t_{\mathrm{D}} = 0.486$, $t_{\mathrm{NG}} = 2$, $\theta_{\mathrm{D}} = 14$, $\theta_{\mathrm{NG}} = 300$) combusts very rapidly and shortly BTDC, suggesting that advancing the pilot fuel injection by 2° CA does not influence the combustion behavior significantly in comparison to B7. Cases B9-B12 are shown in Figure 3.15 and Figure 3.16. Cases B9 ($t_{\mathrm{D}} = 0.486$, $t_{\mathrm{NG}} = 2$, $\theta_{\mathrm{D}} = 16$, $\theta_{\mathrm{NG}} = 300$) and B10 ($t_{\mathrm{D}} = 0.486$, $t_{\mathrm{NG}} = 2$, $\theta_{\mathrm{D}} = 18$, $\theta_{\mathrm{NG}} = 300$) also combusting very rapidly and BTDC, due to the high amount of fuel and very early pilot fuel injection timings, leading to the production of negative work and a lower IMEP. Both cases reach their CA10 BTDC at 2.74° CA for B9 and 3.35° CA BTDC for B10, which slightly increases the combustion durations compared to B8. This indicates that the advance in pilot fuel injection is in this case only shifting the combustion to start earlier and that the main influence on the early combustion is from the pilot fuel and in the second phase from the main fuel combustion. Case B11 ($t_{\mathrm{D}} = 0.486$, $t_{\mathrm{NG}} = 2.5$, $\theta_{\mathrm{D}} = 12$, $\theta_{\mathrm{NG}} = 300$) combusts close to TDC, similar to B5 and B7 which only differ in the amount of NAtural Gas injected, but has a overall low pressure, indicating that the fuel air mixture is not completely mixed or that it is too rich, slowing down the reactivity of the fuel. Case B12 ($t_{\mathrm{D}} = 0.486$, $t_{\mathrm{NG}} = 2.5$, $\theta_{\mathrm{D}} = 14$, $\theta_{\mathrm{NG}} = 300$) is combusting BTDC like B8-B10 with a overall low pressure. Increasing the main fuel amount compared to these cases did therefore not improve the combustion efficiency. Cases B13 ($t_{\mathrm{D}} = 0.55$, $t_{\mathrm{NG}} = 1.5$, $\theta_{\mathrm{D}} = 12$, $\theta_{\mathrm{NG}} = 300$) is shown in Figure 3.17. B13 behaves similar to B7, but with a higher pressure, which is caused by the increased amount of pilot fuel. But since this decreases the substitution rate, this approached was not pursued further. Overall the dual-fuel combustion cases with a single pilot fuel injection suffer from uncertain ignition delays as well as a discrepancy from needing a high amount of Diesel in order to trigger the combustion while simultaneously needing to avoid having a too rich mixture that slows the reactivity of the fuel mixture. Because of this, it was decided to carry out the further experiments with a split pilot fuel injection.

This project has received funding from the European Union Horizon 2020 Research and Innovation programme. Grant Agreement No 861002

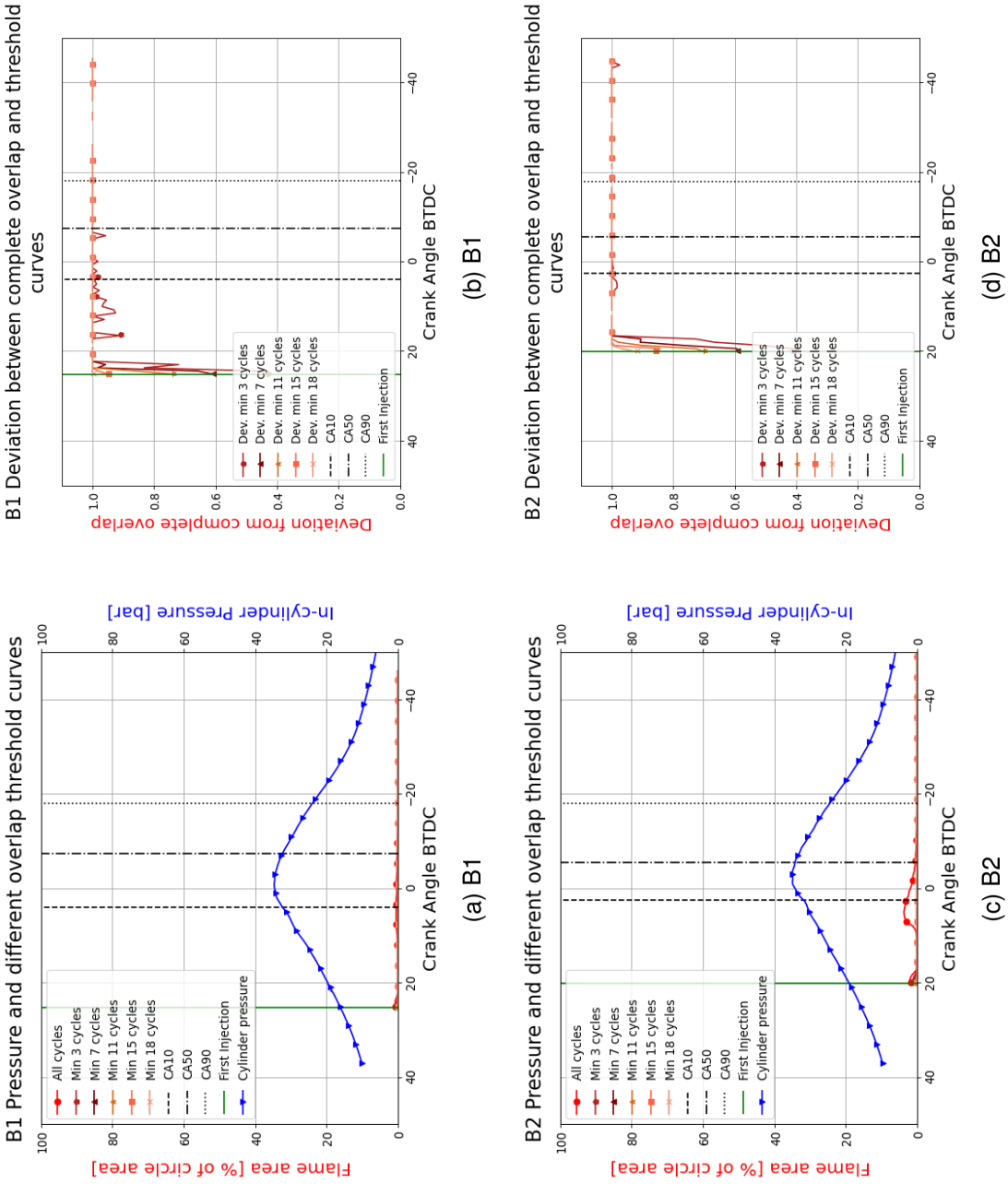


Figure 3.11: Pixel count (left) & Deviation (right) for thresholds and pressure curve case B1 & B2

This project has received funding from the European Union Horizon 2020 Research and Innovation programme. Grant Agreement No 861002

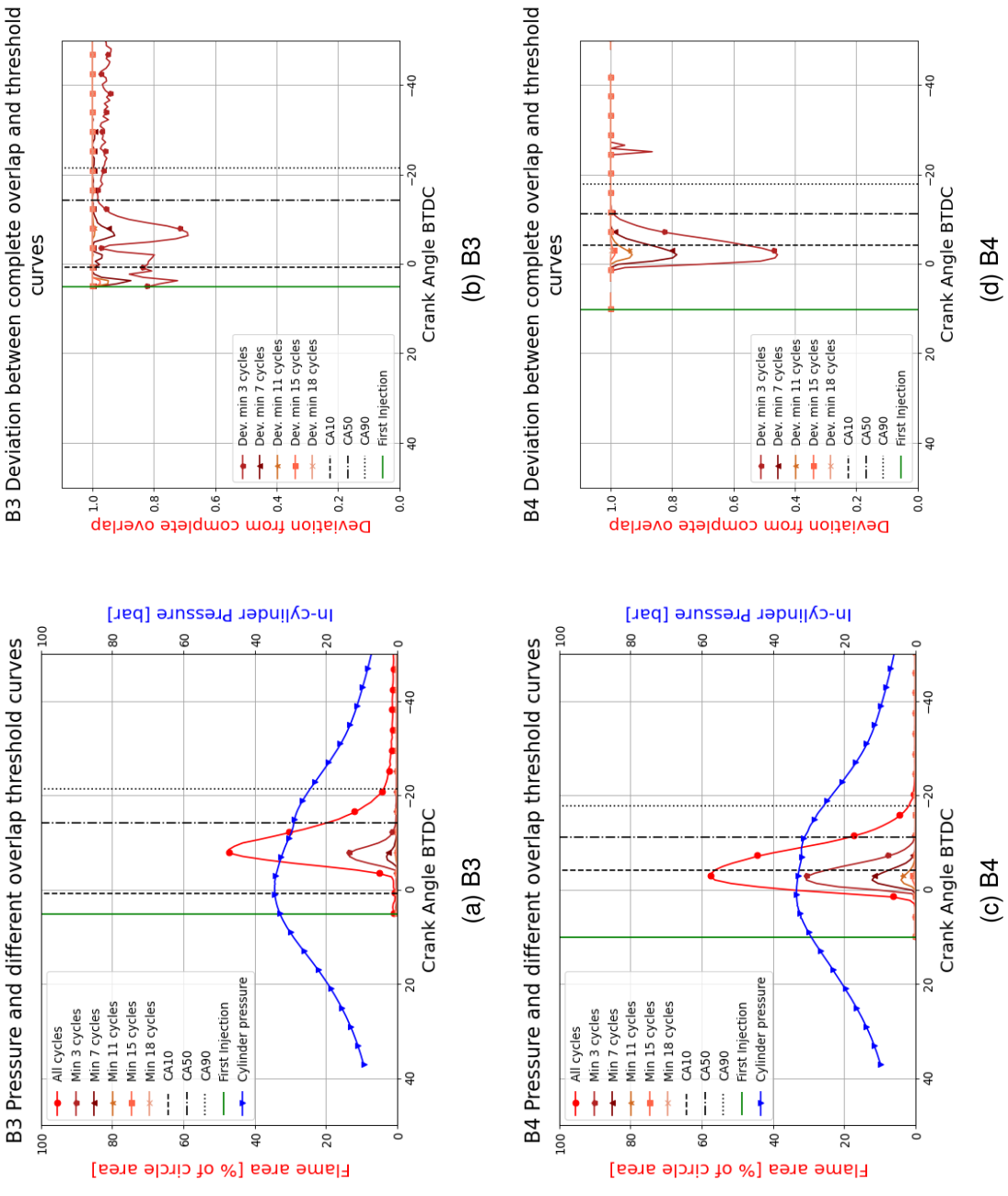


Figure 3.12: Pixel count (left) & Deviation (right) for thresholds and pressure curve case B3 & B4

This project has received funding from the European Union Horizon 2020 Research and Innovation programme. Grant Agreement No 861002

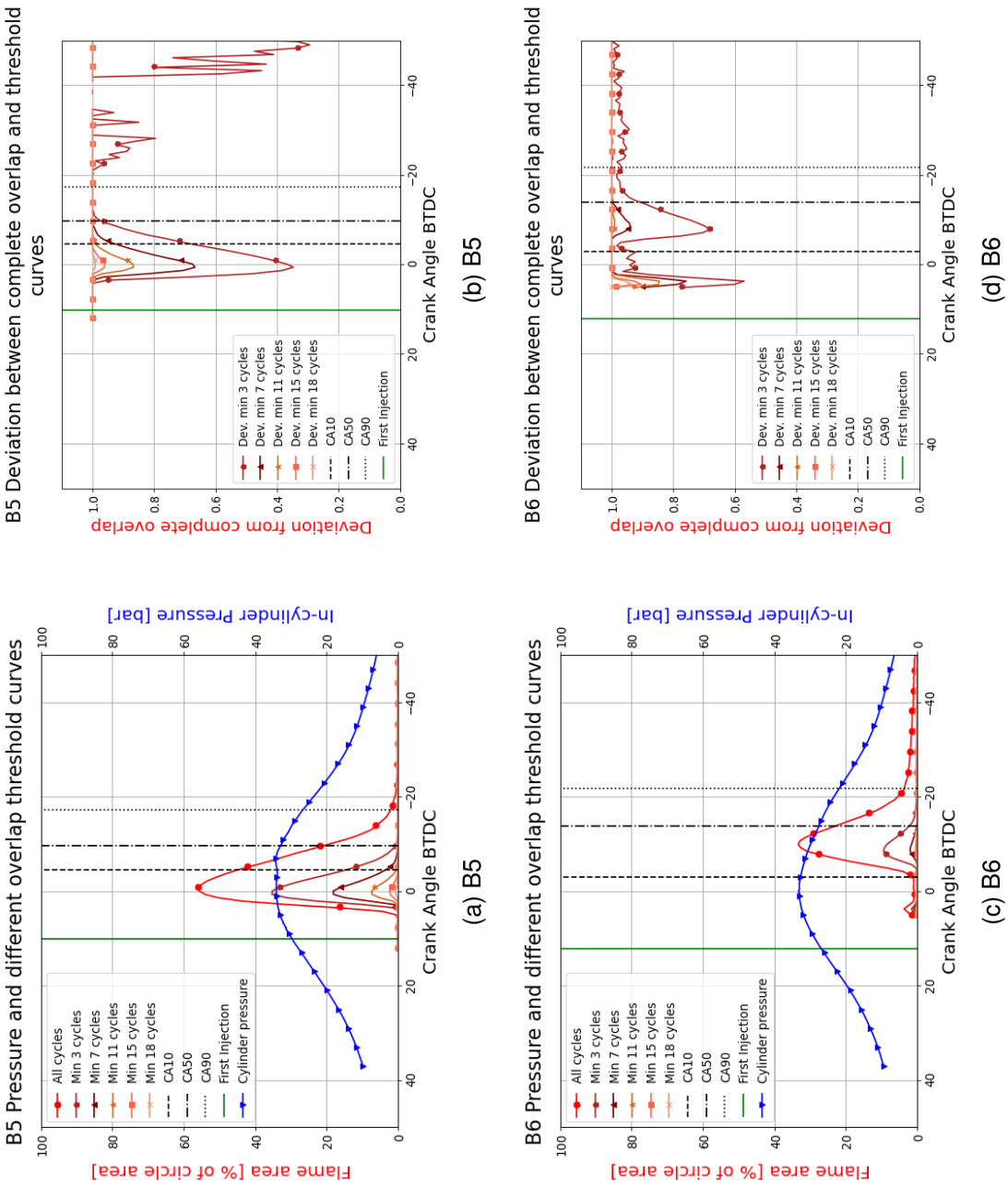


Figure 3.13: Pixel count (left) & Deviation (right) for thresholds and pressure curve case B5 & B6

This project has received funding from the European Union Horizon 2020 Research and Innovation programme. Grant Agreement No 861002

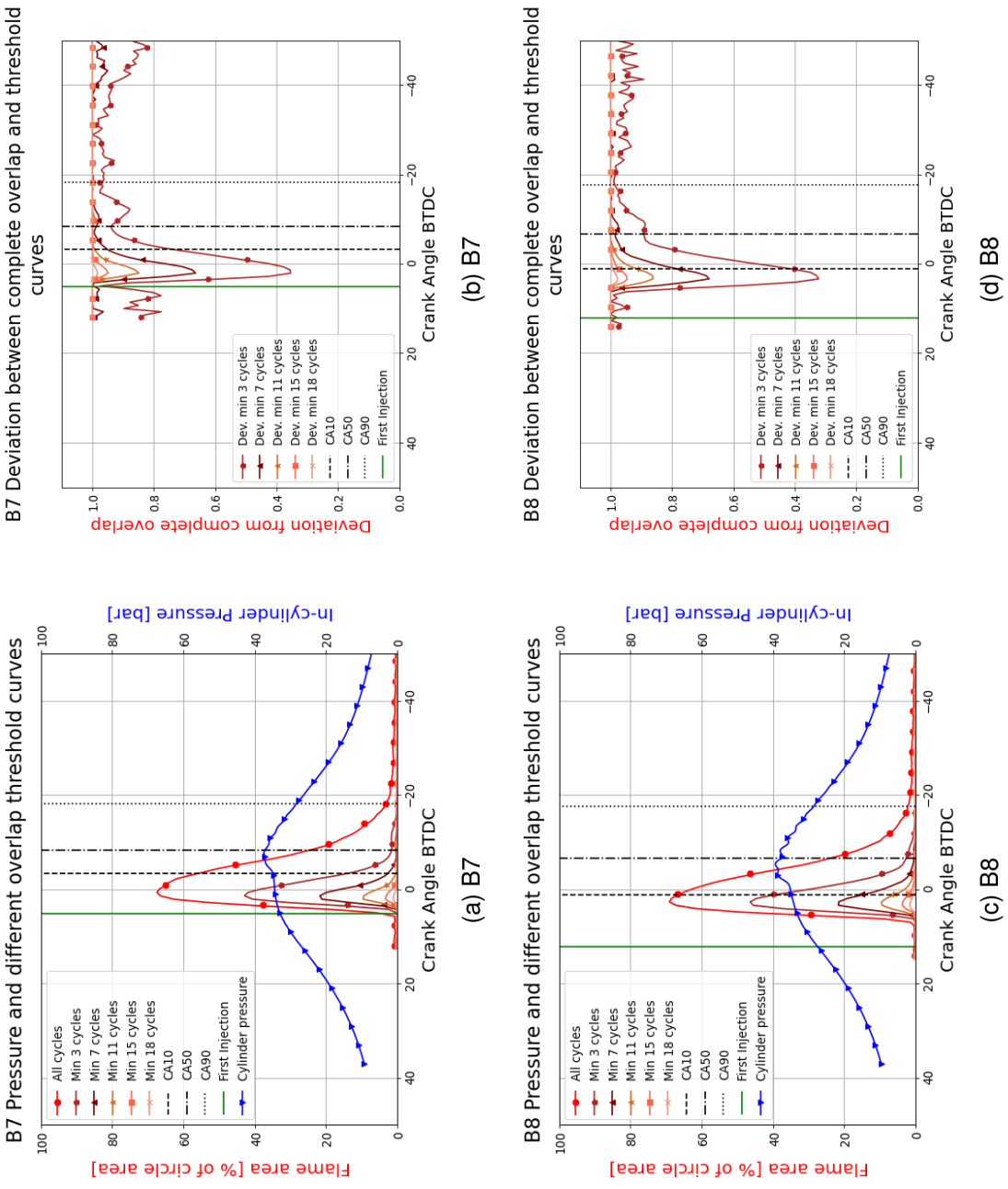


Figure 3.14: Pixel count (left) & Deviation (right) for thresholds and pressure curve case B7 & B8

This project has received funding from the European Union Horizon 2020 Research and Innovation programme. Grant Agreement No 861002

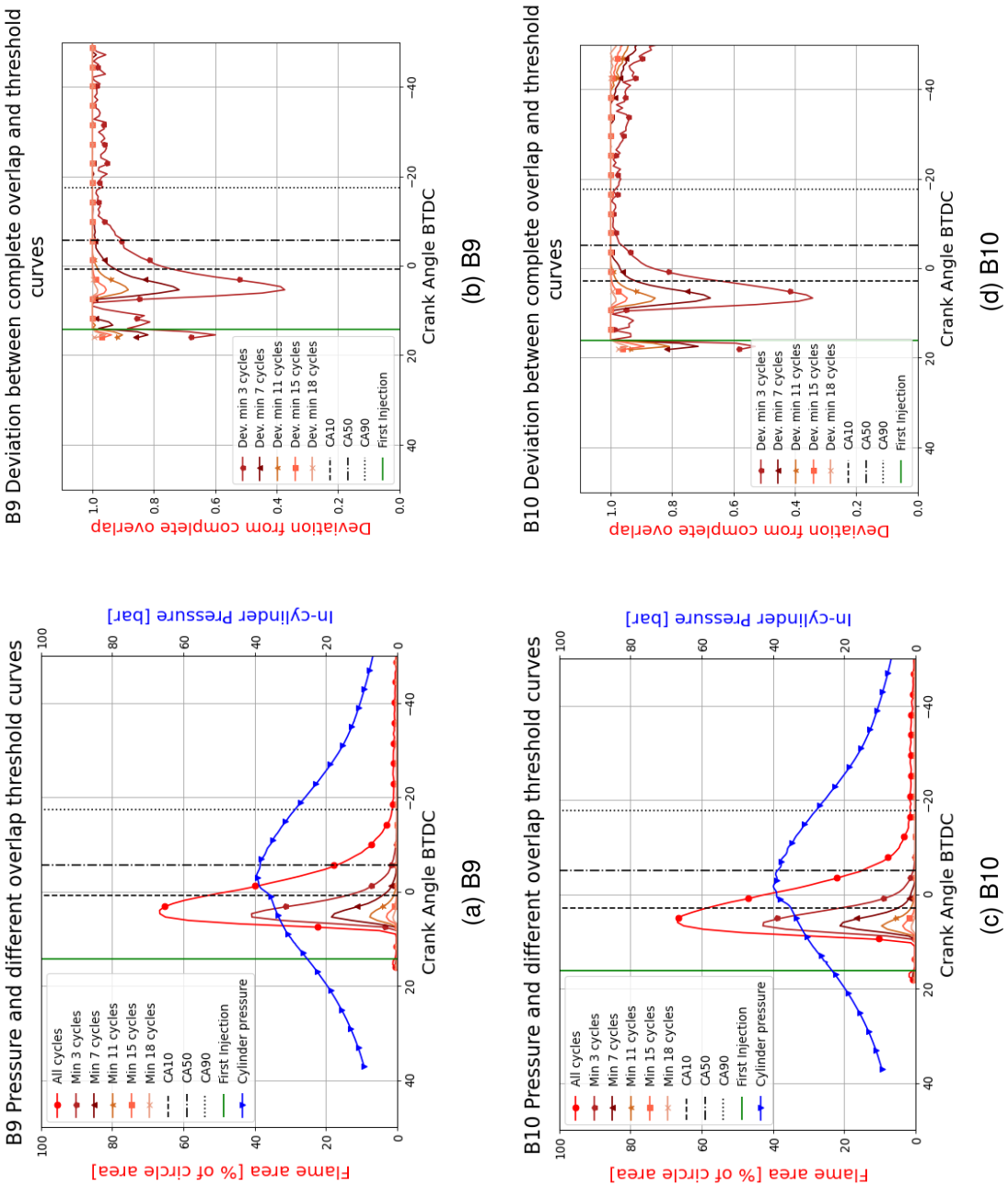


Figure 3.15: Pixel count (left) & Deviation (right) for thresholds and pressure curve case B9 & B10

This project has received funding from the European Union Horizon 2020 Research and Innovation programme. Grant Agreement No 861002

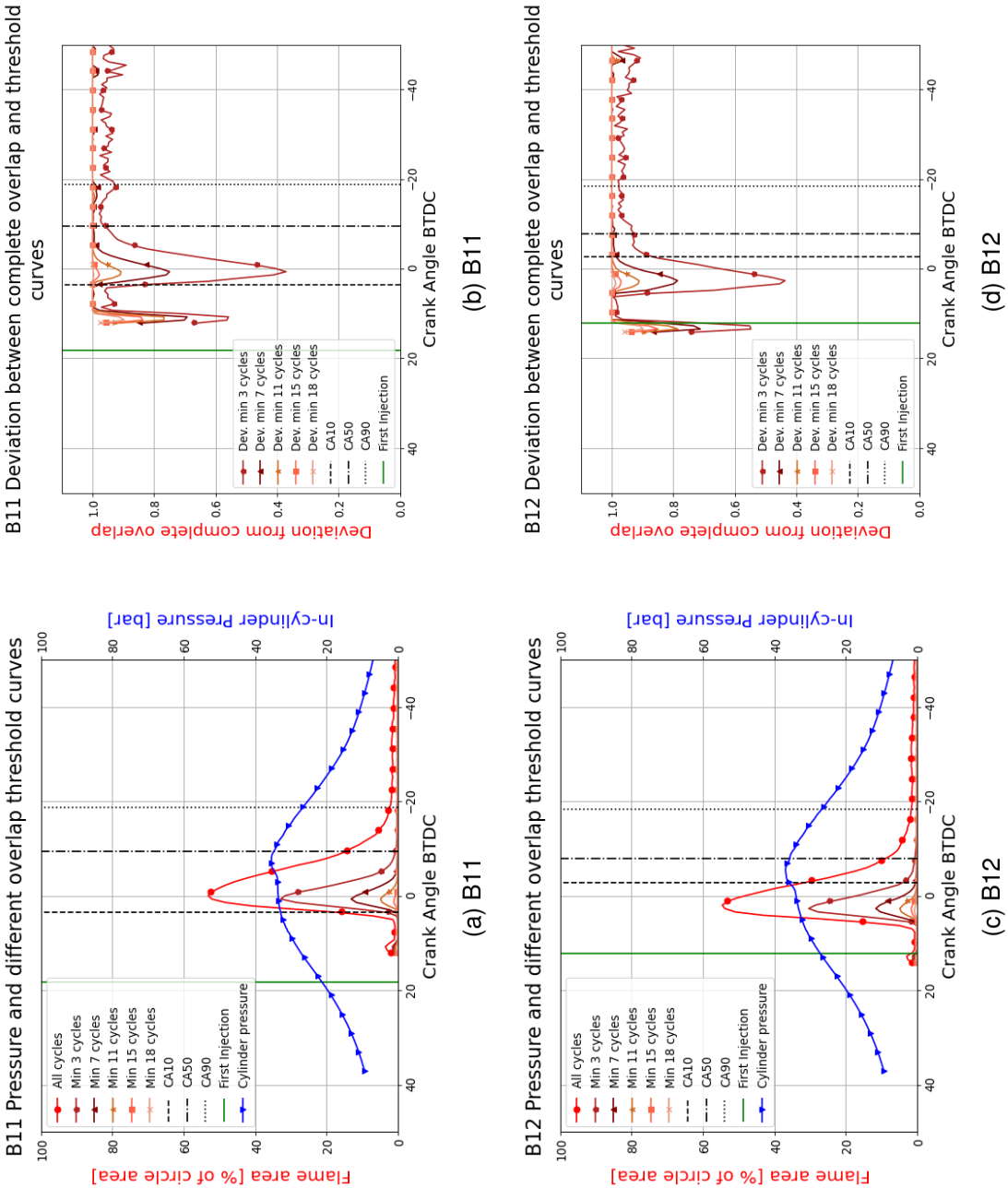
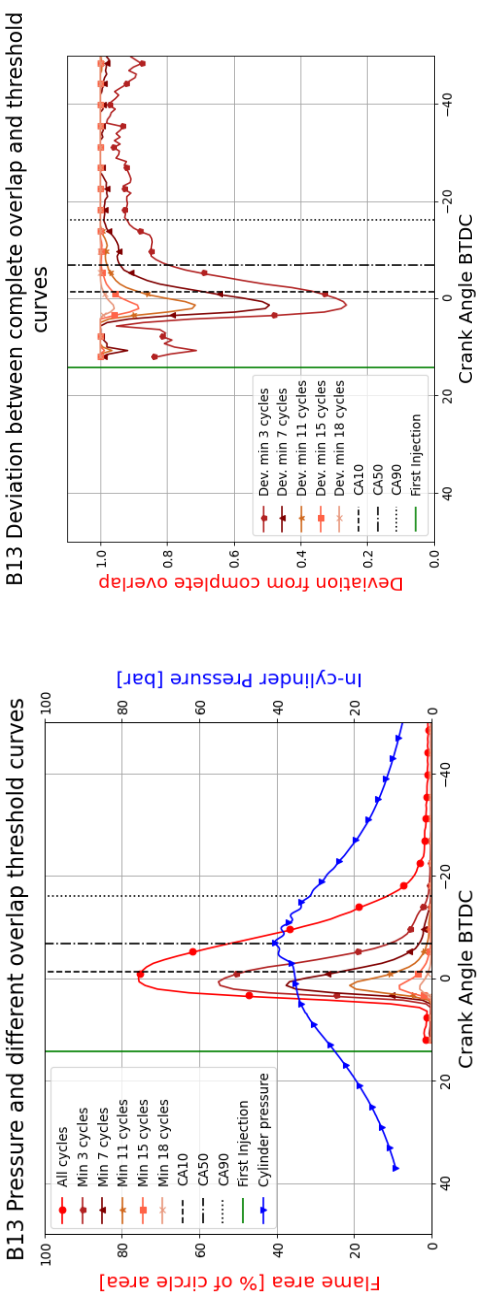


Figure 3.16: Pixel count (left) & Deviation (right) for thresholds and pressure curve case B11 & B12

This project has received funding from the European Union Horizon 2020 Research and Innovation programme. Grant Agreement No 861002



(a) B13 (b) B13

Figure 3.17: Pixel count (left) & Deviation (right) for thresholds and pressure curve case B13

This project has received funding from the European Union Horizon 2020 Research and Innovation programme. Grant Agreement No 861002

Cases C1-C7 represent the dual-fuel combustion with a split pilot fuel injection and a 1.5 ms main fuel injection of Natural Gas. Cases C1-C4 can be seen in Figure 3.18 and Figure 3.19. It can be seen that Case C1 ($t_{\mathrm{D}} = 0.3 + 0.4$, $t_{\mathrm{NG}} = 1.5$, $\theta_{\mathrm{D}} = 17 + 0$, $\theta_{\mathrm{NG}} = 300$) has a small flame developing at around 8° CA BTDC which leads to a more rapid ignition of the second pilot injection at TDC, leading to a high flame area pixel count. The minimum deviation for this case occurs at around 8° CA ATDC, indicating that the main influence from the pilot fuel combustion occurs there but is delayed due to the main fuel presence in the combustion chamber. The case reaches a comparably high pressure rise for having low amounts of Diesel and Natural Gas injected but starts the combustion BTDC. The two pressure peaks indicate that the combustion until CA50 at 11.04° CA is dominated by the pilot fuel and the second phase by the flame propagation phase, which is also indicated by the pixel count. Case C2 ($t_{\mathrm{D}} = 0.35+0.4$, $t_{\mathrm{NG}} = 1.5$, $\theta_{\mathrm{D}} = 10 + (-3)$, $\theta_{\mathrm{NG}} = 300$) has a higher fuel amount for the first injection and has a injection timing at 10° CA BTDC and 3° CA ATDC, leading to less developing time for the initial flame area before the second injection and therefore a slower ignition and a overall lower amount of flame area. From the pressure profile, the pixel count that extends well after CA90 and the longer combustion duration of 27.16° CA it can be interpreted that this combustion is also afterwards dominated by the flame propagation phase. Case C3 ($t_{\mathrm{D}} = 0.35 + 0.4$, $t_{\mathrm{NG}} = 1.5$, $\theta_{\mathrm{D}} = 12 + (-3)$, $\theta_{\mathrm{NG}} = 300$) and C4 ($t_{\mathrm{D}} = 0.35 + 0.4$, $t_{\mathrm{NG}} = 1.5$, $\theta_{\mathrm{D}} = 14 + (-3)$, $\theta_{\mathrm{NG}} = 300$) behave similar to case C1, but are even further delayed, with a flame area peak around 10° CA ATDC. This shows that even with more developing time, the timing and fuel amount for these cases was not at optimum, leading to overall low pressure and low efficiency dual-fuel combustions. The lower pressure levels indicate a reduced conversion of the released chemical energy into useful work, which is consistent with a less favorable combustion phasing and slower heat release. For Case C3 the pixel count is indicating that the second part of the combustion is dominated by the flame propagation again whereas C4 seems to combust most of the main fuel in the beginning of the combustion. This is also suggested by the combustion durations, which are 34.38° CA for C3 and 20.97° CA for C4. The longer combustion duration in C3 suggests a slower energy release, which contributes to the lower pressure development and reduced combustion efficiency observed in this case. Cases C5-C7 are shown in Figure 3.20 and Figure 3.21. C5 ($t_{\mathrm{D}} = 0.35+0.4$, $t_{\mathrm{NG}} = 1.5$, $\theta_{\mathrm{D}} = 15+(-2)$, $\theta_{\mathrm{NG}} = 300$) has the same properties like C4, showing, that an advance of both pilot fuel injections for 10° CA BTDC does not shift the pressure peak closer to TDC. For cases C6 ($t_{\mathrm{D}} = 0.4 + 0.4$, $t_{\mathrm{NG}} = 1.5$, $\theta_{\mathrm{D}} = 5 + 0$, $\theta_{\mathrm{NG}} = 300$) and C7 ($t_{\mathrm{D}} = 0.44 + 0.44$, $t_{\mathrm{NG}} = 1.5$, $\theta_{\mathrm{D}} = 5 + 0$, $\theta_{\mathrm{NG}} = 300$) the amount of pilot fuel was increased, and the timing between the injections was shortened to 5° CA

This project has received funding from the European Union Horizon 2020 Research and Innovation programme. Grant Agreement No 861002

BTDC. Both Test cases reach their CA10 around 8.5° CA ATDC in combination with nearly no flames visible and a low pressure rise, indicating that no initial flame area is forming and the fuel can not ignite properly, leading to a small combustion and flame area peak around 10° CA ATDC.

This project has received funding from the European Union Horizon 2020 Research and Innovation programme. Grant Agreement No 861002

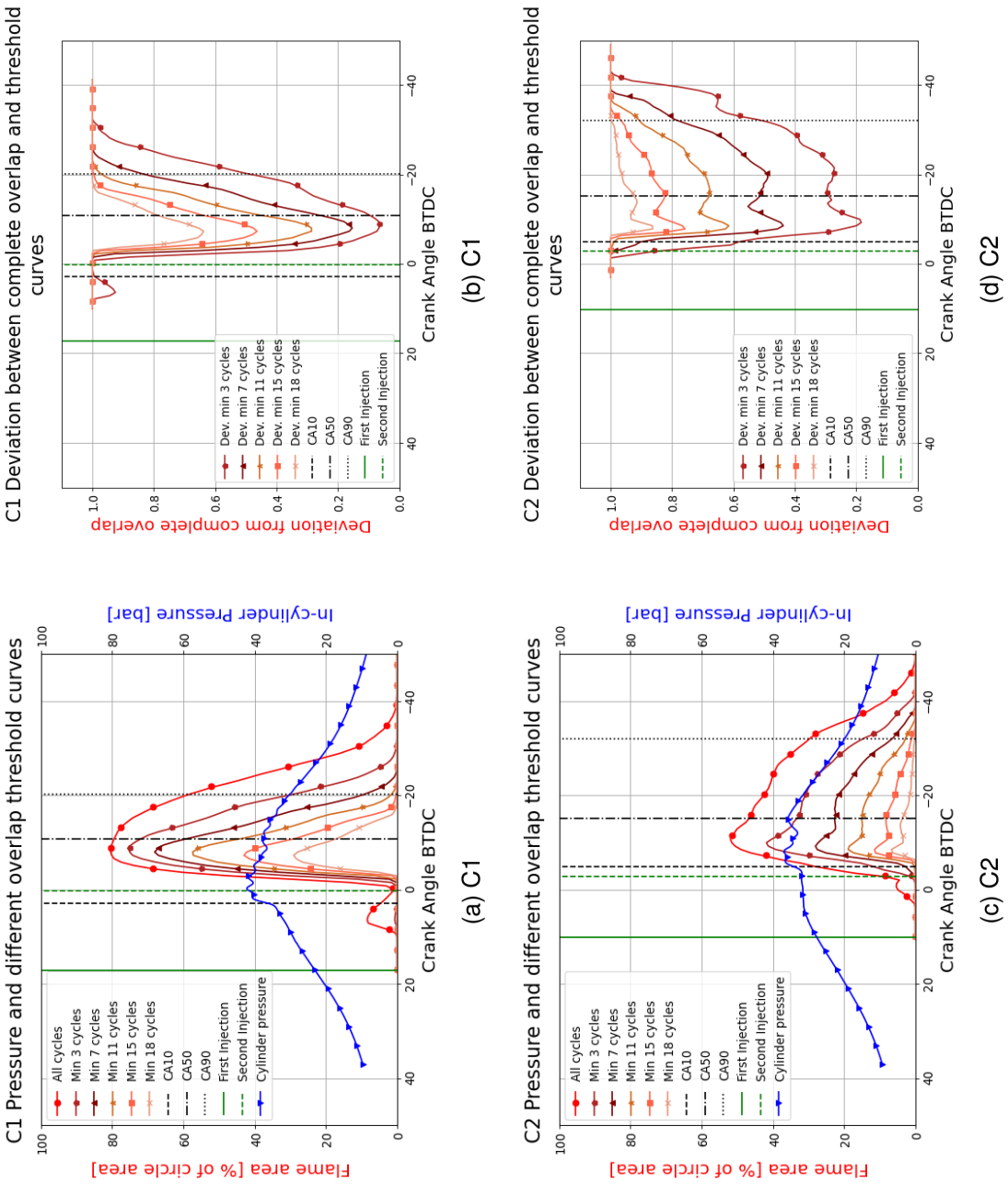


Figure 3.18: Pixel count (left) & Deviation (right) for thresholds and pressure curve case C1 & C2

This project has received funding from the European Union Horizon 2020 Research and Innovation programme. Grant Agreement No 861002

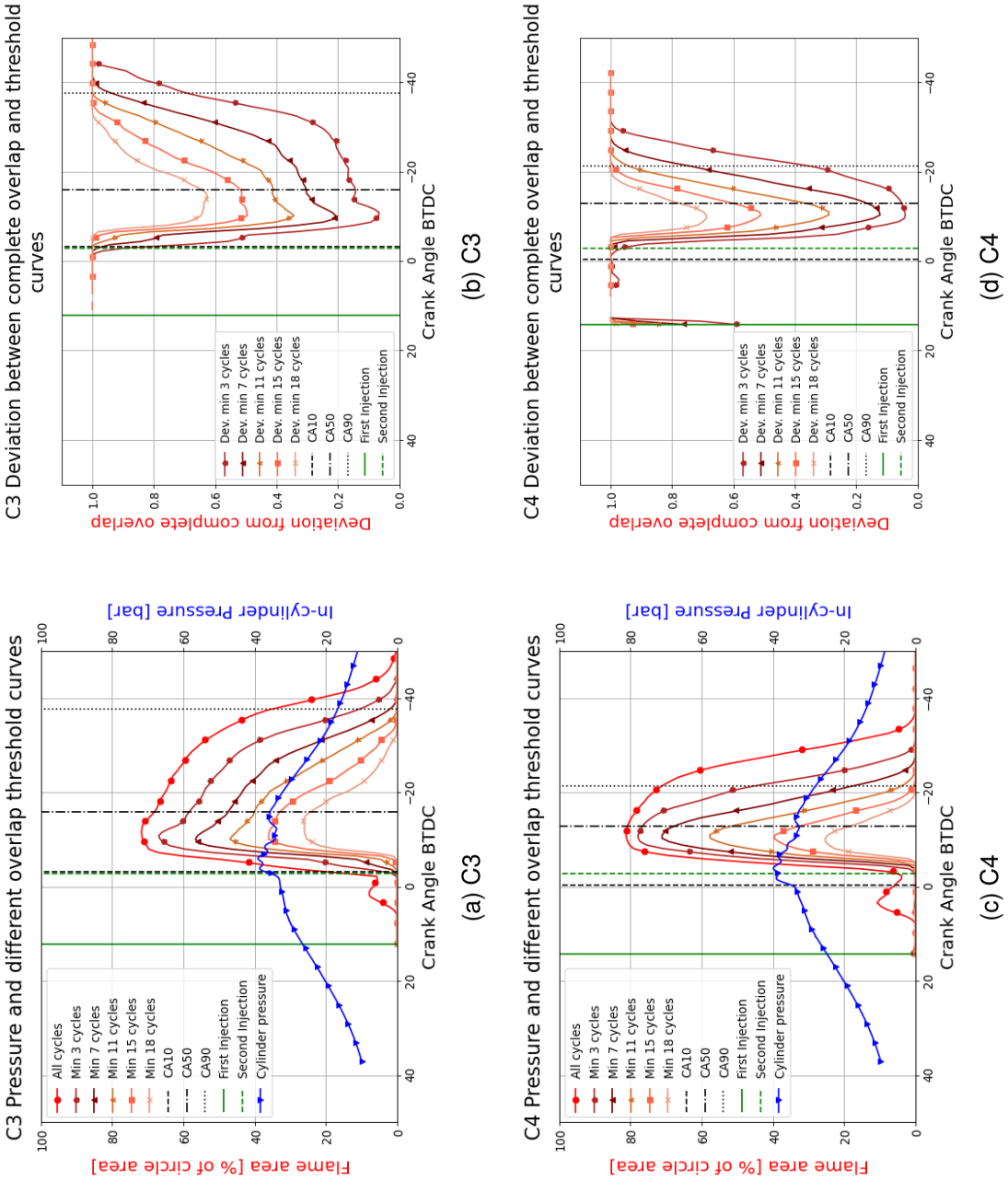


Figure 3.19: Pixel count (left) & Deviation (right) for thresholds and pressure curve case C3 & C4

This project has received funding from the European Union Horizon 2020 Research and Innovation programme. Grant Agreement No 861002

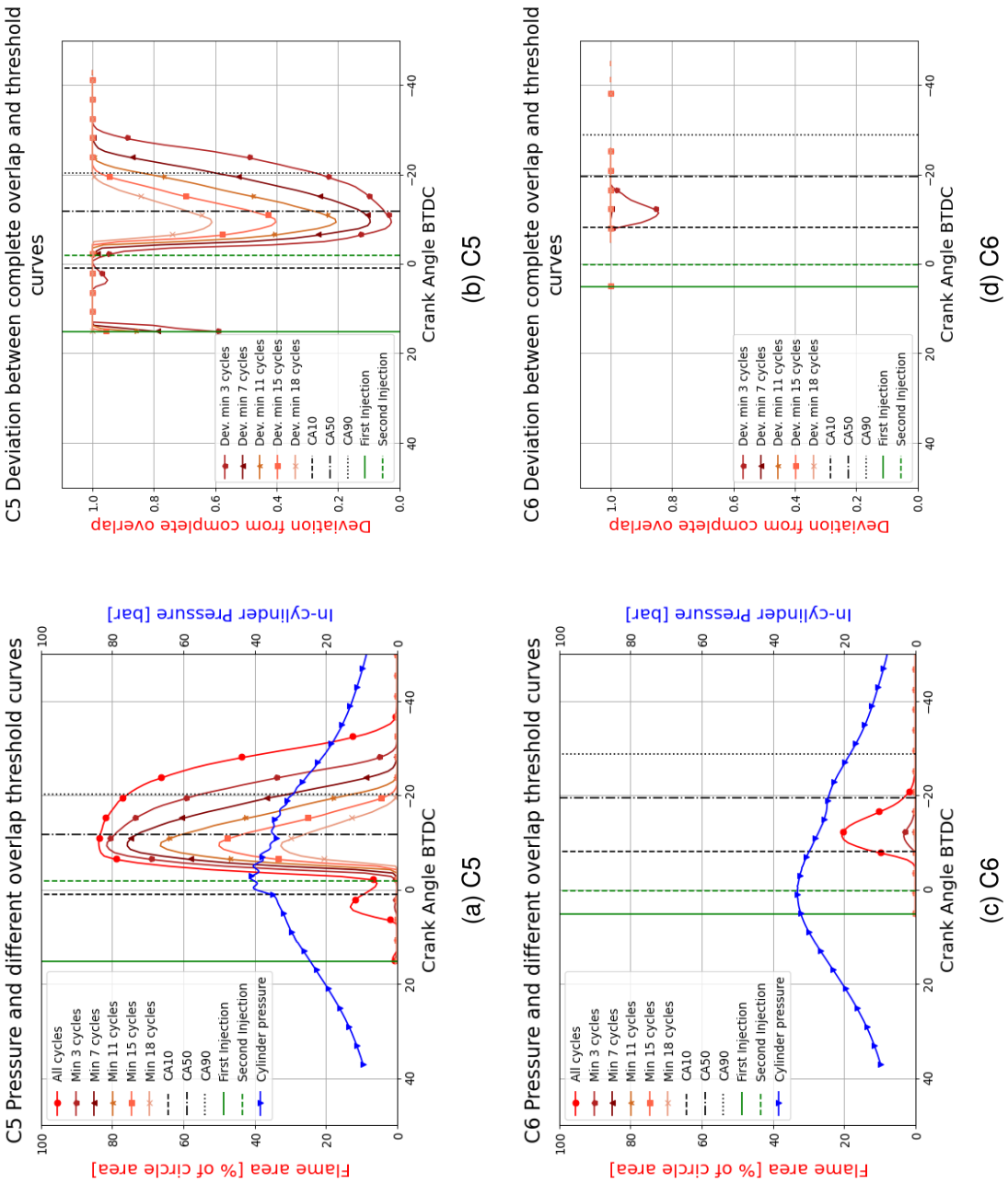
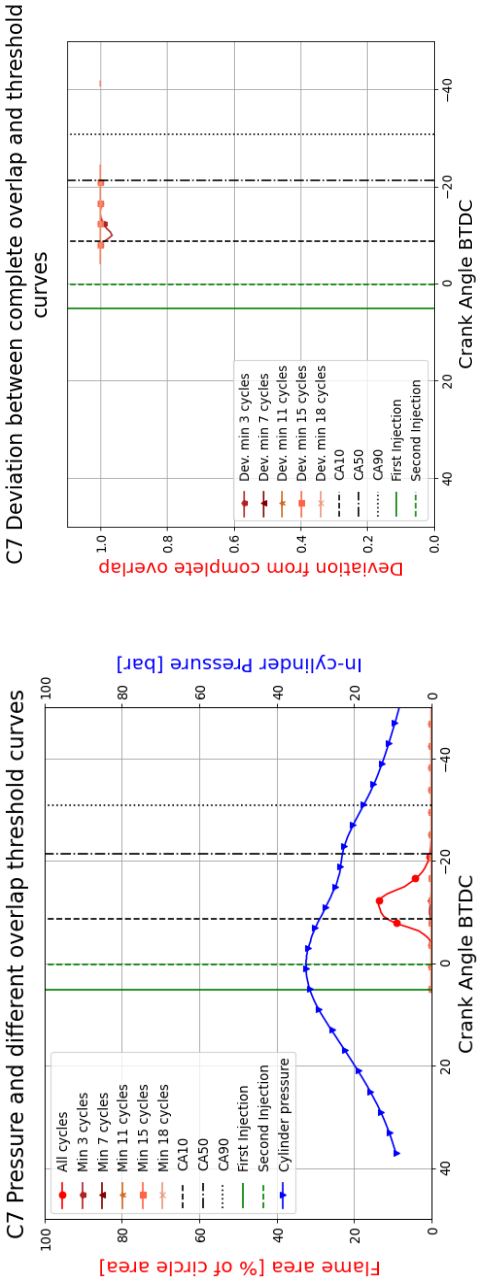


Figure 3.20: Pixel count (left) and deviation (right) for cases C5 and C6

This project has received funding from the European Union Horizon 2020 Research and Innovation programme. Grant Agreement No 861002



(a) C7 (b) C7

Figure 3.21: Pixel count (left) and deviation (right) for case C7

This project has received funding from the European Union Horizon 2020 Research and Innovation programme. Grant Agreement No 861002

Cases D1-D12 represent the dual-fuel combustion with spilt pilot fuel injection and 2 ms Natural Gas injection. Cases D1-D4 are displayed in Figure 3.22 and Figure 3.23. Case D1 ($t_{\mathrm{D}} = 0.4 + 0.35$, $t_{\mathrm{NG}} = 2$, $\theta_{\mathrm{D}} = 12 + (-2)$, $\theta_{\mathrm{NG}} = 300$) has a initial flame forming before the second pilot fuel injection and has its pressure and flame area peak at around 5° CA ATDC. When comparing this case to C3, which has a similar pilot fuel injection and a slightly lower amount of Natural Gas, it can be observed that the pressure and pixel count curves behave similarly. This indicates that the dominating force in this case is the Natural Gas combustion. Since the overall pressure peak for this case is low, it was decided to change the pilot fuel injection ratio for the following cases. Case D2 ($t_{\mathrm{D}} = 0.35 + 0.4$, $t_{\mathrm{NG}} = 2$, $\theta_{\mathrm{D}} = 12 + (-3)$, $\theta_{\mathrm{NG}} = 300$) has a flame area forming at around 3° CA BTDC. This leads to an instantaneous combustion of the second injection. The ignition delay and pressure peak are similar to case C2. The combustion duration of Case D2 is with 33.87° CA significantly longer than D1, which has a duration of 26.85° CA, indicating that the inversion of the two pilot injection durations and the delay of the second pilot fuel injection led to a slower Natural Gas combustion in the initial phase and therefore to a prolonged late combustion. This shows that the ignition delay and pressure peak are dominated by the influence of the pilot fuel injection and a change of the main fuel amount does not have noticeable effects, as long as the mixture does not get to rich, causing a lack of oxygen. The combustion duration of Case D3 ($t_{\mathrm{D}} = 0.35 + 0.4$, $t_{\mathrm{NG}} = 2$, $\theta_{\mathrm{D}} = 12 + (-2)$, $\theta_{\mathrm{NG}} = 300$) is similar to D2 at 32.75° CA, so again the dominating force is probably the slow Natural Gas combustion. Case D4 ($t_{\mathrm{D}} = 0.35 + 0.4$, $t_{\mathrm{NG}} = 2$, $\theta_{\mathrm{D}} = 20 + 0$, $\theta_{\mathrm{NG}} = 300$) has a earlier combustion at around 10° CA ATDC, because the first pilot fuel injection was advanced to 20° CA BTDC. However, the ignition between first and second pilot fuel injection can not form a stable flame and therefore the ignition of the second injection does not lead to a high pressure rise. The combustion behaves similarly to D1-D3 even though the pilot injections were advanced to 20 and 0° CA BTDC, indicating that the change in the pilot injection timing is not having a significant influence on these combustion cases.

Cases D5-D8 are shown in Figure 3.24 and Figure 3.25. Case D5 ($t_{\mathrm{D}} = 0.35 + 0.4$, $t_{\mathrm{NG}} = 2$, $\theta_{\mathrm{D}} = 15 + 0$, $\theta_{\mathrm{NG}} = 300$) behaves similar to case D4 but with a slightly more delayed combustion. Since the duration between both pilot fuel injections is 5° CA shorter than in case D4, this indicates, that for this fuel amounts, 20° CA form a more stable initial flame area and support a more rapid combustion. However, the combustion duration for case D5 is 29.04° CA and longer than for case D4. Both cases reach their CA10 and CA50 at similar timings, but D5 reaches CA90 later, which is again probably caused by the Natural Gas combustion. Case D6 ($t_{\mathrm{D}} = 0.35 + 0.4$, $t_{\mathrm{NG}} = 2$, $\theta_{\mathrm{D}} = 30 + 0$,

This project has received funding from the European Union Horizon 2020 Research and Innovation programme. Grant Agreement No 861002

$\theta_{\mathrm{NG}} = 300$) has a pressure curve similar to the pure Diesel combustion cases, but since the second peak is delayed until 11° CA ATDC, this dual-fuel combustion case is inefficient. The combustion reaches CA50 at the pressure peak and has a duration of 31.91° CA which seems to be spilt equally into the initial burn phase dominated by the pilot fuel combustion phase and the slower main fuel combustion phase. However, the CA10 is at 4.51° CA BTDC and therefore the combustion is producing negative work in the initial phase due to the very advanced first pilot fuel injection at 30° CA BTDC, which leads to an increased mixture homogenization. Case D7 ($t_{\mathrm{D}} = 0.35 + 0.4$, $t_{\mathrm{NG}} = 2$, $\theta_{\mathrm{D}} = 30 + 2$, $\theta_{\mathrm{NG}} = 300$) shows the same behavior as D6, showing that delaying the second pilot fuel injection by 2° CA does not affect this combustion case since the dominating effect is the influence of the first pilot fuel combustion. For Case D8 ($t_{\mathrm{D}} = 0.35 + 0.4$, $t_{\mathrm{NG}} = 2$, $\theta_{\mathrm{D}} = 35 + 0$, $\theta_{\mathrm{NG}} = 300$) it can be observed, that the pressure peak drops when advancing the first pilot fuel injection from 30° CA BTDC to 35° CA BTDC. However, advancing the first pilot fuel injection led to an even longer ignition delay, thereby shifting the start of combustion closer to TDC while also reducing the overall combustion duration to 28.83° CA. This indicates RCCI combustion with a higher degree of mixture homogenization than in D6 and D7, which in turn resulted in a slower heat release rate and pressure rise rate.

Cases D9-D12 are shown in Figure 3.26 and Figure 3.27, which all have a 50-50 split pilot fuel injection. For case D9 ($t_{\mathrm{D}} = 0.38 + 0.38$, $t_{\mathrm{NG}} = 2$, $\theta_{\mathrm{D}} = 12 + (-2)$, $\theta_{\mathrm{NG}} = 300$) it can be observed, that the formation of the flame between the two pilot fuel injections is not developed enough to properly ignite the second injection, leading to a low pressure rise and a long combustion duration of 34.43° CA for the lower amount of fuel injected in this case. Case D10 ($t_{\mathrm{D}} = 0.35 + 0.35$, $t_{\mathrm{NG}} = 2$, $\theta_{\mathrm{D}} = 16 + 5$, $\theta_{\mathrm{NG}} = 300$) does not show any flame formation between the two pilot fuel injections, leading to a weak combustion with nearly no pressure rise and a short duration of 17.34° CA. The absence of flame kernels prior to TDC delays the ignition of the second Diesel injection and worsens combustion phasing. Case D11 ($t_{\mathrm{D}} = 0.35 + 0.35$, $t_{\mathrm{NG}} = 2$, $\theta_{\mathrm{D}} = 10 + 5$, $\theta_{\mathrm{NG}} = 300$) injects the pilot fuel at 10 and 5° CA BTDC with a small sign of flame forming between the two but since the time is not enough, the combustion is delayed, with a peak around 11° CA ATDC. The combustion duration of 13.77° CA is shorter than that of D10 and indicates that this case has a more rapid pilot fuel combustion phase due to the two pilot fuels being injected with a shorter delay and closer to TDC.Case D12 ($t_{\mathrm{D}} = 0.35 + 0.35$, $t_{\mathrm{NG}} = 2$, $\theta_{\mathrm{D}} = 25 + 10$, $\theta_{\mathrm{NG}} = 300$) has a flame area peak around TDC but is overall weak since the first pilot fuel injection was advanced to 25° CA BTDC. The combustion duration and behaviour of this case is similar to D10, even though both pilot fuel injections have been advanced to 25 and

This project has received funding from the European Union Horizon 2020 Research and Innovation programme. Grant Agreement No 861002

10° CA BTDC. The similarity between D10 and D12 may be related to the earlier first Diesel injection in both cases compared with D11. In D10 and D12, the earlier pilot injection provides more time for evaporation, mixing, and interaction with the premixed charge before the second injection occurs. In contrast, the first injection of D11 is at 10° CA BTDC and the second at 5° CA BTDC, which reduces the time available for mixture homogenization which might cause the different combustion behaviour. D10 and D12 show earlier combustion phasing, with CA50 values of 11.20 CA ATDC and 8.83 CA ATDC, respectively, whereas D11 has a later CA50 of 12.78 CA ATDC. This indicates that the later first injection in D11, combined with the shorter interval between the two injections, delays the main heat release compared with D10 and D12. Therefore, the observed difference may be attributed not only to the absolute timing of the first injection, but also to the time interval between the two injections, which affects fuel evaporation, premixing, ignition delay, and the subsequent heat release behavior. Case D12 was intended to highlight the effect of advancing the first pilot injection to 25° CA BTDC. Although a flame area peak is observed around TDC, the overall flame development remains weak. Since the combustion cases D1-D12 did not show an improved combustion it was decided to try dual-fuel combustion cases with a 50/50 split pilot fuel injection.

This project has received funding from the European Union Horizon 2020 Research and Innovation programme. Grant Agreement No 861002

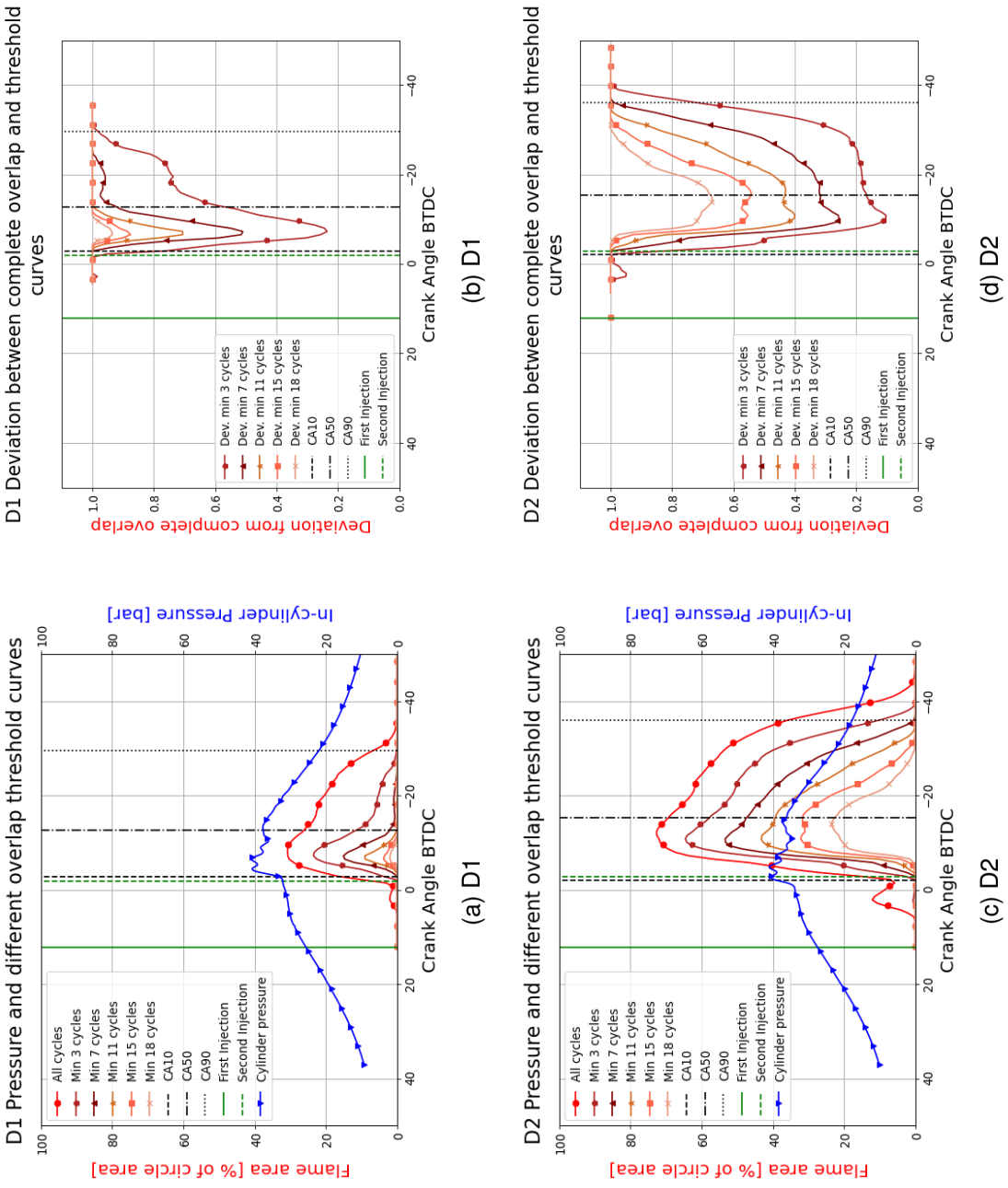


Figure 3.22: Pixel count (left) and deviation (right) for cases D1 and D2

This project has received funding from the European Union Horizon 2020 Research and Innovation programme. Grant Agreement No 861002

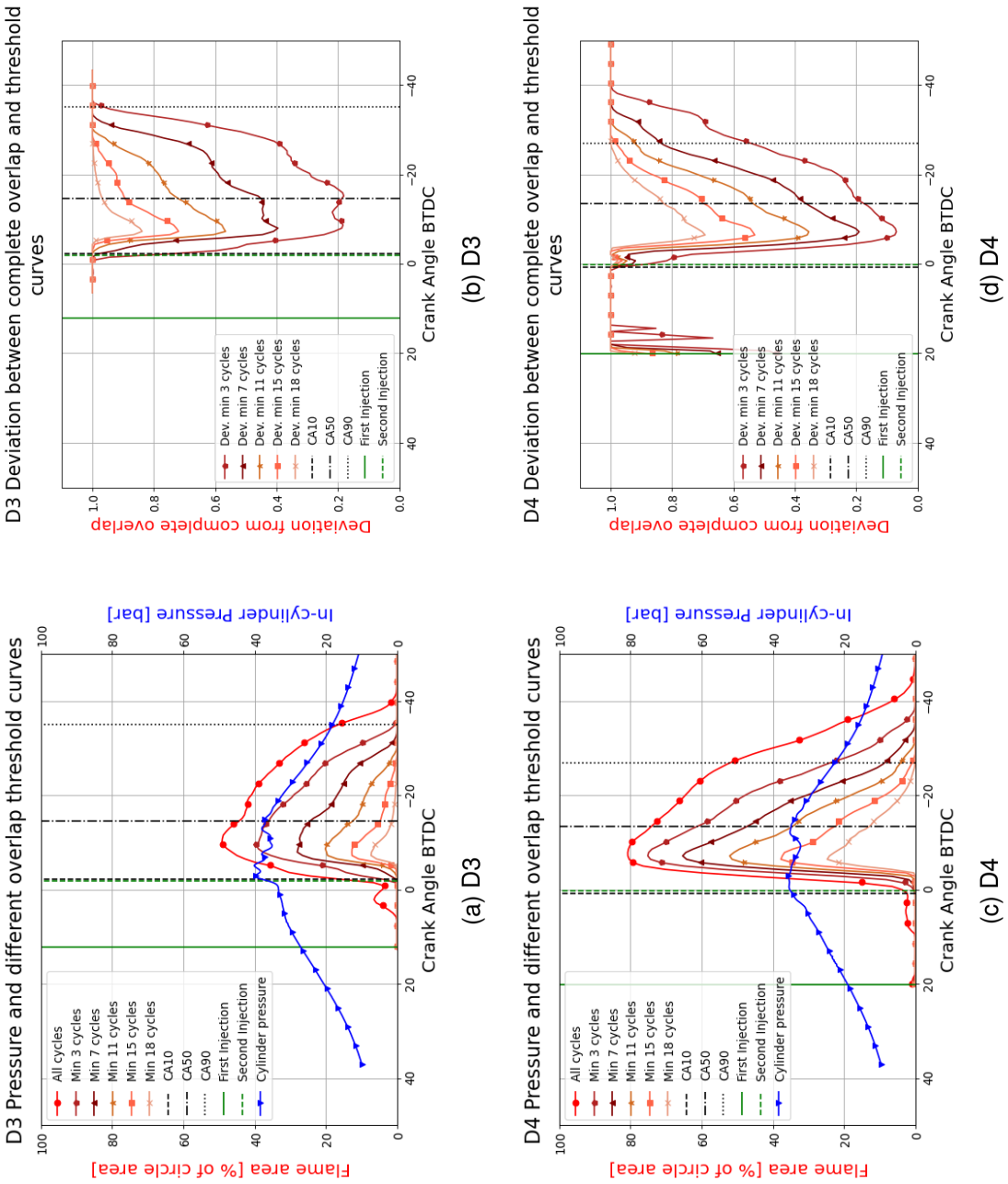


Figure 3.23: Pixel count (left) and deviation (right) for cases D3 and D4

This project has received funding from the European Union Horizon 2020 Research and Innovation programme. Grant Agreement No 861002

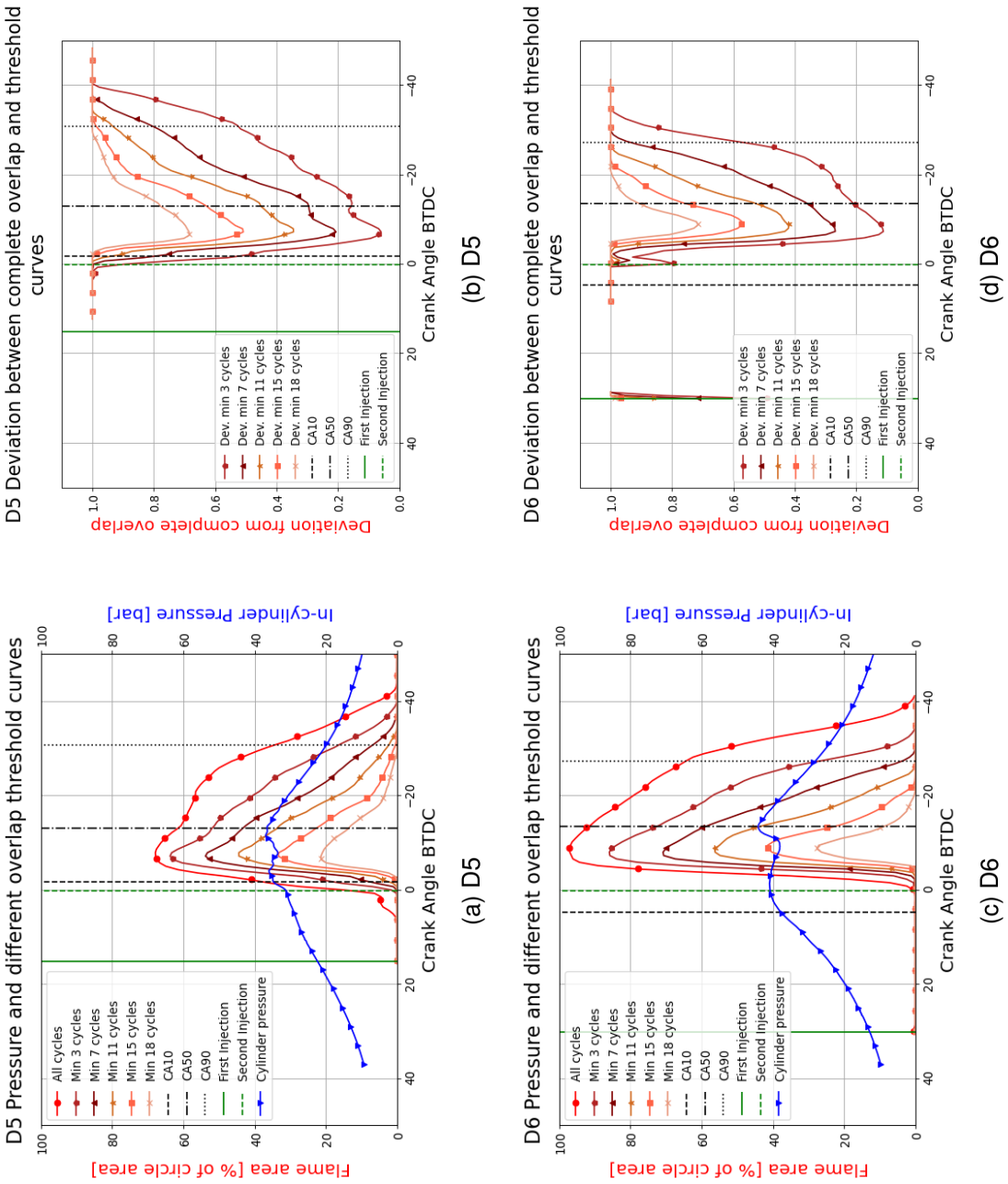


Figure 3.24: Pixel count (left) and deviation (right) for cases D5 and D6

This project has received funding from the European Union Horizon 2020 Research and Innovation programme. Grant Agreement No 861002

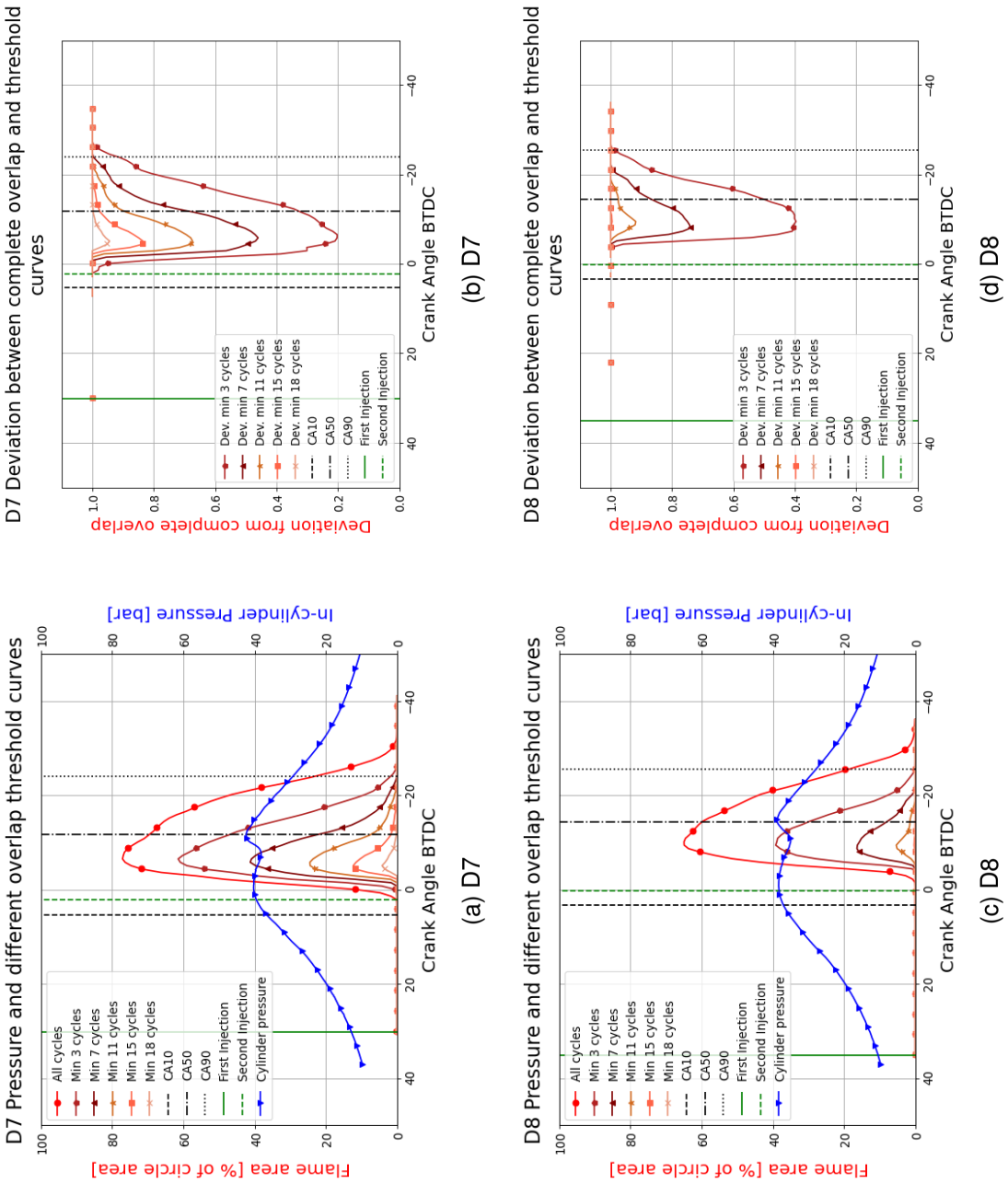


Figure 3.25: Pixel count (left) and deviation (right) for cases D7 and D8

This project has received funding from the European Union Horizon 2020 Research and Innovation programme. Grant Agreement No 861002

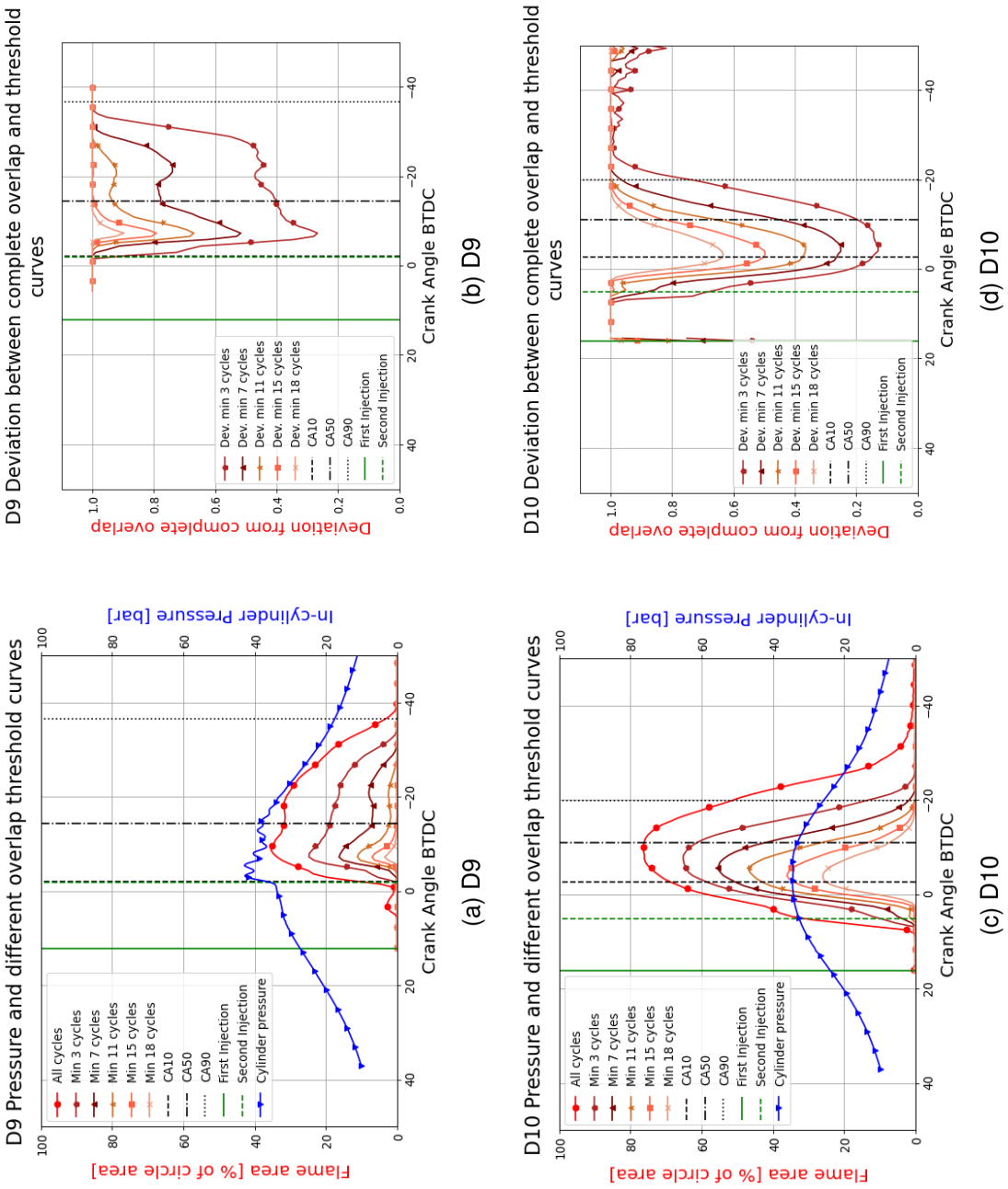


Figure 3.26: Pixel count (left) and deviation (right) for cases D9 and D10

This project has received funding from the European Union Horizon 2020 Research and Innovation programme. Grant Agreement No 861002

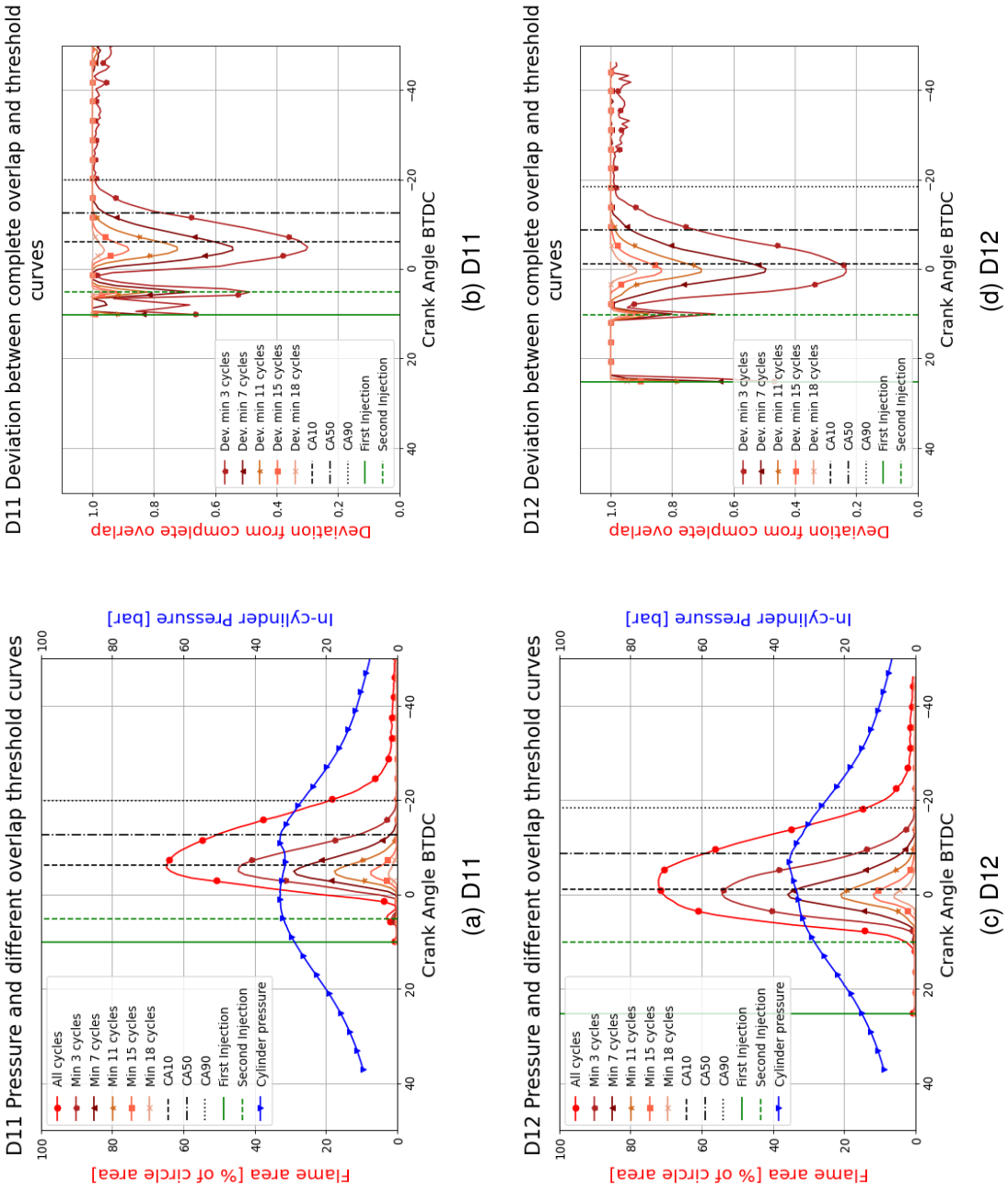


Figure 3.27: Pixel count (left) and deviation (right) for cases D11 and D12

This project has received funding from the European Union Horizon 2020 Research and Innovation programme. Grant Agreement No 861002

Cases E1-E7 represent the dual-fuel combustion cases with a 50-50 split pilot fuel injection with minimum 0.4 ms per split and a 2 ms injection of Natural Gas. Cases E1-E4 are shown in Figure 3.28 and Figure 3.29. Case E1 ($t_{\mathrm{D}} = 0.4 + 0.4$, $t_{\mathrm{NG}} = 2$, $\theta_{\mathrm{D}} = 10 + 6$, $\theta_{\mathrm{NG}} = 300$) behaves similar to case C6, which also has a pilot split injection with the same amount of Diesel, showing that the combustion is mostly influenced by the rapid Diesel combustion phase. Case E2 ($t_{\mathrm{D}} = 0.4 + 0.4$, $t_{\mathrm{NG}} = 2$, $\theta_{\mathrm{D}} = 10 + 5$, $\theta_{\mathrm{NG}} = 300$) behaves accordingly but with a lower pressure peak, showing that extending the time between the two injections reduces the efficiency, but also led to a faster combustion with a duration of 14.04° CA. Case E3 ($t_{\mathrm{D}} = 0.4 + 0.4$, $t_{\mathrm{NG}} = 2$, $\theta_{\mathrm{D}} = 11 + 7$, $\theta_{\mathrm{NG}} = 300$) behaves like case E1, showing that advancing the two pilot fuel injections by 1° CA does not have an impact on this combustion cases, except that the combustion duration for this case is even shorter at 13.57° CA, indicating that this combustion is mainly influenced by the rapid pilot fuel combustion phase. Case E4 ($t_{\mathrm{D}} = 0.4 + 0.4$, $t_{\mathrm{NG}} = 2$, $\theta_{\mathrm{D}} = 15 + 5$, $\theta_{\mathrm{NG}} = 300$) has a low pressure curve, showing, that advancing the first pilot fuel injection to 15° CA BTDC and therefore extending the duration between the two injections to 10° CA does have a very negative impact on the work generated. This is most likely caused by the mixture having fewer localized combustion zones due to the longer time for homogenization.

Cases E5 and E6 are shown in Figure 3.30. Case E5 ($t_{\mathrm{D}} = 0.4 + 0.4$, $t_{\mathrm{NG}} = 2$, $\theta_{\mathrm{D}} = 16 + 5$, $\theta_{\mathrm{NG}} = 300$) is similar to Case E4, displaying, that advancing the first pilot fuel injection by 1° CA does not change the combustion behavior much, yet very late in the expansion stroke there were still some flames visible, indicating that the high level of homogenization led to a low burn rate and afterwards to a slow Natural gas flame propagation phase. Case E6 ($t_{\mathrm{D}} = 0.486 + 0.486$, $t_{\mathrm{NG}} = 2$, $\theta_{\mathrm{D}} = 10 + 5$, $\theta_{\mathrm{NG}} = 300$) has the same injection timings as case E2 but a higher amount of Diesel was injected for each 50-50 split pilot fuel injection. This leads to a lack of oxygen and a very low reactivity with a combustion peak at 20° CA ATDC, making this combustion case very inefficient. This is also visible in the ignition delay since the case reached CA10 only at 15.08° CA and the overall combustion duration was 50.58° CA, leading to an overall very low amount of work being produced in the expansion stroke. Since all of the cases E1-E6 suffered from a too high amount of pilot fuel being present in the mixture, it was decided to reduce the amount for the following cases.

This project has received funding from the European Union Horizon 2020 Research and Innovation programme. Grant Agreement No 861002

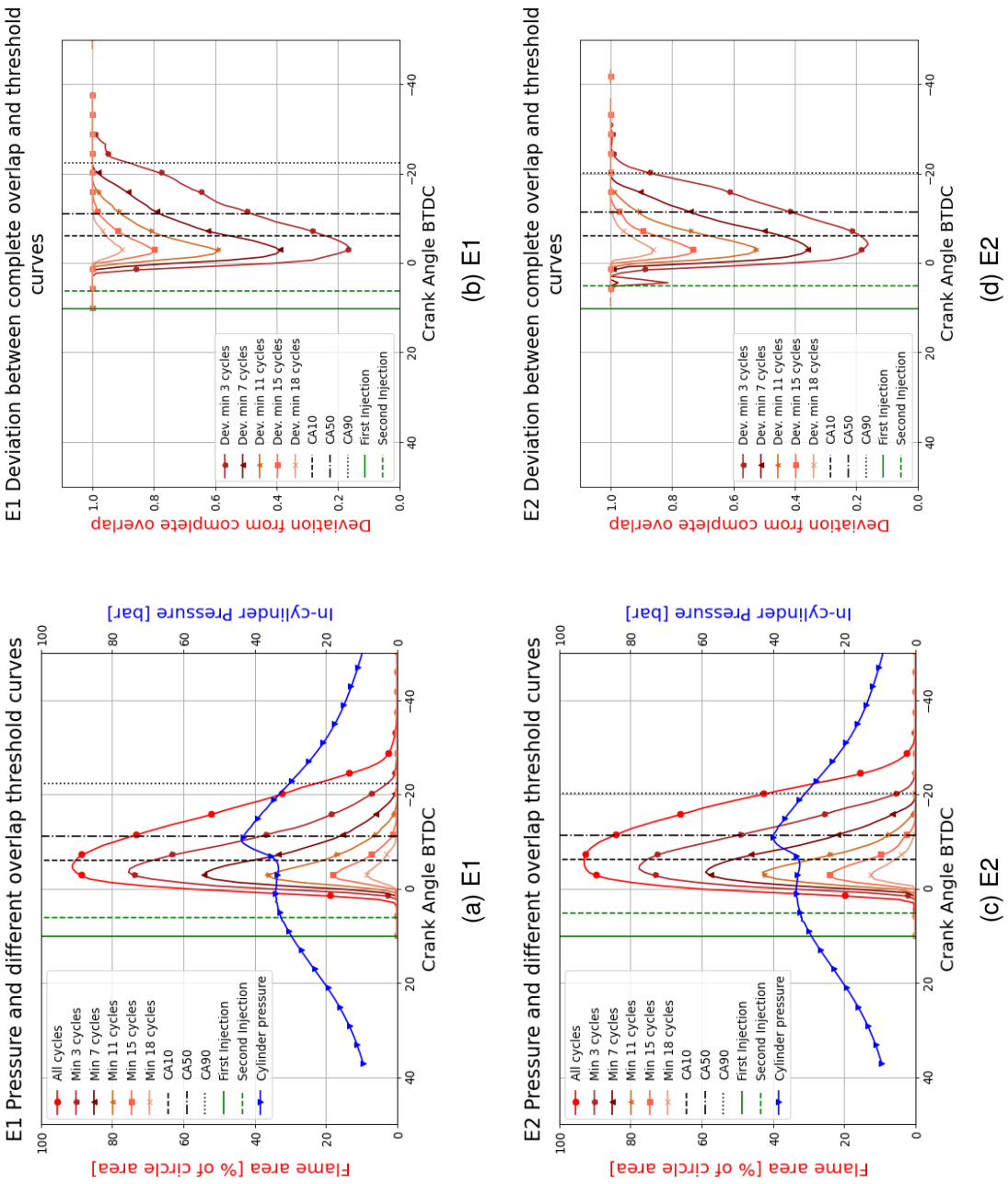


Figure 3.28: Pixel count (left) and deviation (right) for cases E1 and E2

This project has received funding from the European Union Horizon 2020 Research and Innovation programme. Grant Agreement No 861002

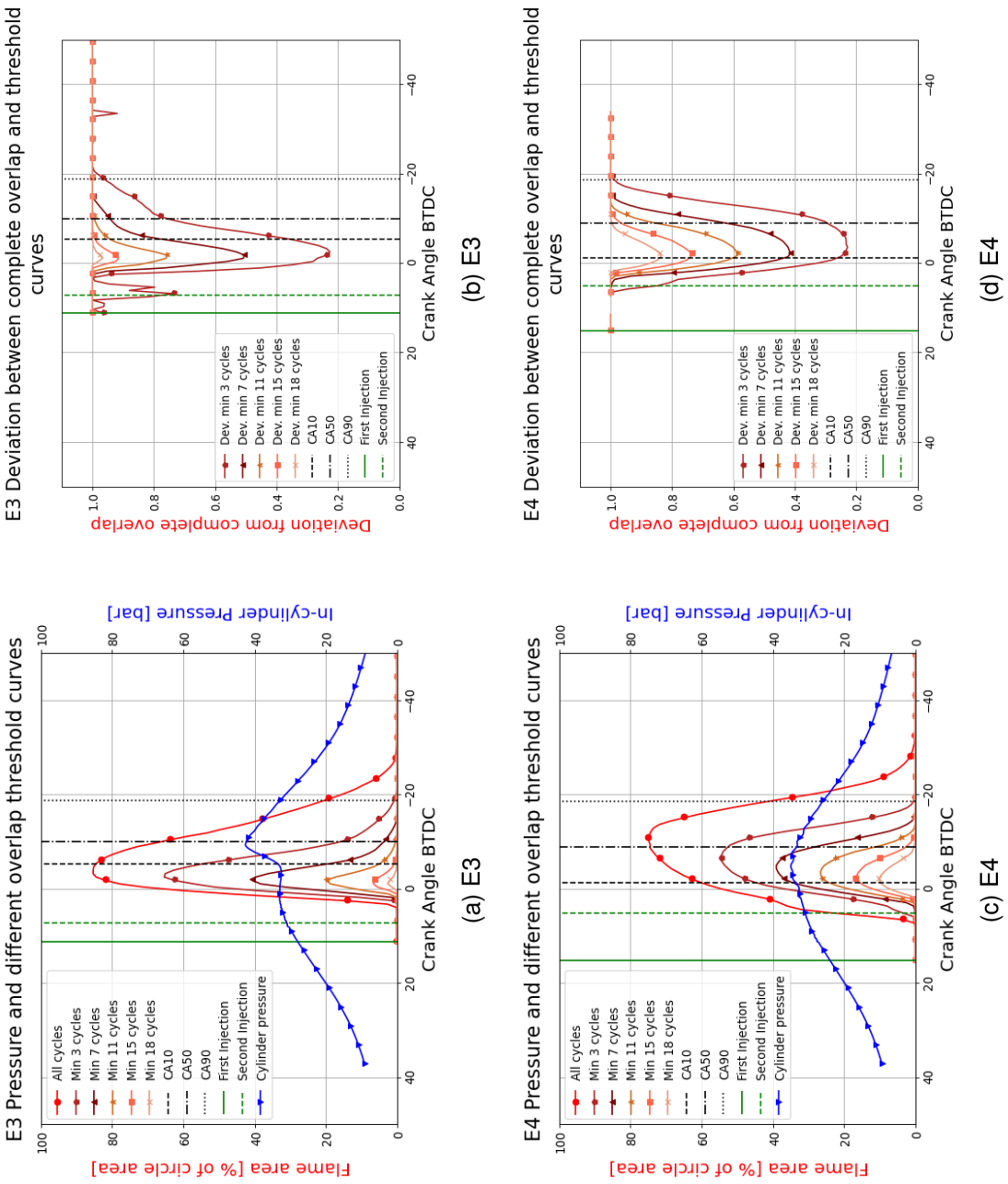


Figure 3.29: Pixel count (left) and deviation (right) for cases E3 and E4

This project has received funding from the European Union Horizon 2020 Research and Innovation programme. Grant Agreement No 861002

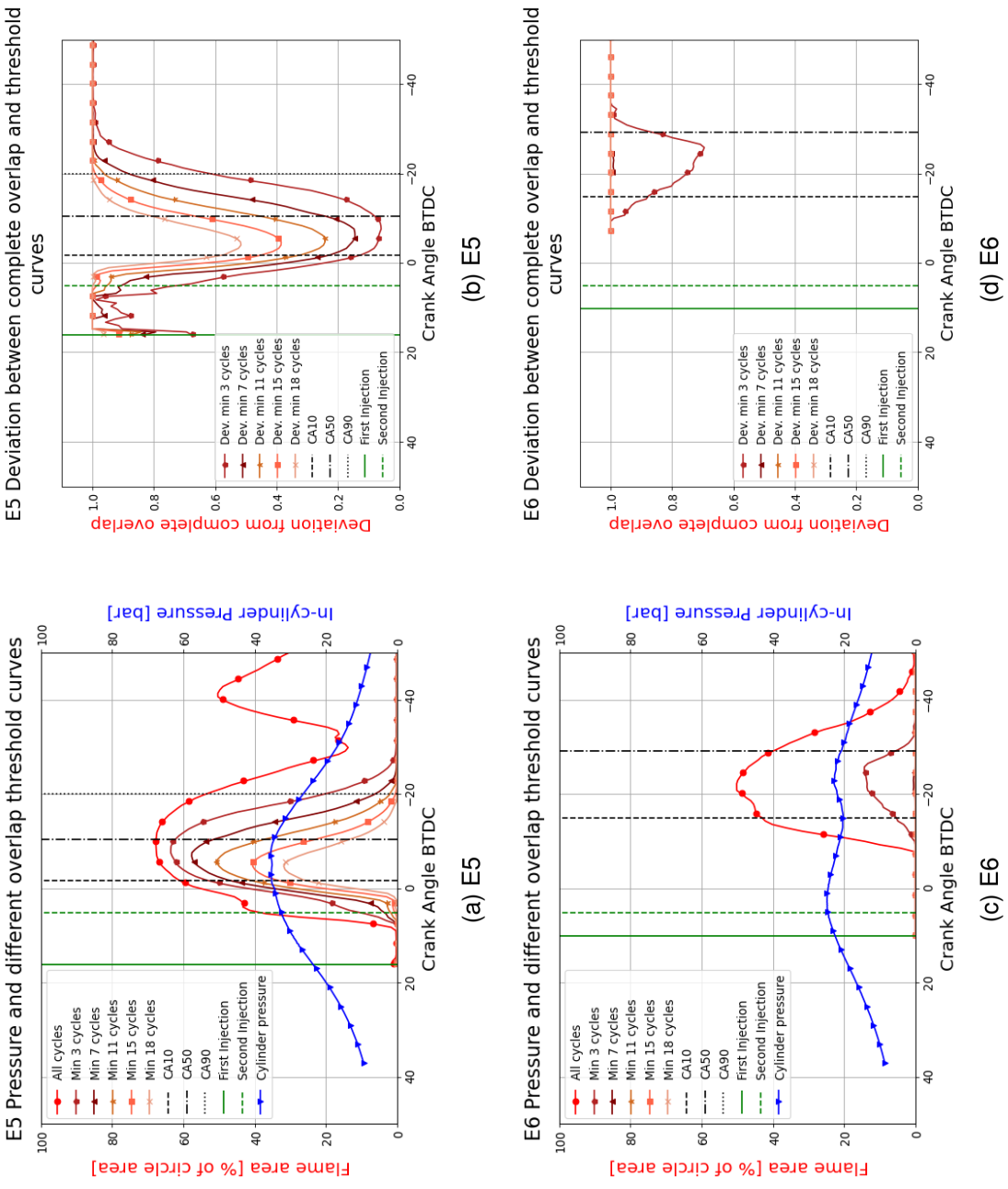


Figure 3.30: Pixel count (left) & Deviation (right) for thresholds and pressure curve case E5, E6

This project has received funding from the European Union Horizon 2020 Research and Innovation programme. Grant Agreement No 861002

Cases F1-F7 represent the dual-fuel combustion with a minimum amount split pilot fuel injection with the first injection between 15 and 12 ° CA BTDC and the second injection between 1 and 2° CA ATDC. This timings were determined due to the observations of the previous cases were flame areas were forming between the two pilot fuel injections, leading to a faster combustion as soon as the second pilot fuel injection starts. The beneficial effect of the initial flame formation can be explained by two combustion mechanisms. First, the pilot injection generates hot combustion products that reduce the kernel-growth time required for ignition of the subsequent injection. Second, the pilot modifies the local equivalence ratio distribution within the cylinder which creates regions with increased reactivity that immediately ignite the second injection and main fuel-air mixture. The cases F1-F7 were designed to optimize the dual-fuel injection strategy. The objective was to establish stable kernel flames before TDC using the minimum amount of Diesel fuel to improve the combustion phasing and duration. The cases F3 and F4 were included to investigate the influence of the changes in injection timing. Once stable combustion was achieved the Natural Gas quantity was increased but this required further adjustments to the pilot injection timing. Cases F1-F4 are shown in Figure 3.31 and Figure 3.32. Case F1 ($t_{\mathrm{D}} = 0.33 + 0.33$, $t_{\mathrm{NG}} = 2$, $\theta_{\mathrm{D}} = 15 + (-2)$, $\theta_{\mathrm{NG}} = 300$) has the initial flame area forming at around 9° CA BTDC with a high deviation of close to 1. The pressure peak is at 1° CA ATDC and the flame area peak at 8° CA ATDC. Due to this small flame front the combustion reaches CA10 at 3.77° CA BTDC but afterwards combusts rapidly with a duration of 21.74° CA. Case F2 ($t_{\mathrm{D}} = 0.3 + 0.3$, $t_{\mathrm{NG}} = 2$, $\theta_{\mathrm{D}} = 15 + (-2)$, $\theta_{\mathrm{NG}} = 300$) behaves similar to case F1 but has a more stable flame area forming between the two pilot fuel injections, which can be seen in the deviation at around 8° CA BTDC. The ignition delay and combustion duration are similar for this case, meaning that the change in the amount of Diesel does not influence this combustion significantly and that the main characteristics are dominated by the Natural Gas combustion. Case F3 ($t_{\mathrm{D}} = 0.3+0.33$, $t_{\mathrm{NG}} = 2$, $\theta_{\mathrm{D}} = 13+(-2)$, $\theta_{\mathrm{NG}} = 300$) has a slightly delayed first pilot fuel injection, compared to cases F1 and F2, at 13° CA BTDC. Overall the combustion behaves similar to case F2, with a small second peak from the Natural Gas combustion visible at CA50 and a slightly prolong Natural Gas combustion phase. Case F4 ($t_{\mathrm{D}} = 0.3 + 0.33$, $t_{\mathrm{NG}} = 2$, $\theta_{\mathrm{D}} = 12 + (-2)$, $\theta_{\mathrm{NG}} = 300$) is similar to case F3 where the combustion influence of the pilot fuel is kept to a minimum with a stable initial flame forming. It was decided to keep the ratio of 0.3 ms for the first and 0.33ms for the second pilot fuel injection for the following cases.

Cases F5-F7 are shown in Figure 3.33 and Figure 3.34. Case F5 ($t_{\mathrm{D}} = 0.3 + 0.33$, $t_{\mathrm{NG}} = 2$, $\theta_{\mathrm{D}} = 12 + (-1)$, $\theta_{\mathrm{NG}} = 300$) has the same behavior as case F3, showing that a 1° CA delay does not influence the combustion. Case F6 ($t_{\mathrm{D}} = 0.3 + 0.33$, $t_{\mathrm{NG}} = 2.5$,

This project has received funding from the European Union Horizon 2020 Research and Innovation programme. Grant Agreement No 861002

$\theta_{\mathrm{D}} = 12 + (-1)$, $\theta_{\mathrm{NG}} = 300$) has a higher amount of Natural Gas but does not show a higher peak pressure compared to case F5, showing that the combustion is mostly influenced by the Diesel. Both cases have a similar combustion duration of about 21° CA, indicating that the higher amount of Natural Gas may not have contributed significantly to the main combustion phase since the pressure rise rates are the same in both cases. Therefore, it was decided to advance the first pilot fuel injection to 15° CA BTDC for case F7 ($t_{\mathrm{D}} = 0.3 + 0.33$, $t_{\mathrm{NG}} = 4 + 4$, $\theta_{\mathrm{D}} = 15 + (-1)$, $\theta_{\mathrm{NG}} = 360 + 320$). Case F7 was included to evaluate the influence of higher Natural Gas amounts on the combustion. The results from F7 showed that even with higher Natural Gas amount, the initial flame kernel is forming in the combustion chamber, but the timing of the minimum pilot fuel injection had to be advanced by 3° CA to reach the same timing. It also has a higher amount of Natural Gas injected into the combustion chamber. The pressure curve shows a very high pressure rise starting around TDC with a peak pressure of 60 bar. This indicates that the advance of the pilot fuel injection led to a longer time to form a stable flame kernel, reaching CA10 close to TDC, and immediate ignition of the second pilot fuel injection and therefore the rest of the fuel-air mixture. This leads to a very rapid first combustion phase where CA50 is already reached at 7.36° CA ATDC followed by a slower Natural Gas combustion phase until 20.42° CA ATDC. Since this combustion approach seemed very promising, it was decided to test similar test conditions with the usage of Hythane.

This project has received funding from the European Union Horizon 2020 Research and Innovation programme. Grant Agreement No 861002

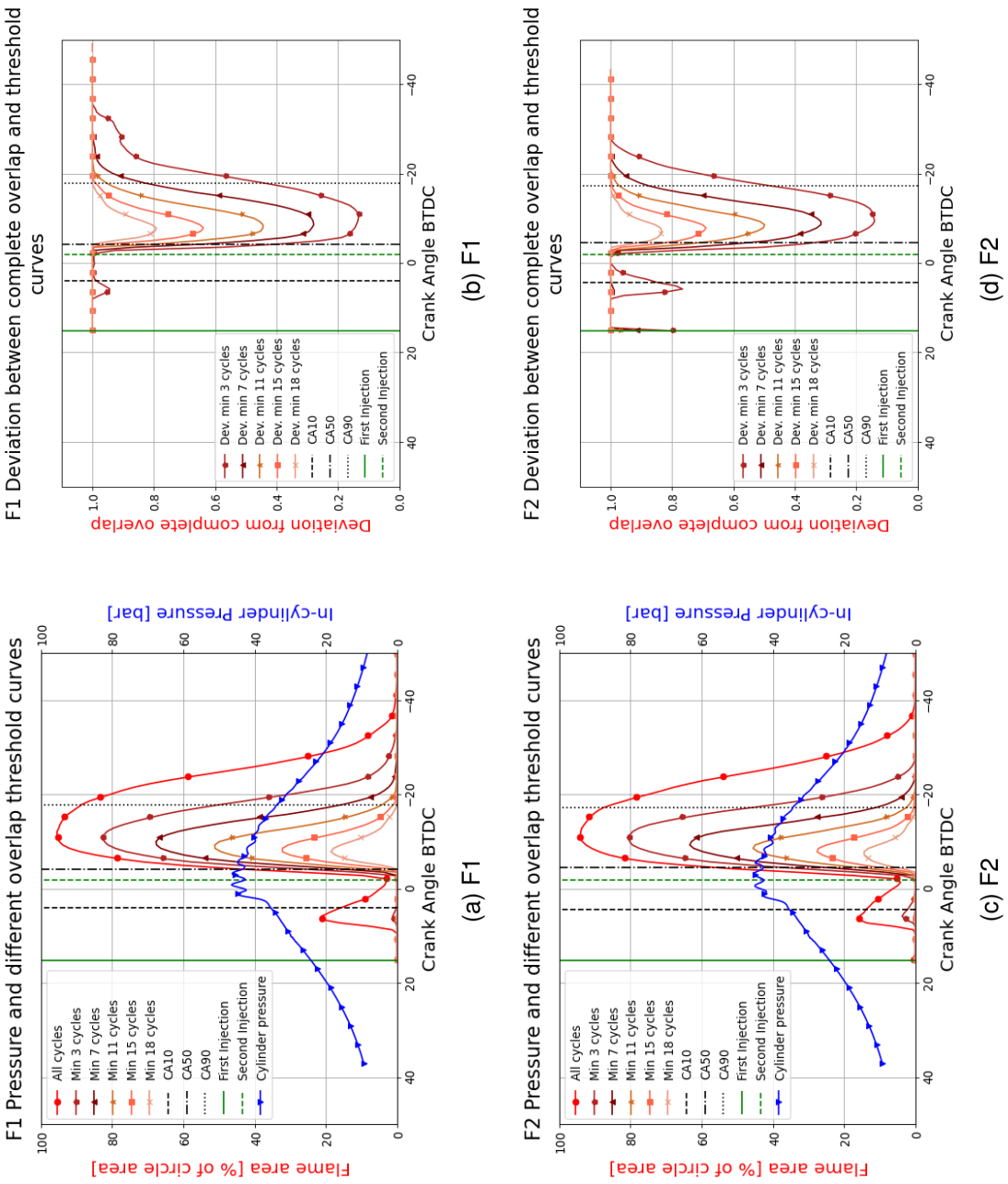


Figure 3.31: Pixel count (left) and deviation (right) for cases F1 and F2

This project has received funding from the European Union Horizon 2020 Research and Innovation programme. Grant Agreement No 861002

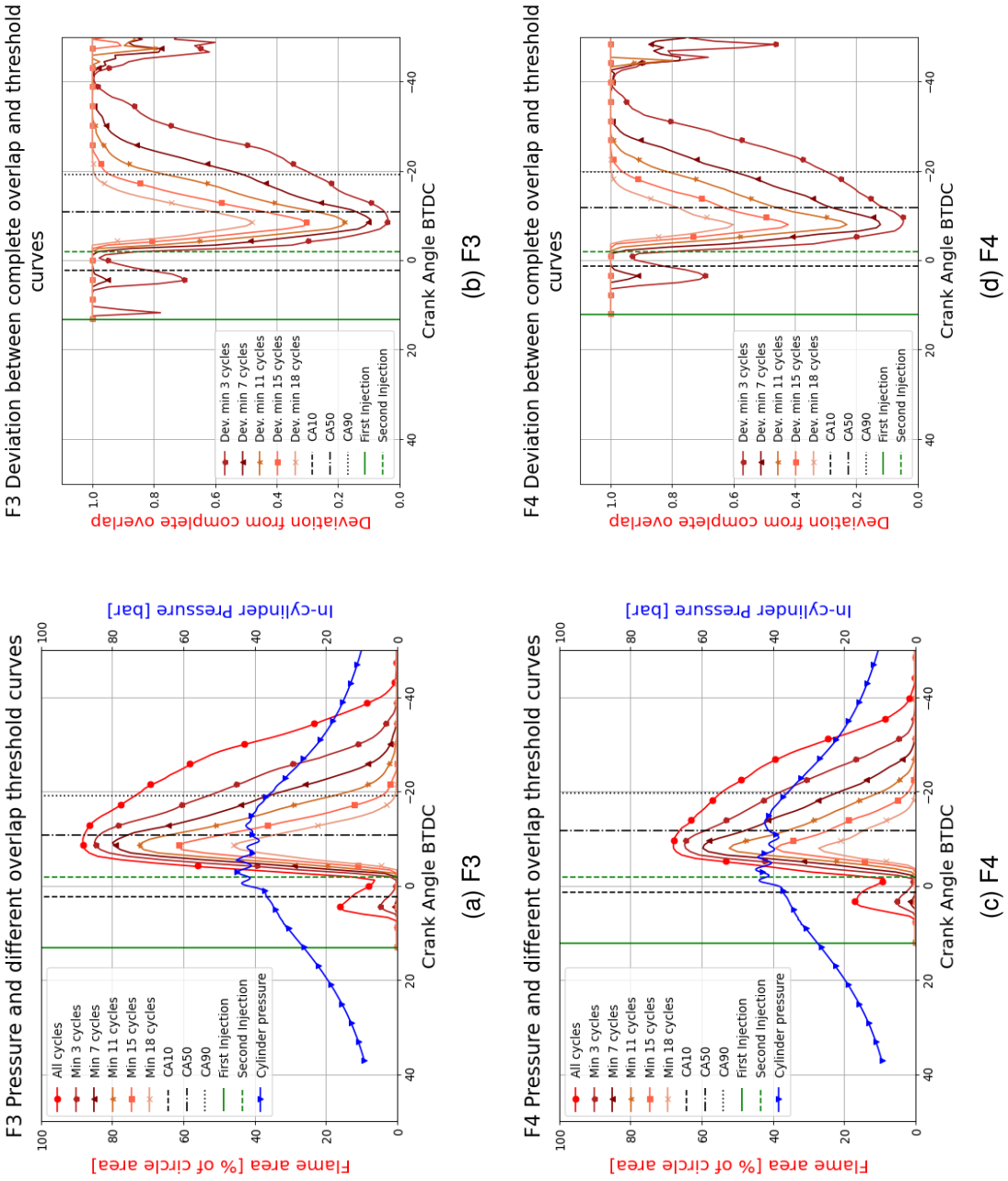


Figure 3.32: Pixel count (left) and deviation (right) for cases F3 and F4

This project has received funding from the European Union Horizon 2020 Research and Innovation programme. Grant Agreement No 861002

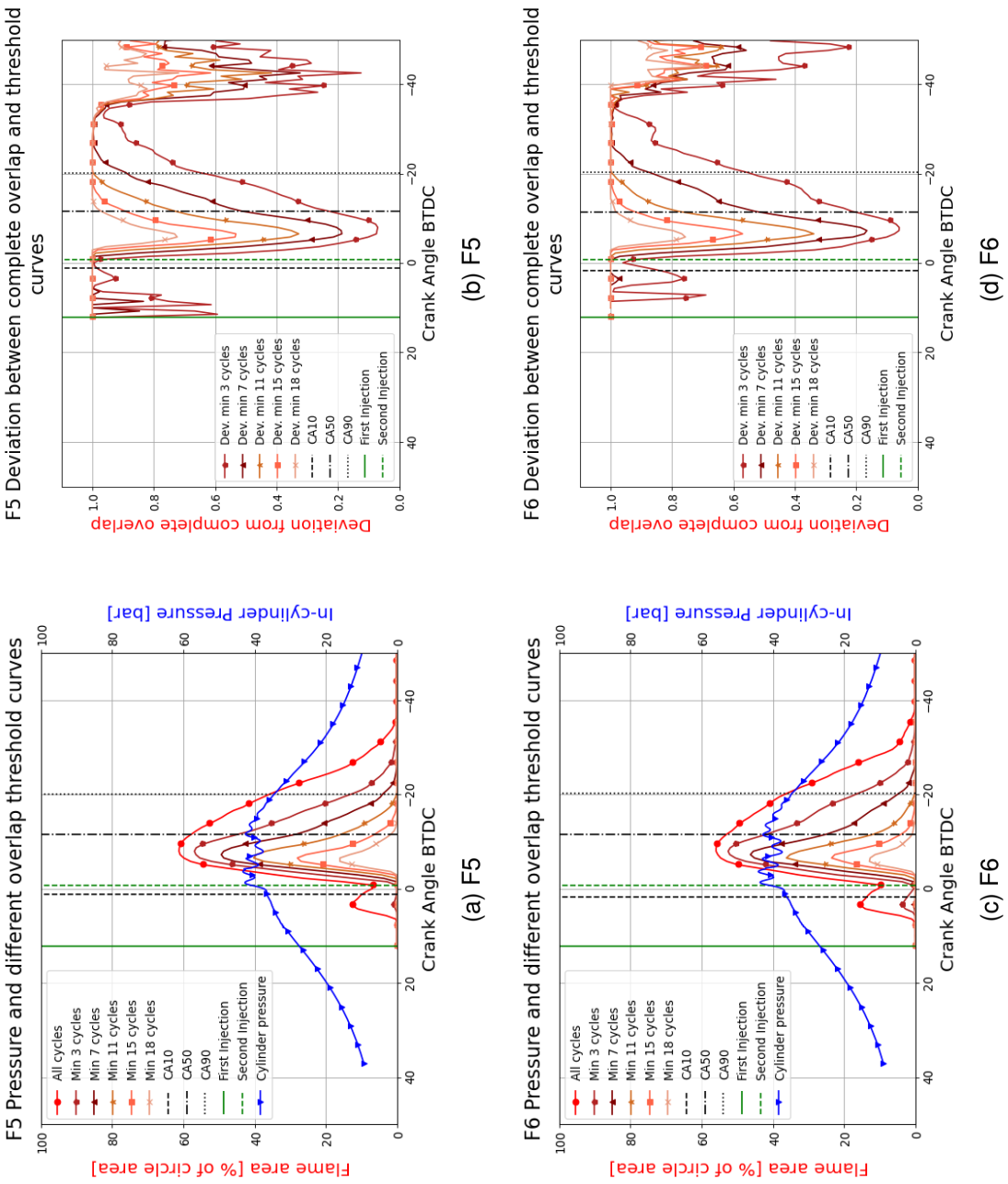
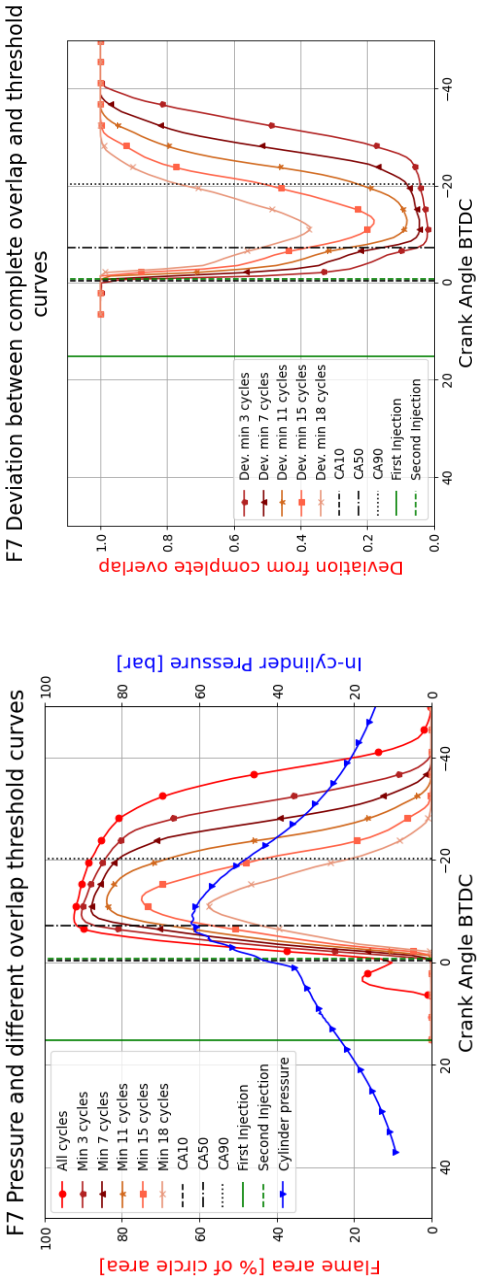


Figure 3.33: Pixel count (left) and deviation (right) for cases F5 and F6

This project has received funding from the European Union Horizon 2020 Research and Innovation programme. Grant Agreement No 861002



(a) F7 (b) F7

Figure 3.34: Pixel count (left) and deviation (right) for case F7

This project has received funding from the European Union Horizon 2020 Research and Innovation programme. Grant Agreement No 861002

The operating conditions investigated in cases F1-F7 resulted in a favorable combustion profile while maintaining a high Natural Gas substitution rate and a high IMEP. It can be observed, that cases with a more concentrated and stable flame area have a higher IMEP and Net HRR. An example of this is shown in Figure 3.35, in which the images from one cycle of case F1 are compared to the same timings for case F7. These images were handselected because they were the closest to the average images from both test cases and would represent the initial flame forming size in the original images with a better visibility than in the aver-age images. After determining, that a small amount of split pilot fuel injection with a timing of 15° CA BTDC and 1° CA ATDC leads to a optimized IMEP and Net HRR, further experiments were carried out with the same combustion timings and Hythane as main fuel.

This project has received funding from the European Union Horizon 2020 Research and Innovation programme. Grant Agreement No 861002

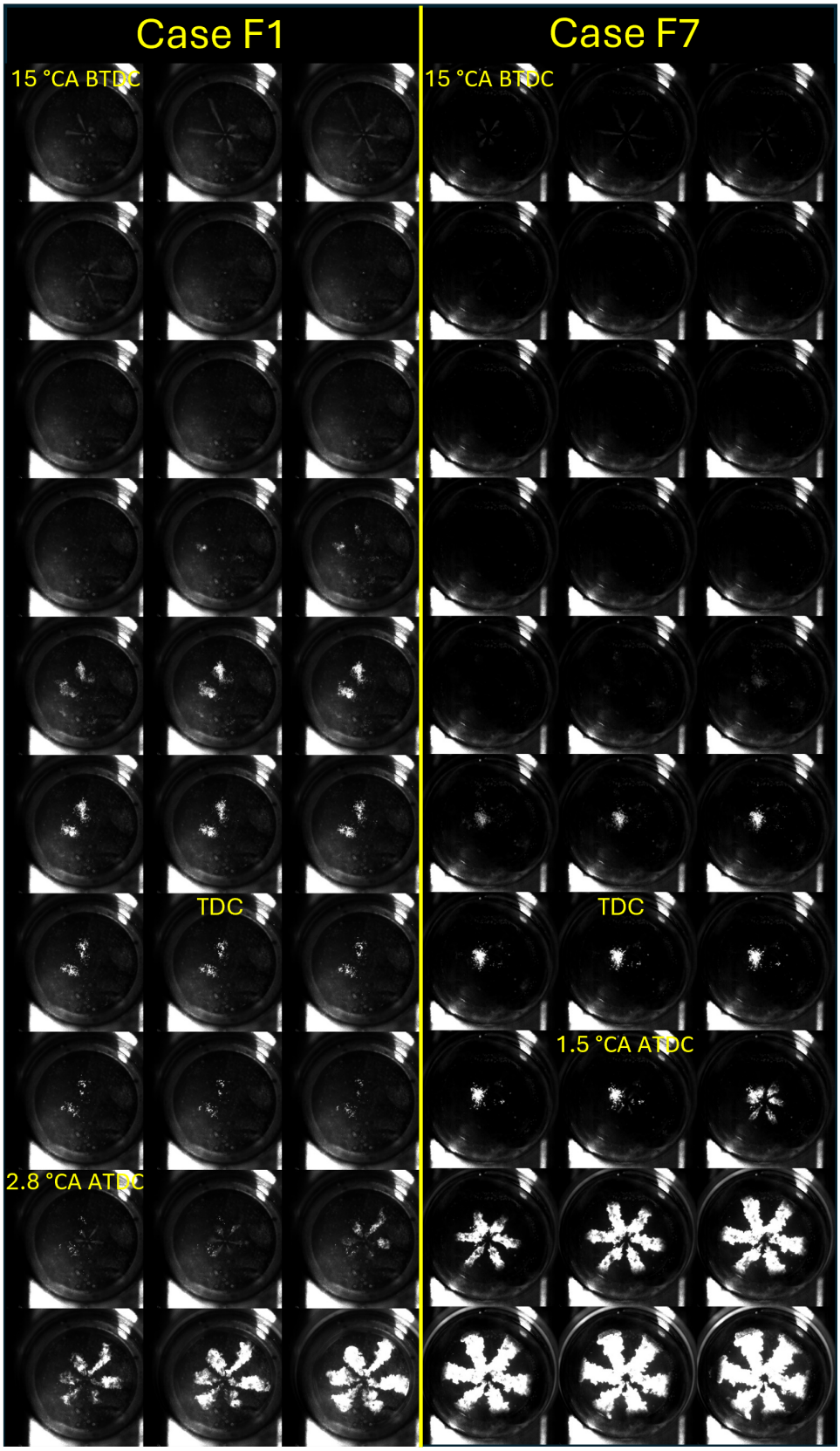


Figure 3.35: Comparison of the initial flame forming between the first and second pilot fuel injection for case F1 (left) and case F7 (right)

This project has received funding from the European Union Horizon 2020 Research and Innovation programme. Grant Agreement No 861002

Cases G1-G5 represent the dual-fuel combustion with Hythane as main fuel. Cases G1-G4 are shown in Figure 3.36 and Figure 3.37. For each of the cases the amount of main fuel was varried. Case G1 ($t_{\mathrm{D}} = 0.3 + 0.33$, $t_{\mathrm{NG}} = 4$, $\theta_{\mathrm{D}} = 15 + (-1)$, $\theta_{\mathrm{NG}} = 360$) has the same properties as case F7 but combusts with a lower peak pressure at around 45bar. Since Hythane was used it was expected that the combustion duration is lower in this test case. However it is longer than in case F7, which is why it was decided to try the same conditions with a lower main fuel amount. Case G2 ($t_{\mathrm{D}} = 0.3 + 0.33$, $t_{\mathrm{NG}} = 2$, $\theta_{\mathrm{D}} = 15 + (-1)$, $\theta_{\mathrm{NG}} = 360$) has a lower amount of main fuel leading to a even lower peak pressure , but nearly no influence on the combustion duration. Case G3 ($t_{\mathrm{D}} = 0.3 + 0.33$, $t_{\mathrm{NG}} = 4 + 2$, $\theta_{\mathrm{D}} = 13 + (-1)$, $\theta_{\mathrm{NG}} = 360 + 320$) has a first pilot fuel injection, which was delayed to 13° CA BTDC to compensate the effect, that Hythane combusts faster than Natural Gas , yet it did also not significantly reduce the combustion duration or improve the pressure rise rate. Case G4 ($t_{\mathrm{D}} = 0.3 + 0.33$, $t_{\mathrm{NG}} = 3 + 3$, $\theta_{\mathrm{D}} = 12 + (-1)$, $\theta_{\mathrm{NG}} = 360 + 320$) has a low amount of split injected main fuel and therefore a low pressure rise rate.

Case G5 ($t_{\mathrm{D}} = 0.3 + 0.33$, $t_{\mathrm{NG}} = 4 + 4$, $\theta_{\mathrm{D}} = 12 + (-1)$, $\theta_{\mathrm{NG}} = 360 + 320$) is shown in Figure 3.38. It has a pilot fuel injection at 12° CA BTDC and 1° CA ATDC. This leads to an even higher pressure rise rate than case F7 with a peak pressure of nearly 70 bar. It can be observed that the overall pixel count is lower than that of G4, which is attributed to the rapid window pollution encountered in this test case. For this reason, the new analysis method was employed in this thesis, as it compares the deviations using a dimensionless parameter that is independent of the degree of window pollution. Also, for G5 the combustion duration is even shorter than in case F7. This shows that Hythane can be used as a more efficient main fuel compared to Natural Gas but the fact that the main fuel combusts faster has to be compensated by adjusting the injection timings.

This project has received funding from the European Union Horizon 2020 Research and Innovation programme. Grant Agreement No 861002

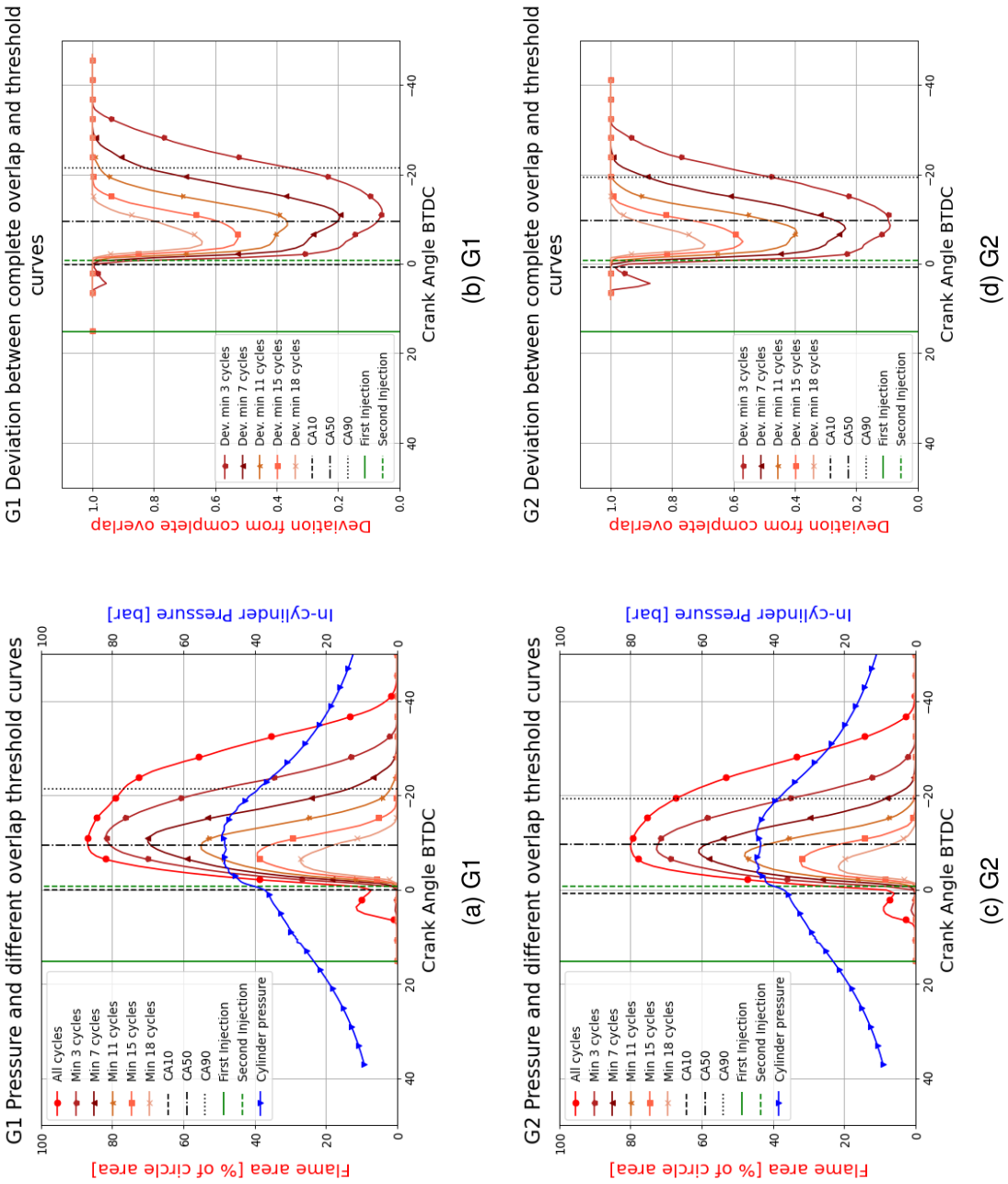


Figure 3.36: Pixel count (left) and deviation (right) for cases G1 and G2

This project has received funding from the European Union Horizon 2020 Research and Innovation programme. Grant Agreement No 861002

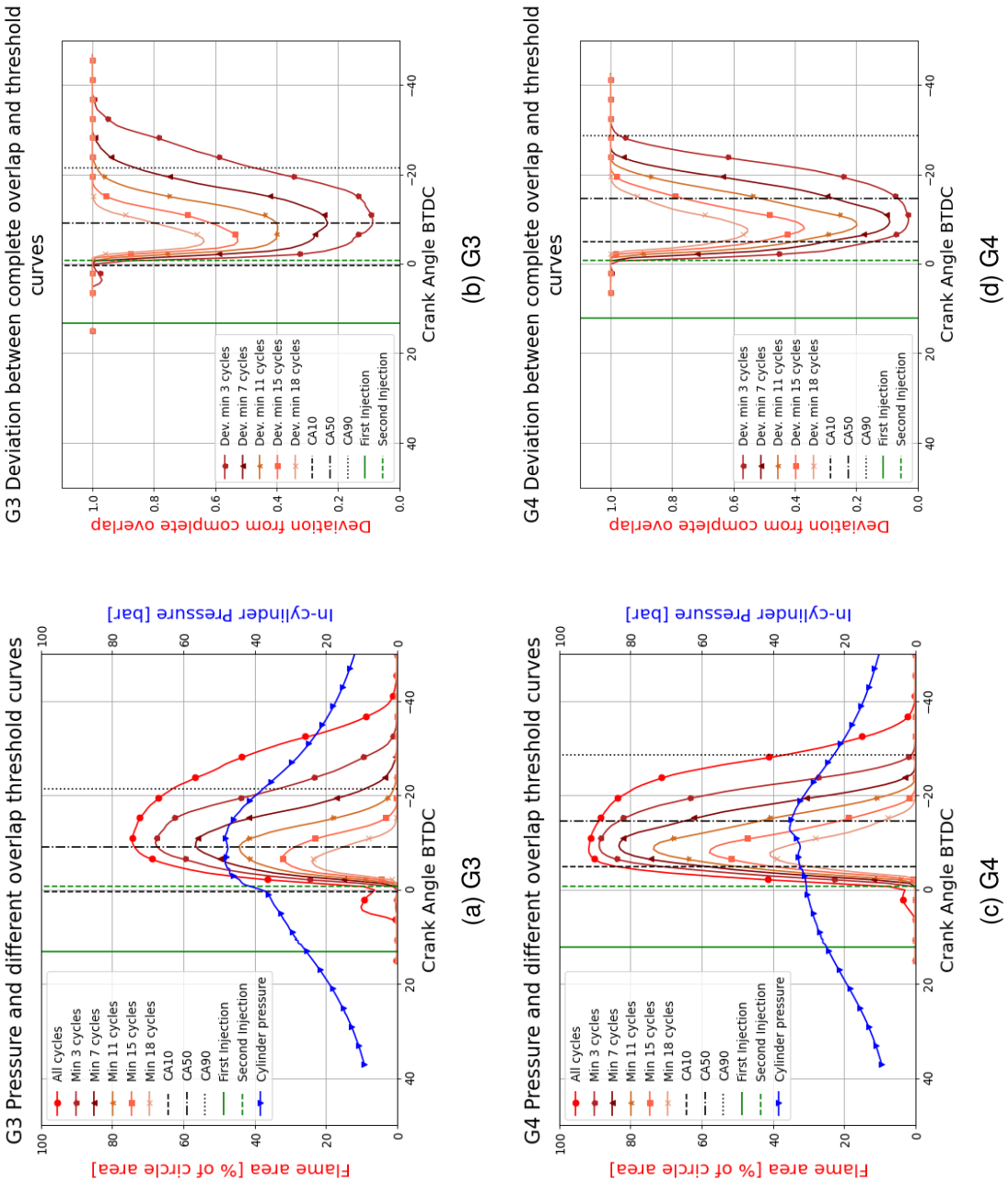
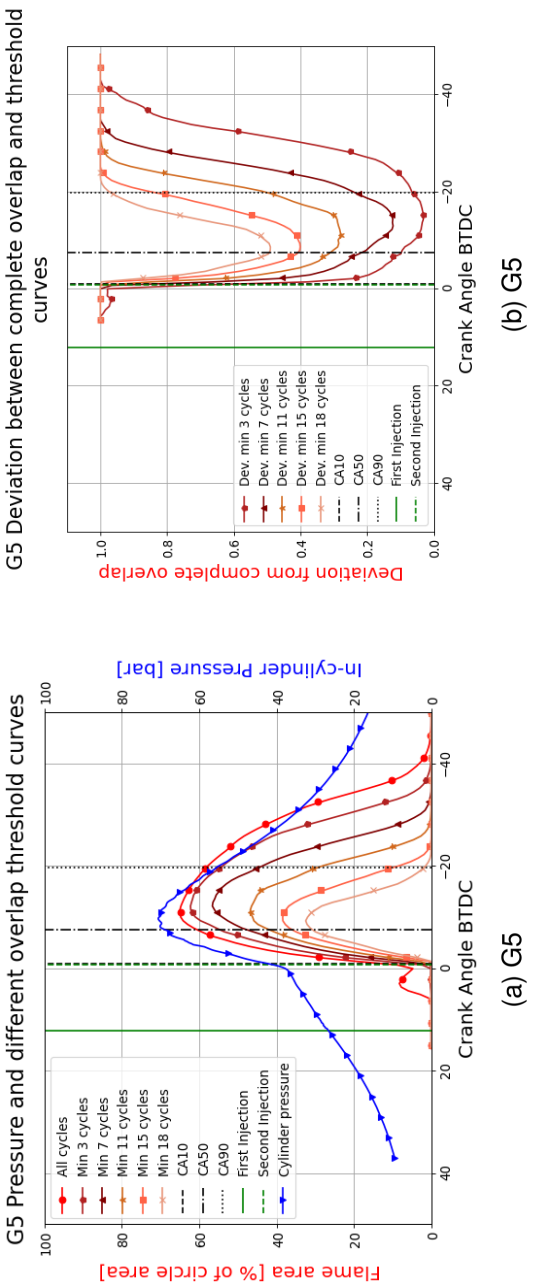


Figure 3.37: Pixel count (left) and deviation (right) for cases G3 and G4

This project has received funding from the European Union Horizon 2020 Research and Innovation programme. Grant Agreement No 861002



(a) G5 (b) G5

Figure 3.38: Pixel count (left) & Deviation (right) for thresholds and pressure curve case G5

This project has received funding from the European Union Horizon 2020 Research and Innovation programme. Grant Agreement No 861002

For a comparison of how the flame ares develop, for each case the average images created at 5° CA BTDC, TDC, 5° CA ATDC and 10° CA ATDC are compared. Cases A1-B10 are shown in Figure 3.39. Cases B11-D3 are shown in Figure 3.40. Cases D4-E5 are shown in Figure 3.41. Cases E6-G5 are shown in Figure 3.42. For some cases a asymmetry in the averaged combustion images can be observed like for cases B7 or E1. The observed asymmetry suggests that combustion is driven by a small number of localized ignition sites rather than by a homogeneous premixed flame propagating throughout the chamber. This highlights the influence of mixture stratification and spray flow interactions on the dual-fuel combustion process.

This project has received funding from the European Union Horizon 2020 Research and Innovation programme. Grant Agreement No 861002

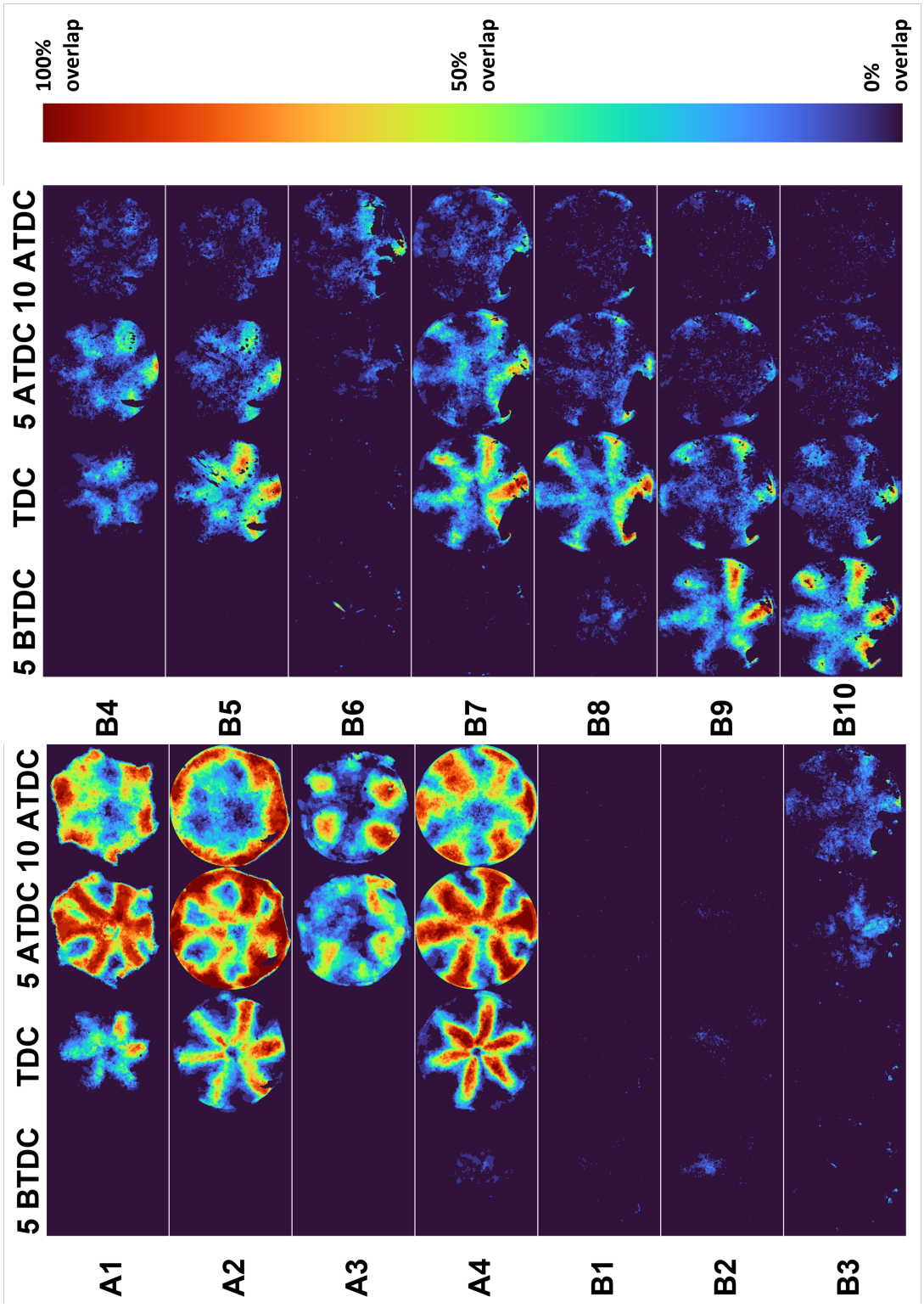


Figure 3.39: Comparison of the average combustion images at 5° CA BTDC, TDC, 5° CA ATDC and 10° CA ATDC for Cases A1-B10

This project has received funding from the European Union Horizon 2020 Research and Innovation programme. Grant Agreement No 861002

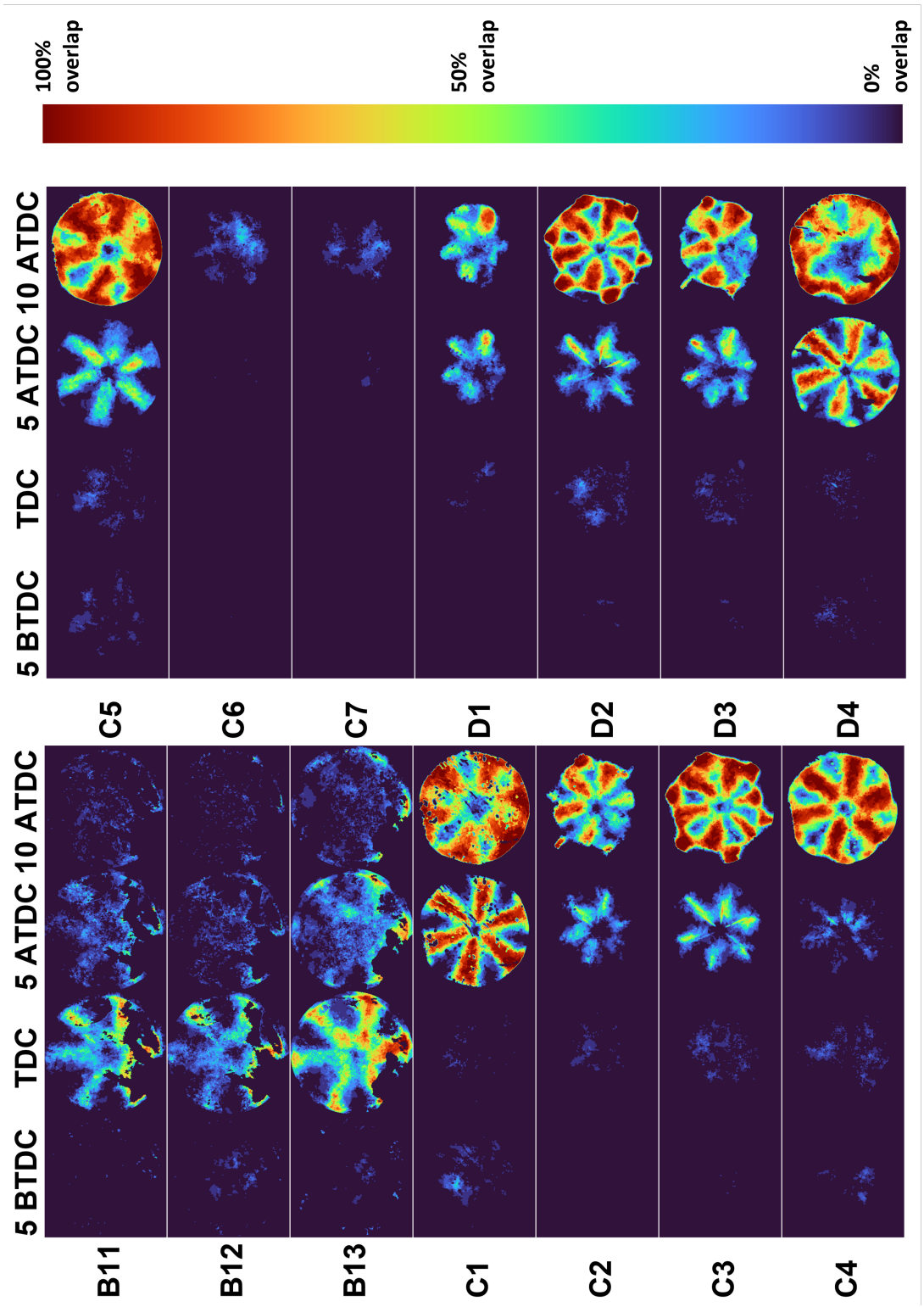


Figure 3.40: Comparison of the average combustion images at 5° CA BTDC, TDC, 5° CA ATDC and 10° CA ATDC for Cases B11-D3

This project has received funding from the European Union Horizon 2020 Research and Innovation programme. Grant Agreement No 861002

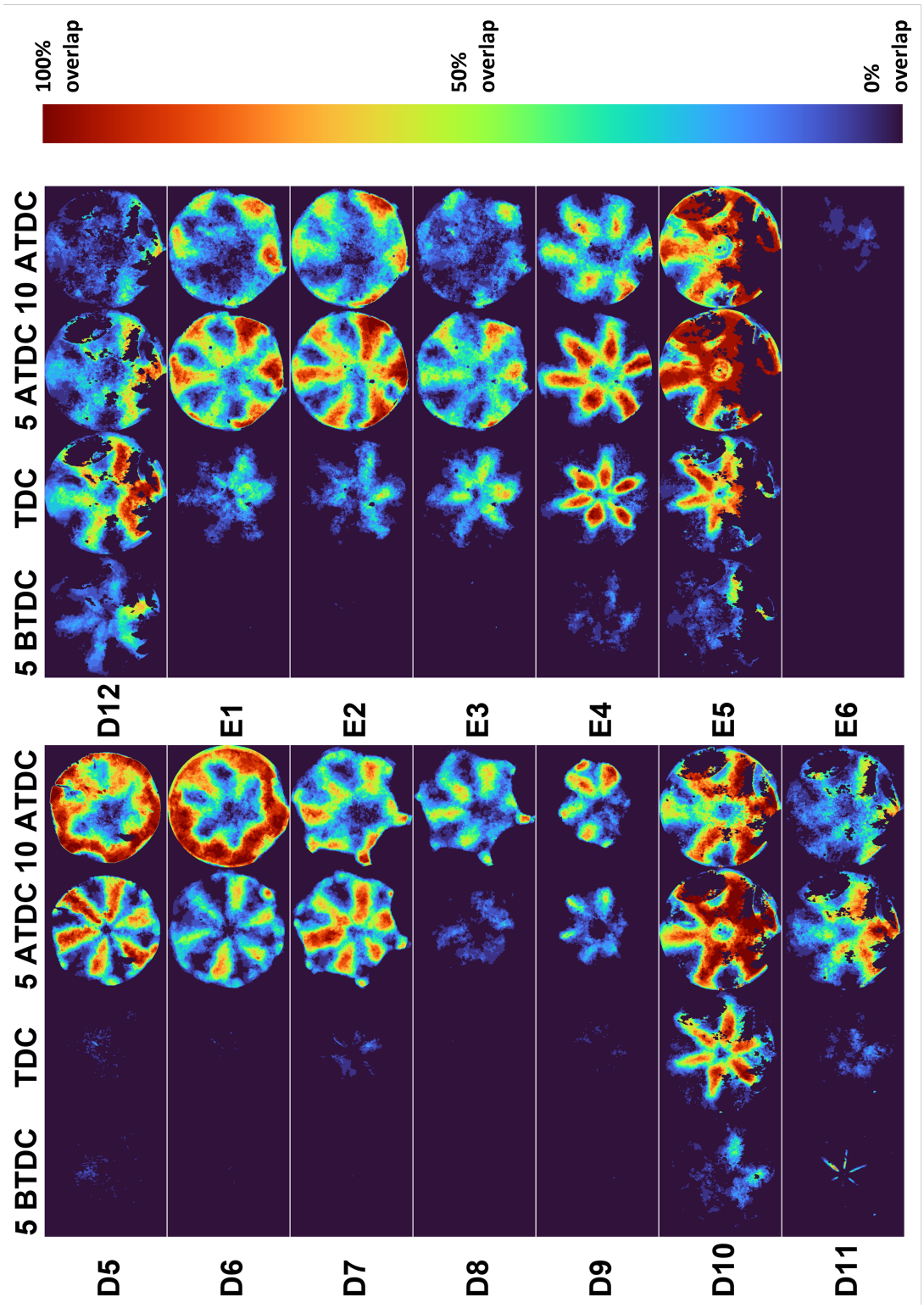


Figure 3.41: Comparison of the average combustion images at 5° CA BTDC, TDC, 5° CA ATDC and 10° CA ATDC for Cases D4-E5

This project has received funding from the European Union Horizon 2020 Research and Innovation programme. Grant Agreement No 861002

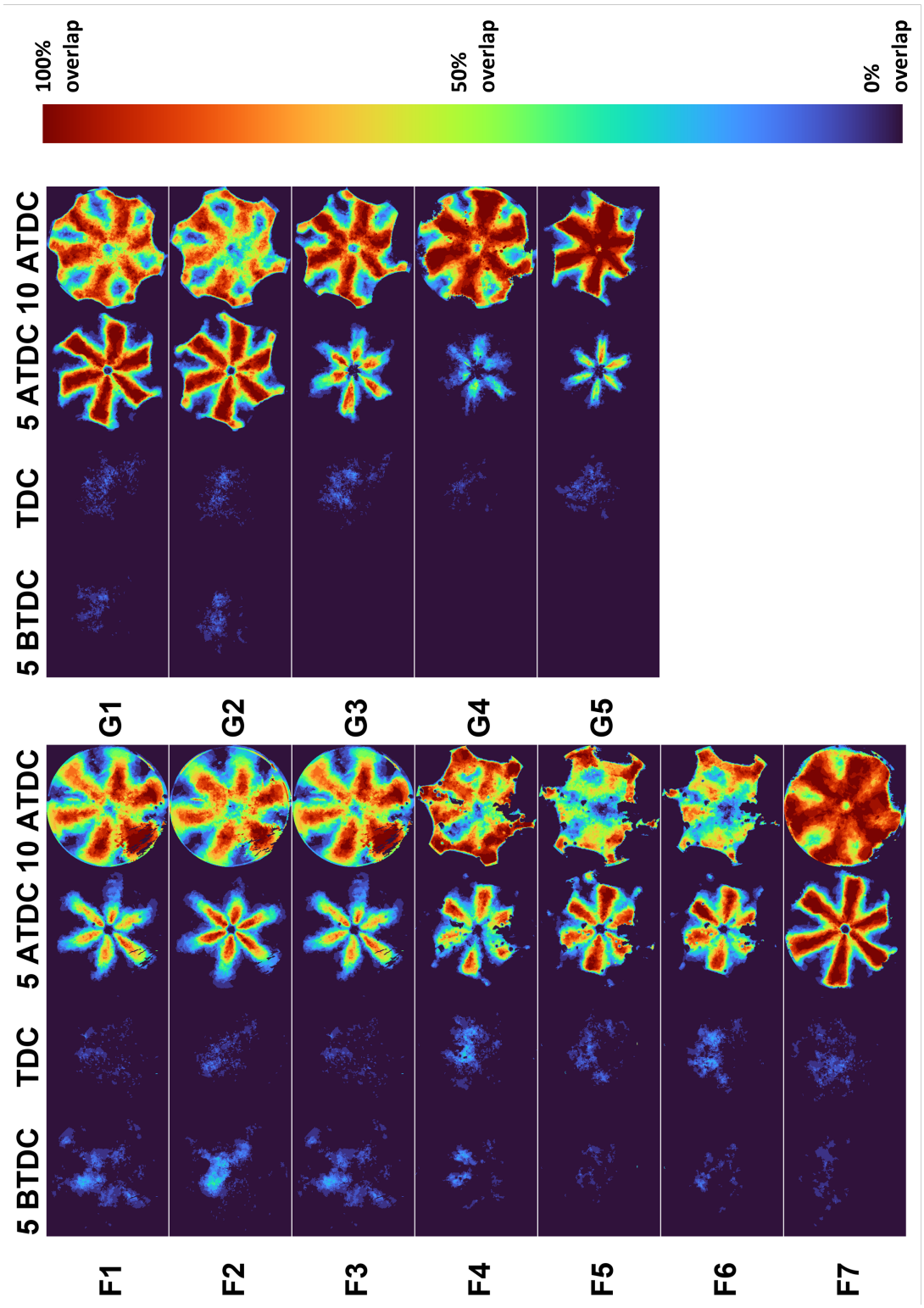


Figure 3.42: Comparison of the average combustion images at 5° CA BTDC, TDC, 5° CA ATDC and 10° CA ATDC for Cases E6-G5

This project has received funding from the European Union Horizon 2020 Research and Innovation programme. Grant Agreement No 861002

Cases A1-A3 all show a similar HRR behaviour, with A1 (IMEP = 3.63 bar, NetHRR = 2.42 kJ), A2 (IMEP = 2.55 bar, NetHRR = 1.92 kJ) and A3 (IMEP = 4.59 bar, NetHRR = 2.84 kJ). Case A3 reaches the highest HRR peak due to the larger fuel quantity injected. Unlike A1, this higher fuel quantity does not negatively influence the combustion due to the lack of oxygen and therefore results in a higher NetHRR and IMEP. Case A4 (IMEP = 2.18 bar, NetHRR = 1.64 kJ) shows an earlier HRR peak, caused by advancing the first pilot injection to 14° CA BTDC. The earlier injection provides more time for fuel evaporation and mixture formation and therefore causes the combustion to start earlier. Cases B1-B5, with B1 (IMEP = -0.18 bar, NetHRR = 0.67 kJ), B2 (IMEP = 0.04 bar, NetHRR = 0.67 kJ), B3 (IMEP = 0.73 bar, NetHRR = 1.03 kJ), B4 (IMEP = -0.05 bar, NetHRR = 0.70 kJ) and B5 (IMEP = -0.04 bar, NetHRR = 0.68 kJ), show overall low HRR peaks. The peaks of B1 and B2 occur around TDC, while B4 and B5 peak around 10° CA ATDC. B3 reaches the highest HRR peak within this group, but the peak occurs even later at approximately 18° CA ATDC. Such late heat release reduces the effectiveness of the combustion process because a larger portion of the fuel energy is released during the expansion stroke. Cases B6-B10, with B6 (IMEP = 0.26 bar, NetHRR = 0.77 kJ), B7 (IMEP = 0.90 bar, NetHRR = 1.09 kJ), B8 (IMEP = 0.77 bar, NetHRR = 1.01 kJ), B9 (IMEP = 0.70 bar, NetHRR = 1.00 kJ) and B10 (IMEP = 0.62 bar, NetHRR = 0.96 kJ) also show low HRR peaks of less than 75 J/CA but with similar peak timings. The low heat release suggests that only a limited portion of the premixed Natural Gas-air mixture participates in combustion and therefore the combustion process is mainly dominated by the Diesel pilot fuel. Cases B11-B13, with B11 (IMEP = 0.67 bar, NetHRR = 0.94 kJ), B12 (IMEP = 0.60 bar, NetHRR = 0.90 kJ) and B13 (IMEP = 1.11 bar, NetHRR = 1.14 kJ), show a slightly higher HRR peak for B13, which is most likely caused by the increased pilot fuel quantity. Overall, cases B1-B13 show very low HRR peaks and NetHRR values compared to the cases A1-A4. This indicates weak and delayed combustion, where the energy release is mainly driven by the Diesel pilot fuel rather than a strong contribution from the Natural Gas-air mixture. Since the observed heat release was dominated by the Diesel injection and the single pilot injection did not provide sufficient ignition support for stable dual-fuel combustion, this strategy was neglected in further tests.

This project has received funding from the European Union Horizon 2020 Research and Innovation programme. Grant Agreement No 861002

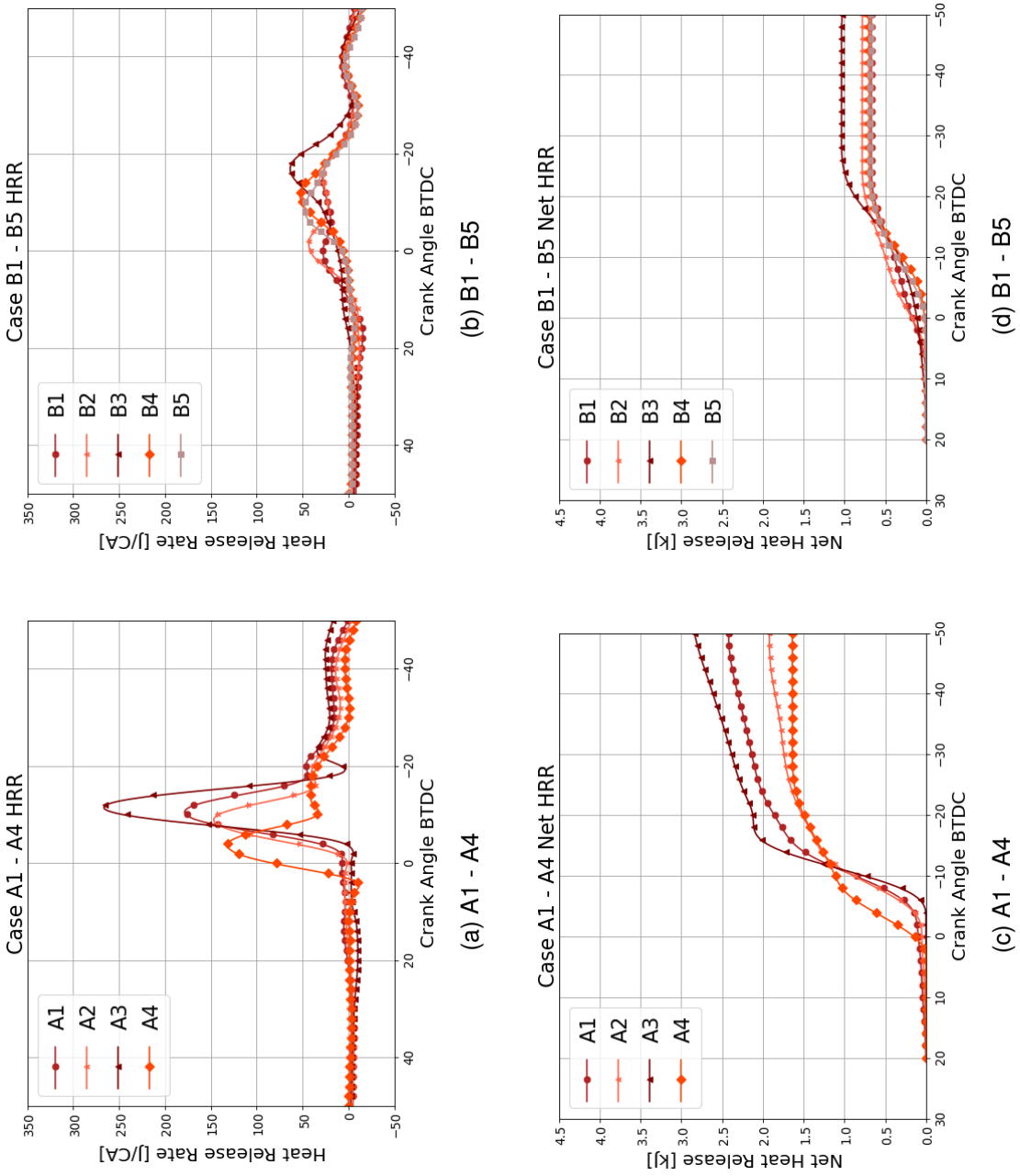


Figure 3.43: Heat Release Rate and Net Heat Release Rate for cases A1-A4 and B1-B5

This project has received funding from the European Union Horizon 2020 Research and Innovation programme. Grant Agreement No 861002

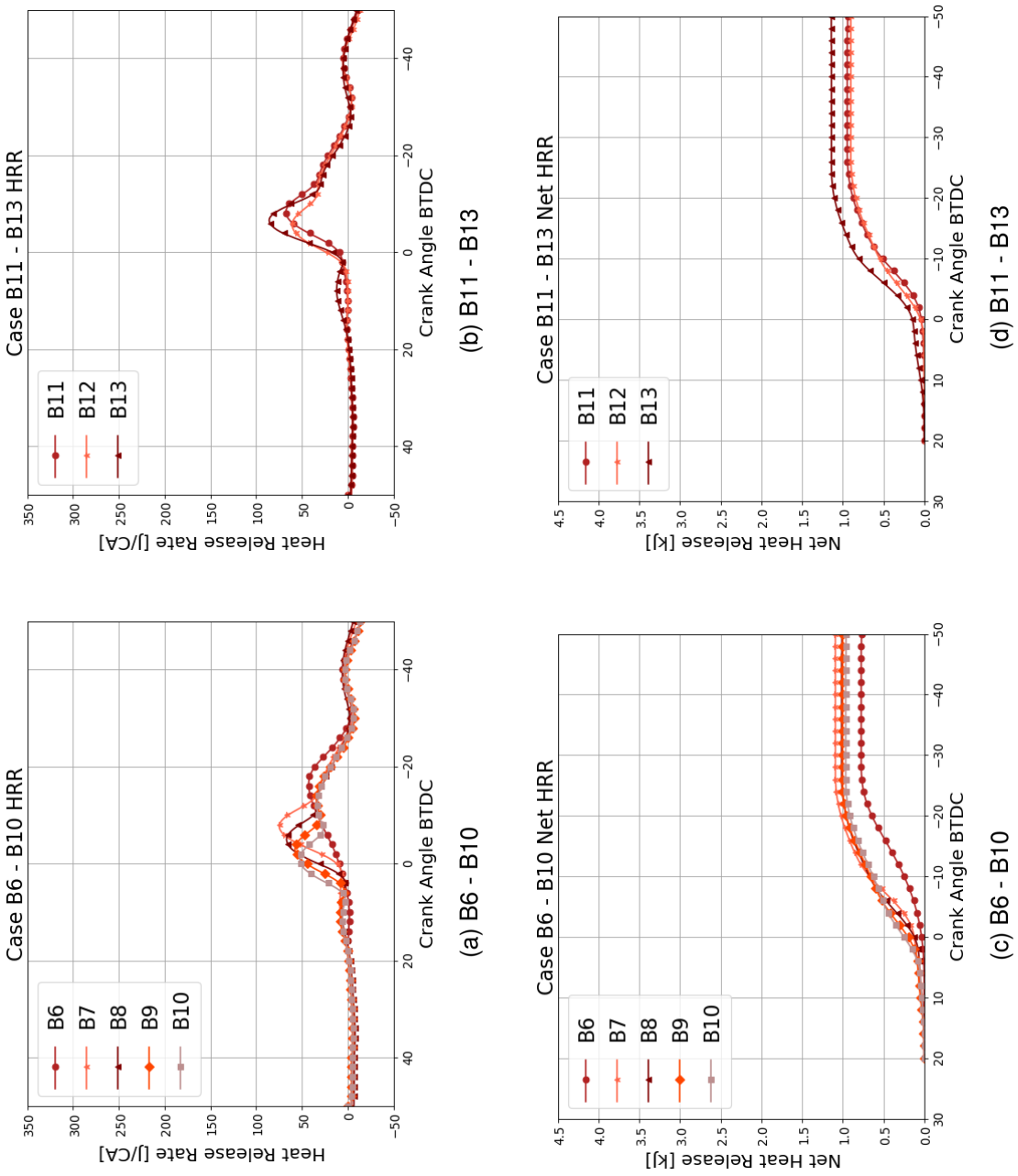


Figure 3.44: Heat Release Rate and Net Heat Release Rate for cases B6-10 and B11-B13

This project has received funding from the European Union Horizon 2020 Research and Innovation programme. Grant Agreement No 861002

Cases C1-C4, with C1 (IMEP = 1.81 bar, NetHRR = 1.52 kJ), C2 (IMEP = 3.02 bar, NetHRR = 2.09 kJ), C3 (IMEP = 3.08 bar, NetHRR = 2.28 kJ) and C4 (IMEP = 1.70 bar, NetHRR = 1.51 kJ) all show two HRR peaks. Cases C1 and C4 have the earliest first peaks, while C2 and C3 show a delayed first peak and a higher second peak. This is probably caused by the delayed first pilot injection in C2 and C3 and a resulting longer ignitin delay. As a result, C2 and C3 achieve higher NetHRR and IMEP values than C1 and C4. The double peak behaviour indicates that the combustion is dominated by the pilot fuel combustion effects in the early combustion phase and then shifts to the effects of the main fuel combustion in the second phase. Cases C5-C7, with C5 (IMEP = 1.73 bar, NetHRR = 1.47 kJ), C6 (IMEP = 0.93 bar, NetHRR = 1.17 kJ) and C7 (IMEP = 1.42 bar, NetHRR = 1.34 kJ), show that C5 behaves similarly to C1-C4 with two HRR peaks, whereas C6 and C7 only show a single peak around 22° CA ATDC. This is most probably caused by the late first pilot injection at 5° CA BTDC which results in a shift of the combustion later into the expansion stroke. Although split pilot injection increases the HRR peaks compared to the B-cases, the combustion is still relatively late and the amount of Natural Gas remains too low to achieve efficient dual-fuel combustion. Cases D1-D4, with D1 (IMEP = 3.06 bar, NetHRR = 2.13 kJ), D2 (IMEP = 2.96 bar, NetHRR = 2.24 kJ), D3 (IMEP = 2.97 bar, NetHRR = 2.19 kJ) and D4 (IMEP = 2.08 bar, NetHRR = 1.81 kJ) show a significant increase in HRR compared to the cases C1-C7. All cases again exhibit two HRR peaks. D1 shows a strong first peak followed by a smaller second peak which is probably caused by the first pilot injection containing a higher Diesel amount than the second. D2 and D3 show nearly identical HRR behaviour, indicating that the 1° CA difference in the second pilot injection has little influence on the combustion process. D4 reaches the lowest first peak, which shows that advancing the first pilot injection to 20° CA BTDC does not improve combustion. The higher HRR peaks compared to the cases C1-C7 indicate that the increased Natural Gas quantity contributes more strongly to the overall heat release. Cases D5-D8, with D5 (IMEP = 2.67 bar, NetHRR = 2.01 kJ), D6 (IMEP = 3.65 bar, NetHRR = 2.57 kJ), D7 (IMEP = 2.76 bar, NetHRR = 2.11 kJ) and D8 (IMEP = 2.85 bar, NetHRR = 2.18 kJ) also show two HRR peaks. D6-D8 exhibit an early first peak before TDC which indicates that the combustion starts during the compression stroke and therefore produces negative work. However, the earlier pilot injection also improves mixture homogenization and leads to a stronger second peak. D6 reaches the highest HRR peak of approximately 160 J/CA, showing that advancing the first pilot injection can improve combustion intensity. However, excessive advancement reduces the overall efficiency due to increased negative work. Overall, D1-D8 show the strongest combustion behaviour with HRR peaks exceeding 150 J/CA.

This project has received funding from the European Union Horizon 2020 Research and Innovation programme. Grant Agreement No 861002

Cases D9-D12, with D9 (IMEP = 3.11 bar, NetHRR = 2.31 kJ), D10 (IMEP = 0.66 bar, NetHRR = 0.96 kJ), D11 (IMEP = 0.94 bar, NetHRR = 1.09 kJ) and D12 (IMEP = 0.73 bar, NetHRR = 0.95 kJ), show generally low HRR peaks. D9 is the only case with a clear double peak and achieves the highest HRR and NetHRR values of this group. This suggests that the symmetrical pilot injections improve ignition stability, although the combustion is still largely dominated by Diesel. D10-D12 show weaker combustion due to the reduced pilot fuel quantity. While advancing the first injection in D12 shifts the heat release closer to TDC, the pilot quantity remains too low to sustain strong dual-fuel combustion. Therefore, highly advanced first pilot injection timings were not investigated further. Cases E1-E3, with E1 (IMEP = 2.60 bar, NetHRR = 1.88 kJ), E2 (IMEP = 2.11 bar, NetHRR = 1.59 kJ) and E3 (IMEP = 2.25 bar, NetHRR = 1.59 kJ), all show a single HRR peak at approximately 12° CA ATDC. E1 reaches the highest peak of around 170 J/CA. The similar HRR behaviour indicates that the small variations in pilot injection timing have little influence on the ignition delay and mixture formation. The combustion process therefore remains mainly controlled by the pilot fuel combustion. Cases E4-E6, with E4 (IMEP = 0.51 bar, NetHRR = 0.90 kJ), E5 (IMEP = 0.97 bar, NetHRR = 1.06 kJ) and E6 (IMEP = 4.31 bar, NetHRR = 2.71 kJ), also show a single HRR peak. E4 and E5 exhibit slow and delayed combustion, most likely because the interval between the two pilot injections is too short to create favourable ignition conditions. E6 reaches a high HRR peak of around 130 J/CA, but the peak occurs at approximately 22° CA ATDC. Although the higher fuel quantity increases the overall heat release, the late combustion reduces the amount of work that can be extracted from the released energy.

This project has received funding from the European Union Horizon 2020 Research and Innovation programme. Grant Agreement No 861002

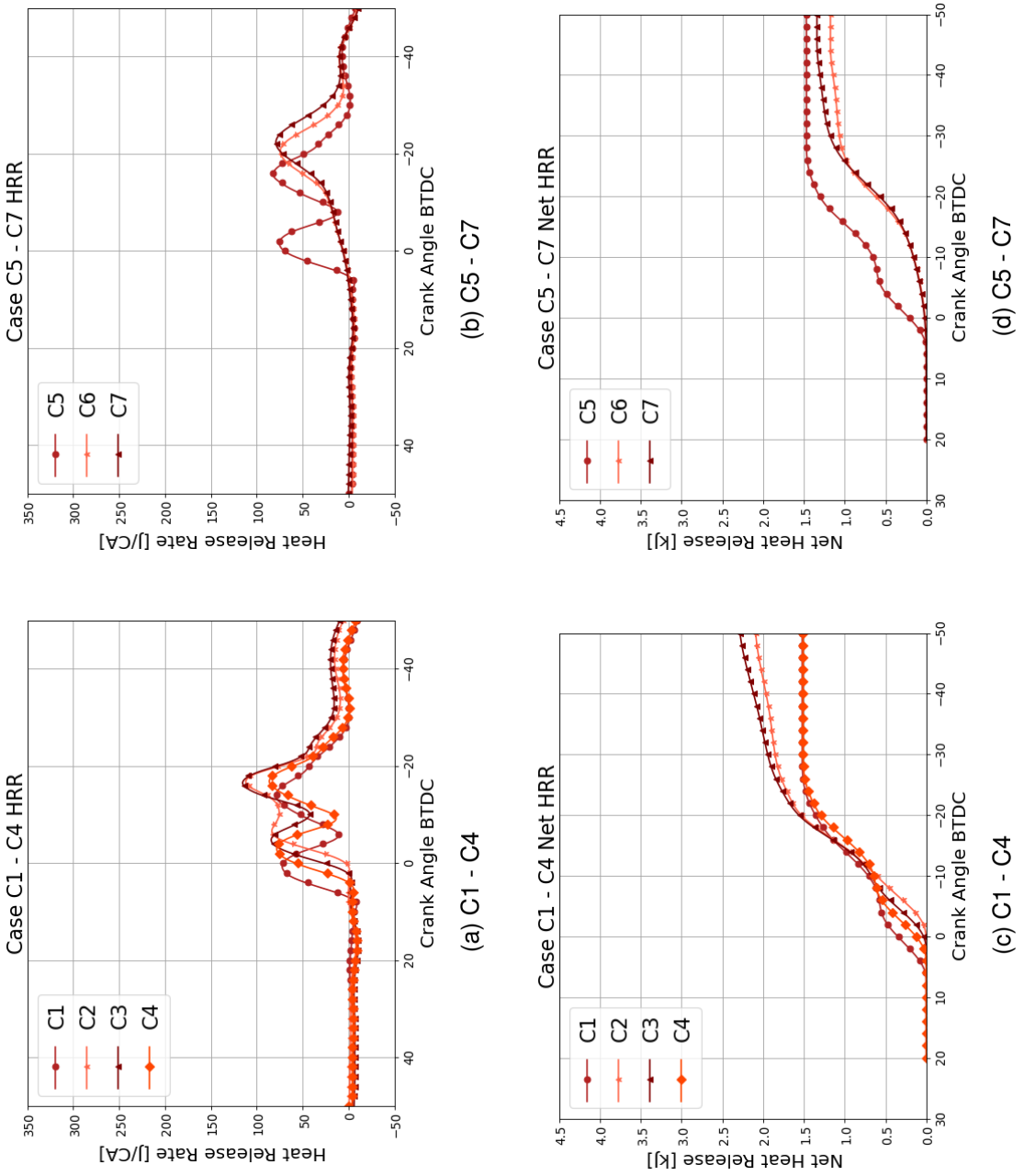


Figure 3.45: Heat Release Rate and Net Heat Release Rate for cases C1-C7

This project has received funding from the European Union Horizon 2020 Research and Innovation programme. Grant Agreement No 861002

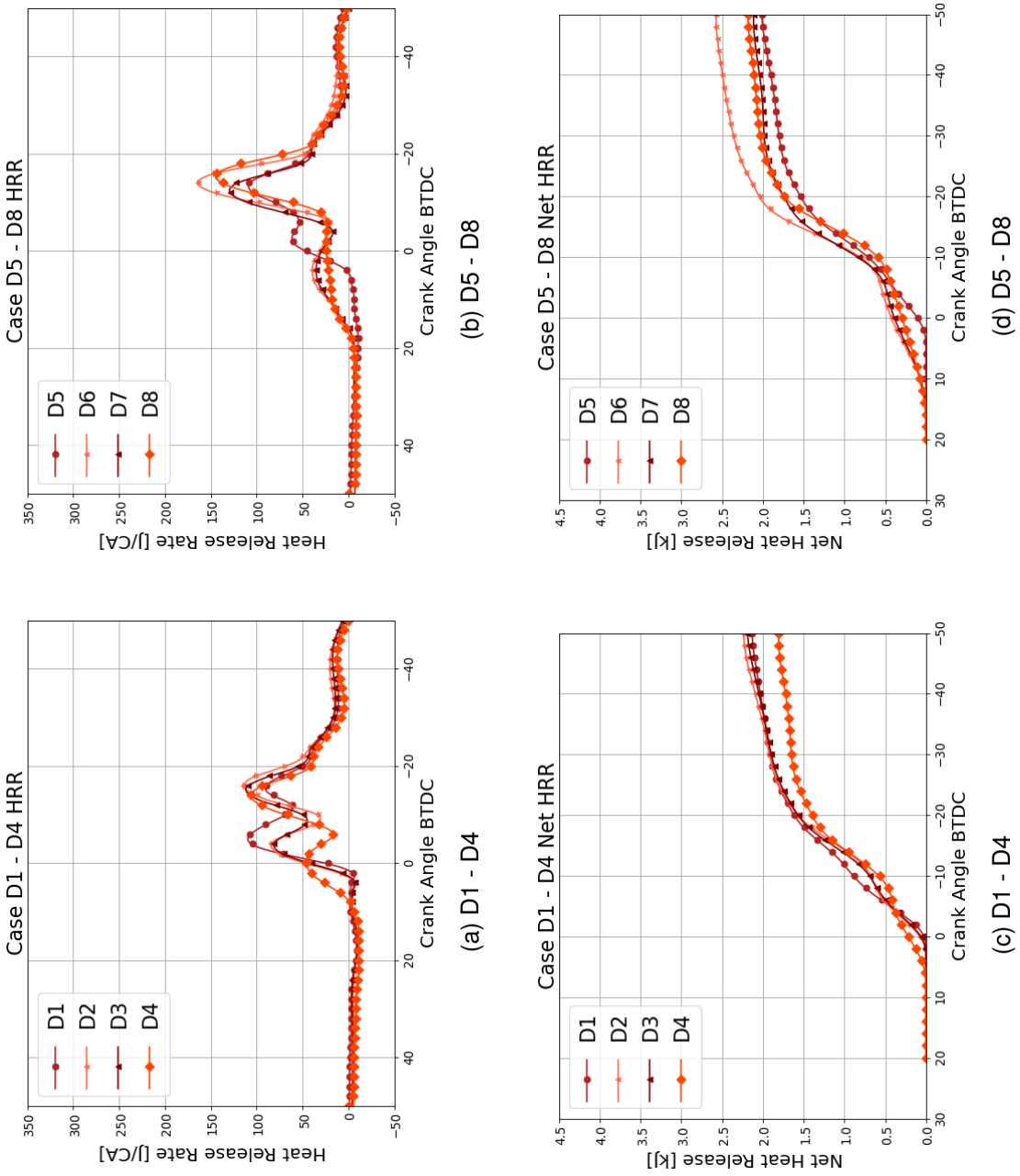
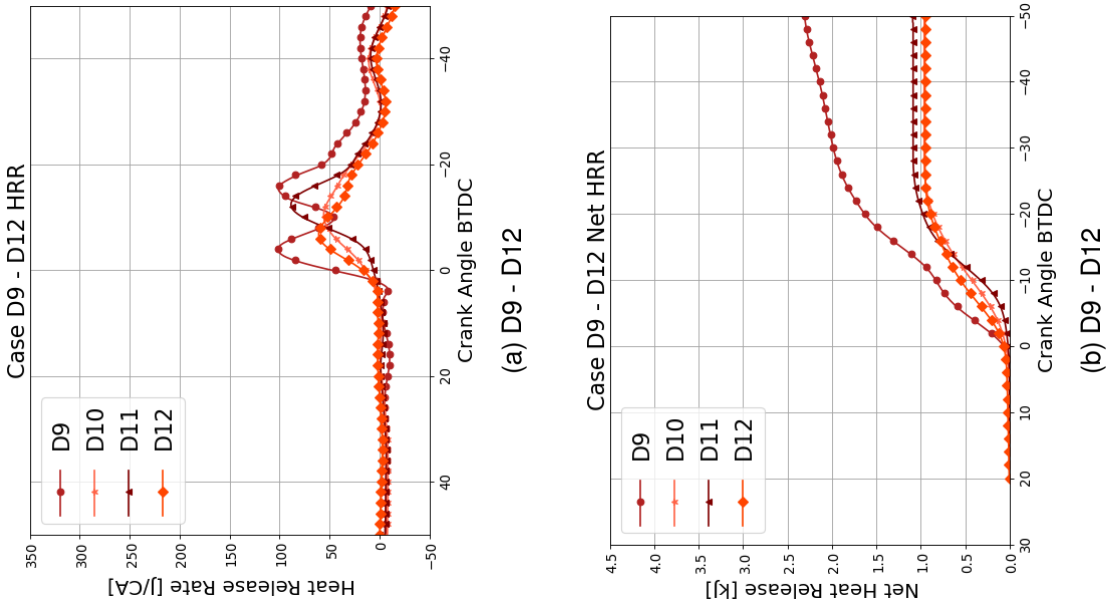


Figure 3.46: Heat Release Rate and Net Heat Release Rate for cases D1-D8

This project has received funding from the European Union Horizon 2020 Research and Innovation programme. Grant Agreement No 861002



(a) D9 - D12

(b) D9 - D12

Figure 3.47: Heat Release Rate and Net Heat Release Rate for cases D9-D12

This project has received funding from the European Union Horizon 2020 Research and Innovation programme. Grant Agreement No 861002

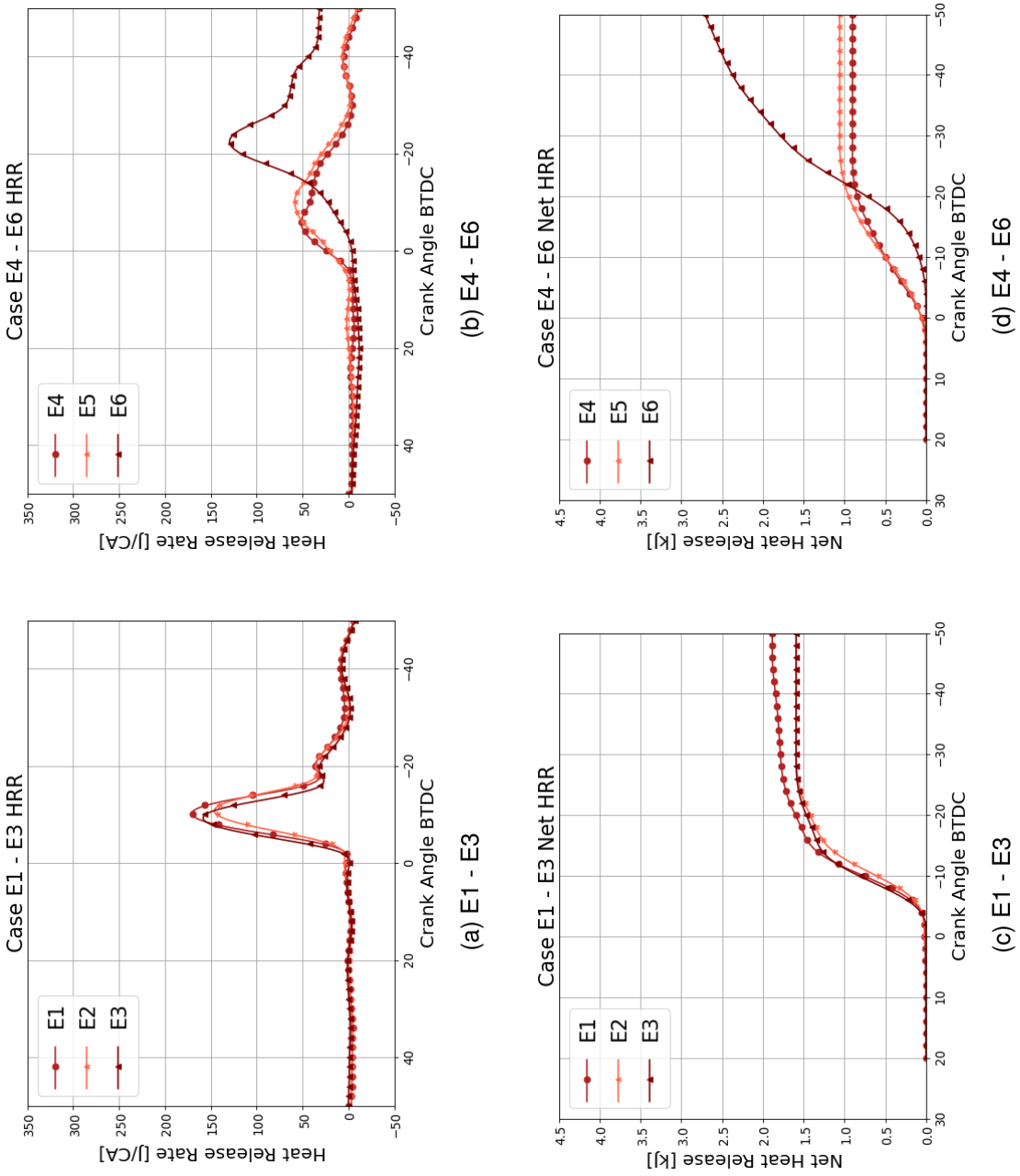


Figure 3.48: Heat Release Rate and Net Heat Release Rate for cases E1-E6

This project has received funding from the European Union Horizon 2020 Research and Innovation programme. Grant Agreement No 861002

The HRR and NetHRR for cases F1-G5 are shown in Figure 3.49 and Figure 3.50. Cases F1-F4, with F1 (IMEP = 1.84 bar, NetHRR = 1.56 kJ), F2 (IMEP = 1.74 bar, NetHRR = 1.54 kJ), F3 (IMEP = 2.95 bar, NetHRR = 2.04 kJ) and F4 (IMEP = 3.10 bar, NetHRR = 2.11 kJ) all show double HRR peaks. Cases F1 and F2 have their highest peak around TDC and a second lower peak at approximately 18° CA ATDC even though F1 has a slightly higher Diesel amount. Cases F3 and F4 show a similar first peak at around 2° CA ATDC, but their second peak increases to approximately 130 J/CA. This indicates that advancing the first pilot injection to 13 and 12° CA BTDC improves mixture preparation which is leading to a stronger second combustion phase and a higher overall heat release. Cases F5-F7, with F5 (IMEP = 2.82 bar, NetHRR = 1.99 kJ), F6 (IMEP = 2.99 bar, NetHRR = 2.08 kJ) and F7 (IMEP = 6.53 bar, NetHRR = 3.68 kJ), show double HRR peaks for F5 and F6 and a single dominant peak for F7. F5 and F6 only differ in the amount of Natural Gas injected, but this does not significantly affect the HRR behaviour. Both cases show an initial peak around 2° CA ATDC and a second larger peak around 18° CA ATDC. In contrast, F7 reaches a maximum HRR of nearly 250 J/CA at approximately 5° CA ATDC. The higher main fuel quantity results in a much stronger combustion event and the highest NetHRR of the cases F1-F7. After the initial pilot fuel dominated combustion phase the combustion becomes increasingly influenced by the Natural Gas which results in a broader heat release and a small plateau around 18° CA ATDC. This indicates that a larger fraction of the Natural Gas participates in the combustion process. Cases G1-G5, with G1 (IMEP = 4.68 bar, NetHRR = 2.91 kJ), G2 (IMEP = 3.72 bar, NetHRR = 2.40 kJ), G3 (IMEP = 4.35 bar, NetHRR = 2.75 kJ), G4 (IMEP = 2.73 bar, NetHRR = 2.14 kJ) and G5 (IMEP = 7.88 bar, NetHRR = 4.42 kJ) show the HRR behaviour of the Diesel-Hythane combustion. Cases G1 and G2 use the same pilot injection timings as F7, at 15 and -1° CA BTDC, but show two distinct HRR peaks between 100 and 150 J/CA. Cases G3 and G4 use a higher Hythane fraction and an earlier first pilot injection, but neither configuration leads to a higher HRR peak than G1 and G2. In contrast, G5 reaches the highest HRR peak of all tested cases with approximately 310 J/CA. Similar to F7, the combustion is dominated by a single strong peak but the heat release occurs more rapidly. This is probably caused by the Hydrogen in the mixture, due to its higher flame speed than Natural Gas. The faster combustion leads to a higher HRR and NetHRR. Overall, the HRR and NetHRR analysis mirrors the results of the flame pixel investigation. It showed that cases with higher deviation in the pixel analysis also produced lower HRR and NetHRR. Also the heat release data showed which fuel was dominant during different stages of the combustion for each case. This highlights the importance of the novel cycle-to-cycle variation analysis introduced in this chapter.

This project has received funding from the European Union Horizon 2020 Research and Innovation programme. Grant Agreement No 861002

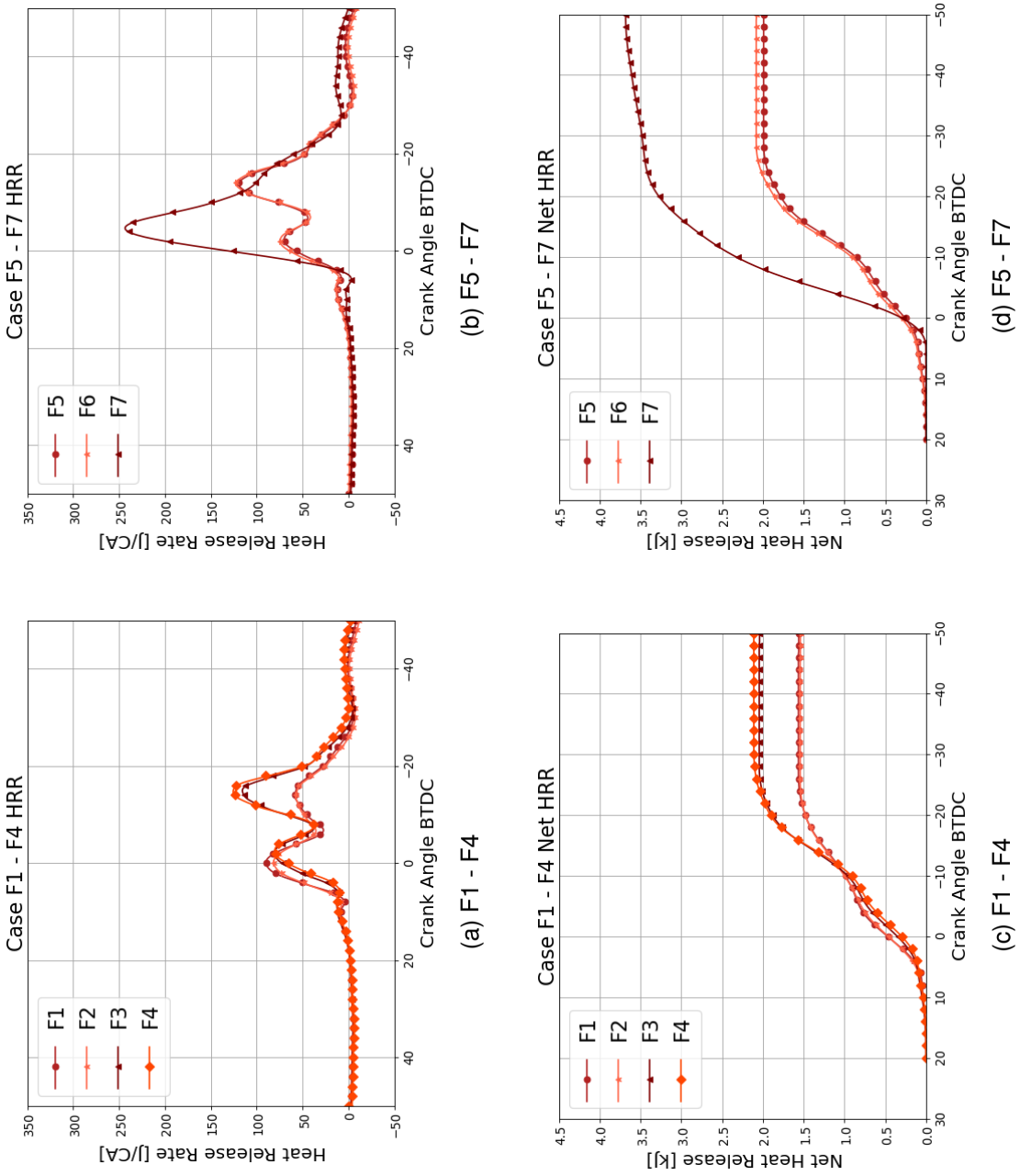
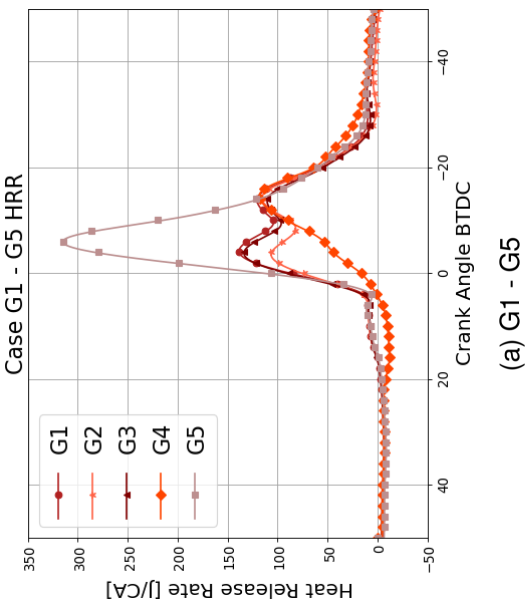
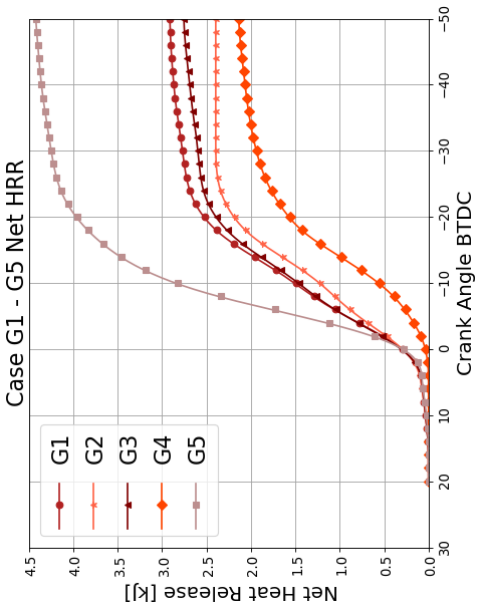


Figure 3.49: Heat Release Rate and Net Heat Release Rate for cases F1-F7

This project has received funding from the European Union Horizon 2020 Research and Innovation programme. Grant Agreement No 861002



(a) G1 - G5



(b) G1 - G5

Figure 3.50: Heat Release Rate and Net Heat Release Rate for cases G1-G5

This project has received funding from the European Union Horizon 2020 Research and Innovation programme. Grant Agreement No 861002

3.4 Summary

From the experiments conducted at Brunel and analysed in this chapter, the following observations were made:

- The split pilot fuel injection strategy resulted in a high IMEP dual-fuel combustion while being able to reduce the Diesel pilot quantity to the minimum required for reliable ignition.
- Sufficient delay between the two pilot injections was required to allow the formation of an initial flame kernel from the mixture of oxygen, Natural Gas and the first pilot injection.
- The time required for the development of this initial flame kernel was influenced by the fuel properties, fuel quantity, and the amount of oxygen available within the combustion chamber.
- The highest IMEP dual-fuel combustion cases were achieved when the first pilot injection was reduced to the minimum quantity capable of initiating stable combustion.
- The cycle-to-cycle variation analysis via comparison of the flame pixels with the average cycle proved to be a reliable method and was in accordance with the HRR of the combustion cases.

These findings contribute to addressing the first research gap identified in this thesis, namely the limited understanding of how pilot Diesel injection timing and duration influence the combustion in low-load dual-fuel operation. The results demonstrate that the successful reduction of Diesel fuel quantity is strongly linked to the formation of stable ignition kernels prior to the second pilot injection and the resulting dual-fuel Natural Gas combustion. Furthermore, the observed differences in flame development between the investigated cases highlight the importance of cycle-to-cycle combustion behaviour, supporting the second research objective of evaluating flame development beyond conventional global combustion parameters. The main objective of this investigation was to improve the understanding of low-load dual-fuel combustion by linking pilot injection strategy, flame-kernel formation and combustion stability. The novelty of this work lies in the combined use of optical flame imaging and pressure based combustion analysis to identify the role of early flame kernel development in achieving stable dual-fuel combustion with minimal Diesel pilot fuel quantities. Furthermore, the demonstrated reduction of the required Diesel pilot fuel quantity while maintaining sta-

This project has received funding from the European Union Horizon 2020 Research and Innovation programme. Grant Agreement No 861002

ble combustion contributes towards increasing the Natural Gas substitution rate and therefore is providing a pathway towards lower CO2 emissions in heavy-duty dual-fuel engines. Based on these observations, it was decided to further investigate the Diesel injection and how to improve the minimum initial injection.

This project has received funding from the European Union Horizon 2020 Research and Innovation programme. Grant Agreement No 861002

Chapter 4

Study of the fuel injection process

In cooperation with the company Woodward L'Orange, experiments were carried out to analyse the TWIN nozzle design and the influence of the different nozzle geometry parameters on the spray characteristics. The aim of this study was to further understand the geometric influences and based on these, to improve the design of the TWIN nozzle to further improve the adjustment of the desired spray characteristics when injecting minimum and maximum amounts of pilot fuel in dual-fuel engines. The TWIN comparison is based on previous internal comparisons from Woodward L'Orange as well as a rudimentary investigation of a bachelor student [102] where in certain cases the spray interaction of the two spray holes would lead to similar spray characteristics in terms of spray penetration length and spray angle.

4.1 Pilot fuel injection measurements

The Diesel injection measurements were carried out at Woodward L'Orange in a Constant Volume Chamber, comparing different nozzle geometries to investigate their influence on the spray characteristics. The aim of this study was to investigate and improve the spray penetration and angle for the TWIN nozzle in order to use it for dual-fuel combustion and be able to inject minimum quantities necessary as well as maximum for pure Diesel combustion. Both of which need to have a high penetration, stable injections and a suitable spray angle. The pilot fuel spray investigation was designed to address the research gaps identified in Chapter 1 regarding the limited understanding of the influence of the geometric parameters on the spray characteristics of the TWIN nozzles. The investigated cases systematically varied the injector geometric parameters in order to quantify their influence on spray penetration, spray angle and spray area. The resulting knowledge contributes to the design and optimization of injectors for heavy-duty dual-fuel combustion applications. For reasons of safety, the chamber

This project has received funding from the European Union Horizon 2020 Research and Innovation programme. Grant Agreement No 861002

was filled with pure Nitrogen before the experiments and calibration fluid was used instead of Diesel since the physical properties are similar, especially density, viscosity, and bulk modulus. This steps prevent accidental combustion during the tests.

4.1.1 Constant Volume Chamber and the TWIN nozzle injector

The CVC used in this study was equipped with three windows with a size of 200 mm x 200 mm each and the volume of the chamber is 34 Liter. Two windows are positioned parallel to the injector to provide a side view of the spray while a third window is positioned opposite the injector to provide a frontal view of the spray. In this study, the side view windows were used to investigate the spray penetration, spray angle, and spray area. The maximum internal pressure was 60 bar but for safety reasons, the experiments had to be carried out at an internal pressure of 59 bar. For all experiments the internal temperature was kept to constant 20° C, this was ensured by a constant cooling through having cooling liquid flowing through the metal frame of the chamber. The spray investigations were conducted in a cold constant-volume chamber at 20° C and an ambient gas pressure of 59 bar to investigate the non-reacting spray behaviour of the TWIN injections under controlled and reproducible conditions. A continuous lightsource was positioned on the opposite side of the camera to record the injection in high speed in order to evaluate the spray angles, areas and penetrations of each nozzle configuration. The experiment layout is shown schematically in Figure 4.1.

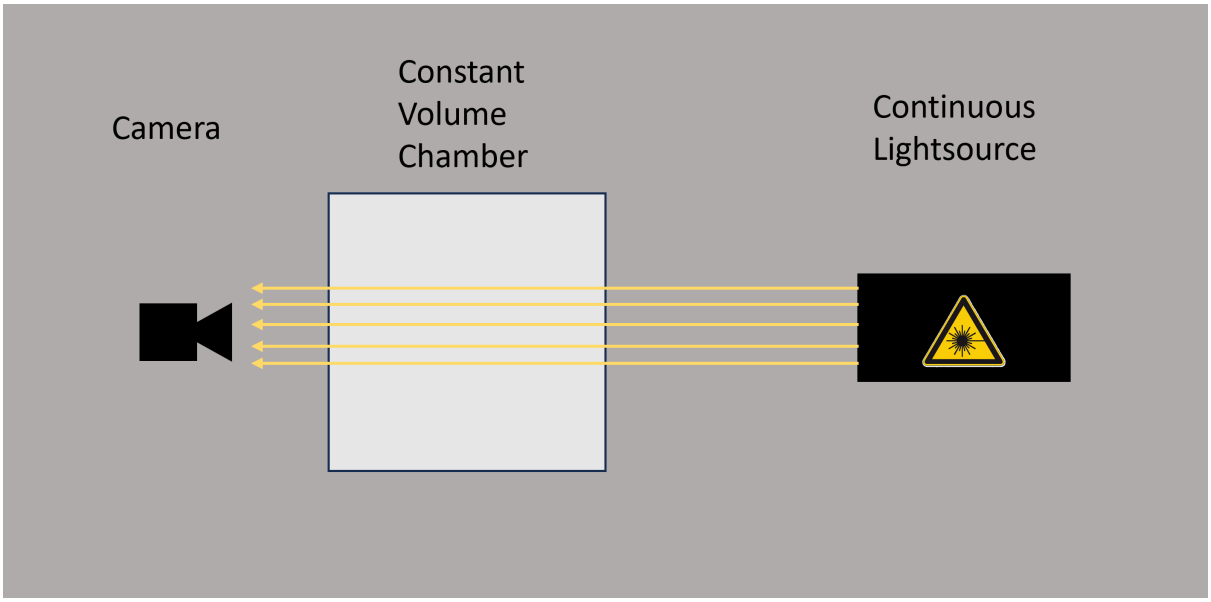


Figure 4.1: Schematics of the back illumination measurements at the CVC

The nozzles are designed, based on the TWIN nozzles from Woodward L'Orange, which have two spray hole rows on top of each other parallel to the needle axis in order

This project has received funding from the European Union Horizon 2020 Research and Innovation programme. Grant Agreement No 861002

to increase the penetration of minimum injections as well as ensure a stable spray and penetration with maximum injection duration. Two SAC hole nozzle geometries, named A and B, were investigated. The two designs differ in the shape and size of the SAC volume. Nozzles with SAC hole A feature a deeper SAC with a rounded bottom, whereas nozzle with SAC hole B have a shallower SAC with a flat bottom. As a result, the SAC volume of nozzles with SAC hole B are having a smaller SAC volume of less than 50% of the SAC volume of nozzles with SAC hole A. The schematic of the TWIN nozzle is shown in Figure 4.2.

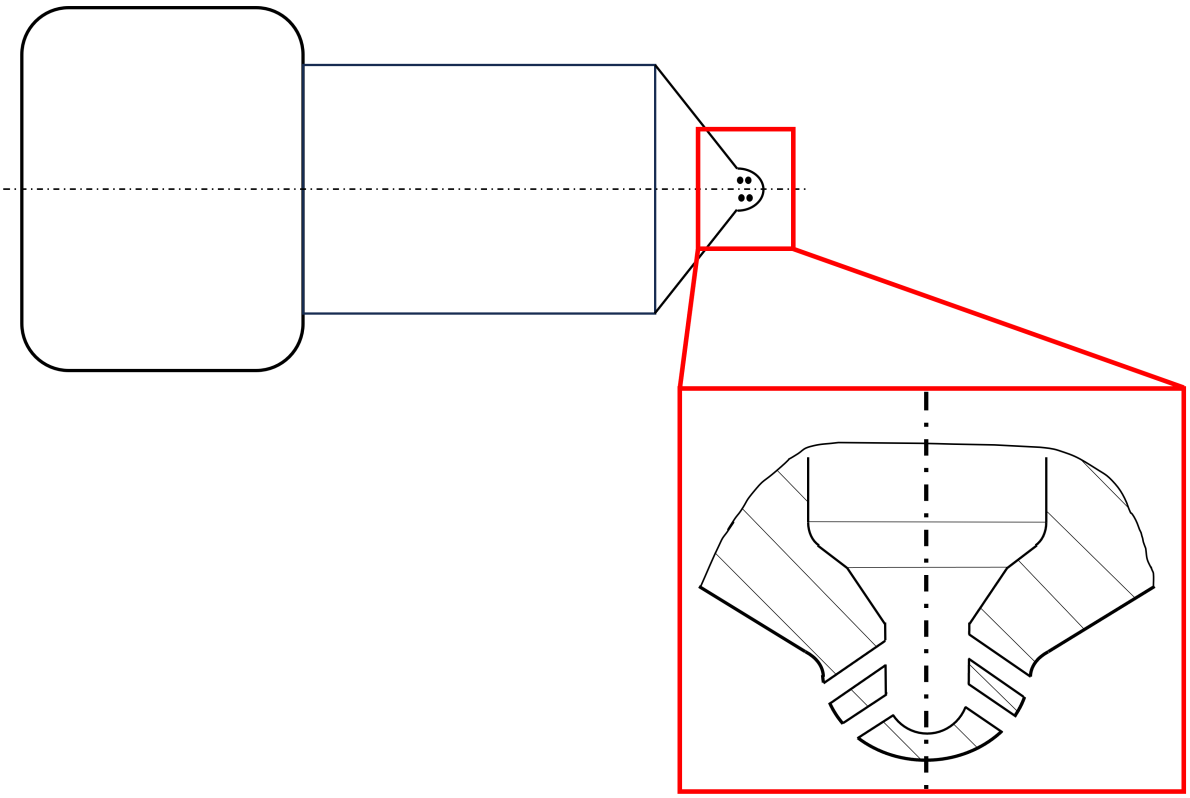


Figure 4.2: Schematics of the TWIN nozzle

The manufactured Diesel nozzles had four variations in the spray hole diameter (d_{min} & d_{min}+0.05 & d_{min}+0.1 & d_{min}+0.125 mm), five variations in the distance between the two spray holes (h_{min} & h_{min}+0.05 & h_{min}+0.1 & h_{min}+0.15 & h_{min}+0.2 mm), two SAC hole types and four variations of the angles between them(-3 & 0 & 2 & 5°), where the angle of the spray holes located closer to the needle were varied and the ones located further away were kept to α. The nozzle design is illustrated in Figure 4.3. The SAC hole schematics are shown in Figure 4.4

This geometric varieties result in 160 different nozzle configurations, but since the minimum distance between the two spray holes had to be kept to h_{min} and the maximum distance was limited by the depth of the SAC hole, the total of tested configura-

This project has received funding from the European Union Horizon 2020 Research and Innovation programme. Grant Agreement No 861002

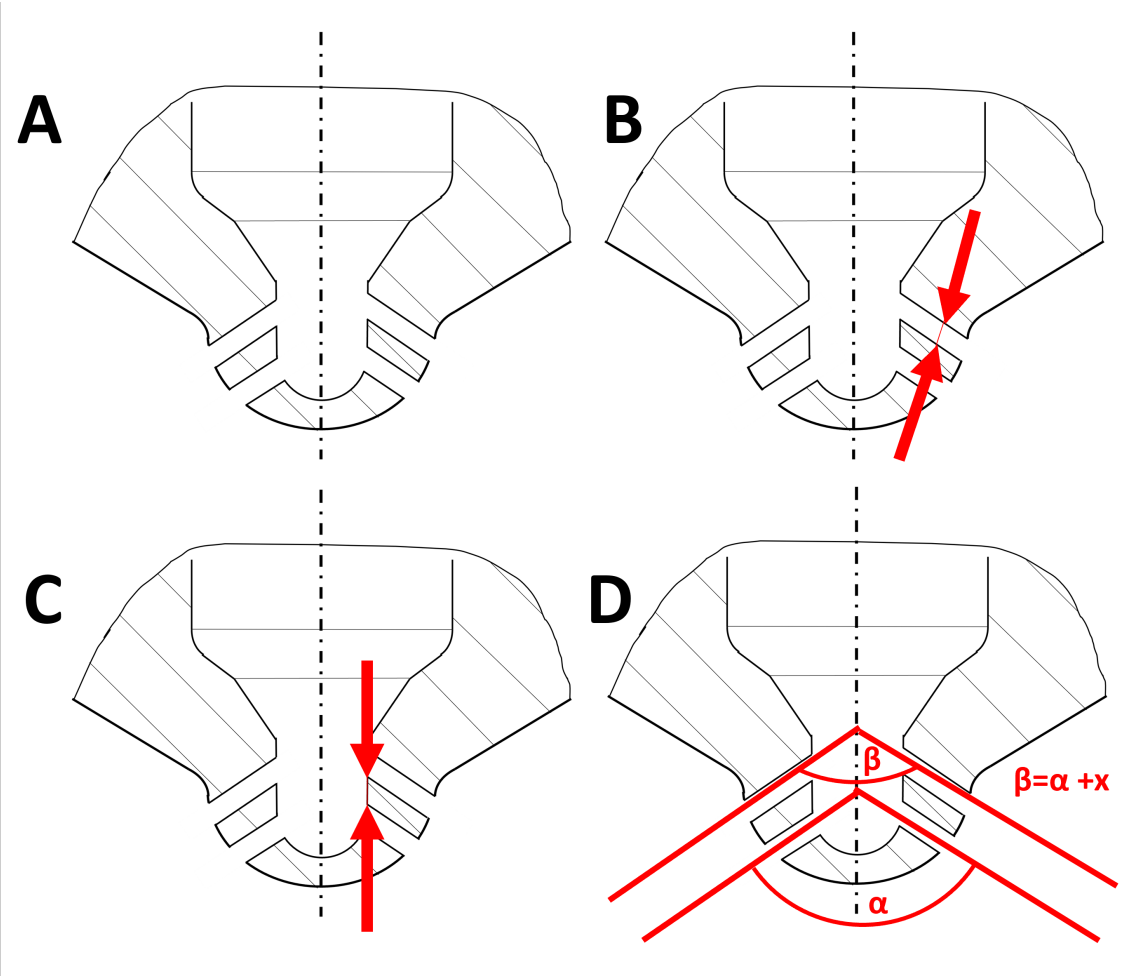


Figure 4.3: Illustration of the tested TWIN nozzles, with A showing the schematic, B showing the spray hole diameter, C showing the spray hole distance and D showing the relative spray hole angle

tions was reduced to 96 spray hole pairs. Each nozzle was manufactured with 2 spray hole pairs to use for side view/back illumination, resulting in 24 Nozzles per SAC hole, 48 in total. The spray hole pairs for each nozzle were classified as standard orientation, which is the lower spray hole pair in the images, and as 180° rotated, which was the upper spray hole pair in the images. To ensure that the different configurations do not influence each other, each nozzle has two spray hole pairs with the same spray hole diameter. On top of that, three comparison single hole nozzles were tested for each SAC hole with an angle of α+1°. This resulted in a total of 54 nozzles, comprising 48 TWIN nozzles and 6 comparison nozzles, which were evaluated in this study. Table 4.1 summarizes all tested configurations (each of them is used for both SAC hole types). N/A indicates that this spray geometry is not applicable to the single hole comparison nozzles.

This project has received funding from the European Union Horizon 2020 Research and Innovation programme. Grant Agreement No 861002

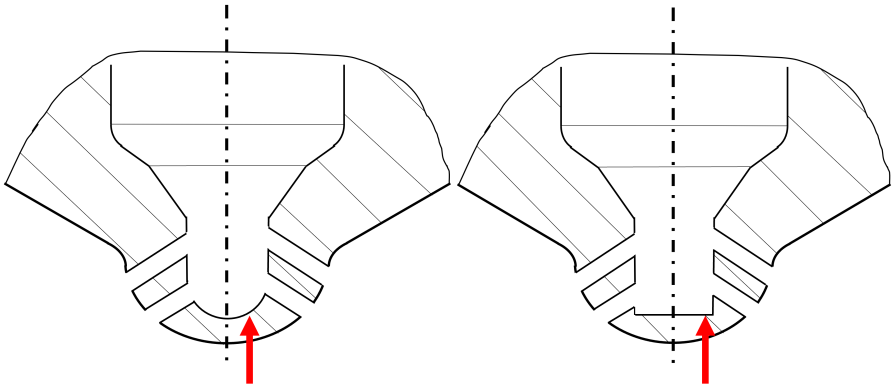


Figure 4.4: Schematics of the TWIN nozzle SAC hole types with SAC hole type A (left) and SAC hole type B (right)

Table 4.1: Tested nozzles

Nozzle name	Spray hole pair orientation γ	Spray hole diameter [mm] d	Distance between spray holes [mm] h	Angle between spray holes [°] β
N 1	Standard Orientation	d_{min}	h_{min}	-3
	180° rotated	d_{min}	h_{min}	0
N 2	Standard Orientation	d_{min}	h_{min}	2
	180° rotated	d_{min}	h_{min}	5
N 3	Standard Orientation	d_{min}	$h_{min} + 0.05$	-3
	180° rotated	d_{min}	$h_{min} + 0.05$	0
N 4	Standard Orientation	d_{min}	$h_{min} + 0.05$	2
	180° rotated	d_{min}	$h_{min} + 0.05$	5
N 5	Standard Orientation	d_{min}	$h_{min} + 0.1$	-3
	180° rotated	d_{min}	$h_{min} + 0.1$	0
N 6	Standard Orientation	d_{min}	$h_{min} + 0.1$	2
	180° rotated	d_{min}	$h_{min} + 0.1$	5
N 7	Standard Orientation	d_{min}	$h_{min} + 0.15$	-3
	180° rotated	d_{min}	$h_{min} + 0.15$	0
N 8	Standard Orientation	d_{min}	$h_{min} + 0.15$	2
	180° rotated	d_{min}	$h_{min} + 0.15$	5
N 9	Standard Orientation	d_{min}	$h_{min} + 0.2$	-3
	180° rotated	d_{min}	$h_{min} + 0.2$	0
N 10	Standard Orientation	d_{min}	$h_{min} + 0.2$	2
	180° rotated	d_{min}	$h_{min} + 0.2$	5

This project has received funding from the European Union Horizon 2020 Research and Innovation programme. Grant Agreement No 861002

Table 4.1: Tested nozzles

Nozzle name	Spray hole pair orientation γ	Spray hole diameter [mm] d	Distance between spray holes [mm] h	Angle between spray holes [°] β
N 11	Standard Orientation	$d_{min} + 0.05$	h_{min}	-3
	180° rotated	$d_{min} + 0.05$	h_{min}	0
N 12	Standard Orientation	$d_{min} + 0.05$	h_{min}	2
	180° rotated	$d_{min} + 0.05$	h_{min}	5
N 13	Standard Orientation	$d_{min} + 0.05$	$h_{min} + 0.05$	-3
	180° rotated	$d_{min} + 0.05$	$h_{min} + 0.05$	0
N 14	Standard Orientation	$d_{min} + 0.05$	$h_{min} + 0.05$	2
	180° rotated	$d_{min} + 0.05$	$h_{min} + 0.05$	5
N 15	Standard Orientation	$d_{min} + 0.05$	$h_{min} + 0.1$	-3
	180° rotated	$d_{min} + 0.05$	$h_{min} + 0.1$	0
N 16	Standard Orientation	$d_{min} + 0.05$	$h_{min} + 0.1$	2
	180° rotated	$d_{min} + 0.05$	$h_{min} + 0.1$	5
N 17	Standard Orientation	$d_{min} + 0.05$	$h_{min} + 0.15$	-3
	180° rotated	$d_{min} + 0.05$	$h_{min} + 0.15$	0
N 18	Standard Orientation	$d_{min} + 0.05$	$h_{min} + 0.15$	2
	180° rotated	$d_{min} + 0.05$	$h_{min} + 0.15$	5
N 19	Standard Orientation	$d_{min} + 0.1$	h_{min}	-3
	180° rotated	$d_{min} + 0.1$	h_{min}	0
N 20	Standard Orientation	$d_{min} + 0.1$	h_{min}	2
	180° rotated	$d_{min} + 0.1$	h_{min}	5
N 21	Standard Orientation	$d_{min} + 0.1$	$h_{min} + 0.05$	-3
	180° rotated	$d_{min} + 0.1$	$h_{min} + 0.05$	0
N 22	Standard Orientation	$d_{min} + 0.1$	$h_{min} + 0.05$	2
	180° rotated	$d_{min} + 0.1$	$h_{min} + 0.05$	5
N 23	Standard Orientation	$d_{min} + 0.125$	h_{min}	-3
	180° rotated	$d_{min} + 0.125$	h_{min}	0
N 24	Standard Orientation	$d_{min} + 0.125$	$h_{min} + 0.05$	2
	180° rotated	$d_{min} + 0.125$	$h_{min} + 0.05$	5
N 25	Both Orientations	d_{min}	N/A	N/A
N 26	Both Orientations	$d_{min} + 0.125$	N/A	N/A
N 27	Both Orientations	$d_{min} + 0.239$	N/A	N/A

This project has received funding from the European Union Horizon 2020 Research and Innovation programme. Grant Agreement No 861002

4.1.2 High speed recording equipment

As mentioned in the previous chapter the injections were recorded with a high speed camera from Photron, model SA5 with a frequency of 10000 fps. Continuous Light-sources were used to illuminate the chamber with a light diffusor to create a uniform white background for the spray images. This is necessary to ensure that the algorithm which analyses the recordings, can differentiate correctly between the spray and the background.

4.1.3 Experimental setup

Each nozzle was tested with 3 different pressures and 7 different energization durations to be able to fully observe the spray characteristics for minimum pilot injection and pure Diesel mode, this leads to 21 test cases for each nozzle and 5 recordings were taken for each test case to be able to evaluate an average spray angle, area and penetration. The minimum energization duration was set to 270 µs since this was the shortest duration at which the injector would open for low pressure and small spray hole diameters. Afterwards it was gradually increased with small timesteps close to the minimum opening time. After 400µs a full spray was developing, therefore it was decided to increase the energization duration in 200 µs timesteps. The pressures and timings are listed in Table 4.2.

Table 4.2: Test pressures with tested energization durations

Pressure	Energization duration [µs]
1400 bar 1800 bar 2200 bar	270
	300
	350
	400
	600
	800
	1000

The different energization times were chosen because the minimum time to open the injector was 270 µs and for the TWIN nozzles the injection characteristics with minimum energization had to be further investigated. This is necessary since conventional Diesel injectors are not able to inject minimum quantities with a stable uniform spray and good penetration. Also the shot-to-shot variation is very high for these, leading to unstable combustions. For comparison to conventional nozzles, the maximum injection

This project has received funding from the European Union Horizon 2020 Research and Innovation programme. Grant Agreement No 861002

duration was set to 1000 µs to ensure, that the needle was fully opened in these cases and the penetration reaches the maximum of the observable area.

4.2 Spray analysis

Different nozzle geometries were tested in order to investigate their effect on the spray. The variation of the parameters (1) spray hole diameter (2) spray hole distance (3) spray hole angle and (4) SAC hole type resulted in 54 different tested nozzles. For each nozzle there were 3 different pressures tested with 7 different energization timings for each and five injections were recorded in high speed for these in order to be able to analyse a medium injection case for each test. An example of these recordings is shown in Figure 4.5, where the image on the left is from a recording with SAC hole type A and the image on the right is from a recording with SAC hole type B. Furthermore, the standard and 180° rotated orientation for all nozzles is illustrated. The spray hole pairs are positioned 180° opposite each other for all investigated TWIN nozzle geometries. This arrangement was chosen to enable the simultaneous recording of two spray hole pairs, thereby reducing the number of required recordings. As a result, the only parameter influencing near-field jet-jet interference is the relative spray hole angle. The analysis of how this parameter affects the spray characteristics is presented later in this chapter. While it was not possible to investigate how jet-jet interference and wall proximity alter the near-field breakup, their influence on the three macroscopic spray characteristics, spray penetration, angle and area, can be assessed from these experiments. Both of the injections have reached the maximum observable distance, which is limited by the combustion chamber windows, which have a size of 200mm x 200mm.

From these recordings, the average spray properties for each frame were analysed with a software programmed by Goldlücke GmbH. The programm created the average values beginning from the first injection frame, which was triggered simultaneously with the energization of the injector, and calculated them from the 5 different recordings taken per test case. Since the images were recorded with a 10000 Hz frame rate, each timestep between two images represents 100 µs. From this evaluation the spray penetration, spray area and spray angle, were measured for each timestep and obtained as results in dependency of the time after the current supply. The parameters are illustrated in Figure 4.6. For each image of all five cases at every time step, the program calculated the spray penetration, area and angle. The spray penetration was determined from the furthest spray pixel from the nozzle, the spray area was obtained using thresholding relative to the background image and the spray angle was calculated based on the center of mass of the detected spray area. The resulting values

This project has received funding from the European Union Horizon 2020 Research and Innovation programme. Grant Agreement No 861002

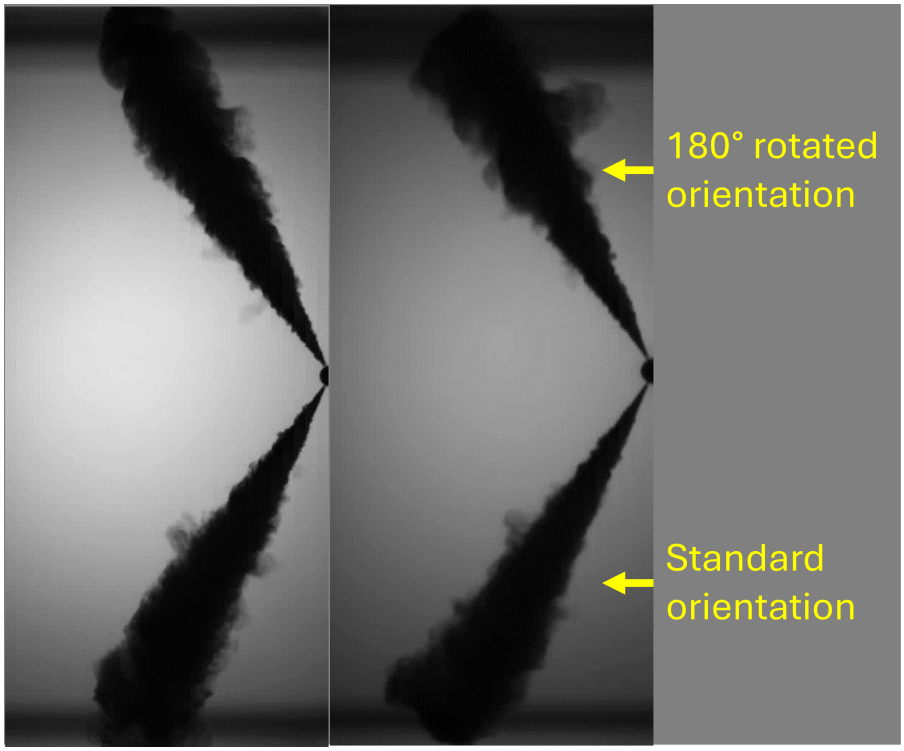


Figure 4.5: Example of a spray injection recordings for SAC hole type A (left) and SAC hole type B (right)

were then averaged for each case. The programm takes the configured distance of the window and stops calculating as soon as the spray cone of a frame crosses the observable area. Since two spray cones were simultaneously recorded per test, the maximum penetration per spray cone was limited to 100 mm – 1/2 nozzle diameter, resulting in a limit for the penetration of around 95 mm per test case.

For comparison, the nozzles were grouped depending on which geometric values they varied, to investigate their influence on the spray behaviour. First, the influence of the spray angle will be investigated with nozzles N5 and N6, with N5 representing the relative angles – 3° in standard and 0° in 180° rotated orientation. Nozzle N6 represents 2° in standard and 5° in 180° rotated orientation. The nozzle N25 was included to have a base single holed nozzle for comparison. The injection pressures of 1400bar and 2200 bar were choosen for the analysis of the influence of the geometric parameters on the TWIN nozzle. These pressures represent the minimum and maximum at which the investigated heavy-duty injectors operates when used in conventional Diesel engines. Injection durations of 300 µs and 1000 µs were selected to investigate the spray during the injector opening phase and under fully developed injection conditions. While injection begins at approximately 270 µs, 300 µs was selected to ensure consistent injection across all nozzle configurations. These four operating points were used throughout the study to provide a consistent comparison of spray behaviour under the

This project has received funding from the European Union Horizon 2020 Research and Innovation programme. Grant Agreement No 861002

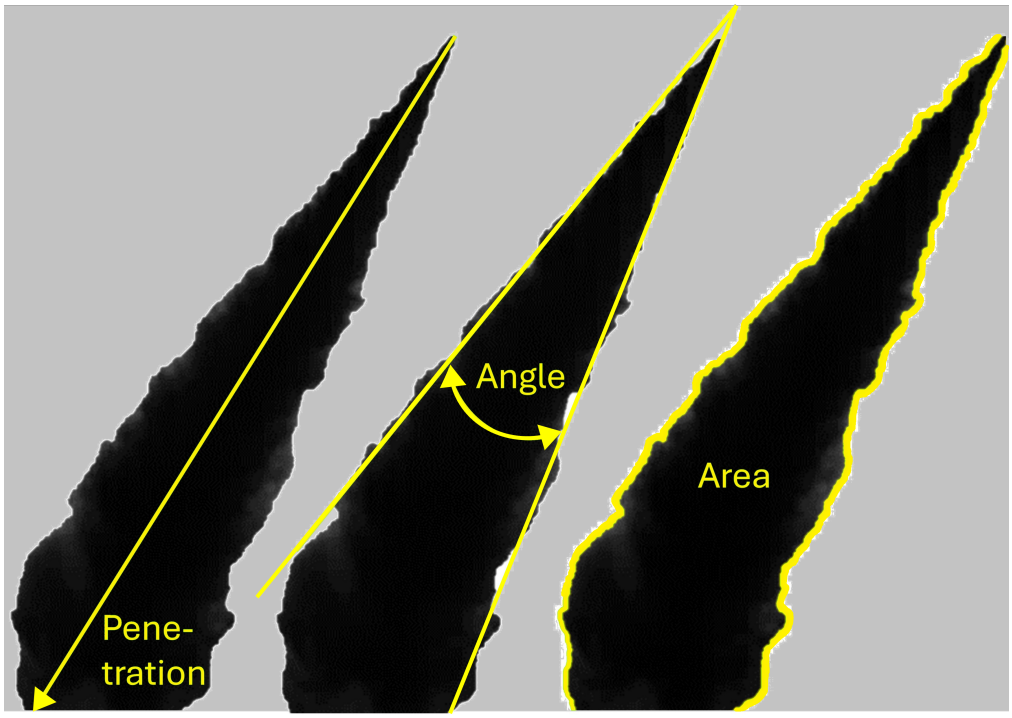


Figure 4.6: Schematic explanation of spray penetration (left), spray angle (middle) and spray area (right)

minimum and maximum injection pressure and duration conditions.

Figure 4.7 shows the development of the spray penetration, angle and area for nozzles N5 , N6 and N25 with 1400 bar injection pressure and 300 µs and Figure 4.8 for 1000 µs energization duration. For 300 µs it can be observed for SAC hole A that the penetration of the comparison nozzle N25 (d=d_{min}) is lower than for N5 and N6. The fastest penetration was achieved by N6 180° rotated orientation (d=d_{min}, h=$h_{min} + 0.1$, $\beta = 5$), which reached a penetration distance of 80 mm at around 1215 µs after energization. This is followed by N5 180° rotated (d=d_{min}, h=$h_{min} + 0.1$, $\beta = 0$), which reaches a penetration distance of 80 µm after 1300 µs. The nozzle spray hole pairs N5 standard (d=d_{min}, h=$h_{min} + 0.1$, $\beta = -3$) and N6 standard orientation (d=d_{min}, h=$h_{min} + 0.1$, $\beta = 2$) reached slightly slower penetrations, traversing 80 mm after 1370 & 1392 µs. For SAC hole B with minimum needle lift, the fastest penetration was achieved by N5 standard, which reaches a distance of 80 mm after 1195 µs, followed by N6 180° rotated, penetrating a distance of 80 mm after 1262 µs and then by N5 180° rotated and N6 standard orientation, which reach 80 mm after 1332 & 1368 µs. The comparison nozzle N25 behaves similar to SAC hole A and achieves a slower penetration, with both injections reaching a maximum distance of 72 & and 74 mm after 1400 µs after energization. The spray angles for all three nozzles vary around 20° – 30° for all cases for both SAC holes. At around 500 – 700 µs after energization nozzle N5 standard

This project has received funding from the European Union Horizon 2020 Research and Innovation programme. Grant Agreement No 861002

orientation shows a wider spray angle variation but afterwards reduces to around 30° and achieves the widest spray angle for SAC hole A at the end of the injection. For SAC hole B the widest angle at the end of the injection is achieved by N25 standard orientation, with an angle of 30.6° followed by N6 standard and N5 180° rotated. The spray area behaves similar to the penetration due to the spray angle being evenly distributed for the spray hole pairs N5, N6 and N25. For SAC hole A the widest spray area at the end of the injection is achieved by N6 180° rotated, with an area of around 821 mm^2 and for SAC hole B it is also achieved by N6 180° rotated, with an area of around 764 mm^2. Only the comparison nozzle N25 shows significant smaller spray area for both orientation in the case of both SAC holes, with all of them below 600 mm^2, similar to the behavior of the penetration. For the energization duration of 1000 µs the fastest penetration for SAC hole A was achieved by N5 180° rotated, which penetrates 80 mm distance after 1207 µs, followed by N5 standard, N6 180° rotated and N6 standard orientation. It can also be observed that in the beginning of the injection at 400 – 500 µs after energization, the fastest penetration was achieved by N25 in both orientations, but after 600 µs of the energization the nozzles N5 and N6 are more rapidly penetrating. For SAC hole B it can be observed that the penetrations are less clustered, showing that N5 180° rotated and N5 standard penetrate more rapid, crossing the distance of 80 mm after 1207 & 1263 µs. N6 180° rotated and N6 standard are following shortly afterwards and N25 both orientations are having the slowest penetration. The spray angle of all cases is in a similar region of 20° – 30° for both SAC hole types. It can be observed again, that in the beginning for SAC hole A there is a small spike for nozzle N5 standard orientation around 500 µs after energization afterwards the widest spray angle is achieved by N5 standard orientation at the end of the penetration, with an angle of 23.1°. For SAC hole B the initial widest spray angle is achieved by N25 180° rotated, but at the end of the penetration the widest spray hole angle is achieved by N5 180° rotated, with an angle of 23.9°. Overall they all lie in the same area around 18° – 24° towards the end. The spray areas for SAC hole A are linearly expanding for all spray hole pairs and only the comparison nozzle N25 in both orientations shows a significantly smaller area. For SAC hole B the widest area is achieved by N5 in both orientations, with an area of 896 & 923 mm^2, followed by N5 in both orientations. The comparison nozzle N25 behaves similar to SAC hole A and show a significantly lower area for both orientations, both below 600 mm^2. For these three nozzles it seems that with SAC hole B the fastest penetration is achieved with a relative spray angle of –3°, while for SAC hole A the best penetration results are achieved with 0° and 5°. The spray angles of all cases behave similar, indicating that there is no influence from the relative spray angle. The spray area

This project has received funding from the European Union Horizon 2020 Research and Innovation programme. Grant Agreement No 861002

behaves in accordance with the penetration results. The nozzles N5 and N6 only differ in their relative spray angle while N25 was included as comparison nozzle. From this investigation it can be observed that the change in the relative spray angle only had a minor influence on the spray characteristics.

This project has received funding from the European Union Horizon 2020 Research and Innovation programme. Grant Agreement No 861002

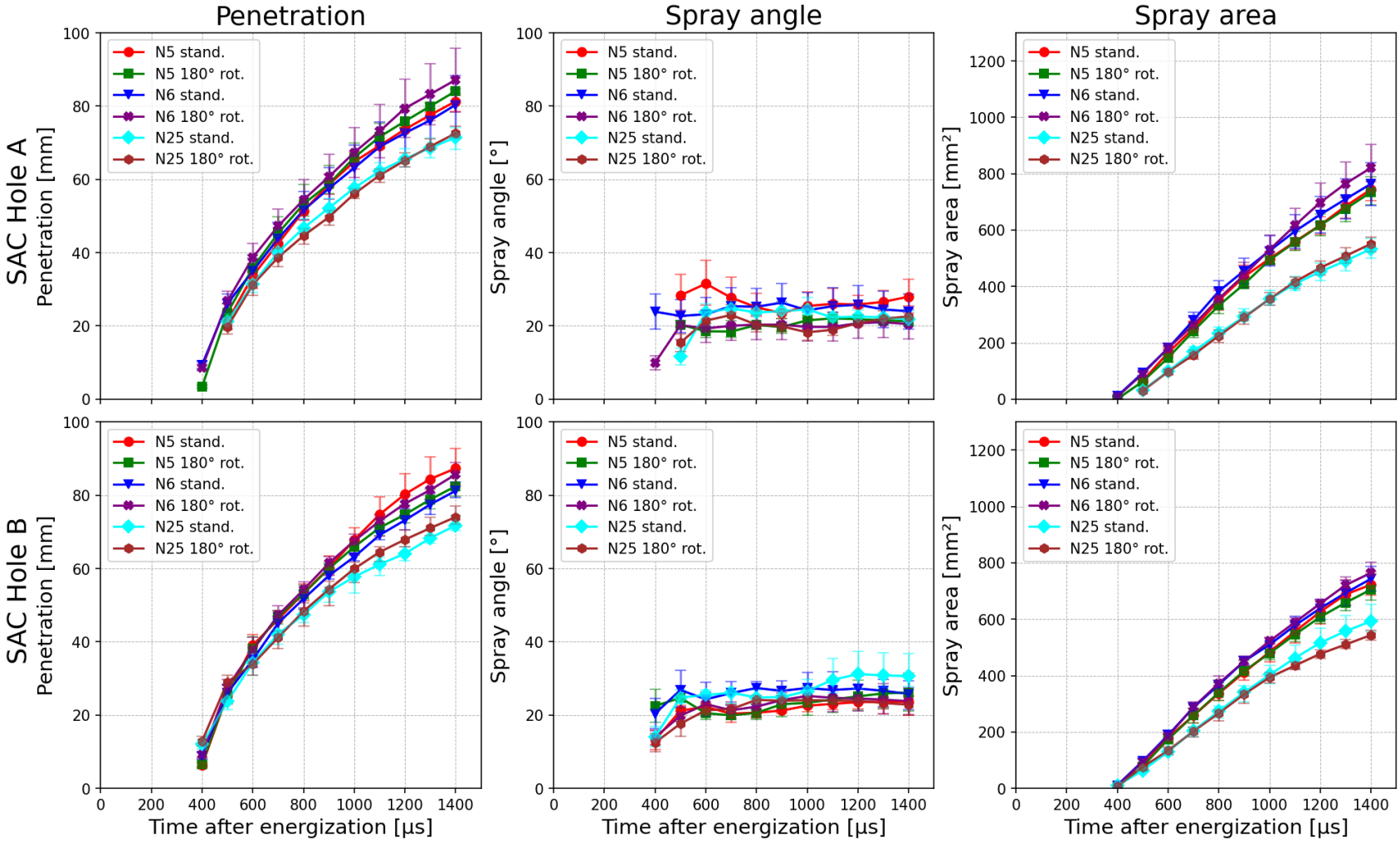


Figure 4.7: Influence of the relative spray angle on the spray characteristics penetration, spray angle and spray area for nozzles N5, N6 and N25 with 300 µs energization duration at 1400 bar

This project has received funding from the European Union Horizon 2020 Research and Innovation programme. Grant Agreement No 861002

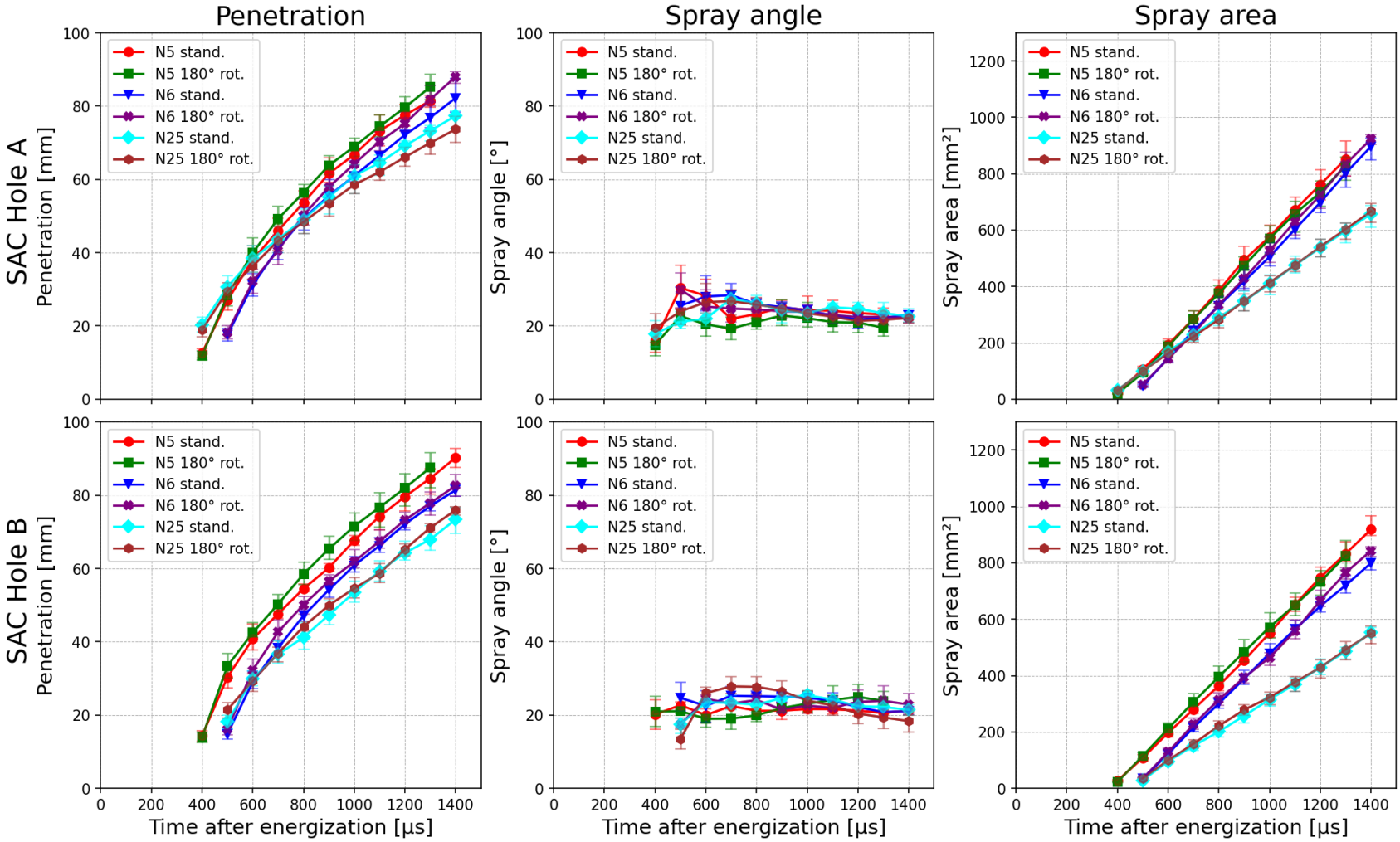


Figure 4.8: Influence of the relative spray angle on the spray characteristics penetration, spray angle and spray area for nozzles N5, N6 and N25 with 1000 µs energization duration at 1400 bar

This project has received funding from the European Union Horizon 2020 Research and Innovation programme. Grant Agreement No 861002

In order to ensure that the spray characteristics that were observed in Figure 4.7 and Figure 4.8 are not caused by other geometric influences the nozzles N15, N16 and N26 were compared as well. They are shown in Figure 4.9 and Figure 4.10 with nozzle N15 standard orientation having the relative angle of –3° and N15 180° rotated having the relative angle of 0°. N16 standard orientation has a relative angle of 2° and N16 180° rotated has a relative angle of 5°. For comparison the single spray hole nozzle N26 was included. The nozzles N15 and N16 have the same spray hole distance of h_{min}+0.1 mm like N6 and N5 and only differ in the spray hole diameter of d_{min}+0.05 mm instead of d_{min} for N5 and N6. The injection pressure was kept to 1400 bar, too, and the energization duration is 300 µs for the first and 1000 µs for the second group of graphs similar to Figure 4.7 and Figure 4.8. For SAC hole A and 300 µs energization duration it can be observed that the fastest penetration is achieved by N15 180° rotated (d=$d_{\min} + 0.05$, h=$h_{\min} + 0.1$, $\beta = 0$), with a maximum penetration of 77 mm at 1400 µs, followed by N15 standard. The other injections from N16 both orientations (d=$d_{\min}$, h=$h_{\min} + 0.1$, $\beta = 2 + 5$) and the comparison nozzle N26 (d=$d_{\min} + 0.125$) in both orientations achieve a nearly equal penetration, with maximum penetration distances between 59 & 63 mm. For SAC hole B the most rapid penetration is achieved by N15 180° rotated (d=$d_{\min} + 0.05$, h=$h_{\min} + 0.1$, $\beta = 0$), which reaches a penetration distance of 80 mm after 974 µs, followed by N26 180° rotated (d=$d_{\min} + 0.125$), then N15 standard (d=$d_{\min} + 0.05$, h=$h_{\min} + 0.1$, $\beta = -3$) and N26 standard (d=$d_{\min} + 0.125$) and N16 both orientations (d=$d_{\min} + 0.05$, h=$h_{\min} + 0.1$, $\beta = 2 + 5$). The spray angle for SAC hole A is more diverged distributed between 500 – 800 µs after energization and afterwards only N16 180° rotated shows a wider angle of around 30° compared to the other nozzles which achieve a spray angle of about 25°. For SAC hole B the spray angle is evenly distributed around 20° except N16 standard overshooting between 600 – 800 µs after energization and N26 180° rotated being below the other injections with an angle of 15.9°. The spray area for SAC hole A is similar to the penetration with N15 180° rotated achieving the largest area of 694 mm^2, followed by N15 standard and the other nozzles having a similar, smaller area. For SAC hole B the highest area is achieved by N26 standard followed by N26 180° rotated and N15 standard orientation, all reaching an area between 856 & 886 mm^2 and then N16 both orientations being significantly smaller then the rest, with an area between 683 & 742 mm^2. For energization duration of 1000 µs for SAC hole A the fastest penetration was achieved by N15 180° rotated, which achieves a penetration distance of 80 mm at 1062 µs, followed by N26 180° rotated, then N16 180° rotated and then N16 standard, N15 standard and N26 standard. For SAC hole B the fastest penetration is achieved by N26 180° rotated, which reaches a distance of 80 mm after 999 µs followed by N15 180°

This project has received funding from the European Union Horizon 2020 Research and Innovation programme. Grant Agreement No 861002

rotated, then N16 180° rotated, afterwards N15 standard, followed by N16 standard and N26 standard. For SAC hole A the widest spray angle at 600 µs after energization is achieved by N16 standard but at the end of the injections, the widest area is achieved by N15 standard with an angle of 33.6°, followed by N16 standard and then all the other injections which achieve an angle of around 25°. For SAC hole B the widest angle at the end of the injection is achieved by N16 standard with an angle of 31.6°, followed by N26 standard and N16 180° rotated. Only N15 180° rotated has a significantly smaller spray angle of 18.2° than the other injections. The spray area of SAC hole A is almost linear expanding, with the largest area expansion from N16 both orientations with both reaching a maximum area of 1035 & 1041 mm^2, then N15 both orientations and N26 both orientations. For SAC hole B also N16 both orientations achieves the fastest area expansion with a maximum area of 932 & 1181 mm^2, followed by N26 both orientations and the N15 both orientations. For both SAC holes the penetration and spray area distribution is tightly grouped. From the observations in Figure 4.9 and Figure 4.10 it seems that the fastest TWIN penetration for SAC hole A and B is with a relative angle of 0°. For both SAC holes it seems that the initial widest spray angle is achieved by a relative angle of 2°, while there is no consistent pattern towards the end of the injection. The spray area shows no observable influence from the relative spray angle. When comparing Figure 4.7 and Figure 4.8 with Figure 4.9 and Figure 4.10 it can be observed that there is no constant pattern visible showing a higher penetration or angle or area in dependency of the angle between the two spray holes when injecting with 1400 bar. SAC hole A seemingly reaches its highest penetration at a relative angle of 0° . However, this variation might also be caused by measurement uncertainties rather than representing a physical correlation.

This project has received funding from the European Union Horizon 2020 Research and Innovation programme. Grant Agreement No 861002

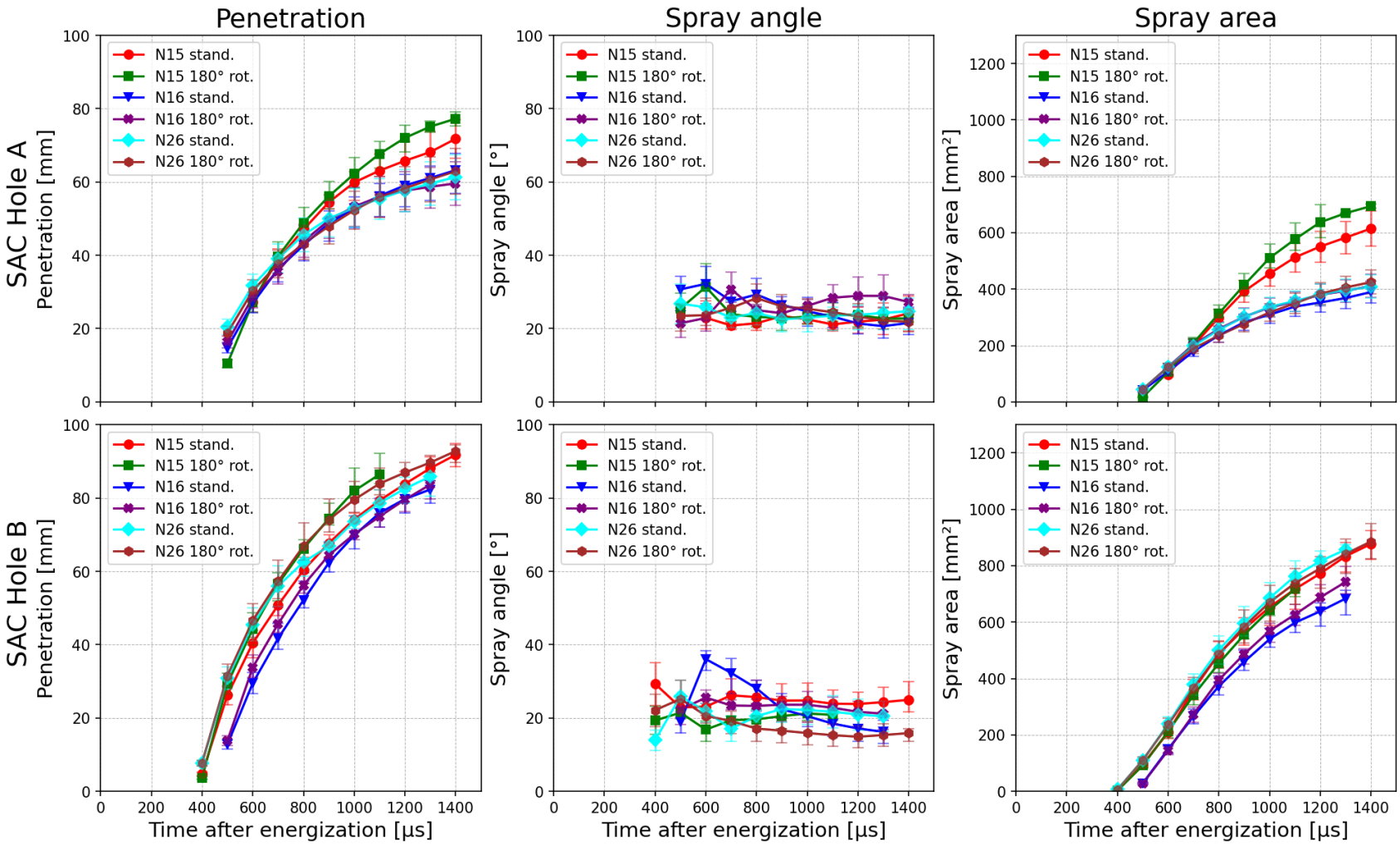


Figure 4.9: Influence of the relative spray angle on the spray characteristics penetration, spray angle and spray area for nozzles N15, N16 and N26 with 300 µs energization duration at 1400 bar

This project has received funding from the European Union Horizon 2020 Research and Innovation programme. Grant Agreement No 861002

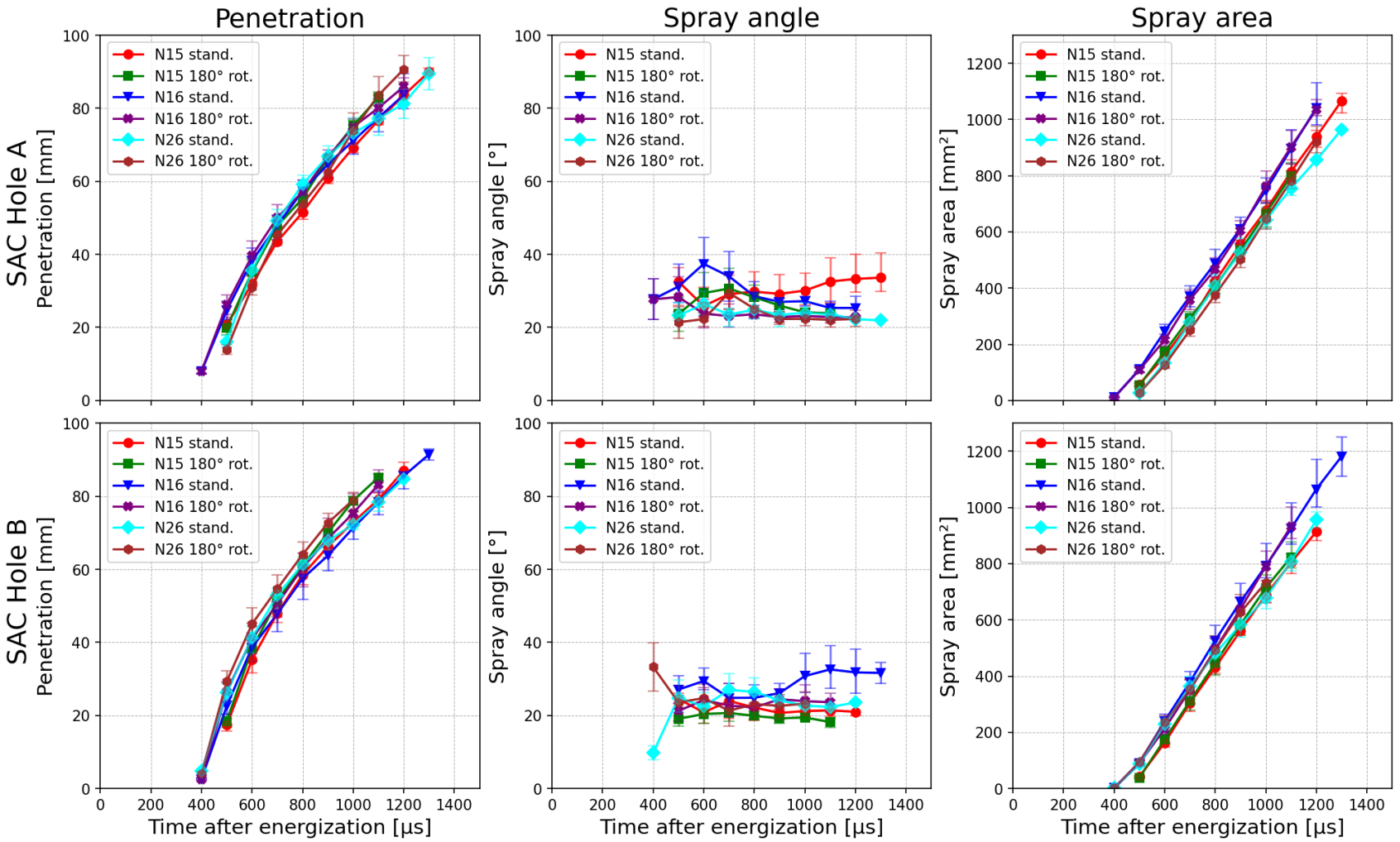


Figure 4.10: Influence of the relative spray angle on the spray characteristics penetration, spray angle and spray area for nozzles N15, N16 and N26 with 1000 µs energization duration at 1400 bar

This project has received funding from the European Union Horizon 2020 Research and Innovation programme. Grant Agreement No 861002

The third group of nozzles compared in order to observe the influence of the relative angle are N21 and N22. They are shown in Figure 4.11 and Figure 4.12 with nozzle N21 standard orientation having the relative angle of –3° and N21 180° rotated having the relative angle of 0°. N22 standard orientation has a relative angle of 2° and N22 180° rotated has a relative angle of 5°. The nozzles N21 and N22 have a spray hole distance of h_{min}+0.05 mm and a diameter of d_{min}+0.1 mm. The injection pressure was kept to 1400 bar, too, and the energization duration is 300 µs for the first and 1000 µs for the second graphs similar to Figure 4.7, Figure 4.8, Figure 4.9 and Figure 4.10. For SAC hole A and 300 µs energization duration it can be observed that the fastest penetration is achieved by N22 180° rotated (d=$d_{\min} + 0.1$, h=$h_{\min} + 0.05$, $\beta = 5$), which reaches a maximum distance of 69 mm at 1400 µs, followed by N22 standard (d=$d_{\min} + 0.1$, h=$h_{\min} + 0.05$, $\beta = 2$). The other injections from N21 (d=$d_{\min} + 0.1$, h=$h_{\min} + 0.05$, $\beta = -3 + 0$) have a very slow penetration and do not reach the end of the observable area, both reaching a maximum distance below 17 mm. For SAC hole B the most rapid penetration is achieved by N21 standard, which reaches a maximum distance of 78 mm at 1300 µs followed by N21 180° rotated, then N22 both orientations. The spray angle for SAC hole A is strongly diverged distributed with N21 180° rotated having the widest angle of around 40°, followed by N22 standard and then N 22 180° rotated and N21 standard. The larger difference observed for N21 standard in comparison to N21 180° rotated is probably caused by the low penetration of the spray. Due to the reduced spray momentum, the surrounding ambient gas can cause a higher dispersion of the spray. For SAC hole B the spray angle is evenly distributed around 25°, with the widest angle created by N22 180° rotated. The spray area for SAC hole A is similar to the penetration with N22 180° rotated achieving the widest area of 592 mm^2, followed by N22 standard and N21 both orientations having nearly no area at all, with areas below 20 mm^2. For SAC hole B the highest area is achieved by N21 both orientations, with areas of 662 & 663 mm^2 and then 22 both orientations. For energization duration of 1000 µs the fastest penetration for SAC hole A is from N21 both orientations, which cross the distance of 80 mm at 11016 & 1034 µs after energization, followed by N22 both orientations with only N22 180° rotated showing a visible lower penetration rate. For SAC hole B the penetration is more divergent with N21 180° rotated penetrating the most rapidly, reaching 80 mm at 834 µs followed by N22 180° rotated, then N21 standard and N22 standard. The spray angle of SAC hole A is divided between 500 – 800 µs after energization with the widest angle from N22 standard at 33.5°, then N21 standard, N22 180° rotated and N21 180° rotated. Towards the end of the injections all angles are similar in a region around 25°. For SAC hole B the spray angles are divided throughout the complete duration of the observed

This project has received funding from the European Union Horizon 2020 Research and Innovation programme. Grant Agreement No 861002

injection, with N22 standard having the widest angle which peaks at 35.2°, followed by N21 standard, then N22 180° rotated and N21 180° rotated. The spray area of the injections from SAC hole A is similar to the penetration and rises nearly linear, with the largest area from N22 standard of 1103 mm^2. The area from SAC hole B is also closely grouped and rises nearly similar, in opposite to the penetration behaviour, with the largest area from N21 standard at 1065 mm^2. Again it can be noted, that for both SAC holes the fastest penetration is from 0° relative angle, except for SAC hole A with 300 µs energization duration, due to the injection not being stable, indicating, that the spray hole diameter was to wide for a sufficient pressure build up within the needle lift duration within the SAC and spray hole. When comparing Figure 4.7, Figure 4.8, Figure 4.9 and Figure 4.10 with Figure 4.11 and Figure 4.12, it can be observed that the only consistent pattern is that the fastest penetration is from 0° relative angle for SAC A for all configurations except for the distance h_{min}+0.05 mm and a diameter of d_{min}+0.1 mm. In the contrary, for SAC hole B the relative angle of 0° reached the fastest penetration except for the distance of h_{min}+0.1 mm and a diameter of d_{min}.

This project has received funding from the European Union Horizon 2020 Research and Innovation programme. Grant Agreement No 861002

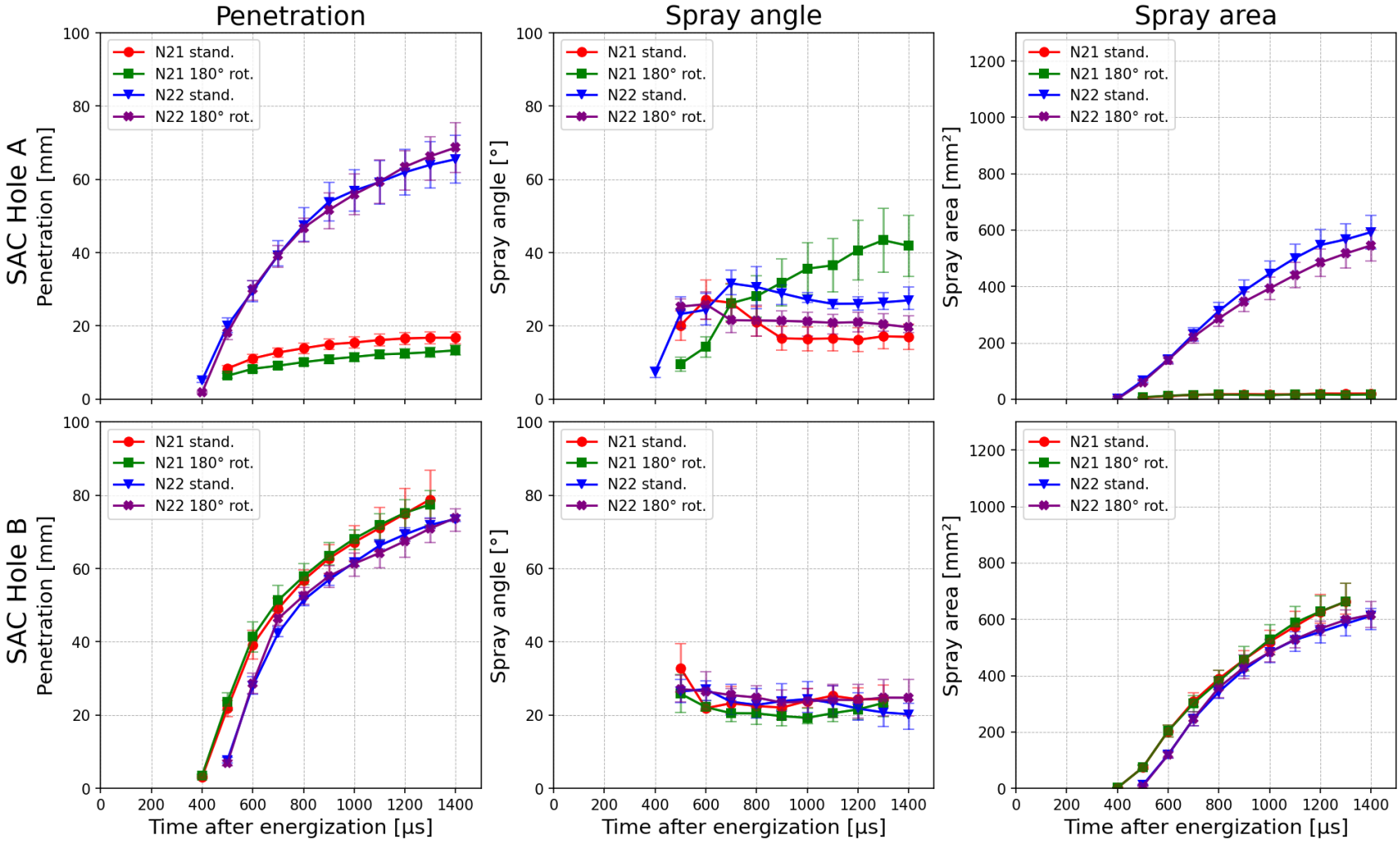


Figure 4.11: Influence of the relative spray angle on the spray characteristics penetration, spray angle and spray area for nozzles N21 and N22 with 300 µs energization duration at 1400 bar

This project has received funding from the European Union Horizon 2020 Research and Innovation programme. Grant Agreement No 861002

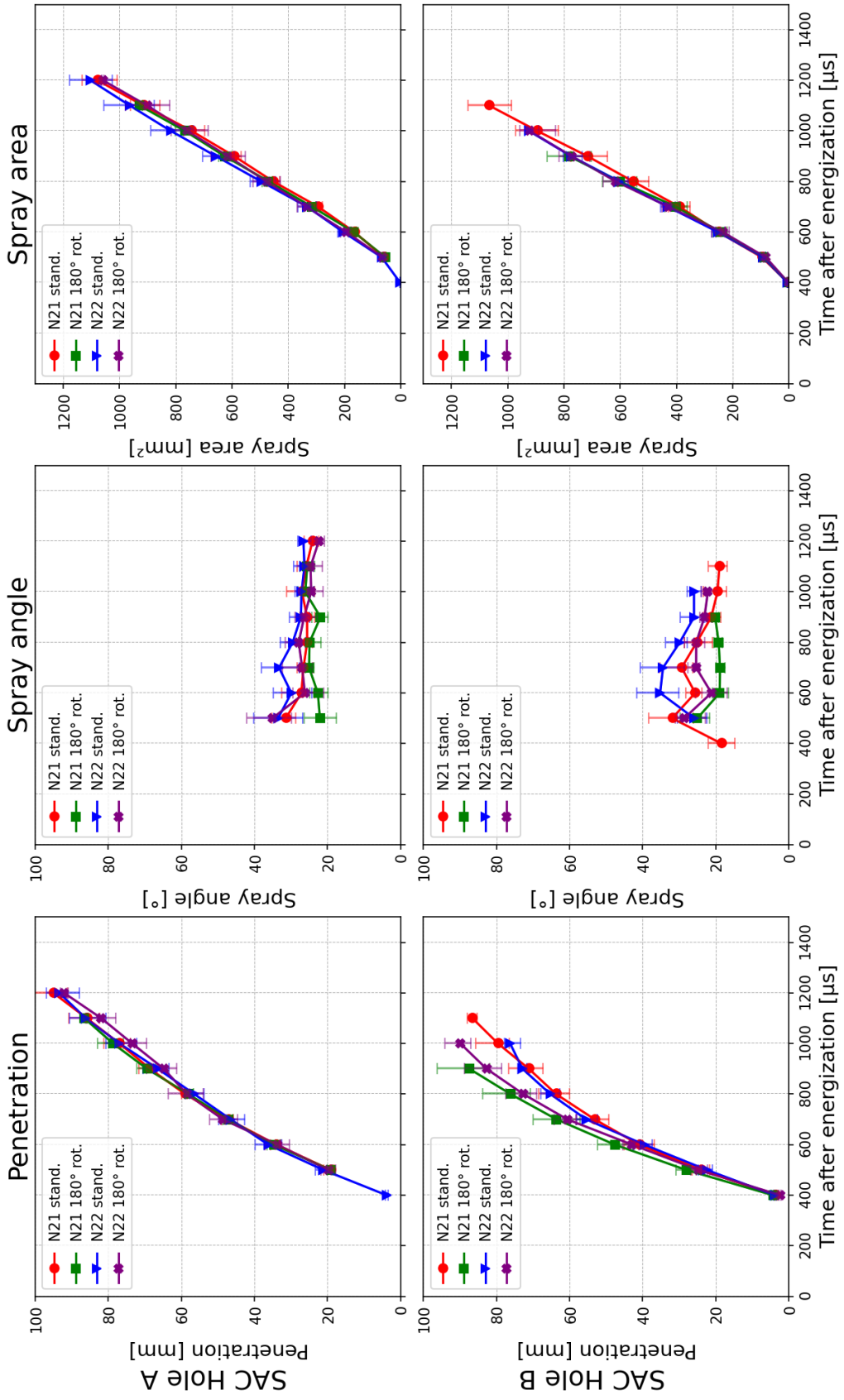


Figure 4.12: Influence of the relative spray angle on the spray characteristics penetration, spray angle and spray area for nozzles N21 and N22 with 1000 µs energization duration at 1400 bar

This project has received funding from the European Union Horizon 2020 Research and Innovation programme. Grant Agreement No 861002

After the spray characteristics for the geometric influence at a low injection pressure were investigated, the same comparisons were carried out at a high injection pressure of 2200 bar. Figure 4.13 and Figure 4.14 show nozzles N5, N6 and N25, similar to Figure 4.7 and Figure 4.8. For the energization duration of 300 µs the fastest penetration with SAC hole A is achieved by N5 180° rotated (d=d_{min}, h=$h_{min} + 0.1$, $\beta = 0$), which achieves a penetration distance of 80 mm at 1066 µs, followed by N6 standard (d=d_{min}, h=$h_{min} + 0.1$, $\beta = 2$), N5 standard (d=d_{min}, h=$h_{min} + 0.1$, $\beta = -3$), N6 180° rotated (d=d_{min}, h=$h_{min} + 0.1$, $\beta = 5$), N25 standard and N25 180° rotated (both d=d_{min}), which is noticeably slower compared to the other injections, reaching the penetration distance of 80 mm after 1374 µs. For SAC hole B the fastest penetration is also achieved by N5 180° rotated, which reaches a distance of 80 mm after 999 µs, followed by N6 180° rotated, N6 standard, N5 standard, N25 180° rotated and N25 standard. The spray angle is widest for SAC hole A at the end of the injection in the case of N6 standard with an angle of 27.6°, N6 180° rotated, N5 standard and N5 180° rotated. The angles for N25 both orientations are the smallest around 20°. For SAC hole B the widest angle was created by N26 standard at 26°, then N6 standard, N5 standard, N6 180° rotated, N5 180° rotated and N25 180° rotated. The spray area is less clustered then the penetration for the nozzles which were manufactured with SAC hole A, with the largest area from the injections from N6 both orientations, with areas of 987 & 954 mm^2, then N5 both orientations and N25 both orientations. For SAC hole B the widest area is from N6 standard with 1056 mm^2, N6 180° rotated, N5 standard, N5 180° rotated and with explicit smaller area N25 both orientations with 716 & 774 mm^2. For the energization duration of 1000 µs, in the case of SAC hole A the most rapid penetration is achieved by N5 standard, which reaches a penetration distance of 80 mm after 1030 µs, then N5 180° rotated, N6 both orientations and N25 both orientations. For SAC hole B the leading spray hole pair is also N5 standard, which penetrates 80 mm after 999 µs, then N5 180° rotated, N6 both orientations, N25 180° rotated and N25 standard. The spray angle for SAC hole A is evenly distributed around 25° at the end of the injections, except N6 180° rotated overshooting to 32.4° between 800 – 1000 µs after energization. For SAC hole B it is similar, with N6 standard having a wide spray angle of 36.8° in the beginning of the injection at 500 µs and N26 180° rotated being noticeably smaller than the other injections at the end of the recordings, with an angle of 18.7°. The spray area is less clustered than the penetration for SAC hole A, with the largest area from N6 both orientations with an area of 973 & 906 mm^2, closely followed by N5 both orientations and N25 standard with significantly smaller area of 660 mm^2. For SAC hole B the largest area is also from N6 both orientations with a spray area of 943 & 885 mm^2, then N5 both orientations, with N5 standard being noticeably

This project has received funding from the European Union Horizon 2020 Research and Innovation programme. Grant Agreement No 861002

smaller and then N25 both orientations similar to SAC hole A. Again, it can be noted, that the overall fastest penetration for both SAC holes is from the relative angle of 0°. Also, the widest spray angles during the start of the injection are caused by 2° relative angle. The spray area behaves similar to the penetration where the fastest expansion is achieved by 5° an 2° relative angle. In comparison to Figure 4.7 and Figure 4.8 it can be observed that all three nozzles behave similar with injection pressures of 1400 bar and 2200 bar.

This project has received funding from the European Union Horizon 2020 Research and Innovation programme. Grant Agreement No 861002

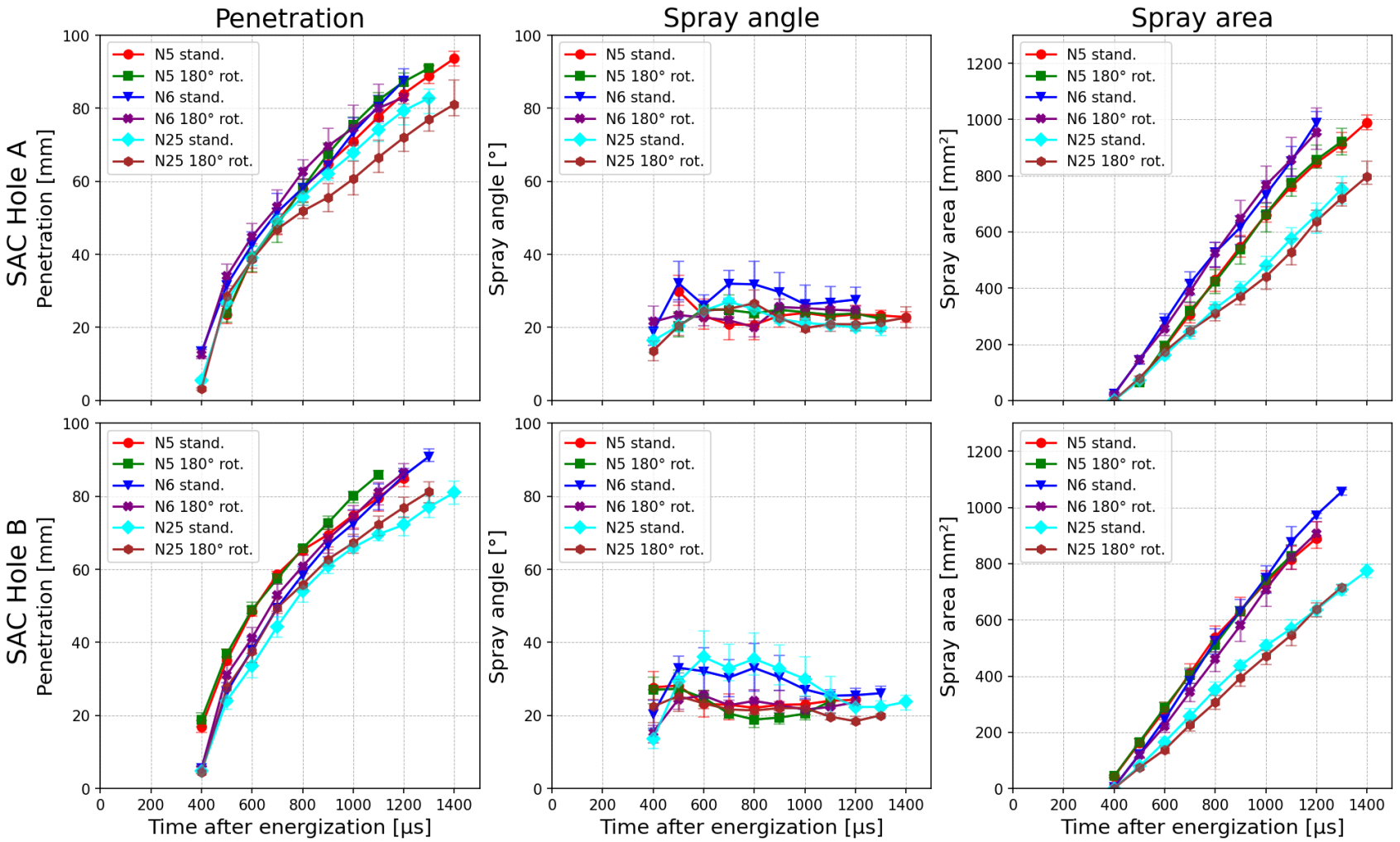


Figure 4.13: Influence of the relative spray angle on the spray characteristics penetration, spray angle and spray area for nozzles N5, N6 and N25 with 300 µs energization duration at 2200 bar

This project has received funding from the European Union Horizon 2020 Research and Innovation programme. Grant Agreement No 861002

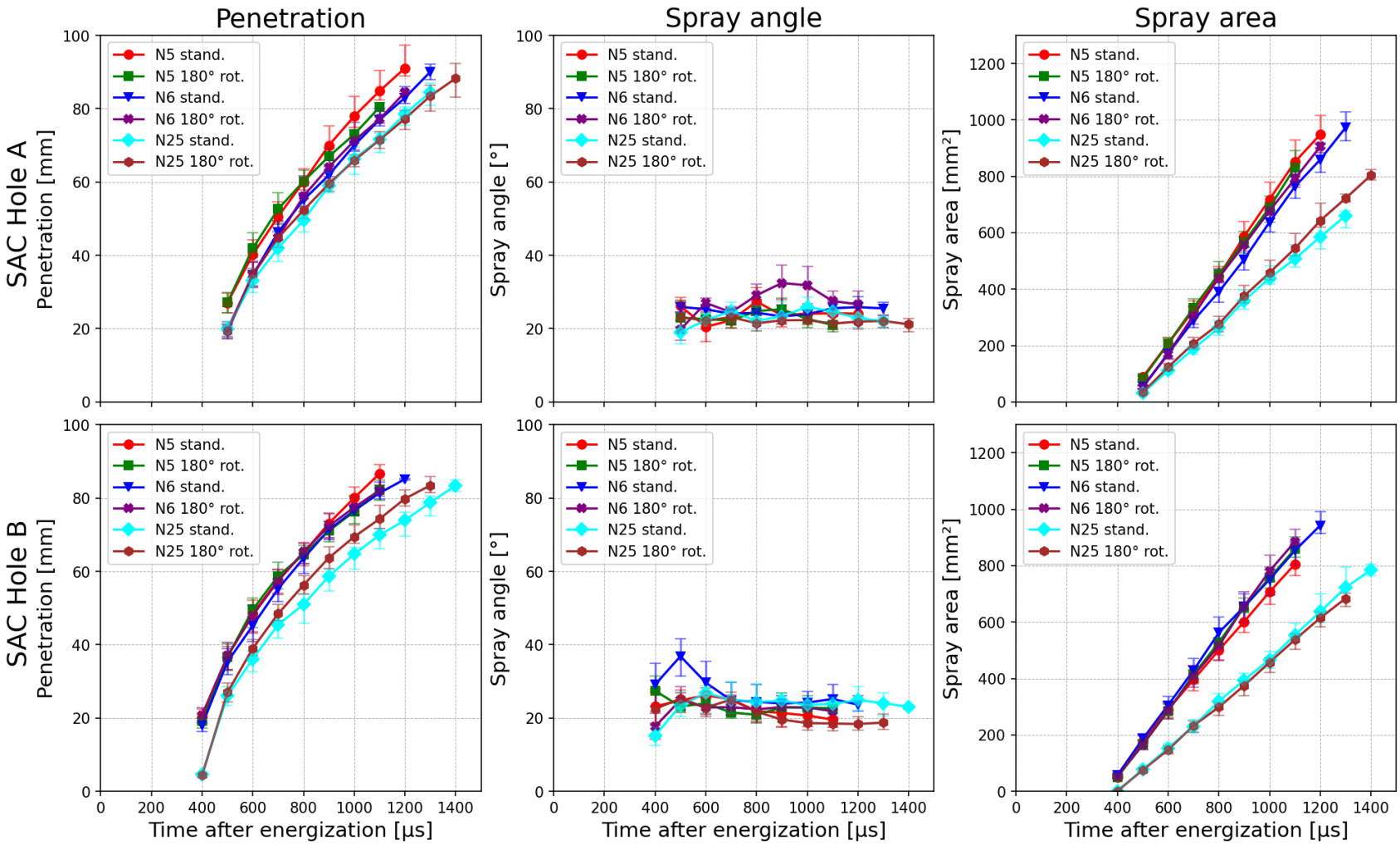


Figure 4.14: Influence of the relative spray angle on the spray characteristics penetration, spray angle and spray area for nozzles N5, N6 and N25 with 1000 µs energization duration at 2200 bar

This project has received funding from the European Union Horizon 2020 Research and Innovation programme. Grant Agreement No 861002

In order to ensure that the observations from Figure 4.13 and Figure 4.14 are not from the influence of geometric parameters other than the relative angle, the nozzles N15, N16 and N26 were compared for 2200 bar, too, in Figure 4.15 and Figure 4.16, in analogy to Figure 4.9 and Figure 4.10. For SAC hole A the fastest penetration was achieved by N26 standard orientation, which reaches the distance of 80 mm after 790 µs, followed by N26 180° rotated (both d=$d_{min} + 0.125$), then N15 180° rotated (d=$d_{min} + 0.05$, h=$h_{min} + 0.1$, $\beta = 0$), N15 standard (d=$d_{min} + 0.05$, h=$h_{min} + 0.1$, $\beta = -3$), N16 180° rotated (d=$d_{min} + 0.05$, h=$h_{min} + 0.1$, $\beta = 5$) and N16 standard (d=$d_{min} + 0.05$, h=$h_{min} + 0.1$, $\beta = 2$). For SAC hole B the fastest penetration was achieved by N15 180° rotated, which crosses 80 mm distance after 853 µs, followed by N26 180° rotated, N15 standard, N26 standard, N16 180° rotated and N16 standard. The spray angles for nozzles manufactured with SAC hole A are diverged between 500 – 800 µs after energization and afterwards are tightly clustered at about 20°, except N16 standard, which is expanding to an angle of around 38° towards the end of the injection. The nozzles with SAC hole B are less clustered compared to SAC hole A, with N16 180° rotated having the widest angle towards the end of the injection at 27.8°, followed by N16 standard, N26 both orientations, and N15 both orientations. The spray area for the nozzles with SAC hole A is in all cases very similar and nearly linearly expanding, with N16 standard reaching the largest area of 1221 mm^2. For SAC hole B the area of all cases is nearly linear expanding too, but they are more clearly separated, with N16 standard orientation having the largest area of 976 mm^2 , then N16 standard, N15 standard, N15 180° rotated and N26 both orientations. For the energization duration of 1000 µs, the fastest penetration with SAC hole A was achieved by N15 180° rotated, which achieves a penetration distance of 80 mm at 888 µs, then N16 180° rotated, N16 standard, and N26 both orientations. For SAC hole B the fastest penetration is from N16 180° rotated, which penetrates the distance of 80 mm after 823 µs, afterwards N15 standard, N16 standard, N15 180° rotated and N26 both orientations. The spray angle for SAC hole A is diverge, with N15 standard having the widest angle in the beginning of the injection of 39.3° and the rapidly reducing. Towards the end, the widest angle is from N16 standard at 29.3°, followed by N26 standard, N15 standard, N16 180° rotated, N15 180° rotated and N26 180° rotated. For SAC hole B the injections with the widest angle at the end of the injection are from N26 both orientations with 30.5° & 25.8°, then N16 both orientations and N15 both orientations. The spray area for the nozzles manufactured with SAC hole A is also nearly linearly expanding with the largest area being from N16 both orientations at 896 & 855 mm^2, then N26 both orientations, closely followed by N15 both orientations. In comparison, the spray area from the nozzles manufactured with SAC hole B is also nearly linearly expanding, but the three

This project has received funding from the European Union Horizon 2020 Research and Innovation programme. Grant Agreement No 861002

different nozzles are not as distinctly clustered, with the largest area being also from N16 both orientations with 1065 & 900 mm^2, followed by N15 standard, N26 standard, N15 180° rotated and then N26 180° rotated. For the energization duration of 300 µs it can be observed that the fastest penetration is achieved by the single hole nozzle N26 and by the relative angle of 0° for both SAC holes. For the spray angle there is no visible influence from the relative angle for these nozzles and for the spray area it can be observed, that at the energization duration of 1000 µs the fastest area expansion is from 2° and 5° relative angle. When comparing the spray characteristics to Figure 4.15, Figure 4.16, Figure 4.13 and Figure 4.14 it can be observed that there seems to be no clearly visible pattern from the relative spray angle of the nozzles influencing the spray characteristics.

This project has received funding from the European Union Horizon 2020 Research and Innovation programme. Grant Agreement No 861002

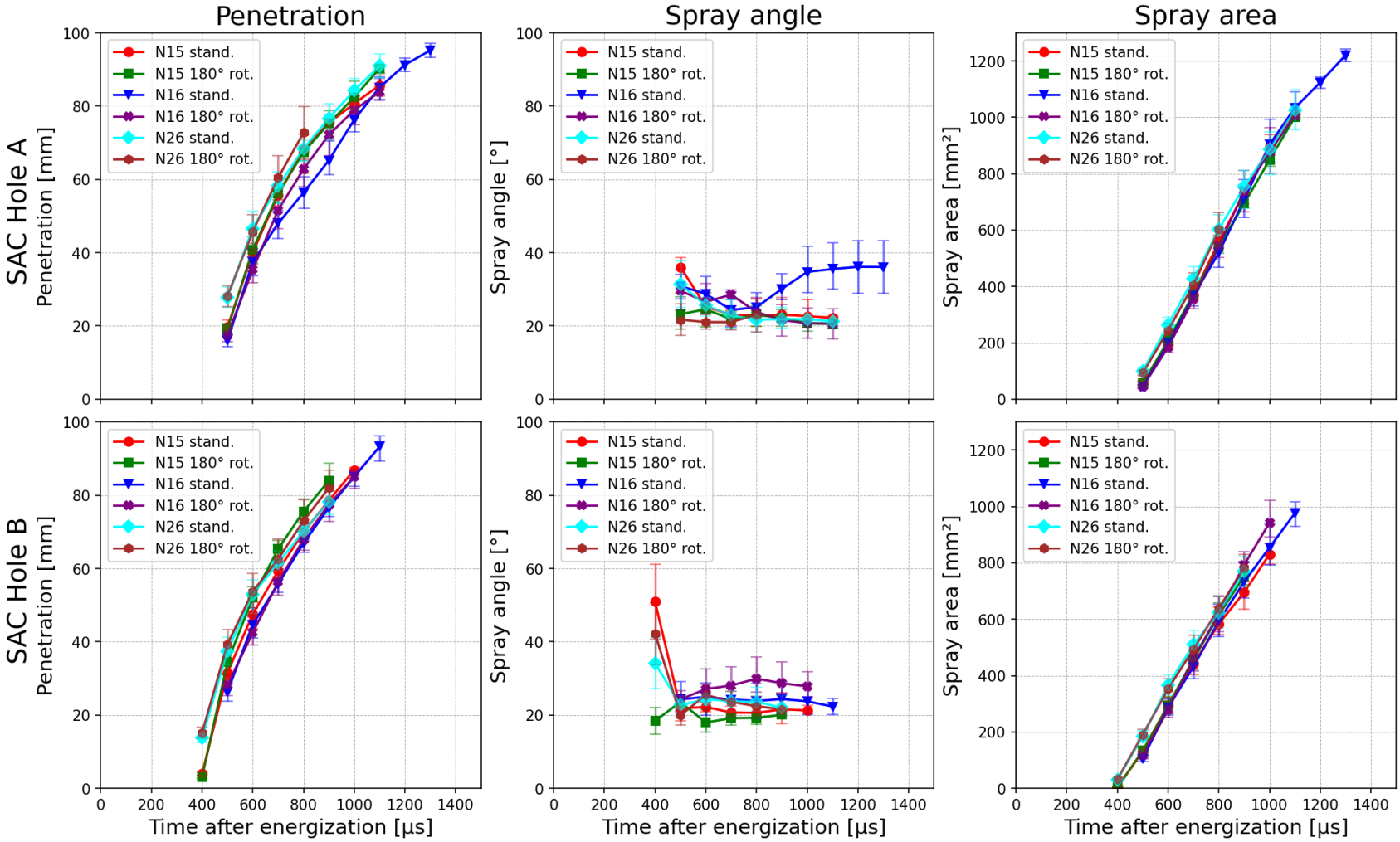


Figure 4.15: Influence of the relative spray angle on the spray characteristics penetration, spray angle and spray area for nozzles N15, N16 and N26 with 300 µs energization duration at 2200 bar

This project has received funding from the European Union Horizon 2020 Research and Innovation programme. Grant Agreement No 861002

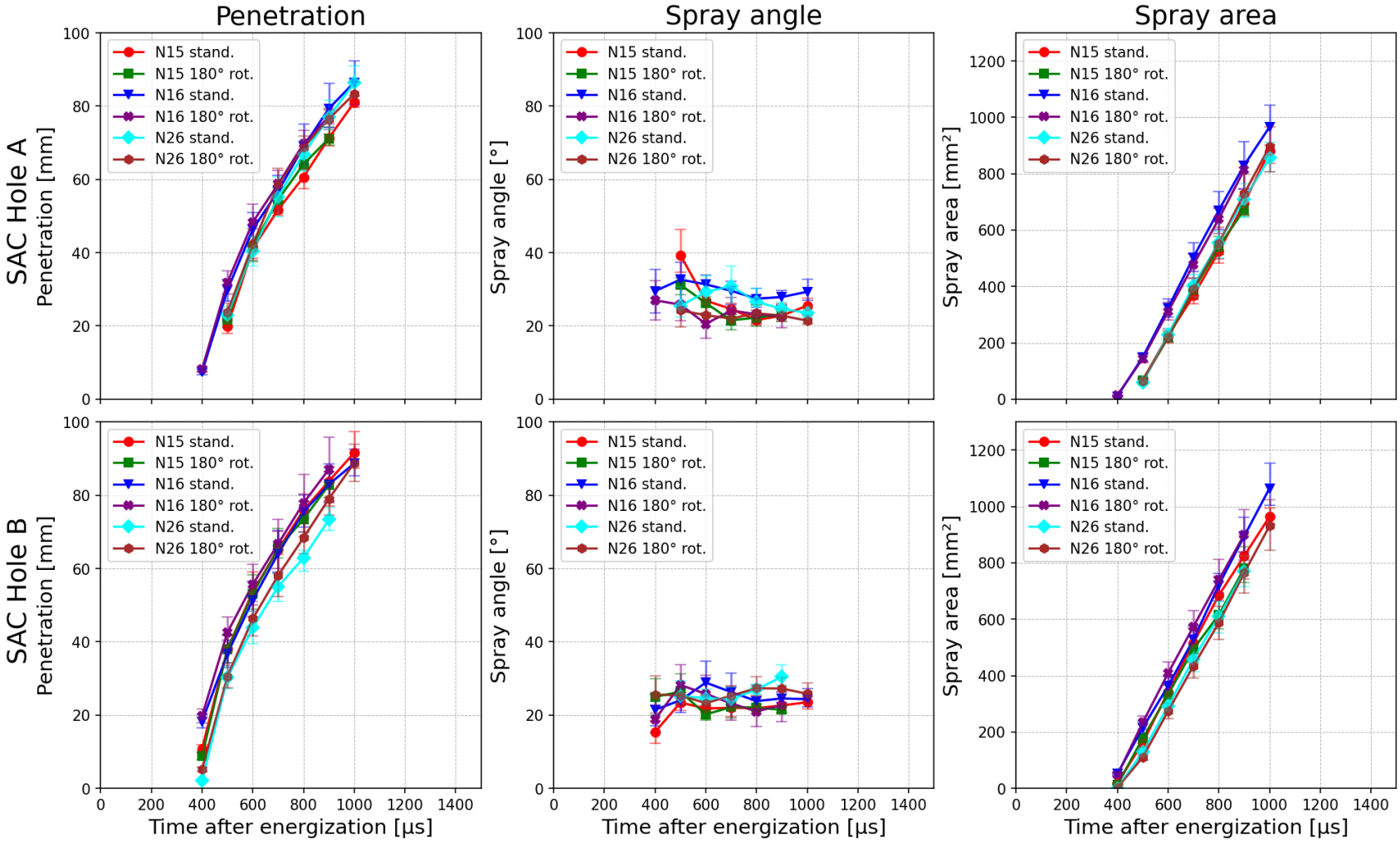


Figure 4.16: Influence of the relative spray angle on the spray characteristics penetration, spray angle and spray area for nozzles N15, N16 and N26 with 1000 µs energization duration at 2200 bar

This project has received funding from the European Union Horizon 2020 Research and Innovation programme. Grant Agreement No 861002

In order to ensure that the previous observations for the influence of the relative spray angle were correct, the last nozzles to compare are N21 and N22 with a injection pressure of 2200 bar. These are shown in Figure 4.17 and Figure 4.18, analogous to Figure 4.11 and Figure 4.12. For the energization duration of 300 µs the fastest penetration for SAC hole A is achieved by N21 both orientations (d=$d_{min}+0.1$, h=$h_{min}+0.05$, $\beta = -3+0$), which reach a penetration distance of 80 mm after 847 & 853µs, followed by N22 both orientations (d=$d_{min}+0.1$, h=$h_{min}+0.05$, $\beta = 2+5$). For SAC hole B, N22 180° rotated penetrated the fastest and reached 80 mm after 766 µs, then N21 180° rotated, N22 standard and N21 standard. The spray angle for the nozzles manufactured with SAC hole A is widest at the end for N22 standard with an angle of 23.9°, followed by N22 180° rotated, N21 standard and N21 180° rotated. In the case of SAC hole B , it can be observed, the widest angle is from N22 standard, with a angle of nearly 37.1° between 500 – 600 µs after energization, followed by N22 180° rotated, N21 180° rotated and N21 standard. The spray area for the nozzles with SAC hole A expands nearly linearly for N21 both orientations which also achieve the fastest area expansion, with a maximum area of 964 & 1143 mm^2, analogous to the penetration. N22 both orientations expands slower but achieves a nearly same area towards the end of the injection. In contrary, for SAC hole B the fastest area expansion is from N22 both orientations, with an final area of 836 & 1042 mm^2, followed by N21 both orientations. For the energization duration of 1000 µs the fastest penetration for SAC hole A is from N22 both orientations, crossing the penetration distance of 80 mm after 853 & 879 µs, followed by N21 both orientations. For SAC hole B the penetration is similar to SAC A with N22 both orientations penetrating the fastest, reaching a penetration distance of 80 mm after 808 & 812 µs, followed by N21 both orientations. The spray angle of SAC hole A is widest with N22 standard with a peak angle of 41.8°, then N21 standard, N22 180° rotated and N21 180° rotated. It can be observed that N22 standard is reaching an angle of above 40°, while the over three are clustered at around 25°. In comparison, for SAC hole B all injections are clustered around 20° at the end of the injection, with also N22 standard reaching the widest angle. For the spray area it can be observed that for SAC A the largest area with the fastest expansion is achieved by N22 both orientations with an area of 972 & 1021 mm^2, followed by N21 both orientations. For SAC hole B the exact same behaviour can be observed, where N22 reaches an area of 1015 & 1065 mm^2. From these observations, it can be noted that at 1000 µs energization duration, the fastest penetration seems to be achieved by 5° and 2° relative angle for both SAC holes. The widest spray angle for both SAC holes and energization durations seems to be achieved by 2° relative spray angle. The spray area at 1000 µs behaves in accordance with the penetration. Comparing this observations with Figure 4.11 and

This project has received funding from the European Union Horizon 2020 Research and Innovation programme. Grant Agreement No 861002

Figure 4.12 we can observe a similar behaviour for SAC hole A at 1000 µs.

This project has received funding from the European Union Horizon 2020 Research and Innovation programme. Grant Agreement No 861002

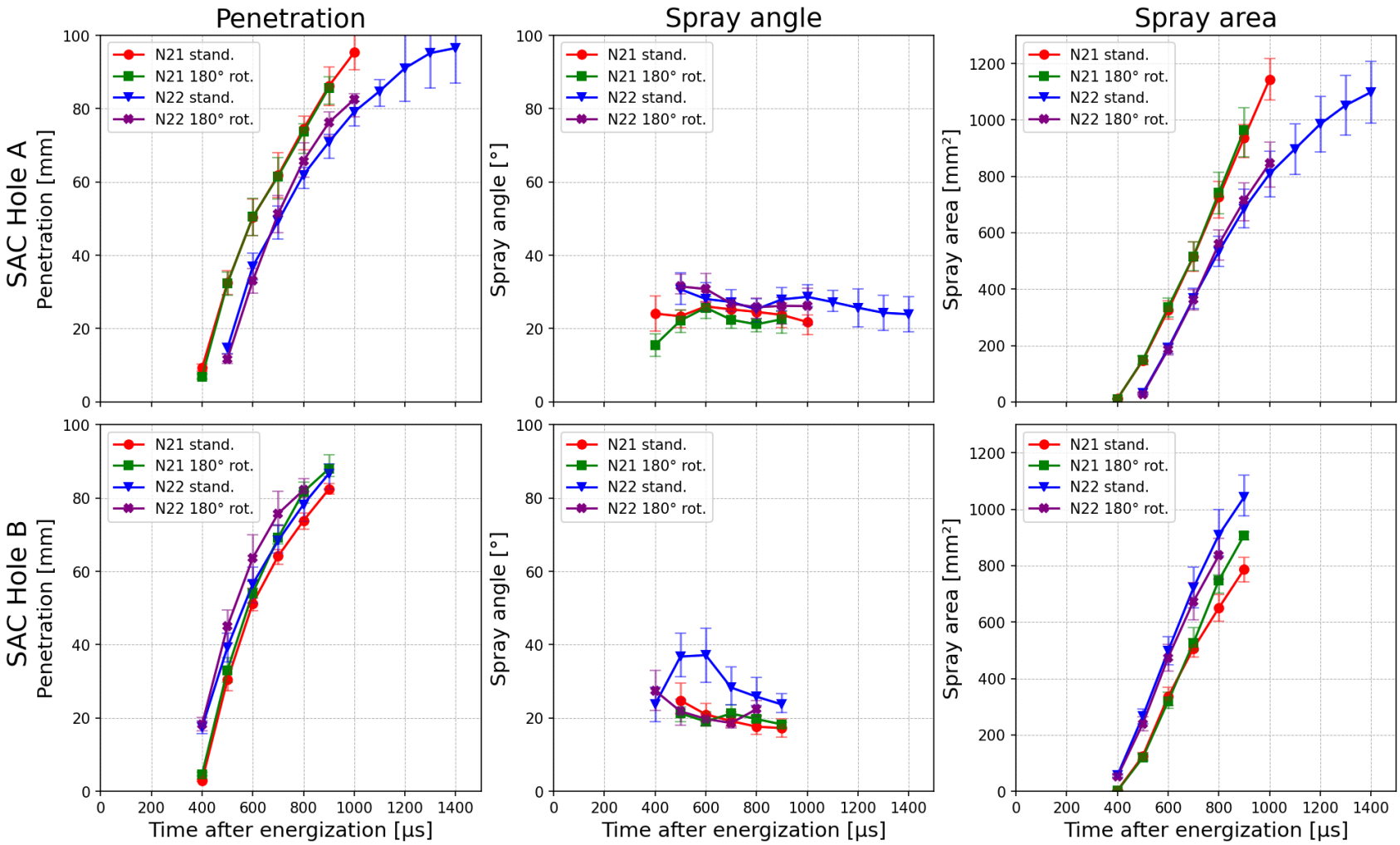


Figure 4.17: Influence of the relative spray angle on the spray characteristics penetration, spray angle and spray area for nozzles N21 and N22 with 300 µs energization duration at 2200 bar

This project has received funding from the European Union Horizon 2020 Research and Innovation programme. Grant Agreement No 861002

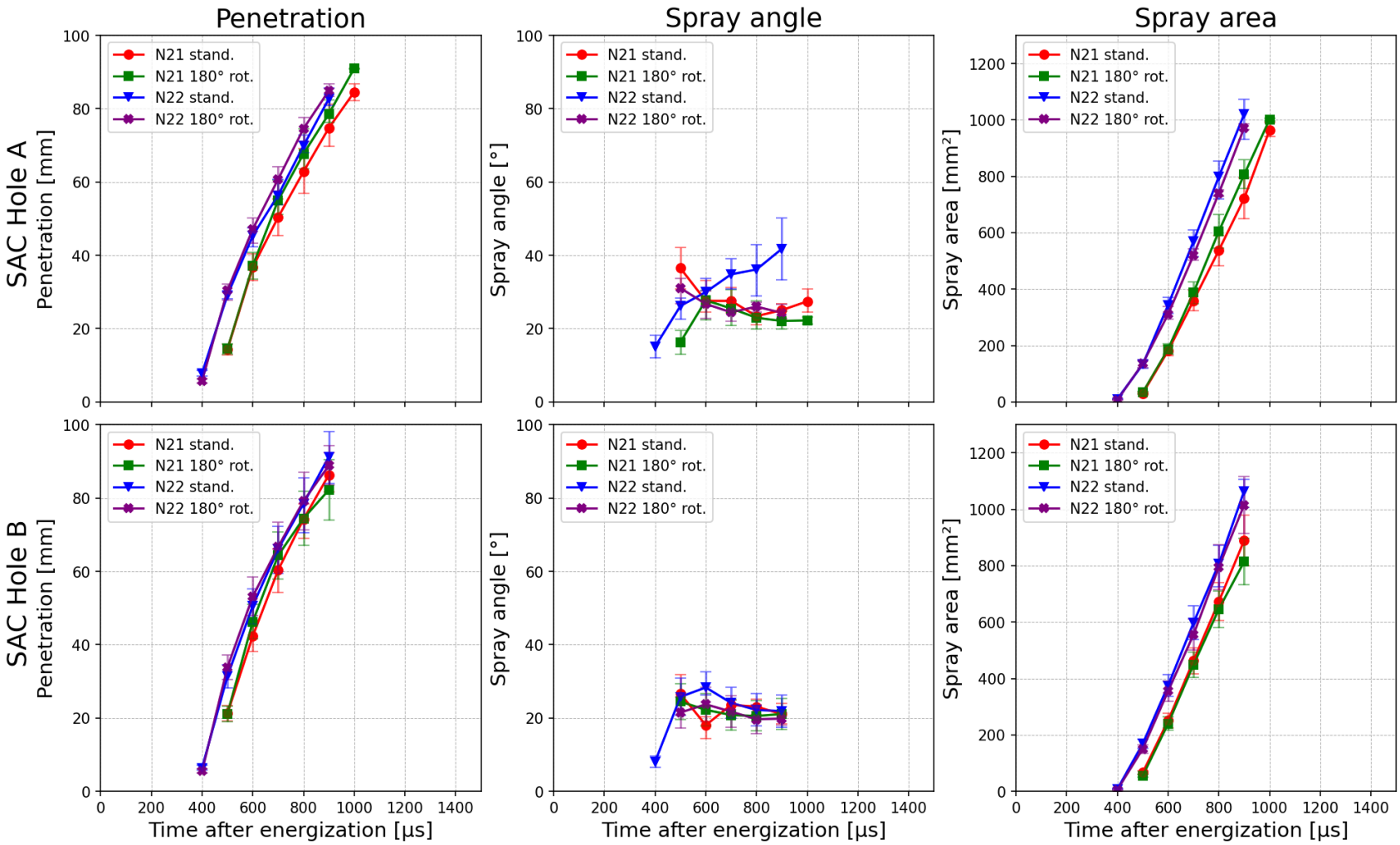


Figure 4.18: Influence of the relative spray angle on the spray characteristics penetration, spray angle and spray area for nozzles N21 and N22 with 1000 µs energization duration at 2200 bar

This project has received funding from the European Union Horizon 2020 Research and Innovation programme. Grant Agreement No 861002

When comparing Figure 4.7 – Figure 4.18 in order to observe the influence of the relative spray angle between the two spray holes, it can be noticed, that the influence in the range of –3° until 5° is not showing any obvious relation. Only for the configuration of the nozzles N15 and N16 it can be observed, that the relative angles of –3° and 0° have the fastest penetration rate for the energization duration of 300 µs with 1400 bar and 2200 bar for both SAC hole types. However, with the energization duration of 1000 µs it can be noticed, that for 1400 bar the relative angles of 0° and 5° achieve the fastest penetration for both SAC holes. For 2200 bar, there is no clear pattern visible, except 5° relative angle leading to the fastest penetrations for SAC hole B at 1000 µs energization duration. The spray angles for all relative angles are very similar and most anomalies are from injections with 300 µs energization duration, due to spray irregularities. Nevertheless, it can be observed, that the relative angle of 2° has a tendency to create wider spray angles in the beginning of the injection, but also leads to smaller angles towards the end. For the spray area it is noticeable that for the nozzles N5 and N6 the relative angle of 2° and 5° seem to lead to the fastest area expansion for the energization duration of 300 µs. For the nozzles N15, N16, N21 and N22 it can be observed that for 1000 µs energization duration, the fastest area expansion is caused by 5° and 2° for both injection pressures and both SAC holes. Overall, there seems to be no consistent pattern of the relative spray angle improving or degenerating the spray characteristics due to the influence of the other parameters. The partial overlap of the two spray plumes from the TWIN nozzle promotes momentum exchange within the interaction region and is causing the combined spray structure to behave similarly to a single larger jet. Previous investigations from Woodward L'Orange [102] have shown that larger relative spray angles can reduce spray penetration due to weaker interaction between the two spray plumes. Therefore, the relative spray angles investigated in this thesis were limited to -3° to +5° . However, the present results indicate that small variations of the relative spray angle have little to no influence on the spray characteristics.

After the relative spray angle, the influence of the spray hole distance is investigated. For the first comparison, the nozzles N1, N3, N5, N7, N9 and N25 were chosen, with N1 having a distance of h_{min}, N3 having a distance of h_{min}+0.05 mm, N5 having a distance of h_{min}+0.1 mm, N7 having a distance of h_{min}+0.15 mm, N9 having a distance of h_{min}+0.2 mm and N25 for comparison. The spray characteristics for the standard orientation of the nozzles are shown in Figure 4.19 and Figure 4.20, meaning, all of the spray hole pairs which are compared in this Figures, have a relative angle of –3. The injection pressure was kept to 1400 bar and the energization duration were 300 µs and 1000 µs. For 300 µs and SAC hole A it is visible, that the fastest penetration is from N3

This project has received funding from the European Union Horizon 2020 Research and Innovation programme. Grant Agreement No 861002

(d=d_{min}, h=$h_{min} + 0.05$, $\beta = -3$) at the beginning of the injection and towards the end from N1 (d=d_{min}, h=h_{min}, $\beta = -3$), which reaches a penetration distance of 80 mm after 1276 µs. Following are N5 (d=d_{min}, h=$h_{min} + 0.1$, $\beta = -3$), N7 (d=d_{min}, h=$h_{min} + 0.15$, $\beta = -3$), N9 (d=d_{min}, h=$h_{min} + 0.2$, $\beta = -3$) and N25 (d=d_{min}). For SAC hole B the most rapid penetration is from N5 and N9, which achieve a distance of 80 mm after 1195 & 1214 µs, then N7, N3 and N25. The nozzle N1 with SAC hole B did not inject. The spray angle for SAC hole A is clustered around 20° – 30°, with the widest angle from N5, then N25, N9, N7, N3 and N1. For SAC hole B the angles are more divided, with the widest angle from N25 with a angle of 30.6°, then N7, N9, N5 and N3. The spray area is nearly linearly expanding for SAC hole A with the largest area being achieved by N7 with an area of 846 mm^2, then N1, N5, N3, N9 and N25. For SAC hole B it can be observed that the area expands less rapid for all injections towards their ends. The fastest expansion is from N9 with a maximum area of 708 mm^2, then N5, N7, N25 and N3. For the energization duration of 1000 µs for SAC hole A the fastest penetration is from N7, which crosses the distance of 80 mm after 1177 µs, then N1, N3, N5, N9 and N25. For SAC hole B the most rapidly penetrating nozzle is N5, which reaches 80 mm penetration distance at 1208 µs after the beginning of the energization, then N1, N3, N7, N9 and N25. The spray angle for SAC hole A is clustered around 20° and only in the beginning of the injection it can be observed that the angle is wider for N5 and N25. For SAC hole B the angles are grouped around 25°, with the widest angle from N9, N25, N5, N3, N5 and N1. The spray area of SAC hole A is expanding nearly linear again, with the most rapid expansion from N7and an area of 885 mm^2, N5, N9, N3, N1 and N25. For SAC hole B the nozzle that expands the area the fastest is N5 with an area of 918 mm^2, followed by N3, N9, N1, N7 and N25. From this it can be observed that there is no consistent pattern regarding the influence of the spray hole distance on the spray penetration and spray angle, except for SAC hole A and 300 µs energization duration, it seems that the penetration speed is declining with the spray hole distance. For the spray area with SAC hole A it can be observed that a higher spray hole distance seems to lead to a faster area expansion. Also all TWIN cases penetrate faster than the comparison nozzle. N25 was included as a single hole comparison nozzle. Since this nozzle only contains one spray hole, it has no spray hole distance and is therefore not used to evaluate the influence of spray hole spacing. The smaller spray area observed for N25 is caused by the shorter penetration length shows the potential of the TWIN nozzle to improve the spray penetration under similar conditions. The spray area behaves in accordance with the penetration for this case.

This project has received funding from the European Union Horizon 2020 Research and Innovation programme. Grant Agreement No 861002

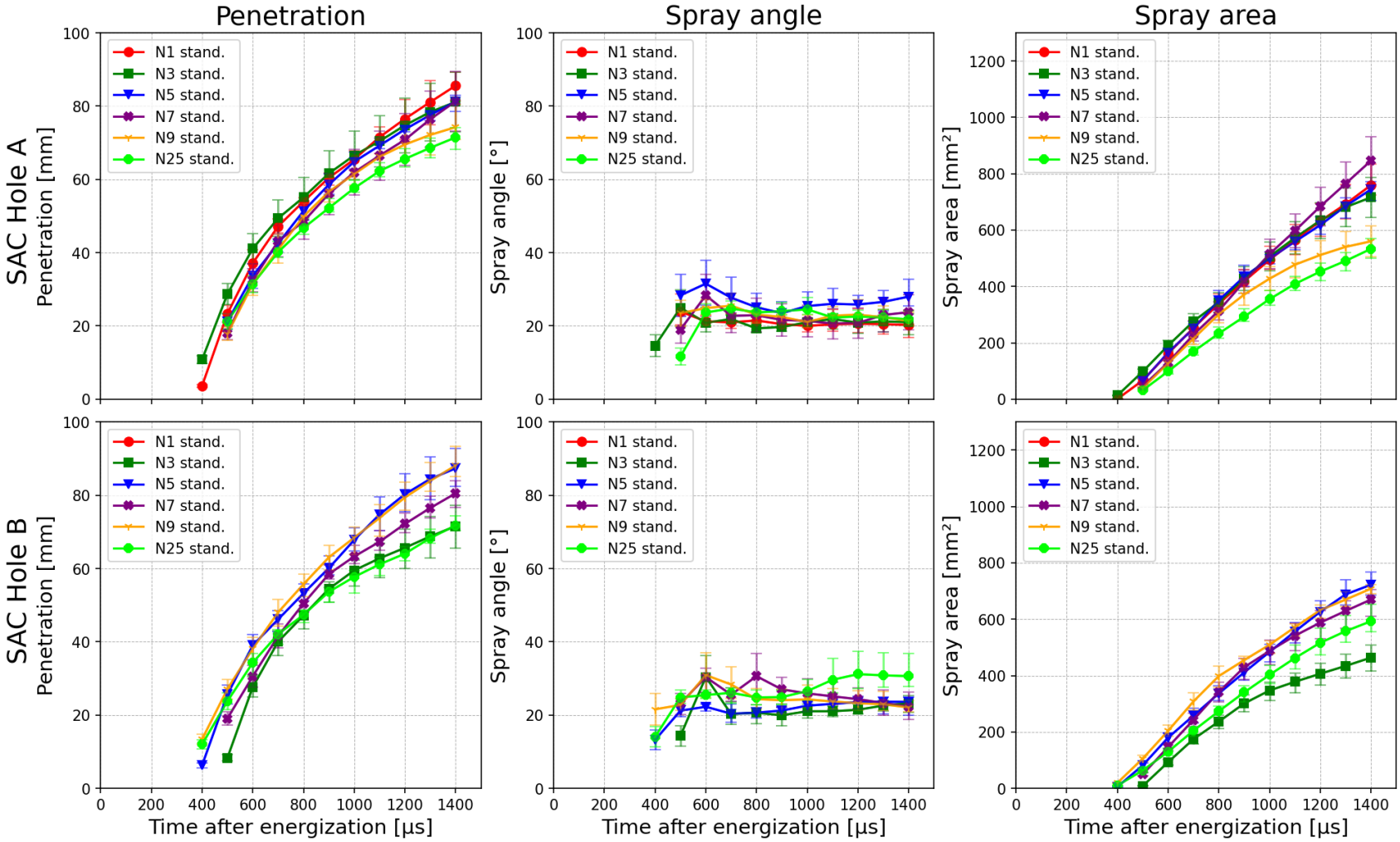


Figure 4.19: Influence of the relative spray hole distance on the spray characteristics penetration, spray angle and spray area for nozzles N1, N3, N5, N7, N9 and N25 in standard orientation with 300 µs energization duration at 1400 bar

This project has received funding from the European Union Horizon 2020 Research and Innovation programme. Grant Agreement No 861002

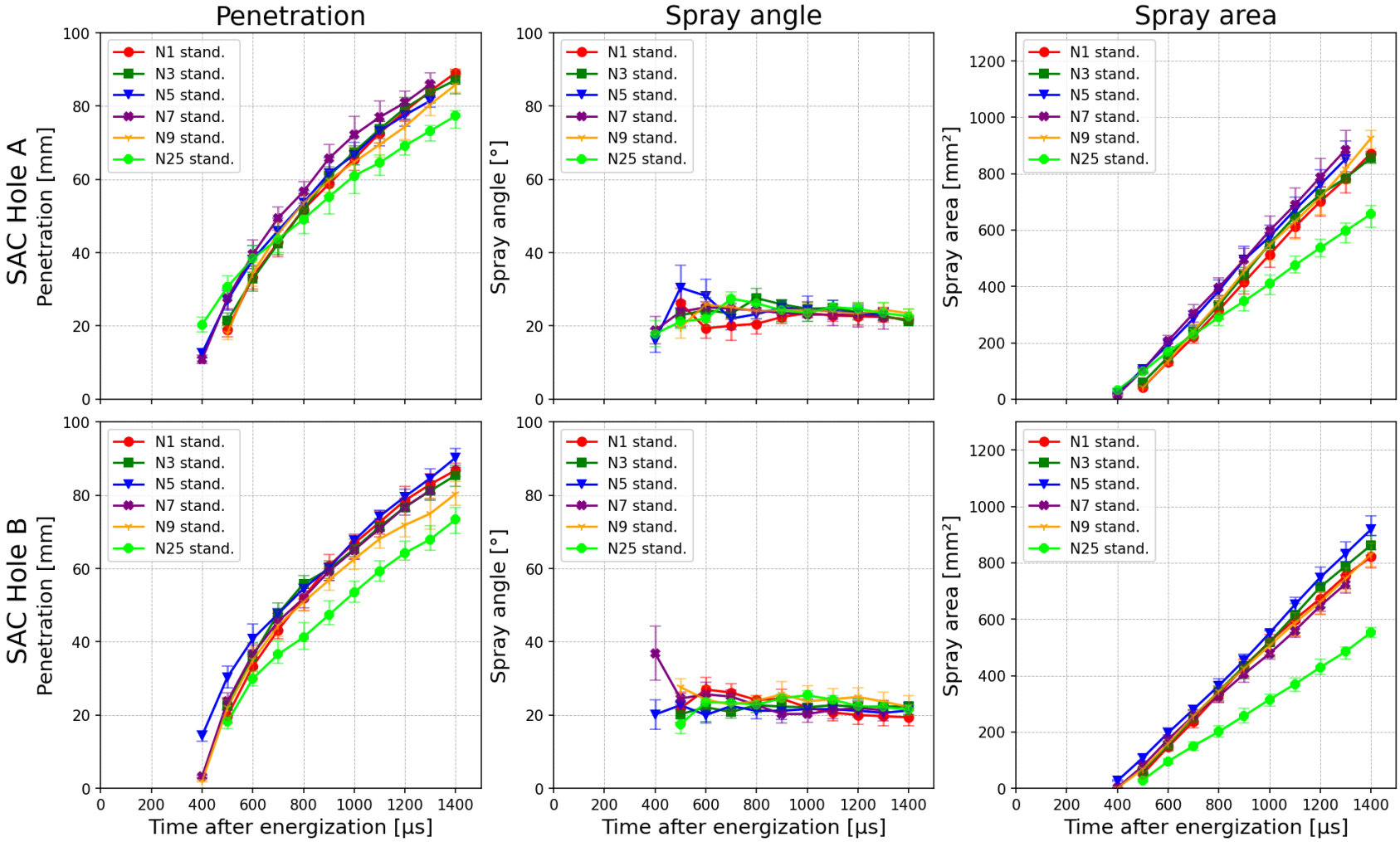


Figure 4.20: Influence of the relative spray hole distance on the spray characteristics penetration, spray angle and spray area for nozzles N1, N3, N5, N7, N9 and N25 in standard orientation with 1000 µs energization duration at 1400 bar

This project has received funding from the European Union Horizon 2020 Research and Innovation programme. Grant Agreement No 861002

In order to ensure that the observations made in Figure 4.19 and Figure 4.20 are not influenced by the relative spray angle, the same nozzles were compared in 180° rotated orientation, meaning a relative angle of 0°, as shown in Figure 4.21 and Figure 4.22. For SAC hole A with 300 µs energization duration the fastest penetration was achieved by N1 (d=d_{min}, h=h_{min}, $\beta = 0$), penetrating 80 mm of distance at 1163 µs after energization, then N3 (d=d_{min}, h=$h_{min} + 0.05$, $\beta = 0$), N5 (d=d_{min}, h=$h_{min} + 0.1$, $\beta = 0$), N7 (d=d_{min}, h=$h_{min} + 0.15$, $\beta = 0$), N9 (d=d_{min}, h=$h_{min} + 0.2$, $\beta = 0$), N25 (d=d_{min}). This is consistent with the penetration results from Figure 4.19. For SAC hole B the fastest penetration is from N9, with 80 mm distance after 1215 µs, followed by N5, N7, N25 and N3. N1 did not inject for this pressure and energization duration. The spray angle of SAC hole A is tightly clustered around 20° during the whole duration of all injections, with N3 showing the widest angle of 23.7°. For SAC hole B the spray angle curves are more deviated with N5 and N7 having the widest angle towards the end of the injection with 25.6° & 26.1°. The spray area for SAC hole A expands the fastest for N1 with an area of 747 mm^2, followed by N7, then N3, N5, N9 and N25. For SAC hole B the spray area expansion is slower than SAC hole A in general, with the most rapid expansion from N9 with an area of 714 mm^2, then N5, N7, N25 and N3. For the energization duration of 1000 µs for SAC hole A the fastest penetration is from N3 which reaches a distance of 80 mm after 1174 µs, followed by N5, N7, N1, N9 and N25. For SAC hole B the quickest penetration is from N5 crossing the distance of 80 mm after 1163 µs, then N3, N9, N7, N1 and N25. The spray angle from SAC hole A is showing spikes around 400 - 600 µs with angles between 20° – 30°, with N7 achieving the initial widest angle but towards the end of the injection, the widest angle is from N1 of 24.3°, even though all injections are closely around 20°. For SAC hole B the angle is further distributed with a spike around 600 - 900 µs, where the widest angle is from N25 of 27.8°, followed by N9. At the end of the injection, the widest angle is achieved by N3 and N5 with an angle of 25 & 23.9°. The spray area for SAC hole A expands nearly linear, with the fastest area gain from N7 which reaches an area of 949 mm^2, then N5, N3, N1, N9 and N25. For SAC hole B the fastest expansion is from N5 with a final area of 825 mm^2, then N7, N3, N9, N1 and N25. The penetration for both SAC holes behaves similar to Figure 4.19 and Figure 4.20. The spray angles show no similar pattern, meaning that they are influenced by the relative spray angle. The spray area for both relative spray angles behaves similar.

This project has received funding from the European Union Horizon 2020 Research and Innovation programme. Grant Agreement No 861002

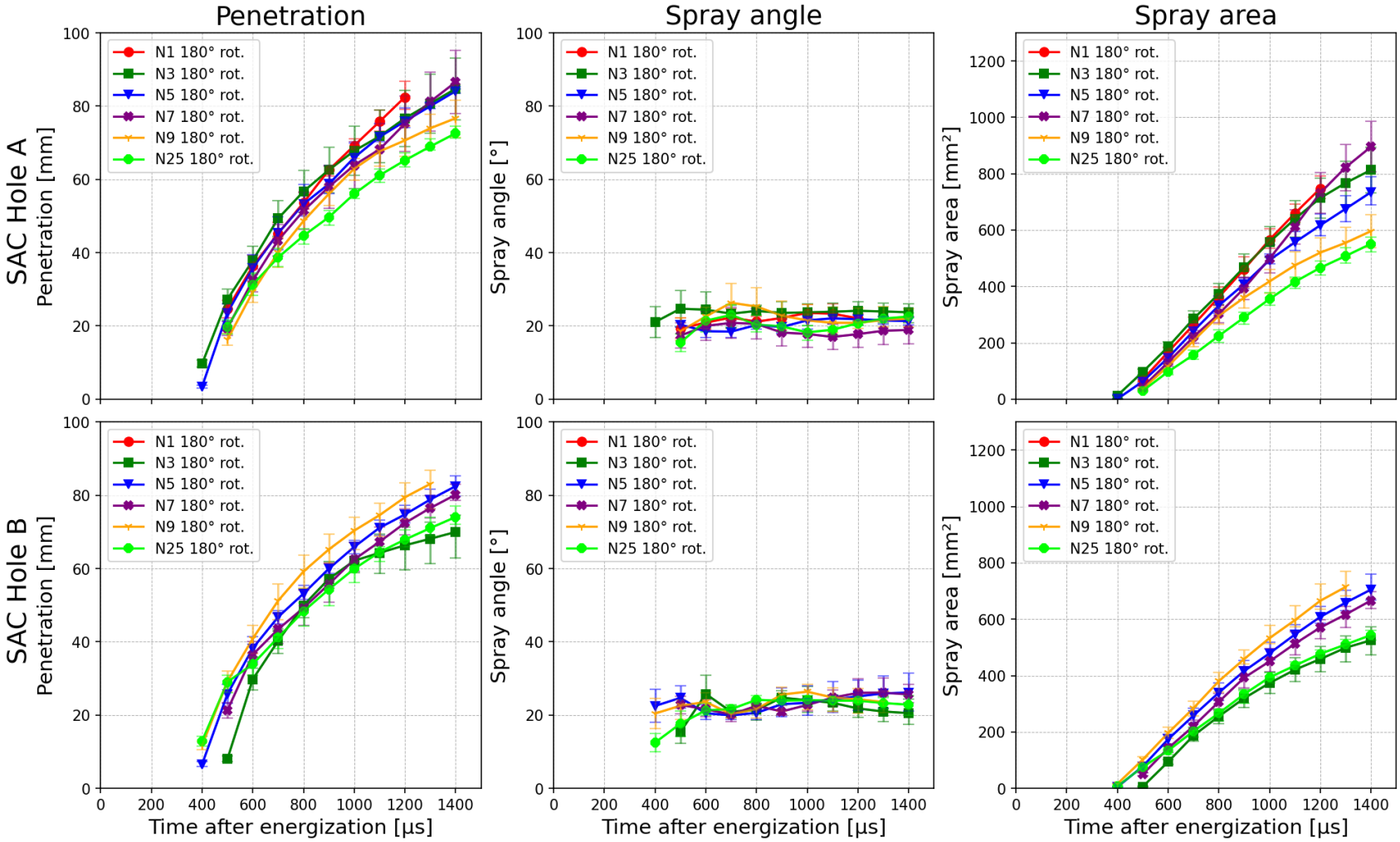


Figure 4.21: Influence of the relative spray hole distance on the spray characteristics penetration, spray angle and spray area for nozzles N1, N3, N5, N7, N9 and N25 in 180° rotated orientation with 300 µs energization duration at 1400 bar

This project has received funding from the European Union Horizon 2020 Research and Innovation programme. Grant Agreement No 861002

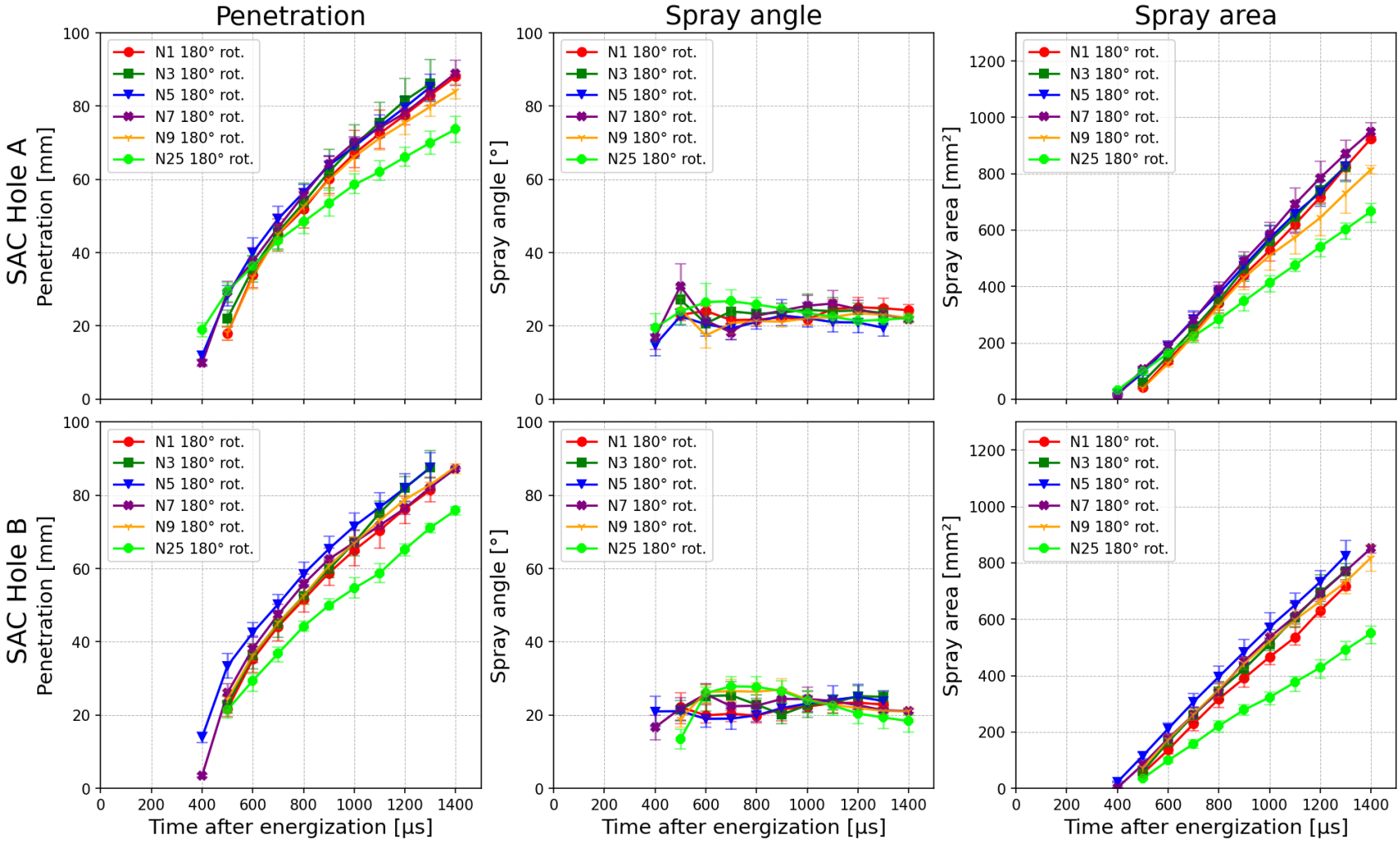


Figure 4.22: Influence of the relative spray hole distance on the spray characteristics penetration, spray angle and spray area for nozzles N1, N3, N5, N7, N9 and N25 in 180° rotated orientation with 1000 µs energization duration at 1400 bar

This project has received funding from the European Union Horizon 2020 Research and Innovation programme. Grant Agreement No 861002

After comparing the influence of the spray hole distance for low pressure applications, the same nozzles were chosen to be compared for injections with 2200 bar pressure. Similar to Figure 4.19 and Figure 4.20 the nozzles N1, N3, N5, N7, N9 and N25 with standard orientation are shown in Figure 4.23 and Figure 4.24. For the energization duration of 300 µs it can be observed that the fastest penetration for SAC hole A is achieved by N1 (d=d_{min}, h=h_{min}, $\beta = -3$) penetrating the distance of 80 mm at 999 µs after energization, followed by N9 (d=d_{min}, h=$h_{min} + 0.2$, $\beta = -3$), N7 (d=d_{min}, h=$h_{min} + 0.15$, $\beta = -3$), N3 (d=d_{min}, h=$h_{min} + 0.05$, $\beta = -3$), N5 (d=d_{min}, h=$h_{min} + 0.1$, $\beta = -3$) and N25 (d=d_{min}). For SAC hole B the most rapid penetration is from N7, which achieves a penetration of 80 mm at 1010 µs, then N9, N3, N1, N5 and N25. The spray angle for SAC hole A is diverted, with the widest angle from N9 at 29°. For SAC hole B all injections are clustered around 25°, except N25, which has a wider angle of 30 – 36° between 500 - 1000 µs, but afterwards narrows down to around 25°, too. For the spray area it can be observed, that for SAC hole A the nozzles N9, N3 and N1 are expanding the fastest, achieving a final area of 1098 & 947 & 764 mm^2, afterwards the next group is from N7 and N5 and with a visible slower expansion N25. For SAC hole B, the spray areas for all TWIN injections are more tightly clustered, with the fastest expansion from N7 with an area of 975 mm^2, N3, N5, N9 and N1, and only N25 is clearly slower. For the energization duration of 1000 µs it is visible, that for SAC hole A the most rapid penetration is from N1, crossing 80 mm after 1018 µs, then N5, N3, N9, N7 and N25. For SAC hole B the fastest penetrating injection is from nozzle N7, which reaches a distance of 80 mm after 969 µs, followed by N9, N5, N3, N1 and N25. The spray angles for SAC hole A are clustered around 25° with only N9 shortly spiking around 900 µs with an angle of 32°. For SAC hole B the spray angles are widely diverged at the beginning of the injections and are clustered around 25° towards the end. The spray area is nearly linear expanding for the injections with SAC hole A, where the fastest expansion is from N1 with an area of 853 mm^2, then N5, N3, N9, N7 and clearly apart N25. For SAC hole B the areas are behaving similar but expand slower than from the injections with SAC hole A, also the most rapid expansion is from N7, which achieves an area of 867 mm^2, then N9, N5, N3, N1 and again apart from N25. After investigating the injection curves for this cases, it can be observed that for SAC hole A the fastest penetration is from the distance of h_{min}, while for SAC hole B the fastest penetration is achieved by a spray hole distance of h_{min}+0.15 mm and h_{min}+0.2 mm. Again the single hole nozzle is penetrating the slowest in all cases. For the spray angle it seems that the widest spray angles are achieved by a spray hole distance of h_{min}+0.05 mm and the single hole nozzle. The spray area behaves in accordance with the penetration.

This project has received funding from the European Union Horizon 2020 Research and Innovation programme. Grant Agreement No 861002

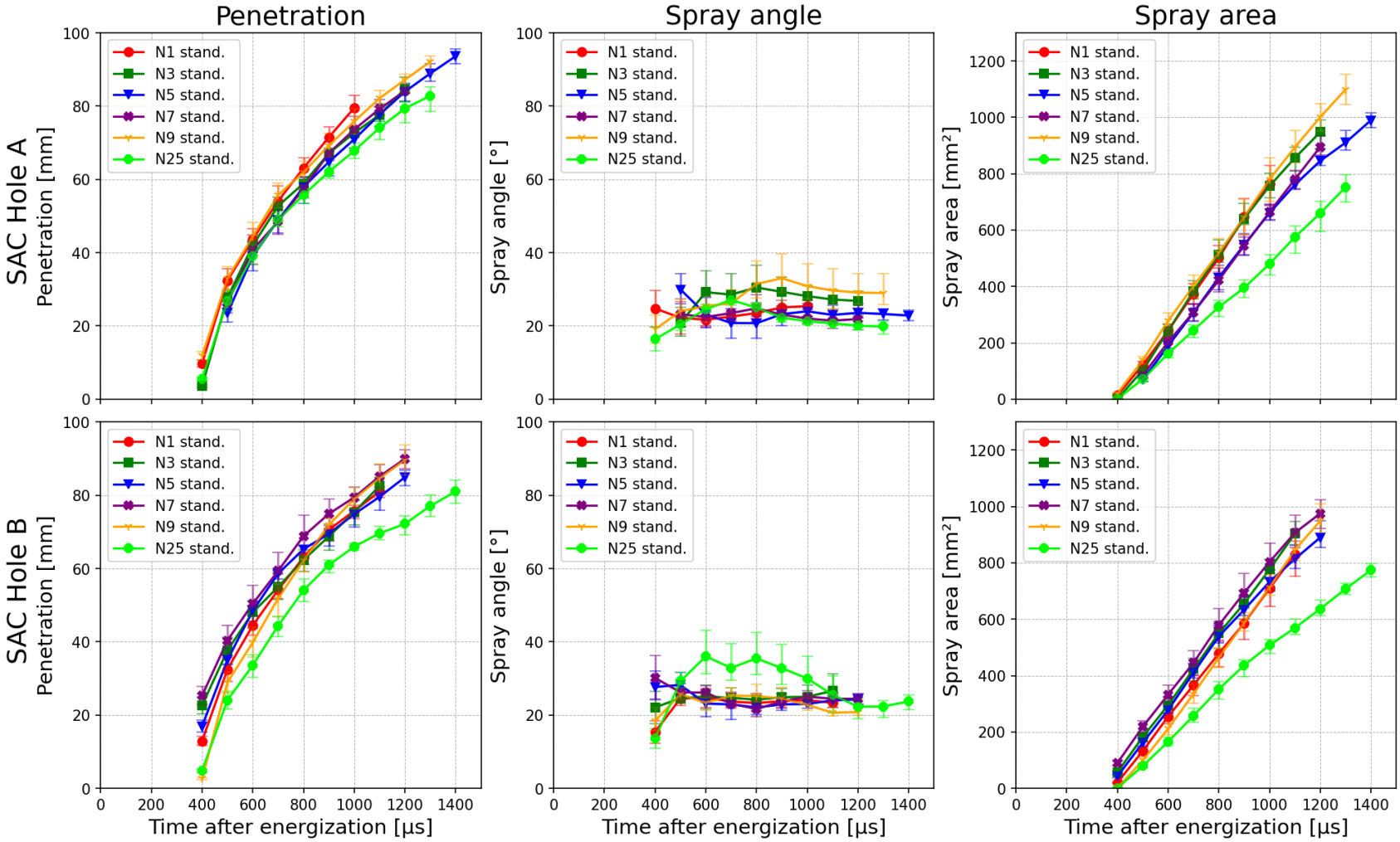


Figure 4.23: Influence of the relative spray hole distance on the spray characteristics penetration, spray angle and spray area for nozzles N1, N3, N5, N7, N9 and N25 in standard orientation with 300 µs energization duration at 2200 bar

This project has received funding from the European Union Horizon 2020 Research and Innovation programme. Grant Agreement No 861002

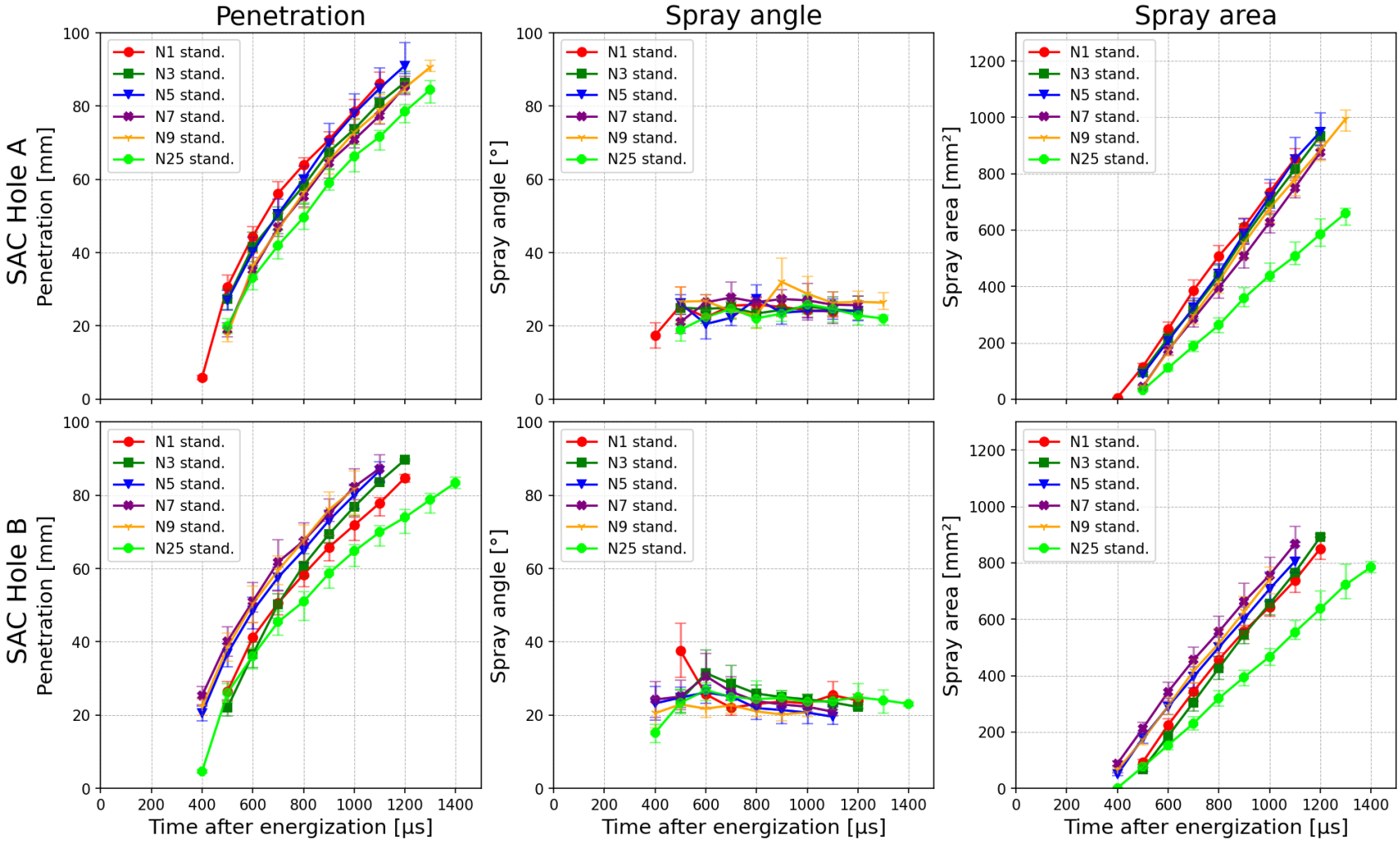


Figure 4.24: Influence of the relative spray hole distance on the spray characteristics penetration, spray angle and spray area for nozzles N1, N3, N5, N7, N9 and N25 in standard orientation with 1000 µs energization duration at 2200 bar

This project has received funding from the European Union Horizon 2020 Research and Innovation programme. Grant Agreement No 861002

In accordance with Figure 4.21 and Figure 4.22, the same nozzles were compared for 2200 bar and 180° rotated orientation. These are shown in Figure 4.25 and Figure 4.26. For the energization duration of 300 µs it is observable that the fastest penetration for SAC hole A is from N1 (d=d_{min}, h=h_{min}, $\beta = 0$), which reaches a distance of 80 mm after 930 µs, then N9 (d=d_{min}, h=$h_{min} + 0.2$, $\beta = 0$), N3 (d=d_{min}, h=$h_{min} + 0.05$, $\beta = 0$), N5 (d=d_{min}, h=$h_{min} + 0.1$, $\beta = 0$), N7 (d=d_{min}, h=$h_{min} + 0.15$, $\beta = 0$) and N25 (d=d_{min}), which is distinctly slower than the rest. For SAC hole B it can be observed that the injections from all nozzles are divided at the start of the injection, with the fastest penetration from N7, crossing 80 mm after 999 µs, N3, N5, N1, N9 and N25. Towards the end of the observed time, all injections reached the same penetration, only N25 is distinctly slower like with SAC hole A. For the spray angle of SAC hole A all injection angles are closely around 25°. For SAC hole B the angles are less uniform with the widest angle in the beginning of the injection from N5 of 27.3°, around 700 – 900 µs the widest angle is from N7 of 24.8° and at the end of the injection the widest angle is from N5 again with 23.8°. The spray area for SAC hole A is expanding uniformly for all TWIN injections, with the fastest area expansion from N1 with a final area of 790 mm^2, then N9, N3, N7 and N5. Only N25 performs clearly slower. For SAC hole B the fastest area expansion is similar to SAC A, only the order for the TWIN pairs is different, the fastest being N7 with an area of 819 mm^2, then N5, N1, N3 and N9. N25 expands slower again. Overall, the experiments showed that a higher inejction pressure mostly influences the TWIN nozzles with a larger spray hole diameters at short energization durations. In contrast, the smaller spray hole diameters exhibited similar spray behaviour at both pressure levels. For the energization duration of 1000 µs the penetration of SAC hole A is fastest from nozzle N1, which achieves a penetration distance of 80 mm after 993 µs, followed by N3, N9, N5 N7 and N25. For SAC hole B the beginnings of the penetration are clustered in two group, with N7, N9, N5 being the faster nozzles, reaching a distance of 80 mm after 921 & 969 & 1061 µs and N25, N1 and N3 being slower. At the end the penetration curves are divergent, with the fastest penetration from N7, then N9, N5, N1, N3 and N25. The spray angle for SAC hole A is similar for all injections with all of them having an angle of around 25°. For SAC hole B the spray angles are wider up to 30° and N25 having a visible lower angle then the rest. The spray area for SAC hole A is expanding fastest for the injection from N1 with an area of 869 mm^2, followed by N5, N3, N9, N7 and N25. For SAC hole B the spray area expansions from the different injections are more grouped again, with the fastest group being N7, N9 and N5 having final areas of 784 & 935 & 858 mm^2, followed by N3 and N1 and further off N25. Again it can be observed that for SAC hole A the fastest penetration is from the distance of h_{min}, while for SAC hole B the fastest penetration is

This project has received funding from the European Union Horizon 2020 Research and Innovation programme. Grant Agreement No 861002

achieved by a spray hole distance of h_{min}+0.15 mm and h_{min}+0.2 mm. Also the single hole nozzle is penetrating the slowest in all cases. For the spray angle it seems that the widest spray angles are achieved by a spray hole distance of h_{min}+0.05 mm and the single hole nozzle. The spray area behaves in accordance with the penetration. This is in accordance with the observations from Figure 4.23 and Figure 4.24.

This project has received funding from the European Union Horizon 2020 Research and Innovation programme. Grant Agreement No 861002

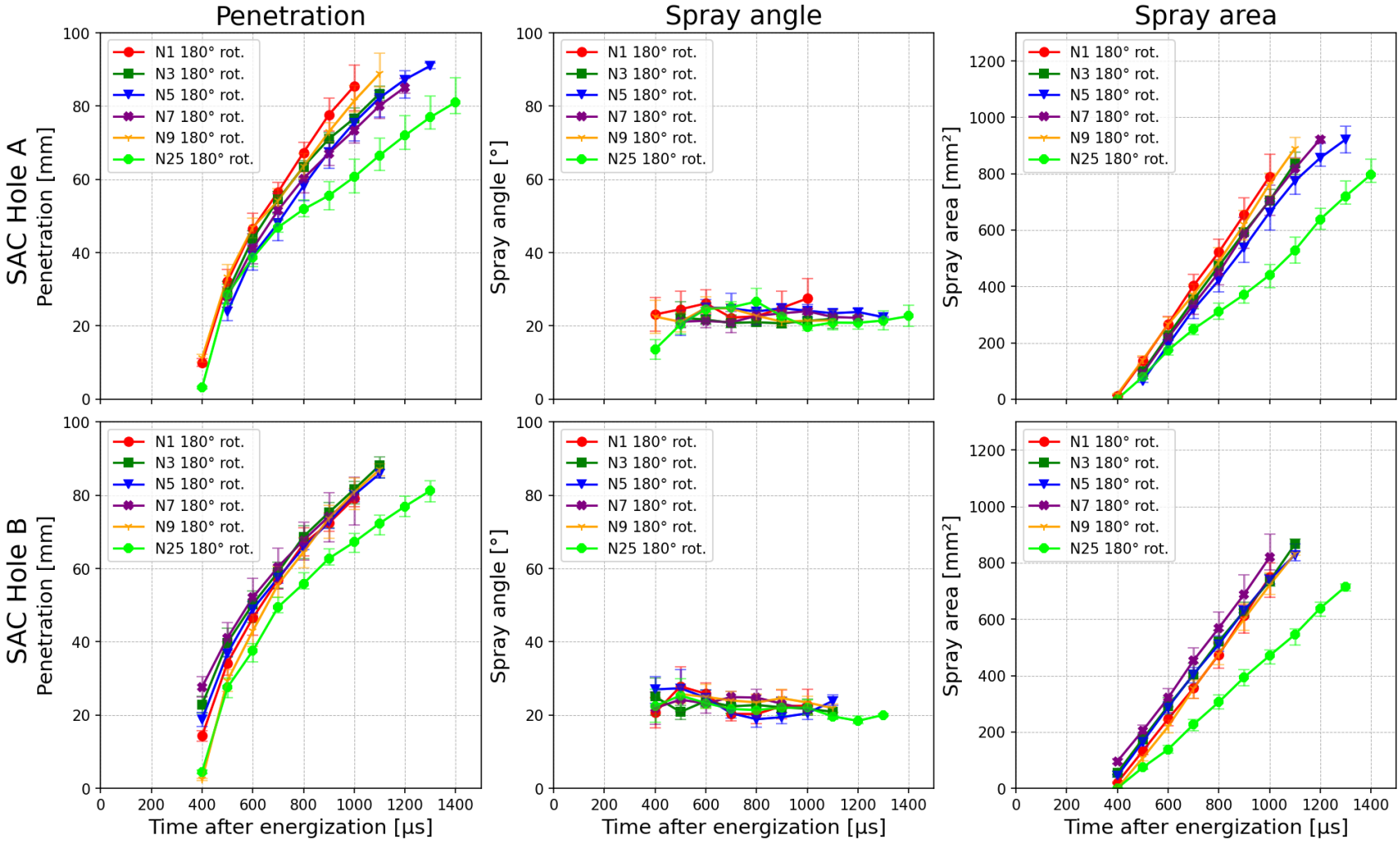


Figure 4.25: Influence of the relative spray hole distance on the spray characteristics penetration, spray angle and spray area for nozzles N1, N3, N5, N7, N9 and N25 in 180° rotated orientation with 300 µs energization duration at 2200 bar

This project has received funding from the European Union Horizon 2020 Research and Innovation programme. Grant Agreement No 861002

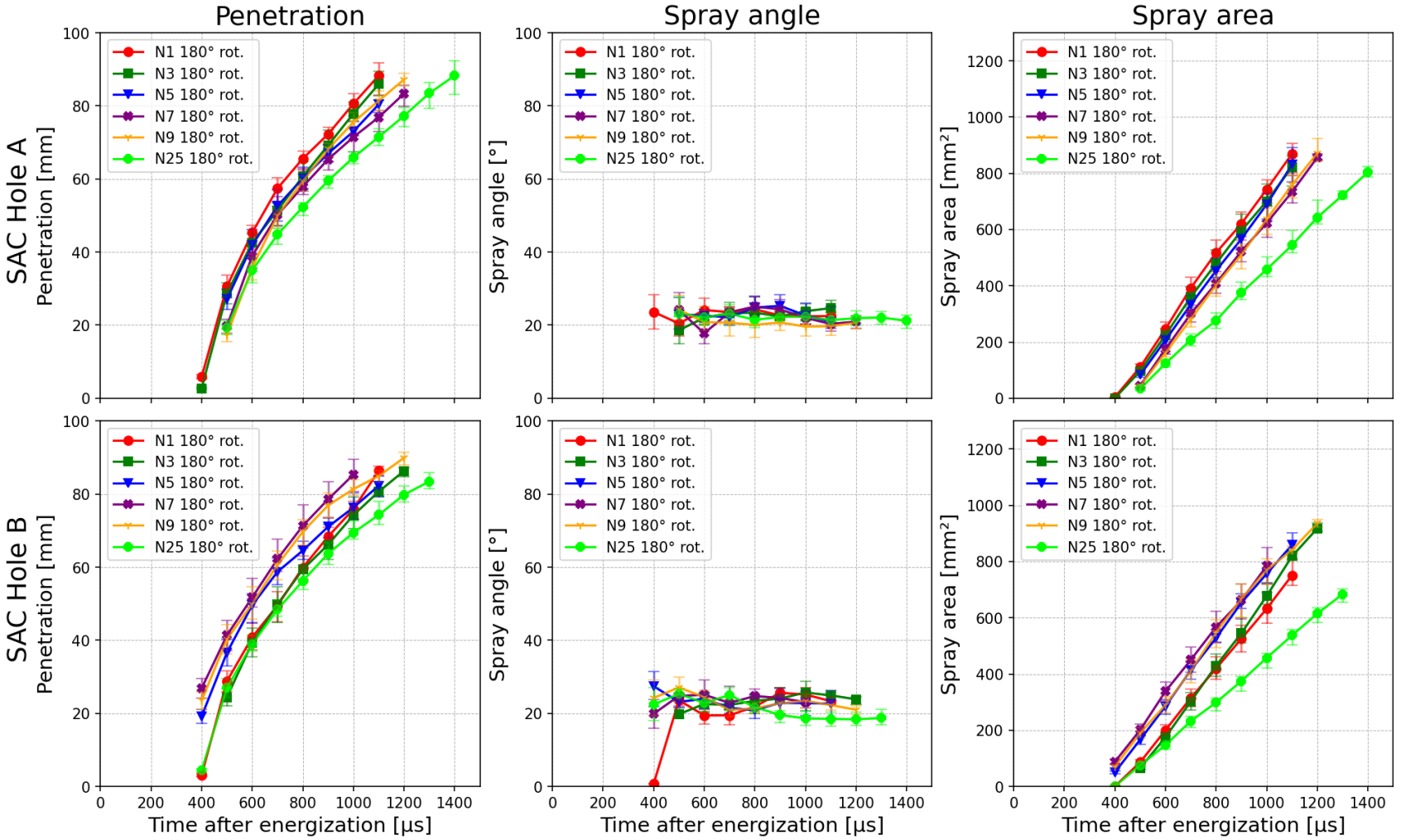


Figure 4.26: Influence of the relative spray hole distance on the spray characteristics penetration, spray angle and spray area for nozzles N1, N3, N5, N7, N9 and N25 in 180° rotated orientation with 1000 µs energization duration at 2200 bar

This project has received funding from the European Union Horizon 2020 Research and Innovation programme. Grant Agreement No 861002

In order to ensure, that the observed behaviours of the injections are not influenced by the spray hole diameter, the nozzles N12, N14, N16 and N18 as well as the comparison nozzle N26 are compared, too. All the nozzles have a spray hole diameter of d_{min}+ 0.05 mm and vary in the spray hole distance, with N12 having a spray hole distance of h_{min}, N14 has a distance of h_{min}+ 0.05 mm, N16 has h_{min}+ 0.1 mm and N18 has h_{min}+ 0.15 mm. The injections for these in standard orientation with 1400 bar are shown in Figure 4.27 and Figure 4.28. It can be observed, that for the energization duration of 300 µs the penetration for the nozzles manufactured with SAC hole A is grouped in 3 different sets. The fastest penetrating injections are from N16 (d=$d_{min} + 0.05$, h=$h_{min} + 0.1$, $\beta = 2$) and N26 (d=$d_{min} + 0.125$), which reach a maximum penetration distance of 61 & 63 mm, followed by N14 (d=$d_{min} + 0.05$, h=$h_{min} + 0.05$, $\beta = 2$) and N18 (d=$d_{min} + 0.05$, h=$h_{min} + 0.15$, $\beta = 2$) and then N12 (d=$d_{min} + 0.05$, h=h_{min}, $\beta = 2$). For SAC hole B the penetration curves are more clustered with the most rapid ones from N26, which crosses 80 mm after 1134 µs, then N14, N16, N18 and further apart N18. The spray angle for SAC hole A shows that the injection curves are widely spread, with the widest angle from N18 of 27.4°, then N16, N26, N14 and N12. For SAC hole B it can be observed, that at the beginning of the injections the spray angle is rapidly expanding, with the widest from N14 and N16 at 600 µs reaching an angle of 37°. Towards the end of the injections, all angles are around 25° except N16 at 16.2°. The spray area of the injections with the nozzles with SAC hole A behaves similar to the penetrations, with the fastest area expansion from N26 and N16 with areas of 408 & 390 mm^2, followed by N18 and N14 and N12 nearly not reaching any area at all. For SAC hole B the spray area expansion is less clustered than the penetration curves, with three groups distinguishable, the fastest expanding injections are from N26 and N14 with final areas of 856 & 786 mm^2, followed by N16 and N12 and then N18. For the energization duration of 1000 µs it is visible that the penetration from the injections with SAC hole A are similarly behaving, only N16 and N14 start injecting faster, towards the end all of them reach a similar penetration speed, crossing 80 mm distance after 1125 – 1168 µs. For SAC hole B the penetration behaviour is similar but the curves flatten faster than with SAC hole A and in this case only N12 starts injecting later, the cases reach a penetration distance of 80 mm between 1074 – 1137 µs. The spray angles for SAC hole A are diverged again, with the widest angle from N14 of 32.2°, then N18, N16, N12 and N26. For SAC hole B the beginning of the injections is more clustered, compared to 300 µs in the beginning and towards the end of the injections it can be observed that N16 reaches the widest angle of 31.6°. The spray areas are expanding more linear compared to the energization duration of 300 µs for both SAC holes. For SAC hole A it can be observed, that N14 and N16 expand

This project has received funding from the European Union Horizon 2020 Research and Innovation programme. Grant Agreement No 861002

their area the fastest, reaching an area of 1034 & 1041 mm^2, followed by N12 and N18 and then N26. For SAC hole B the spray area curves are more similar with the fastest area increase from N16 with an area of 1182 mm^2, then N18, N14, N26 and N12. In all cases it can be observed that the fastest penetration is achieved by the single hole nozzle, followed by the TWIN nozzle with a distance of h_{min}+ 0.05 mm for SAC hole A and with h_{min}+ 0.1 mm for SAC hole B. The initial widest spray angle is achieved by the spray hole distance of h_{min}+ 0.1 mm for all cases but towards the end of the injection the widest angle is from h_{min}+ 0.15 mm except for SAC hole B with 1000 µs energization duration. For 300 µs energization duration, the spray area behaves similar to the penetration. For 1000 µs it expands fastest for a spray hole distance of h_{min}+ 0.1mm in contrary to the penetration.

This project has received funding from the European Union Horizon 2020 Research and Innovation programme. Grant Agreement No 861002

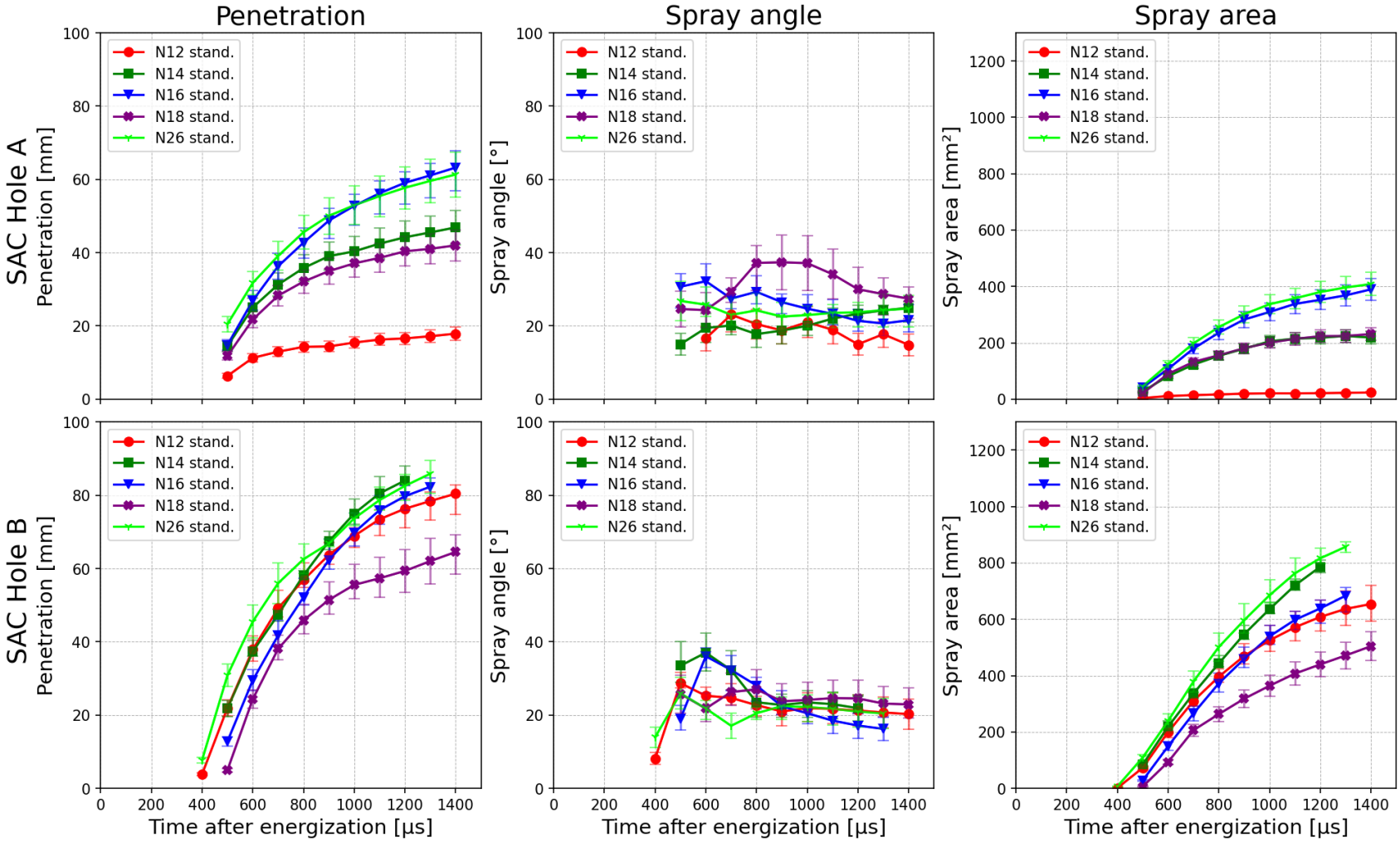


Figure 4.27: Influence of the relative spray hole distance on the spray characteristics penetration, spray angle and spray area for nozzles N12, N14, N16, N18 and N26 in standard orientation with 300 µs energization duration at 1400 bar

This project has received funding from the European Union Horizon 2020 Research and Innovation programme. Grant Agreement No 861002

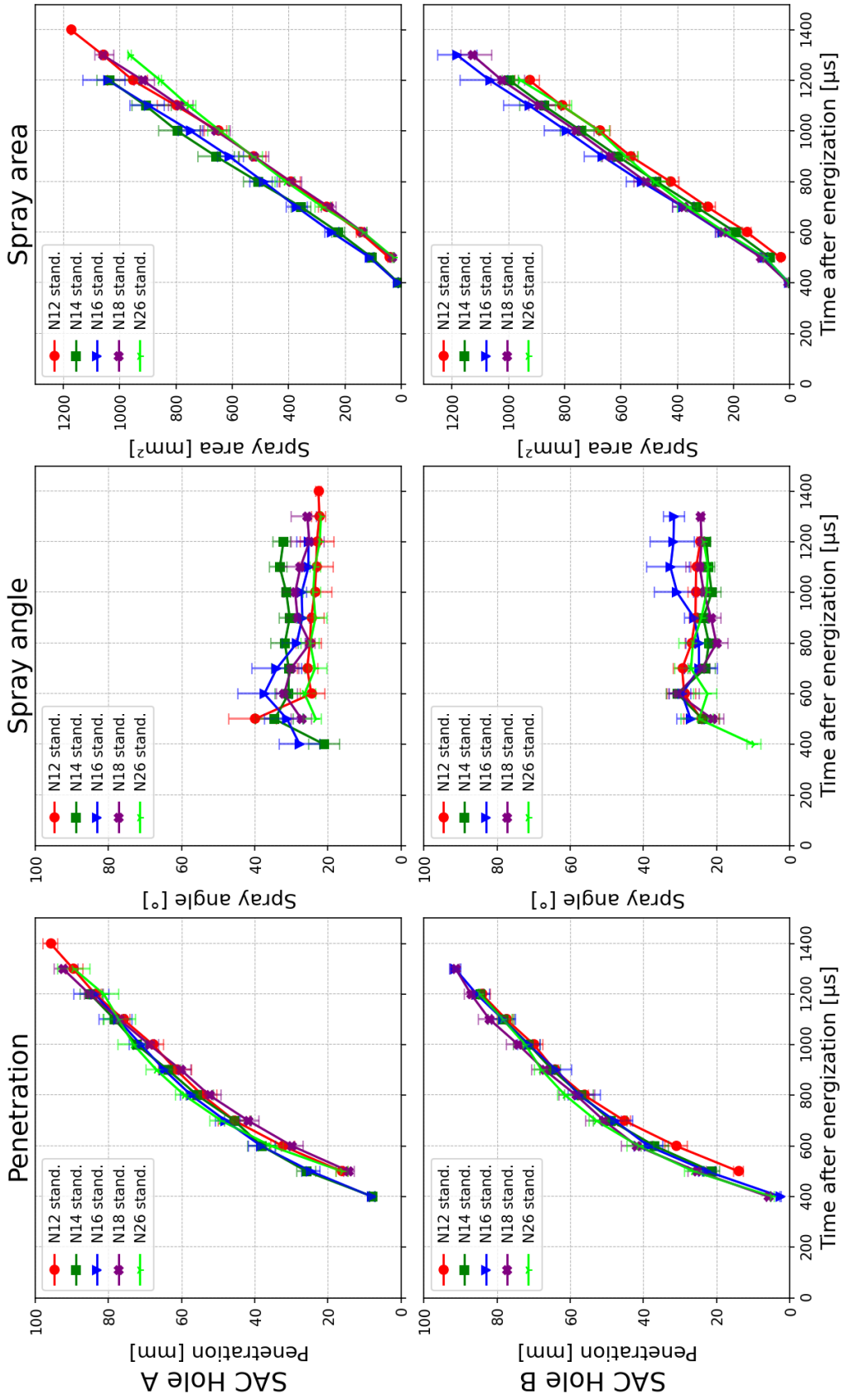


Figure 4.28: Influence of the relative spray hole distance on the spray characteristics penetration, spray angle and spray area for nozzles N12, N14, N16, N18 and N26 in standard orientation with 1000 µs energization duration at 1400 bar

This project has received funding from the European Union Horizon 2020 Research and Innovation programme. Grant Agreement No 861002

The same nozzles were also compared in their 180° rotated orientation, to ensure that the observations are not influenced by other parameters, these are shown in Figure 4.29 and Figure 4.30. For the energization duration of 300 µs it can be observed that the penetration curves for SAC hole A behave in accordance with the observations from Figure 4.27, with N16 (d=$d_{min}+0.05$, h=$h_{min}+0.1$, $\beta = 5$) and N26 (d=$d_{min}+0.125$) penetrating the fastest, with maximum penetration distances of 60 and 63 mm, followed by N14 (d=$d_{min}+0.05$, h=$h_{min}+0.05$, $\beta = 5$) and N18 (d=$d_{min}+0.05$, h=$h_{min}+0.15$, $\beta = 5$) and then N12 (d=$d_{min}+0.05$, h=h_{min}, $\beta = 5$). For SAC hole B the penetration curves are also similar to the relative angle of –3°, but the second group is more secluded, with the fastest penetration from N26 and N14, which reach a distance of 80 mm after 1014 & 1032 µs, then N16 and N12 and N18. The spray angle for SAC hole A is spread between 20° and 40° towards the end of the injections, with the widest angle from N18 of 38.3°, then N12, N16, N14 and N26. For SAC hole B the spray angles are closer together between 17° and 22° with the widest angle from N14 and N16 of 21.2 & 22.1°, then N12, N18 and N26. The spray area behaves similar to the penetration curves and in accordance with the standard orientation injections. For SAC hole A the fastest area increases are from N16 and N26 with maximum areas of 742 & 885 mm^2, followed by N14 and N18 and then N12. For SAC hole B the fastest expanding area is from N12 with an area of 955 mm^2, then N26, then N16, N12 and N18. For the energization duration of 1000 µs the penetration for SAC hole A behave similar to standard orientation with N16 and N26 starting the injection the fastest, reaching a distance of 80mm after 1062 & 1089 µs. For SAC hole B it is also similar to the standard orientation with N26, N18 and N16 starting the injection the fastest, achieving a 80 mm penetration distance after 998 – 1059 µs. The spray angles of the injections with SAC hole A are more tightly clustered than with standard orientation and only spike at around 500 - 700 µs with a widest angle of 33.2°. For SAC hole B the spray angles are also more tightly clustered around 25°. The spray areas for the injections with SAC hole A are grouped, with the fastest increase from N16 and N14 with areas of 892 & 1035 mm^2, and then N26, N12 and N18. For the SAC hole B the spray area curves are similar for all cases and in accordance with the injections with standard orientations, with N16 reaching an area of 932 mm^2. From the comparison of Figure 4.27, Figure 4.28, Figure 4.29 and Figure 4.30 it can be observed that the change of the relative angle seems to only significantly influence the spray angle. This is in accordance with the observations from Figure 4.27 and Figure 4.28.

This project has received funding from the European Union Horizon 2020 Research and Innovation programme. Grant Agreement No 861002

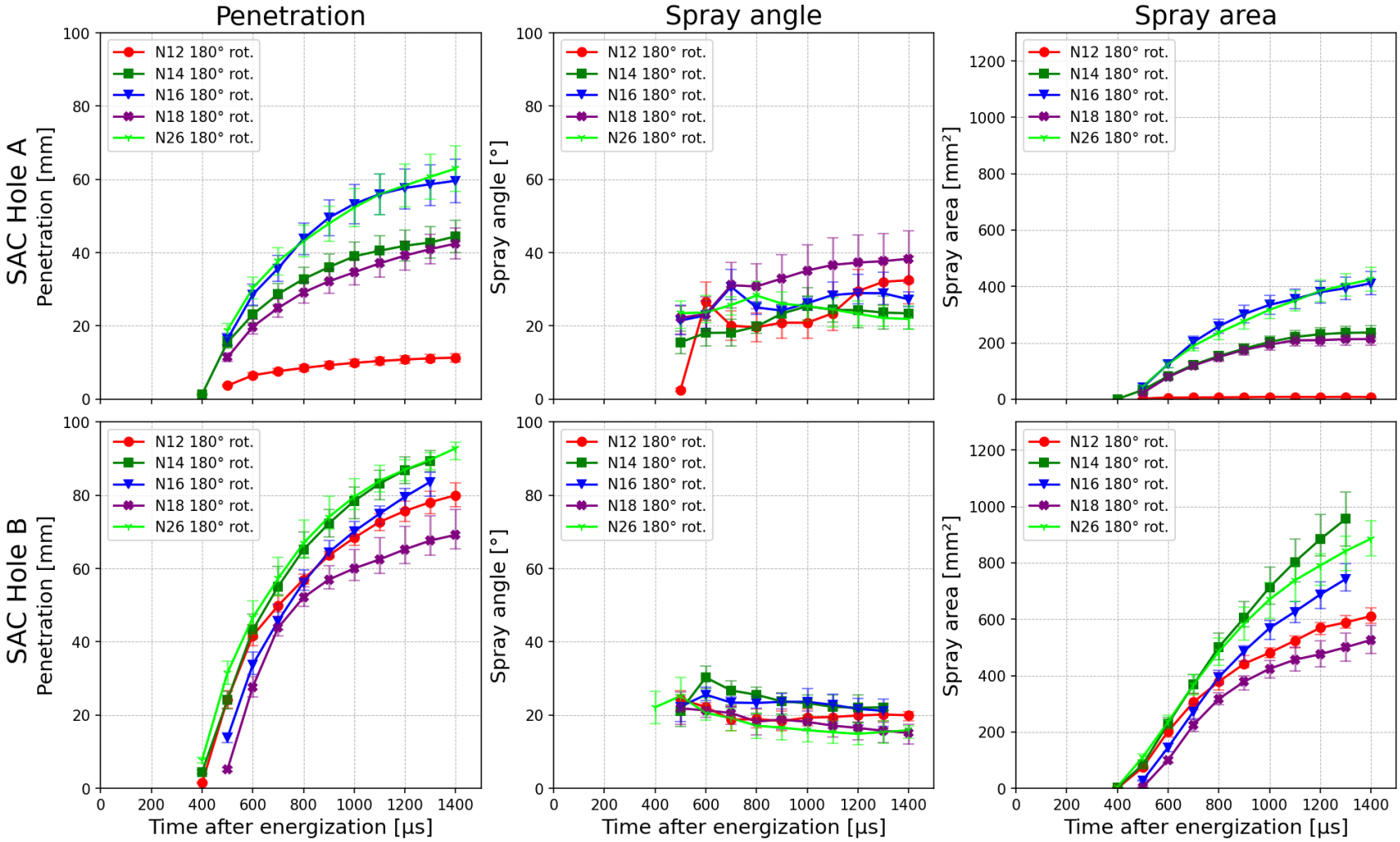


Figure 4.29: Influence of the relative spray hole distance on the spray characteristics penetration, spray angle and spray area for nozzles N12, N14, N16, N18 and N26 in 180° rotated orientation with 300 µs energization duration at 1400 bar

This project has received funding from the European Union Horizon 2020 Research and Innovation programme. Grant Agreement No 861002

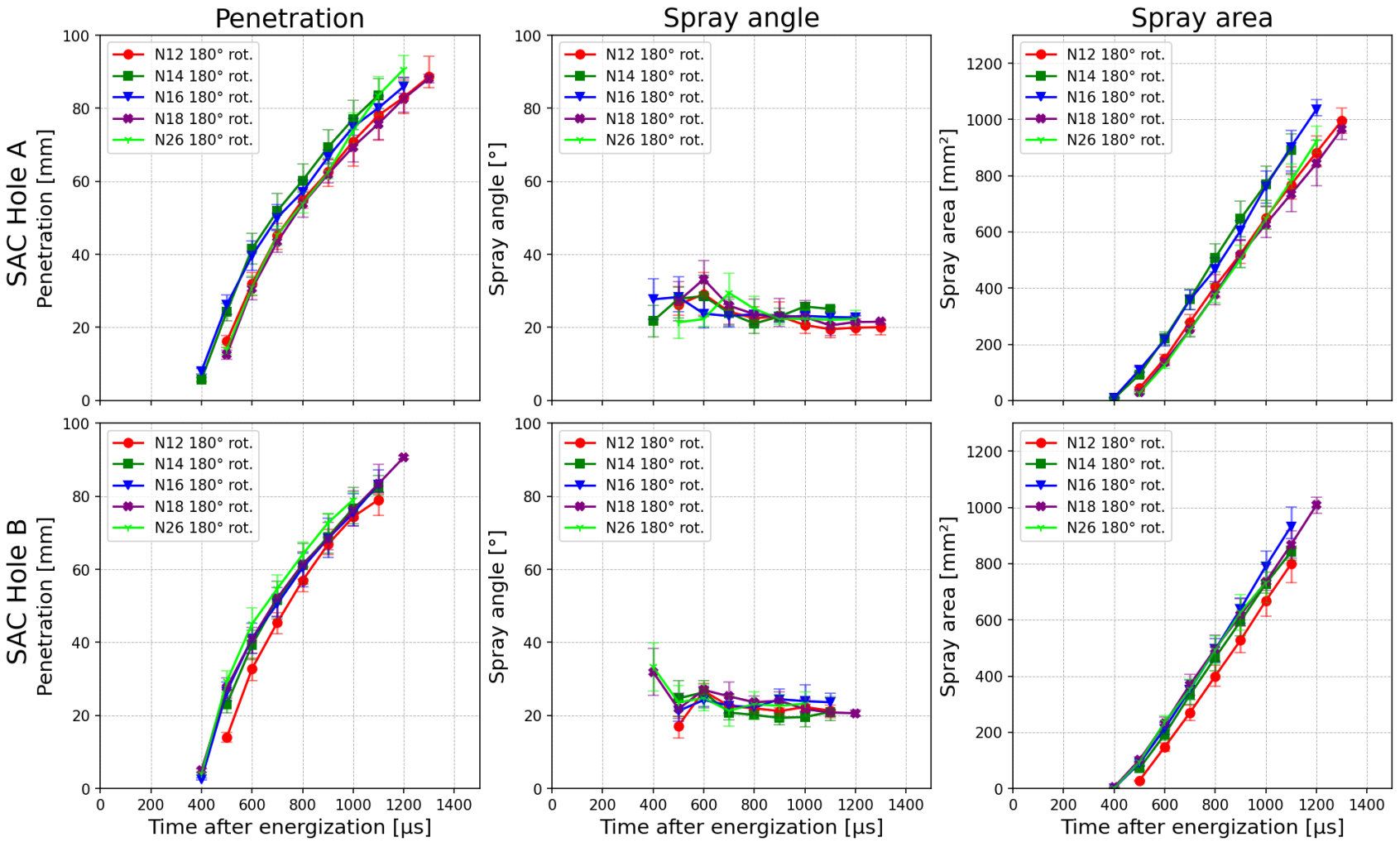


Figure 4.30: Influence of the relative spray hole distance on the spray characteristics penetration, spray angle and spray area for nozzles N12, N14, N16, N18 and N26 in 180° rotated orientation with 1000 µs energization duration at 1400 bar

This project has received funding from the European Union Horizon 2020 Research and Innovation programme. Grant Agreement No 861002

In accordance with Figure 4.27, Figure 4.28, Figure 4.29 and Figure 4.30, the nozzles with spray hole diameter d_{min}+0.05 mm and ranging spray hole distance were also compared for high pressure injections with 2200 bar. The injections for the standard orientation are shown in Figure 4.31 and Figure 4.32. For the energization duration of 300 µs it can be observed, that for SAC hole A the fastest penetration is from N26 (d=$d_{\min} + 0.125$), which achieves a penetration distance of 80 mm at 943 µs after energization and then with some distance are all TWIN nozzle injections grouped, with only N18 (d=$d_{\min} + 0.05$, h=$h_{\min} + 0.15$, $\beta = 2$) penetrating slower towards the end of the injection. For SAC hole B all injections are closely grouped, only at the beginning the nozzles N18 and N26 inject faster, followed by N12. The nozzle N26 achieves as first a distance of 80 mm after 897 µs. The spray angles for SAC hole A are spiking at the beginning of the injection with a peak angle from N18 of 39° and start to flatten towards the end, with the widest angle from N16 of 36.1°, then N14, N12, N18 and N26. For SAC hole B the spray angle from the injection with N18 spikes in the beginning of the injection, too, with the widest angle of 32.6° from N26. Towards the end of the injection, the widest angle is from N16 of 23.6, then N12, N14, N26 and N18. The spray area is expanding quite linear for all injections with SAC hole A but diverge towards the end, with the fastest area expansion from N12 with an area of 1174 mm^2, N16, N26, N14 and N18. For SAC hole B the injections also diverge toward the end, with the fastest area increase from N14 with 980 mm^2, then N12, N18, N26 and N16. For the energization duration of 1000 µs it can be observed that the penetration curves for the injections with SAC hole A are separated with N12 and N16 injecting faster, crossing the penetration distance of 80 mm after 909 & 920 µs and towards the end all injections reach the same penetration velocity, except N18. For SAC hole B the only injection that is not penetrating with a similar curve compared to the rest is N16, which injects faster, reaching a distance of 80 mm after 860 µs. The spray angles for SAC hole A are divided, with the widest angle toward the end from N18 of 36.9°, then N16, N12, N14 and N26. For SAC hole B all spray angles spike around 600 µs with a peak from N18 with 29° and towards the end of the injection the widest angle is from N26 of 30.5°. For the spray area all injections with SAC hole A are increasing nearly linearly, with N12 and N16 starting faster then the other injections, with final areas of 1015 & 966 mm^2. For SAC hole B the fastest area expansion as well as start is from N16, in accordance with the penetration curve, reaching an area of 1065 mm^2.

This project has received funding from the European Union Horizon 2020 Research and Innovation programme. Grant Agreement No 861002

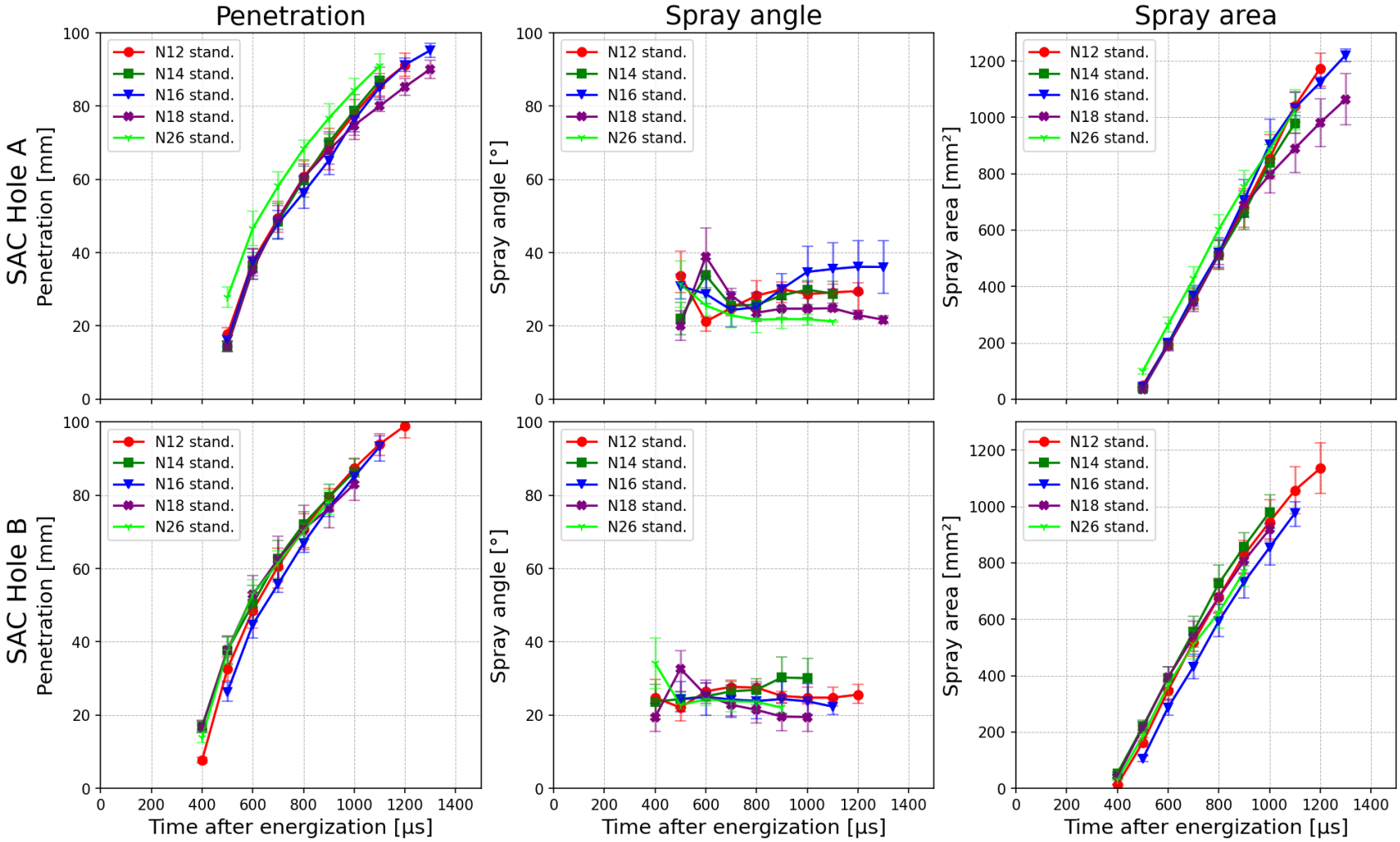


Figure 4.31: Influence of the relative spray hole distance on the spray characteristics penetration, spray angle and spray area for nozzles N12, N14, N16, N18 and N26 in standard orientation with 300 µs energization duration at 2200 bar

This project has received funding from the European Union Horizon 2020 Research and Innovation programme. Grant Agreement No 861002

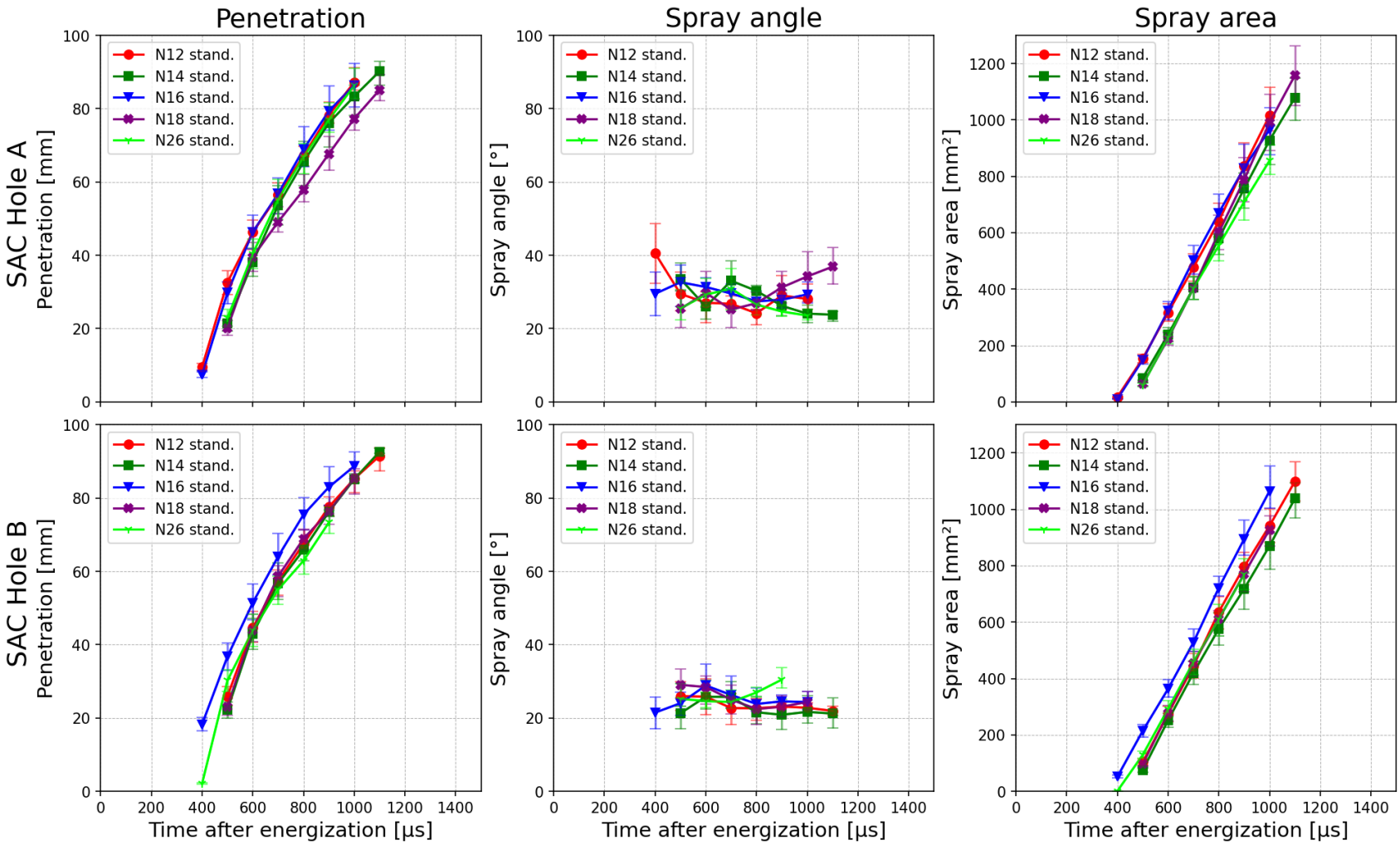


Figure 4.32: Influence of the relative spray hole distance on the spray characteristics penetration, spray angle and spray area for nozzles N12, N14, N16, N18 and N26 in standard orientation with 1000 µs energization duration at 2200 bar

This project has received funding from the European Union Horizon 2020 Research and Innovation programme. Grant Agreement No 861002

In order to check whether the observed behaviours from Figure 4.31 and Figure 4.32 are influnced by the relative spray angle, the same nozzles were compared in 180° rotated orientation, meaning a relative angle of 0°, as shown in Figure 4.33 and Figure 4.34. For the energization duration of 300 µs the fastest penetration is from N26 (d=$d_{\min} + 0.125$), which achieves the penetration distance of 80 mm after 790 µs, then the TWIN nozzles, which are closely clustered, this is a similar behaviour to the standard orientation injections. For SAC hole B the injections are more diverged than with standard orientation, with the fastest penetration from N14, which reaches 80 mm at 822 µs, N18 and N26. The spray angles for SAC hole A are different from the injections with standard orientation with the widest angle from N18 and N12 of 33 & 29.9°. For SAC hole B the angles are mostly diverge in the beginning of the injection and flatten afterwards, with the widest angle at the end from N16 of 27.8 °. The spray area is expanding linearly for SAC hole A, but they differ from the standard orientation injections towards the end since they stay grouped, with the maximum area from N12 at 1276 mm^2. For SAC hole B the spray areas are grouped with N14 and N18 increasing the fastest, with final areas of 862 & 904 mm^2, also differing from the injections with standard orientation. For the energization duration of 1000 µs the penetration curves of the injections with both SAC holes are similar to the standard orientations. For SAC A the fastest injection to cross 80 mm distance is from N12 at 894 µs. For SAC hole B it is from N16 at 823 µs. The spray angles for SAC hole A behave different than the ones with a relative angle of –3°, with the widest angle from N14 and N18 of 24.8 & 25.2°. For SAC hole B the spray angle curves are less clustered towards the end, with the widest angle from N12, N18 and N26 of 25.8 – 26.8°. For the spray area with SAC hole A the graphs are grouped in two sets, in opposite to the standard orientation injections, with N16 and N12 increasing the fastest with a final area of 838 mm^2. For SAC hole B the spray area behaves more similar to the standard orientation injections, with the widest area from N18 of 1029 mm^2.

This project has received funding from the European Union Horizon 2020 Research and Innovation programme. Grant Agreement No 861002

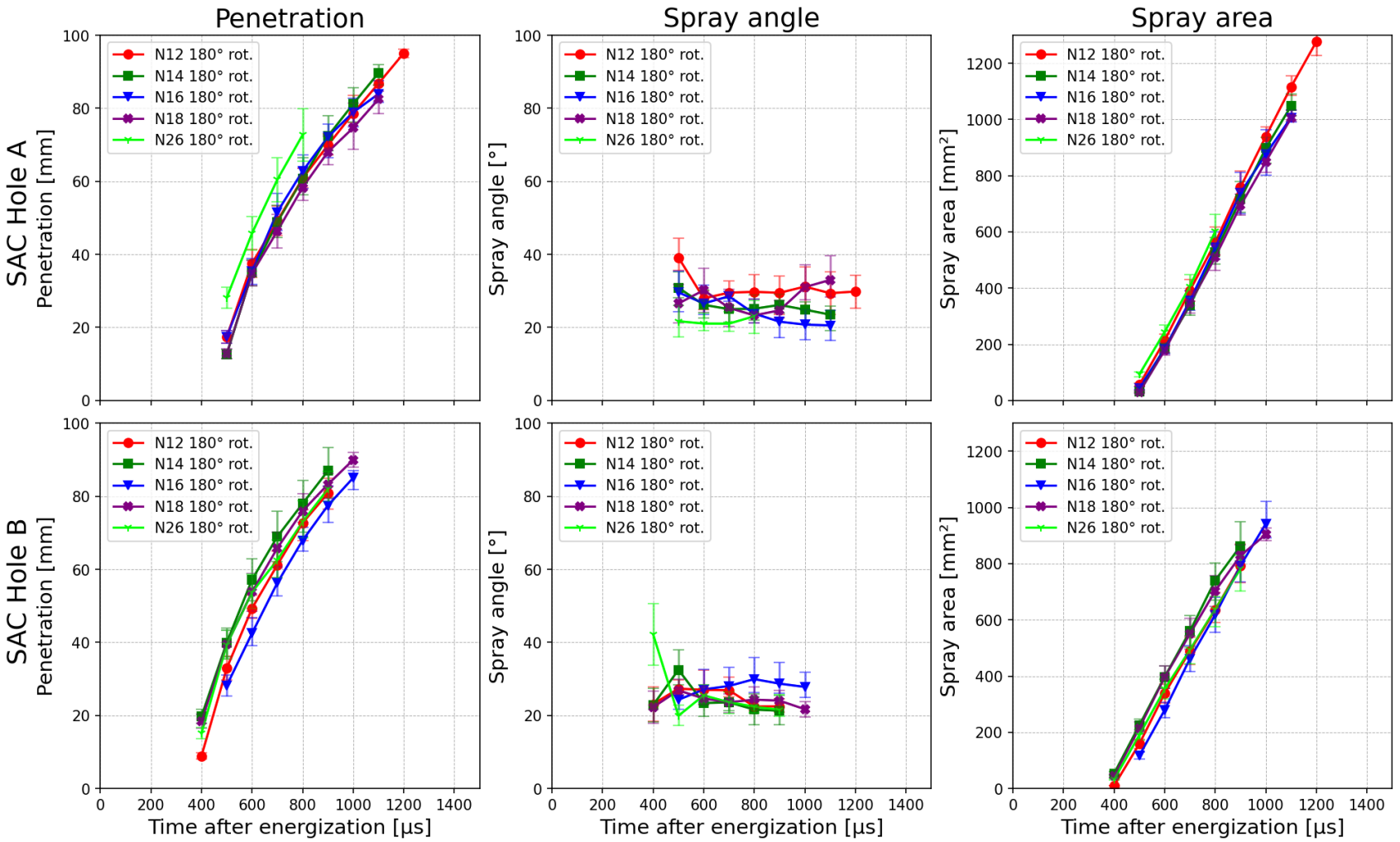


Figure 4.33: Influence of the relative spray hole distance on the spray characteristics penetration, spray angle and spray area for nozzles N12, N14, N16, N18 and N26 in 180° rotated orientation with 300 µs energization duration at 2200 bar

This project has received funding from the European Union Horizon 2020 Research and Innovation programme. Grant Agreement No 861002

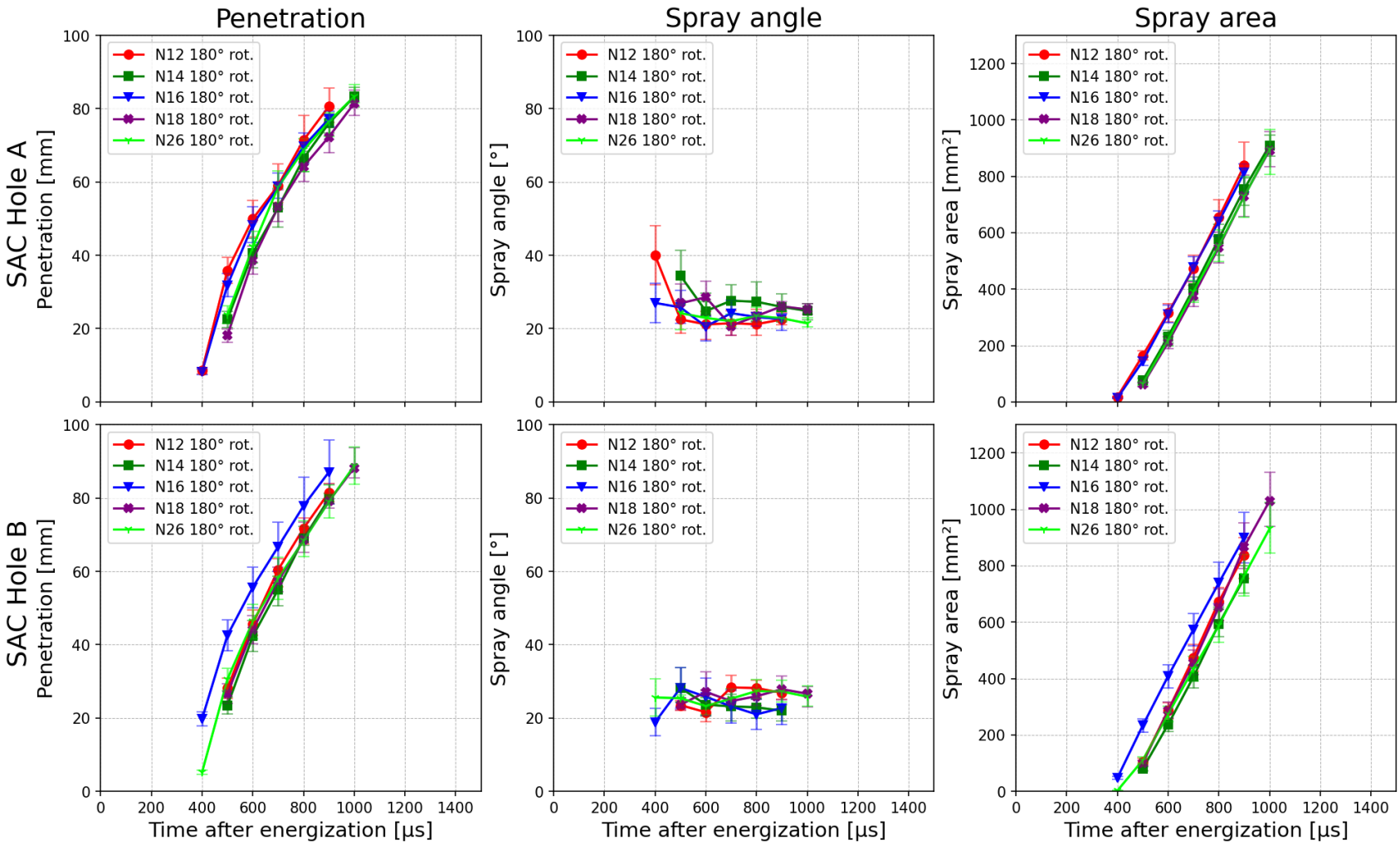


Figure 4.34: Influence of the relative spray hole distance on the spray characteristics penetration, spray angle and spray area for nozzles N12, N14, N16, N18 and N26 in 180° rotated orientation with 1000 µs energization duration at 2200 bar

This project has received funding from the European Union Horizon 2020 Research and Innovation programme. Grant Agreement No 861002

When comparing Figure 4.19 – Figure 4.34 in order to observe the influence of the distance and angle between the two spray holes, it can be noticed, that there is no universal optimum but for some different nozzles a pattern was recognizable. For the nozzles manufactured with SAC hole A , spray hole diameter d_{min}, with both relative spray angles and 1400 bar injection pressure, the fastest penetration was from the nozzle with the distance h_{min}. Whereas for SAC hole B in the same conditions it was from the nozzle with a distance of h_{min}+0.1 mm. Whereas the same nozzles with 2200 bar injection pressure resulted in the fastest penetration for SAC A with the distance h_{min} again, but for SAC hole B there was no consistent pattern visible anymore. For the nozzles with diameter d_{min}+0.5mm the fastest penetration for SAC A for 1400 bar is from h_{min}+ 0.1 mm since some injections do not reach the observable maximum due to the short energization duration. For SAC hole B there is no pattern visible. For 2200 bar there is no consistent pattern observable. At lower injection pressures the lower jet momentum makes the spray more sensitive to jet-jet interaction effects from variations in the spray hole distance and relative spray hole angle. With increasing injection pressure, the sprays become increasingly momentum dominated, reducing the relative importance of plume interactions and causing injection pressure and spray hole diameter to govern the spray development.

After the spray hole distance, the influence of the spray hole diameter is investigated. For this the nozzles N1, with a diameter of d_{min}, N11, with a diameter of d_{min}+0.05 mm, N19, with a diameter of d_{min}+0.1 mm, and N23, with a diameter of d_{min}+0.125 mm, were chosen to be investigated, as well as the two comparison nozzles N26 and N27. The spray characteristics of the injections from these nozzles for 1400 bar injection pressure and in standard orientation, meaning a relative angle of –3°, are shown in Figure 4.35 and Figure 4.36. For the energization duration of 300 µs it can be observed, that the fastest penetration for the nozzles manufactured with SAC hole A is from N1 (d=$d_{\min}$, h=$h_{\min}$, $\beta = -3$), which reaches a penetration distance of 80 mm after 1276 µs, followed by N26 (d=$d_{\min} + 0.125$), then N27 (d=$d_{\min} + 0.239$) and N19 (d=$d_{\min} + 0.1$, h=$h_{\min}$, $\beta = -3$), N11 (d=$d_{\min} + 0.05$, h=$h_{\min}$, $\beta = -3$) and N23 (d=$d_{\min} + 0.125$, h=$h_{\min}$, $\beta = -3$). For SAC hole B the fastest penetration is from N26, which achieves a distance of 80 mm after 1134 µs, followed by N11, N19, N23 and N27. The spray angles for SAC hole A are diverged between 17.5° – 35.2°. The widest angles towards the end of the injection are achieved by N19 and N23, with 34.4° and 24.9°. For SAC hole B the spray angles are widely divided in the beginning of the injection with N27 reaching an angle of 42.1°, but towards the end of the injection the all reach an angle of around 21°. The spray area for the injections with SAC hole A is expanding nearly linear for N1, the other spray area curves flatten out at around 800 µs

This project has received funding from the European Union Horizon 2020 Research and Innovation programme. Grant Agreement No 861002

and reach low areas of 408 mm^2 and below. For SAC hole B all injections start to flatten towards the end of the injection, with N26 expanding the fastest, reaching a maximum area of 857 mm^2. For the energization duration of 1000 µs it can be observed, that for SAC hole A the fastest penetration is from N27, which crosses the penetration distance of 80 mm after 1024 µs, then N23, N11, N19, N26 and N1. For SAC hole B it is visible, that the most rapid penetration is from N19, reaching 80 mm of penetration after 915 µs, followed by N23, N27, N11, N26 and N1. The spray angles for SAC hole A are spiking at the beginning of the injection with up to 32.6° from N27 and flatten out at around 25° towards the end of the injection. For SAC hole B the behaviour is similar but the initial divided phase is shorter, with a spike from N27 at also 32°. The spray areas for SAC hole A for all cases expand in a similar velocity except N26 and N1, both of which are visible slower, the maximum areas are from N26 with 964 mm^2 and N27 with 929 mm^2. For SAC hole B it is similar, with also N26 and N1 performing less rapid, but the other injections are also more divided towards the end, too. The maximum area is from N27 with 1223 mm^2

This project has received funding from the European Union Horizon 2020 Research and Innovation programme. Grant Agreement No 861002

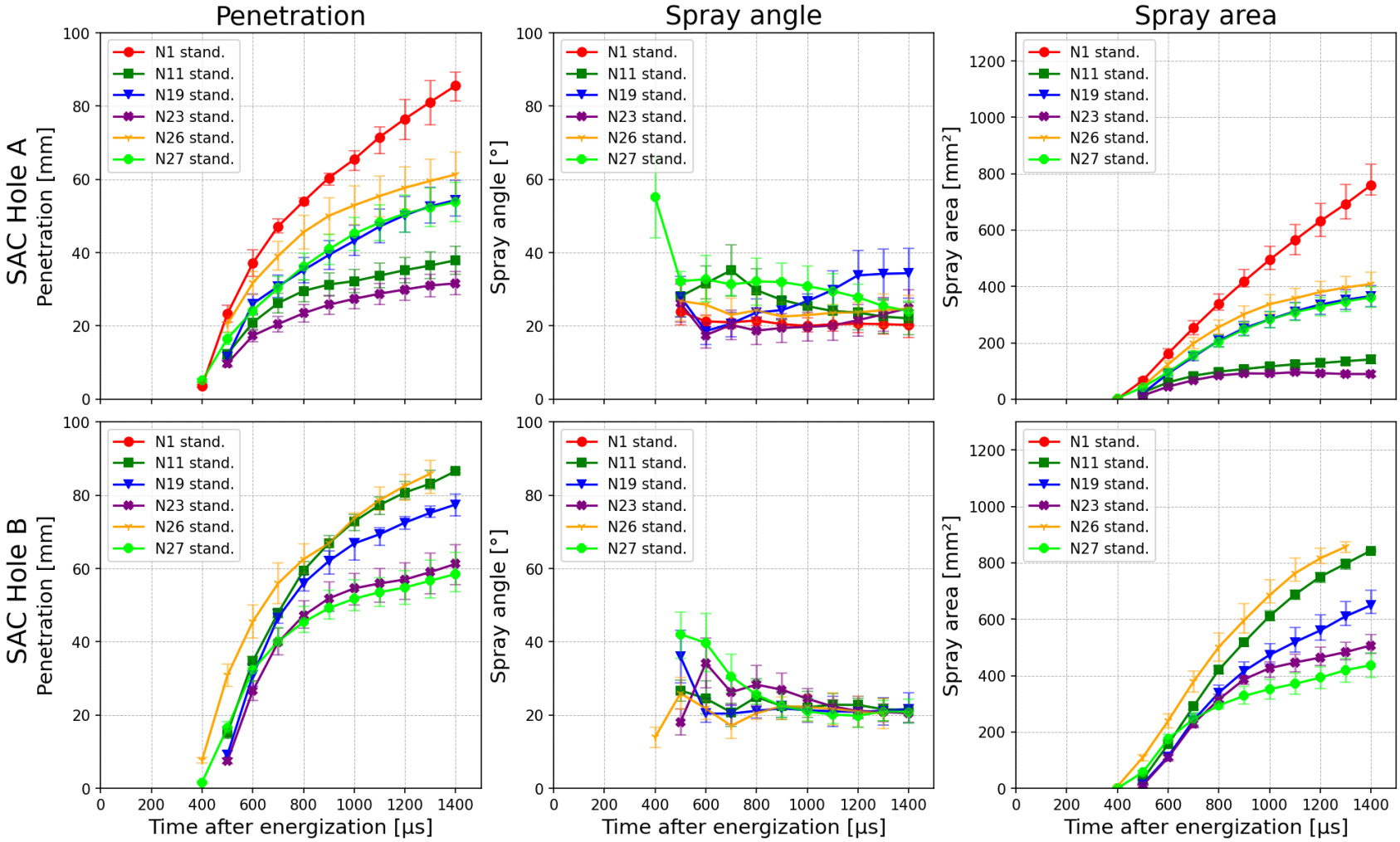


Figure 4.35: Influence of the relative spray hole diameter on the spray characteristics penetration, spray angle and spray area for nozzles N1, N11, N19, N23, N26 and N27 in standard orientation with 300 µs energization duration at 1400 bar

This project has received funding from the European Union Horizon 2020 Research and Innovation programme. Grant Agreement No 861002

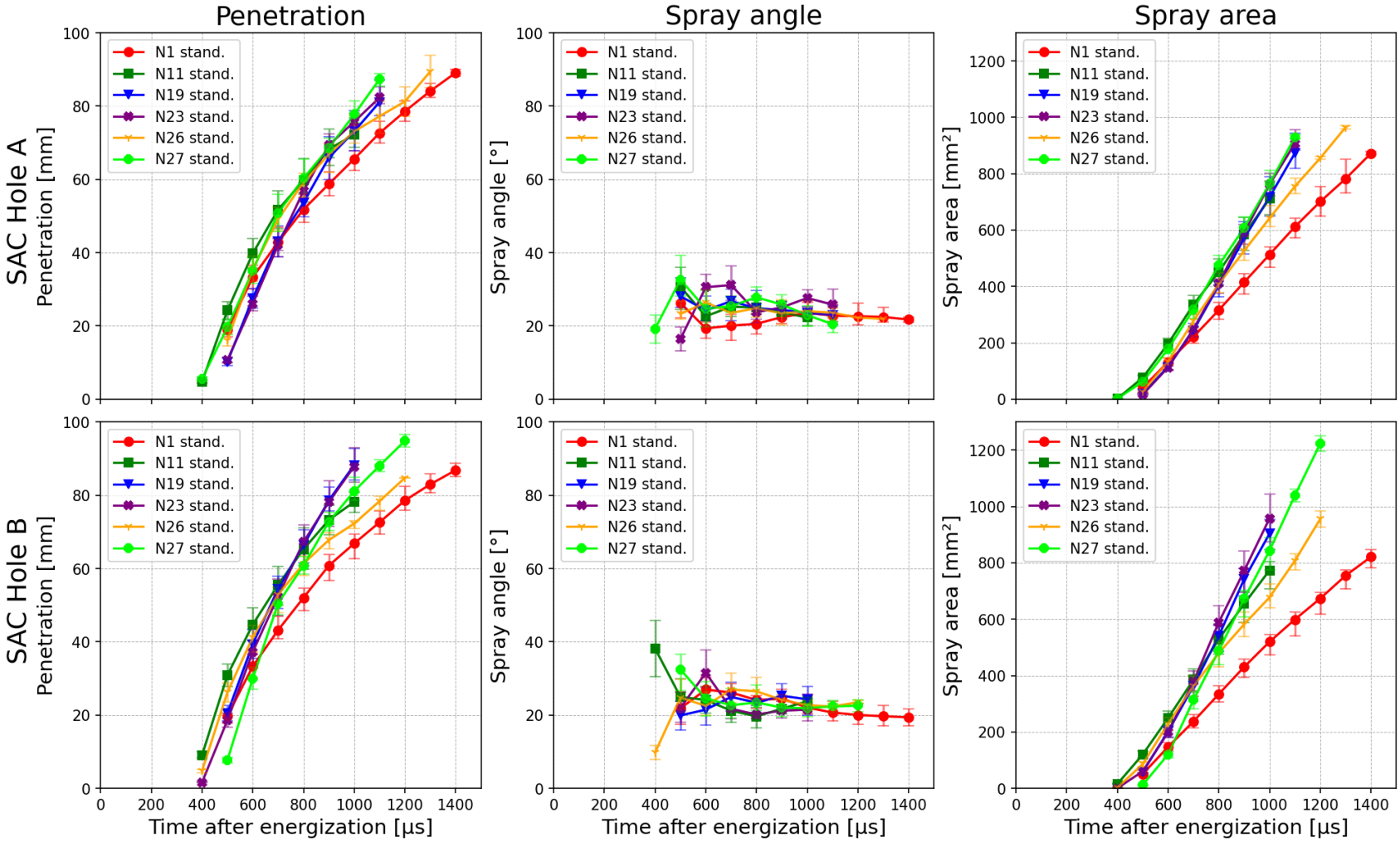


Figure 4.36: Influence of the relative spray hole diameter on the spray characteristics penetration, spray angle and spray area for nozzles N1, N11, N19, N23, N26 and N27 in standard orientation with 1000 µs energization duration at 1400 bar

This project has received funding from the European Union Horizon 2020 Research and Innovation programme. Grant Agreement No 861002

Analog to Figure 4.35 and Figure 4.36 the same nozzles were investigated with a relative angle of 0°, meaning in 180° rotated orientation, as shown in Figure 4.37 and Figure 4.38. For the energization duration of 300 µs it is visible that for SAC hole A the fastest penetration is from N1 (d=d_{min}, h=h_{min}, $\beta = 0$), reaching a penetration of 80 mm after 1163 µs, then N26 (d=$d_{min} + 0.125$), N27 (d=$d_{min} + 0.239$), N19 (d=$d_{min} + 0.1$, h=h_{min}, $\beta = 0$), N11 (d=$d_{min} + 0.05$, h=h_{min}, $\beta = 0$) and N23 (d=$d_{min} + 0.125$, h=h_{min}, $\beta = 0$). This is in accordance with the observations from the standard orientation injections. For SAC hole B is can be observed, that the fastest penetration is from N26, which achieves a penetration distance of 80 mm at 1010 µs after energization, followed by N11, N19, N27 and N23. N1 did not inject in this case. This results are also in accordance with the ones from Figure 4.35. For the spray angle with SAC hole A it is visible, that the curves are divided, with the widest angle from N11 of 37.4°, then N27, N19, N26, N1 and N23. For SAC hole B the spray angle curves are evolving nearly parallel, with the widest angle from N27 of 34.2°, followed by N11, N19, N23 and N26. The spray area from SAC hole A shows, that the area is expanding nearly linearly for N1, with a final area of 748 mm^2, but the other curves flatten out after 800 µs, with areas of 425 mm^2 and below. For SAC hole B it can be observed that all curves are flattening out, even though at a higher area compared to SAC hole A, with the fastest expansion from N26, which reaches a maximum area of 886 mm^2. For the energization duration of 1000 µs it can be noticed, that for SAC hole A, all penetration curves are clustered at the beginning, but diverge towards the end, with N1 penetrating clearly slower than the rest. The fastest injection is from N27, crossing 80 mm after 994 µs. For SAC hole B the penetration is similar, though the curves are less clustered in the beginning. Here N1 also performs slower than the rest, but the fastest penetration is from N23, reaching the distance of 80 mm after 917 µs. The spray angles for SAC A are clustered around 25° with only N27 spiking in the beginning with an angle of 37.3°. For SAC hole B the spray angle curves flatter towards 20° and also only N27 has a wider angle peaking at 28.5°. The spray area of SAC hole A is expanding similar for all cases, but the fastest expansion is from N27, with a maximum area of 1024 mm^2, followed by N19, N23, N11, N26 and further apart N1. For SAC hole B it is visible, that the spray area curves are close together for N19, N23 and N27, with areas of 939 & 905 & 884 mm^2, followed apart by N19 and N26 and further away N1.

This project has received funding from the European Union Horizon 2020 Research and Innovation programme. Grant Agreement No 861002

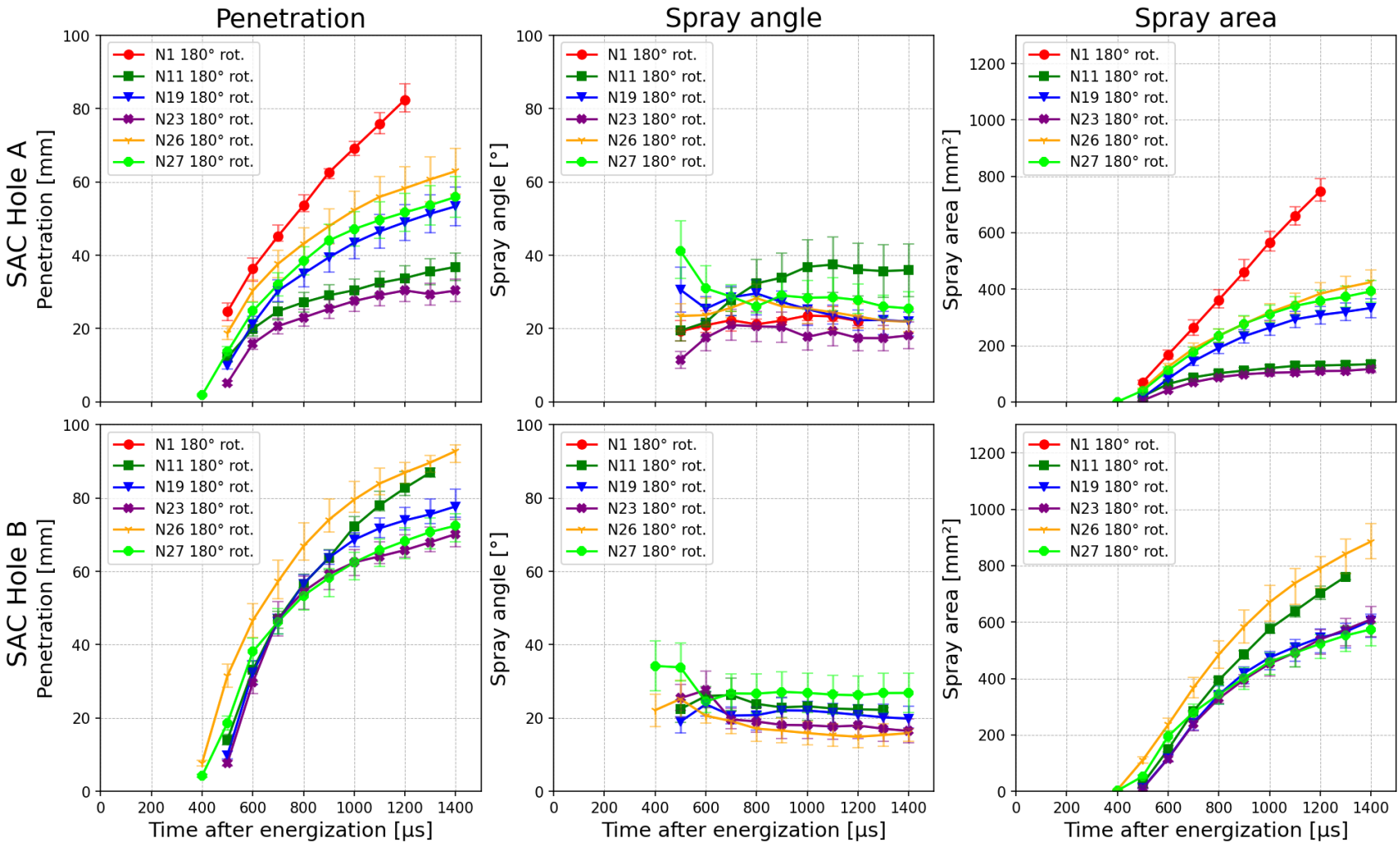


Figure 4.37: Influence of the relative spray hole diameter on the spray characteristics penetration, spray angle and spray area for nozzles N1, N11, N19, N23, N26 and N27 in 180° rotated orientation with 300 µs energization duration at 1400 bar

This project has received funding from the European Union Horizon 2020 Research and Innovation programme. Grant Agreement No 861002

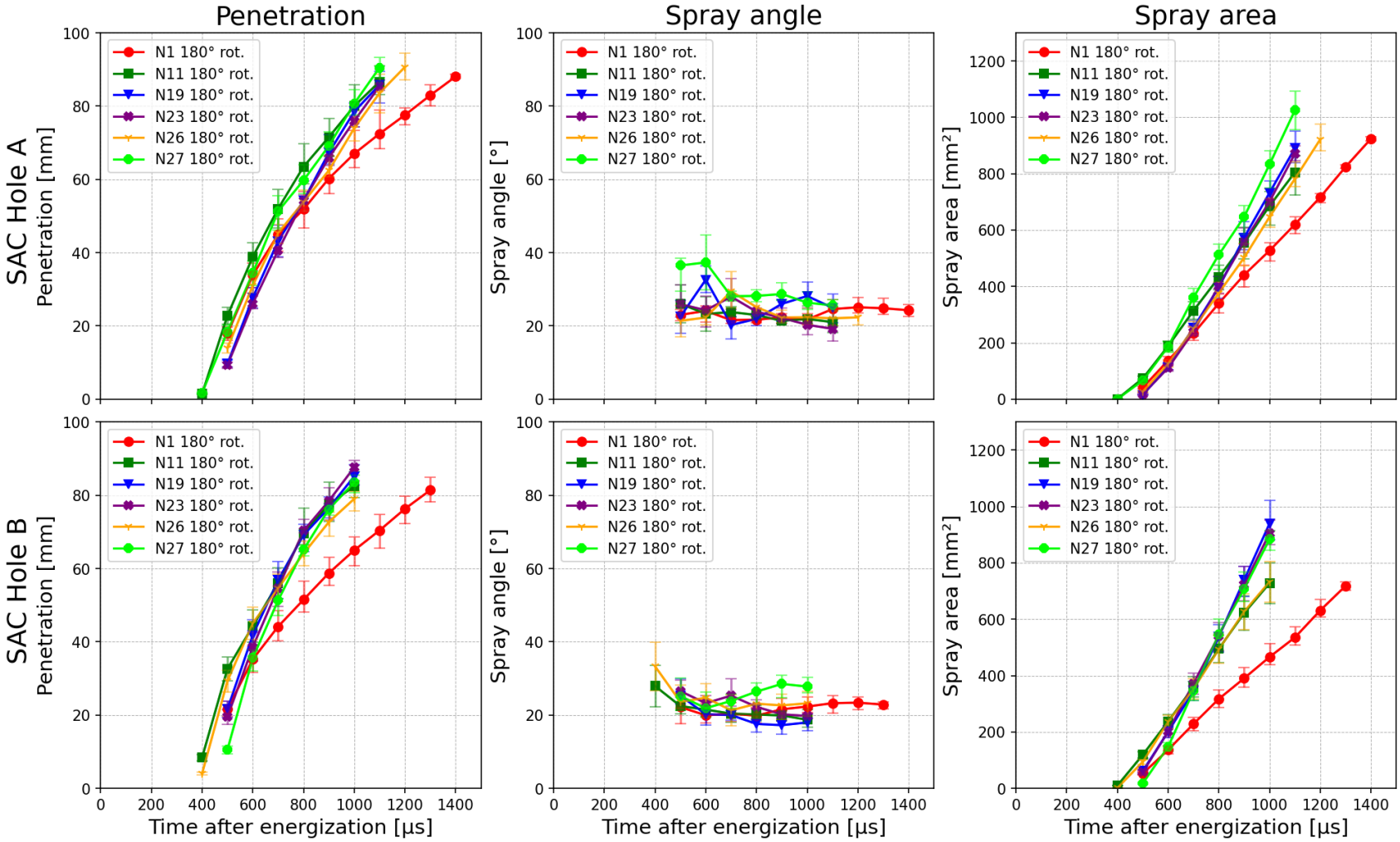


Figure 4.38: Influence of the relative spray hole diameter on the spray characteristics penetration, spray angle and spray area for nozzles N1, N11, N19, N23, N26 and N27 in 180° rotated orientation with 1000 µs energization duration at 1400 bar

This project has received funding from the European Union Horizon 2020 Research and Innovation programme. Grant Agreement No 861002

In accordance to the previous Figures, the influence of the spray hole diameter was also compared for injections with 2200 bar pressure. The spray characteristics for the injections with a relative angle of –3° are shown in Figure 4.39 and Figure 4.40. For the energization duration of 300 µs it is noticeable, that the penetration for SAC hole A is fastest from the injection with nozzle N19 (d=$d_{min} + 0.1$, h=h_{min}, $\beta = -3$), crossing the penetration distance of 80 mm after 891 µs, followed by N26 (d=$d_{min} + 0.125$), N23 (d=$d_{min} + 0.125$, h=h_{min}, $\beta = -3$), N27 (d=$d_{min} + 0.239$), N1 (d=d_{min}, h=h_{min}, $\beta = -3$) and N11 (d=$d_{min} + 0.05$, h=h_{min}, $\beta = -3$). For SAC hole B, it can be observed, that the most rapid penetration is from N11, which reaches a distance of 80 mm after 871 µs, then N23, N19, N27, N26 and N1. For the spray angle it can be observed, that the injection from N27 starts at a high angle of 56° and then slowly reduces to an angle of 20 – 25° like the other injections towards the end. For SAC hole B, it is visible, that all the spray angle curves spike between 400 – 600 µs, with a peak of 37.5° from N19 and also flatten out to 20 – 25° towards the end. The spray area for SAC hole A expands nearly linearly in all cases, with N19, N23 and N27 increasing the fastest, followed by N26, with the maximum area of 1026 mm^2, then N11 and N1. For SAC hole B it is visible, that all spray area curves expand nearly the same, except N1 which performs visibly slower and N11 reaches the maximum area of 966 mm^2. For the energization duration of 1000 µs it is visible, that for SAC hole A the fastest penetration is from N23, which reaches a penetration distance of 80 mm after 833 µs, N27 and N19, followed by N26 and then N11 and N1. For SAC hole B it can be noticed, that the penetrations are less clustered, with the most rapid from nozzle N23, crossing a penetration distance of 80 mm after 787 µs, then N27, N19, N11, further apart N26 and N1. The spray angle for SAC hole A is clustered with a spike in the beginning, especially from N27 with an angle of 40.2° and then flattens around 25° for all injections. For SAC hole B the behaviour is similar, with a initial maximum angle of 37.6° from N1. The spray area for SAC hole A expands linearly in three groups, with the most rapid area increase from N23, N27 and N19, reaching areas of 932 & 690 & 863 mm^2, followed by N11 and N26 and then N1. For SAC hole B the order of the area increase speed is similar but less grouped than for SAC hole A, here the maximum area is from N23 with 1043 mm^2.

This project has received funding from the European Union Horizon 2020 Research and Innovation programme. Grant Agreement No 861002

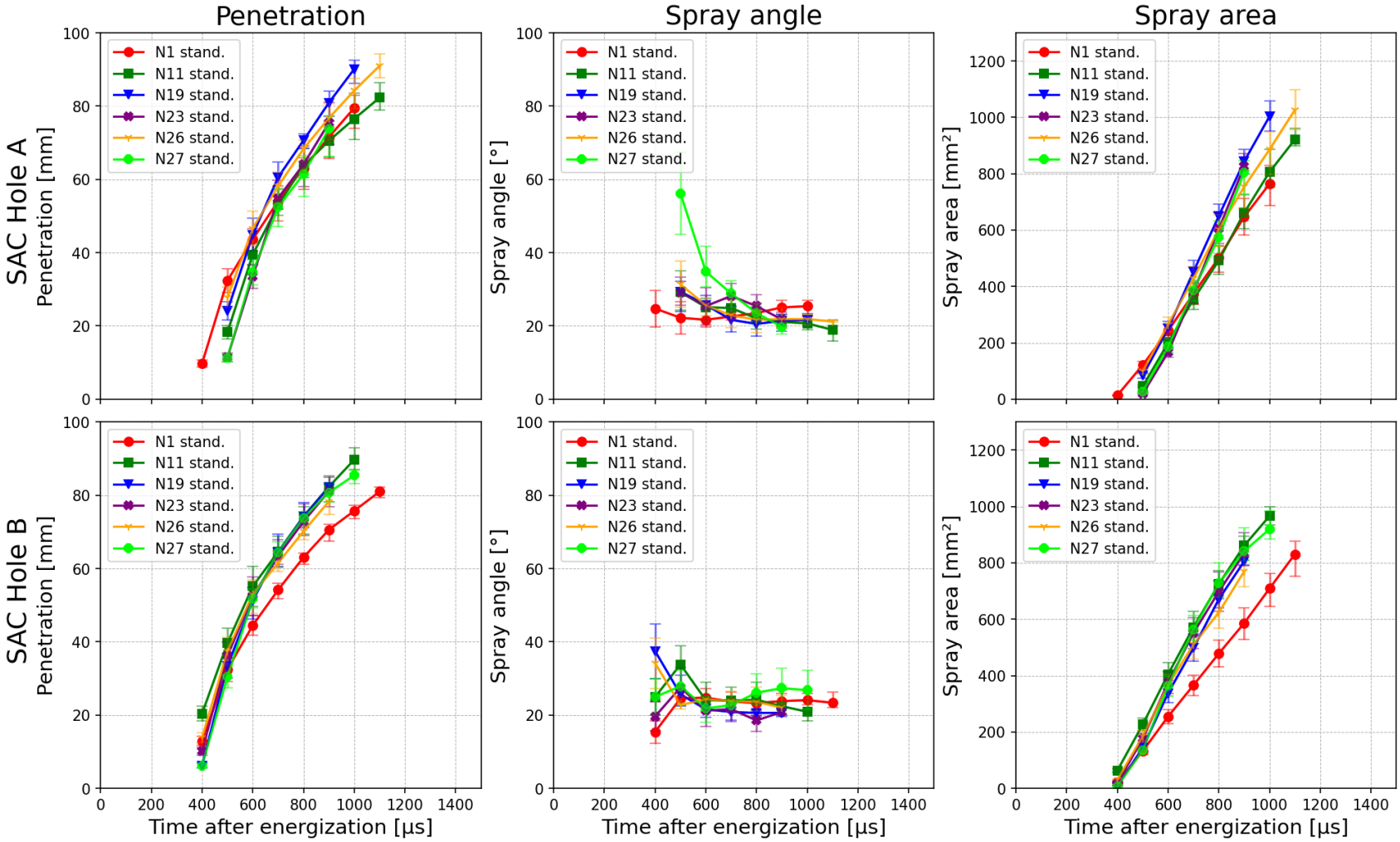


Figure 4.39: Influence of the relative spray hole diameter on the spray characteristics penetration, spray angle and spray area for nozzles N1, N11, N19, N23, N26 and N27 in standard orientation with 300 µs energization duration at 2200 bar

This project has received funding from the European Union Horizon 2020 Research and Innovation programme. Grant Agreement No 861002

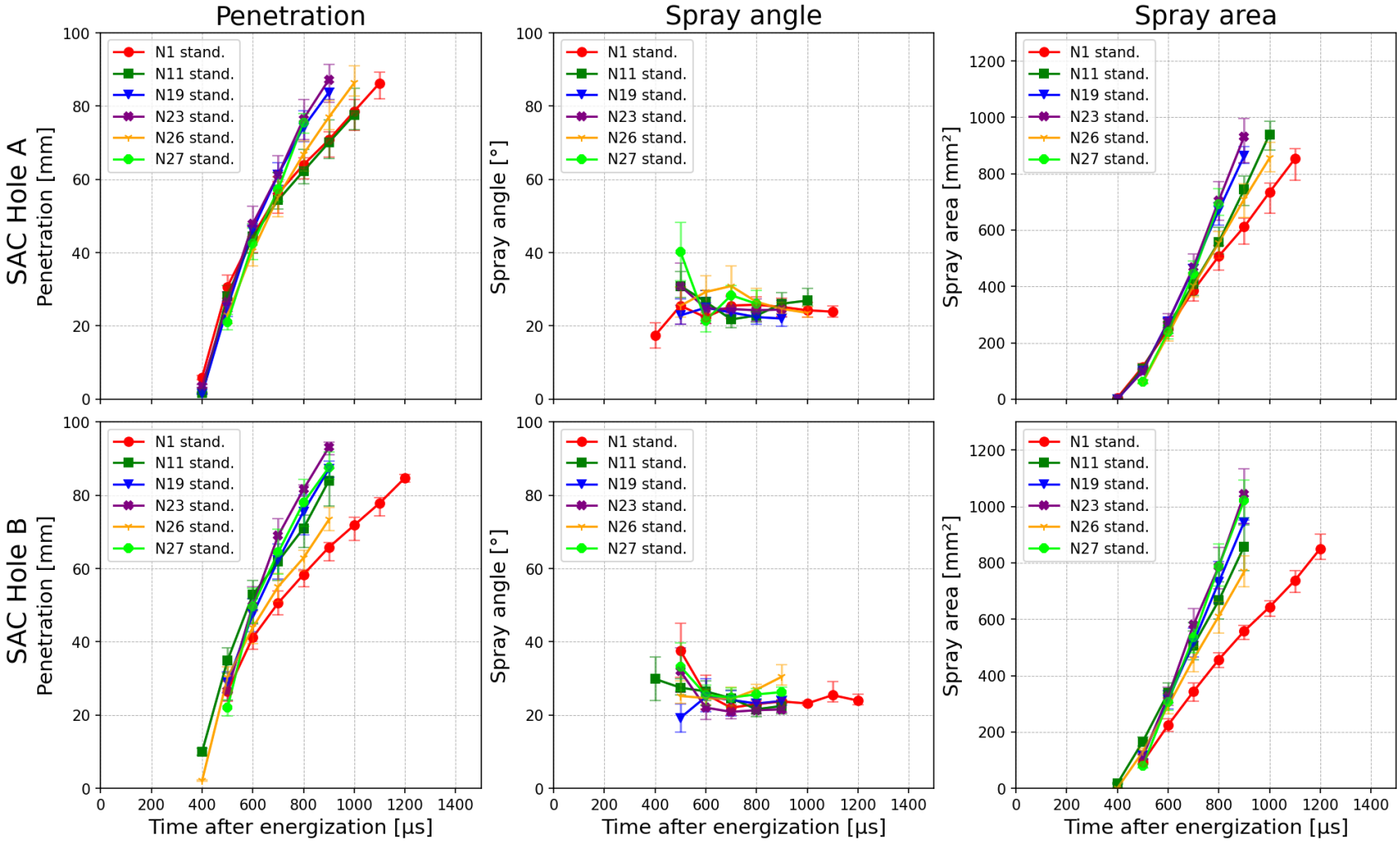


Figure 4.40: Influence of the relative spray hole diameter on the spray characteristics penetration, spray angle and spray area for nozzles N1, N11, N19, N23, N26 and N27 in standard orientation with 1000 µs energization duration at 2200 bar

This project has received funding from the European Union Horizon 2020 Research and Innovation programme. Grant Agreement No 861002

The last spray characteristics to be investigated are the injections from the same nozzles as shown in Figure 4.39 and Figure 4.40 but with a relative angle of 0°, as shown in Figure 4.41 and Figure 4.42. For the energization duration of 300 µs it is visible, that for SAC hole A the penetration curves are tightly clustered towards the end of the injection, in opposite to the injections with standard orientation, the fastest injection to reach a penetration distance of 80mm is from N23 (d=$d_{min} + 0.125$, h=h_{min}, $\beta = 0$) at 878 µs. For SAC hole B it is noticeable, that the penetrations are grouped, except N1 performing slower, which is similar to the injections with –3° relative angle. Here the fastest injection is from N11, which crosses the distance of 80 mm at 792 µs after energization. The spray angle for SAC hole A starts at around 40° for N23, N27 and N11, but towards the end of the injection, most angles are around 23 – 27° except N11 and N23, which reach angles of 19.8° and 20°. For SAC hole B all injections spike at the beginning with a maximum of 42.2° from N26 and flatten out at around 16 – 24° at the end. The spray area for SAC hole A expands grouped in accordance to the area curves with standard orientation, the maximum area is from N19 with 1007 mm^2. For SAC hole B the spray area curves are also similar to the ones in Figure 4.39, with a maximum area of 895 mm^2 from N11. For the energization duration of 1000 µs it can be noted for SAC hole A, that all injections start at the same time, except N27, but towards the end only N26 and N1 penetrate slower than the rest, with the fastest penetration from N19, which reaches a distance of 80 mm after 836 µs. For SAC hole B it is visible, that all injections start grouped, but towards the end they are divided, with the fastest penetration from N23, reaching a distance of 80 mm after 786 µs, then N19, N27, N11, N26 and N1. The spray angle for SAC hole A starts similar for all graphs except N27 which starts with an angle of 45.9°. Towards the end, all angles are between 20 – 23°. For SAC hole B it is visible, that the graphs are diverged, with the widest angle towards the end from N1 and N26 of 23.3 & 25.8°. For the spray area, it can be seen, that the curves behave similar to the penetration, with only N26 and N1 being visible slower at the expansion rate, reaching areas of 896 & 869 mm^2. For SAC hole B, the behaviour is similar to the penetration, too with N26 and N1 also performing slower, reaching areas of 930 & 750 mm^2. Both SAC holes perform similar to the standard orientation injections.

This project has received funding from the European Union Horizon 2020 Research and Innovation programme. Grant Agreement No 861002

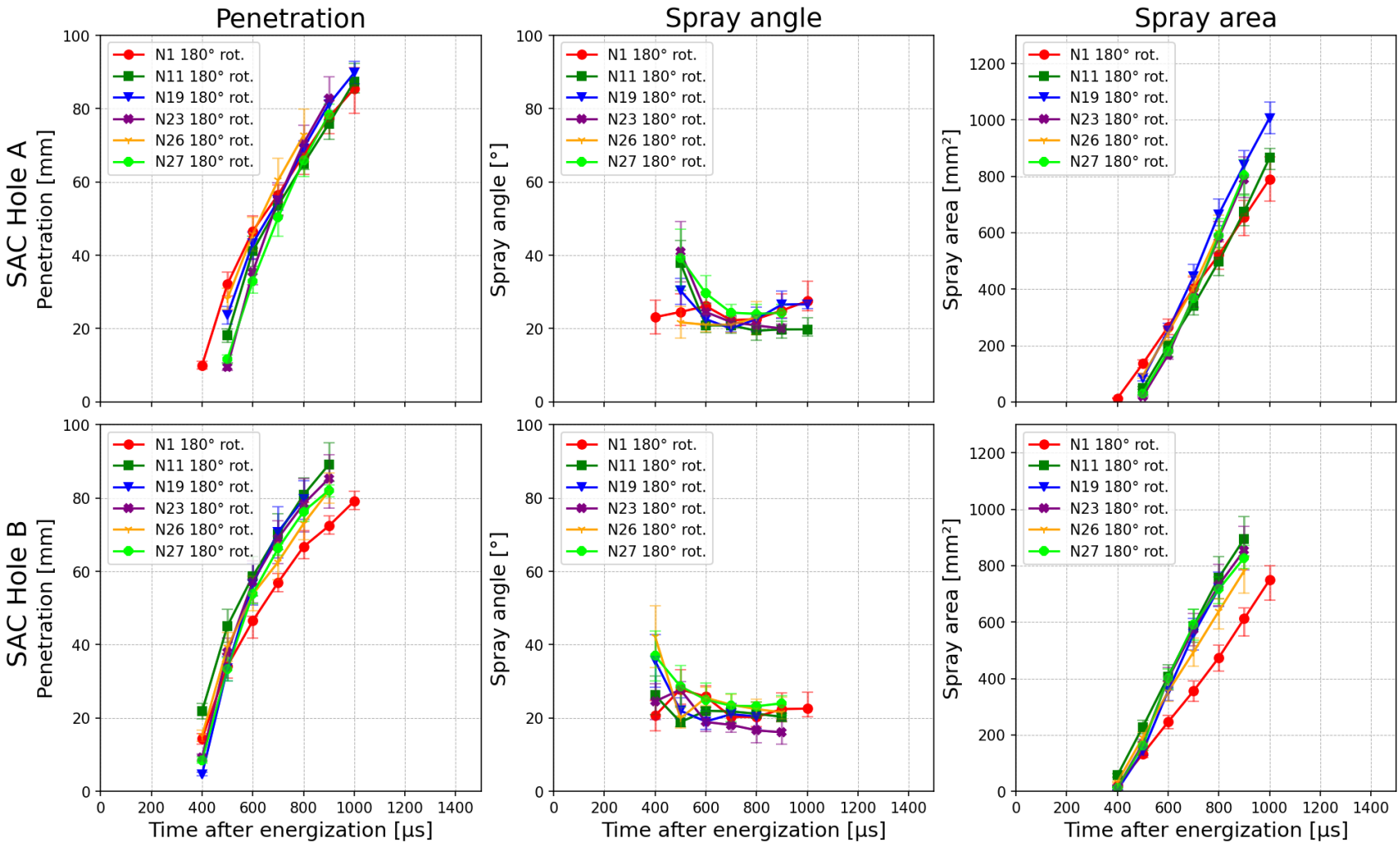


Figure 4.41: Influence of the relative spray hole diameter on the spray characteristics penetration, spray angle and spray area for nozzles N1, N11, N19, N23, N26 and N27 in 180° rotated orientation with 300 µs energization duration at 2200 bar

This project has received funding from the European Union Horizon 2020 Research and Innovation programme. Grant Agreement No 861002

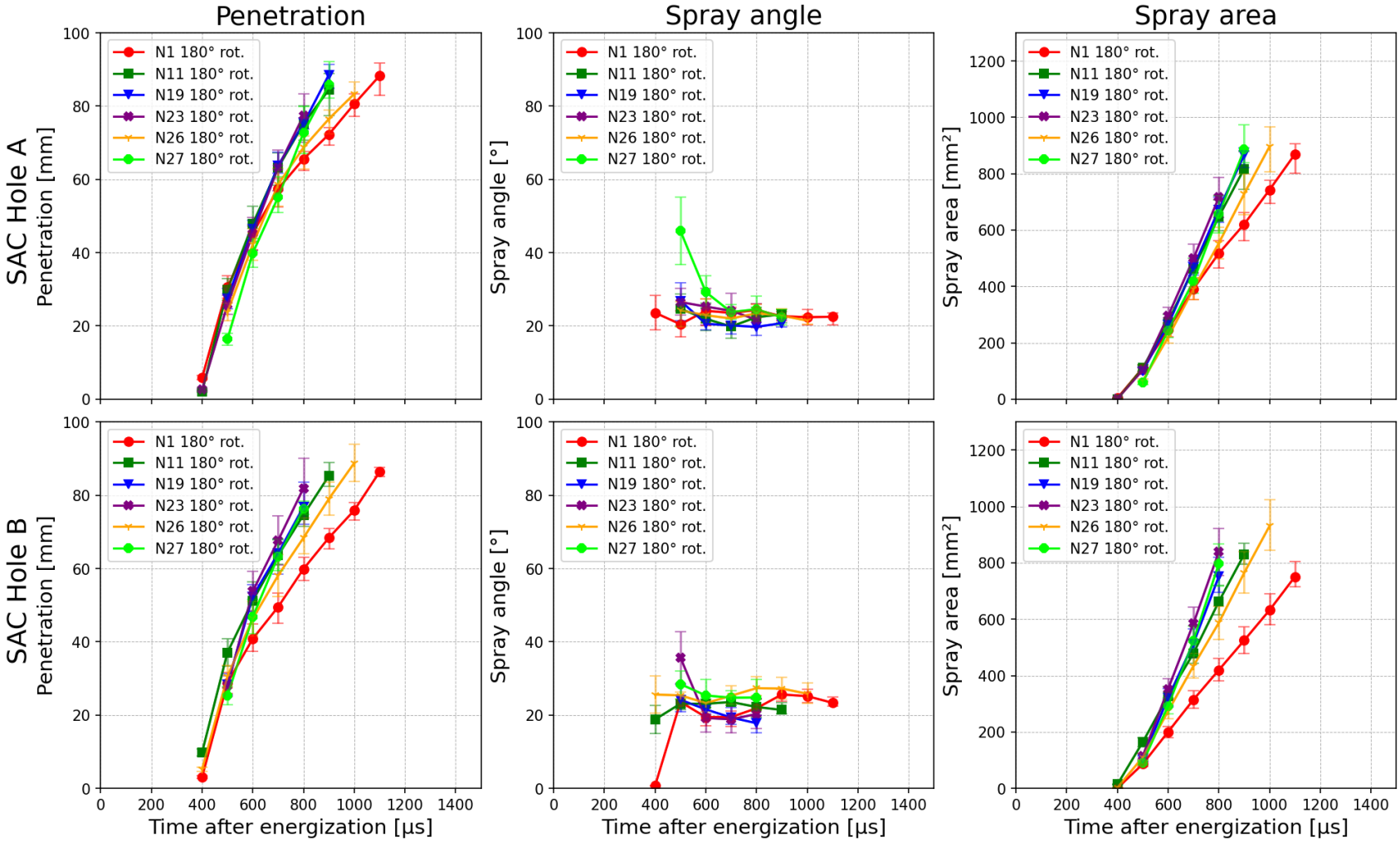


Figure 4.42: Influence of the relative spray hole diameter on the spray characteristics penetration, spray angle and spray area for nozzles N1, N11, N19, N23, N26 and N27 in 180° rotated orientation with 1000 µs energization duration at 2200 bar

This project has received funding from the European Union Horizon 2020 Research and Innovation programme. Grant Agreement No 861002

After the different injections with varrying spray hole diameter were observed an compared, the following influences were visible. For 1400 bar and SAC hole A with short energization durations the diameter d_{min} leads to the fastest penetration. For SAC hole B with 1400 bar there is no pattern visible. For 2200 bar and SAC hole A, smaller diameters inject faster but towards the end of the injection the bigger spray hole diameters penetrate faster, whereas for SAC hole B the medium spray hole diameter inject the fastest. For high injection pressures, for both SAC holes, the initial angles are wider than 30° but towards the end, they are all similar between 20 – 30°. After all the observations for the influence of the geometric nozzle parameters have been compared, the results and a recommendation for future comparisons are shown in the following section.

4.3 Results of the geometric investigation

Since the comparison of the different injections is depending on the injection pressure and energization duration, multiple injection graphs need to be compared. Therefore, it would be recommended to also compare the nozzles for a fixed timeframe or penetration distance, for example when observing the time at which they are reaching a fixed penetration of 80 mm, to observe the influence of the pressure and energization duration. An example of this is shown in Figure 4.43 for nozzle N1 (d=$d_{\min}$, h=$h_{\min}$, $\beta = -3 + 0$), Figure 4.44 for nozzle N16 (d=$d_{\min} + 0.05$, h=$h_{\min} + 0.1$, $\beta = 2 + 5$) and Figure 4.45 for nozzle N23 (d=$d_{\min} + 0.125$, h=$h_{\min}$, $\beta = -3 + 0$).

In Figure 4.43 it can be observed that the fastest penetrations are from injections with 2200bar and 1000 or below 600 µs energization duration for SAC hole A, showing that also the duration of the current can impact the penetration speed. For SAC hole B on the contrary, the optimum energization duration seems to be at 800 µs where the fastest penetrations are achieved by 1800 & 2200 bar. The observed difference between the standard and 180° orientations of N1 may be attributed to the change in relative spray angle. Since N1 has the smallest spray hole distance and spray hole diameter of the investigated TWIN nozzles, the spray interaction is expected to be more sensitive to geometric variations. As a result, changes in the relative spray orientation may have a larger influence on the spray characteristics than for the other nozzle configurations.

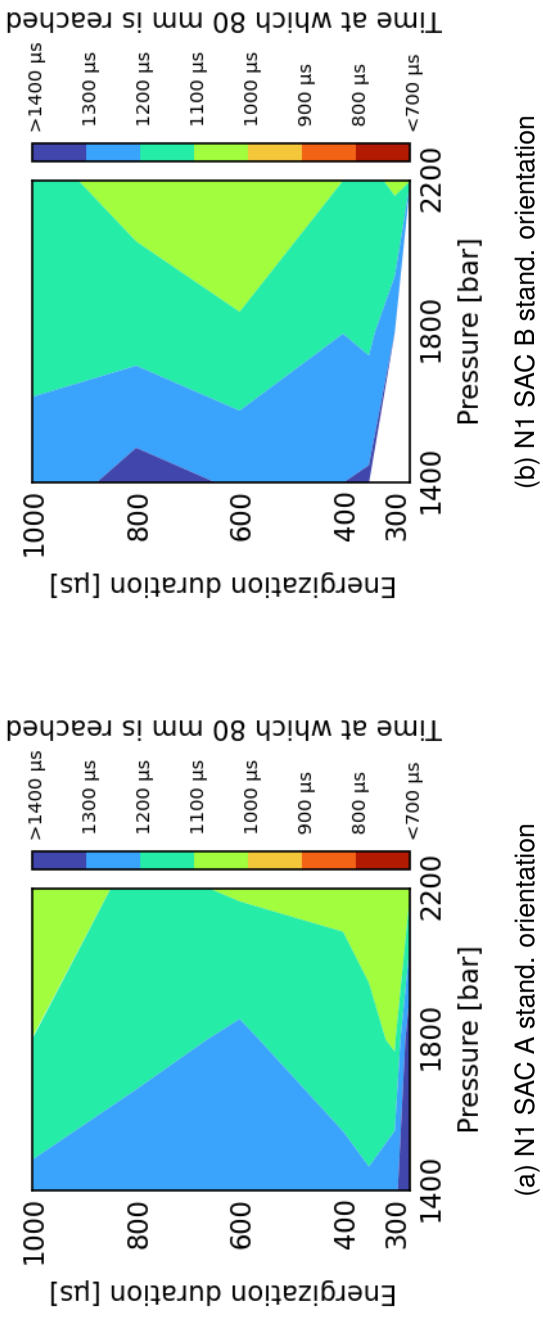
In Figure 4.44 it can be observed that the fastest penetrations are from injections with 2200bar and 800 µs energization duration for SAC hole A, showing that there seems to be a shift of the optimum with the change of the spray hole diameter, distance and relative angle. For SAC hole B it is also shifted towards shorter energization

This project has received funding from the European Union Horizon 2020 Research and Innovation programme. Grant Agreement No 861002

durations with the peak at 400 – 600 µs where the fastest penetrations are achieved by 1800 & 2200 bar again. Since 400 – 600 µs corresponds to the time required for the injector needle to reach its full lift, the reduction in penetration observed for durations exceeding 600 µs could potentially be caused by changes in internal nozzle flow, such as flow instabilities or cavitation.

In Figure 4.45 it can be observed that the fastest penetrations are from injections with 2200bar and 800 – 1000 µs energization duration for SAC hole A, shifting back to the higher energization durations with the maximum spray hole diameter. For SAC hole B it is also shifted towards 1000 µs where the fastest penetrations are achieved by 2200 bar in this case. When comparing Figure 4.44 with Figure 4.45 it can be observed for example that with a higher injection pressure and SAC hole B the penetration times reduce for long energization durations > 400 µs whereas the penetration duration for short energization durations with low injection pressures increases.

This project has received funding from the European Union Horizon 2020 Research and Innovation programme. Grant Agreement No 861002



(a) N1 SAC A stand. orientation

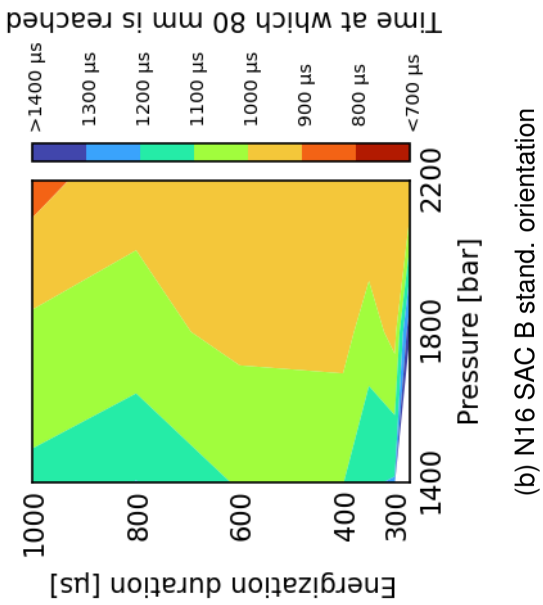
(b) N1 SAC B stand. orientation

(c) N1 SAC A 180° rot.

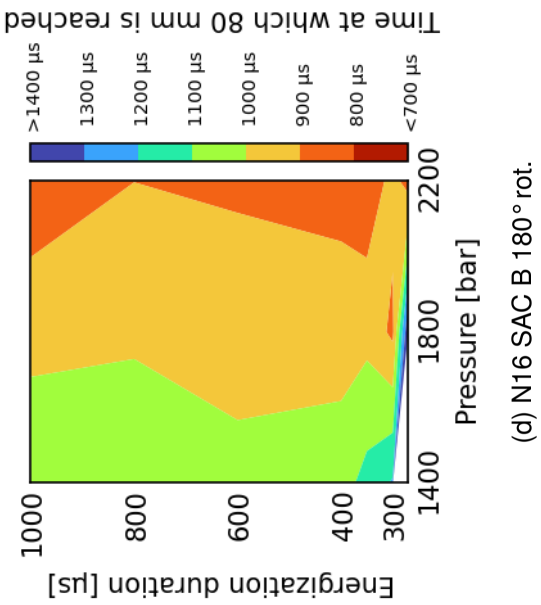
(d) N1 SAC B 180° rot.

Figure 4.43: N1 contour diagram for 80 mm penetration timing

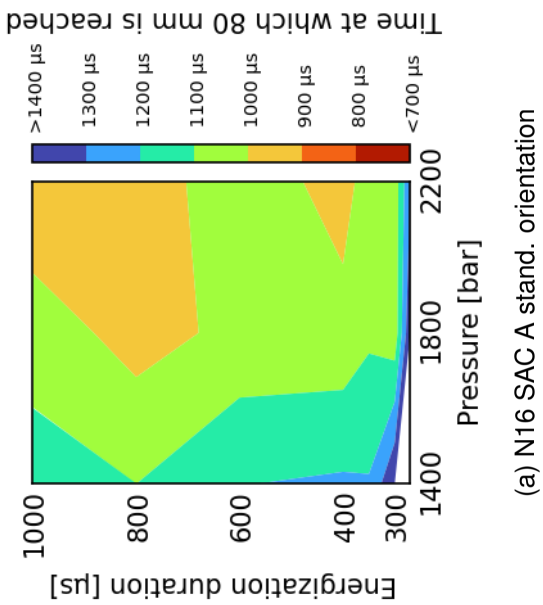
This project has received funding from the European Union Horizon 2020 Research and Innovation programme. Grant Agreement No 861002



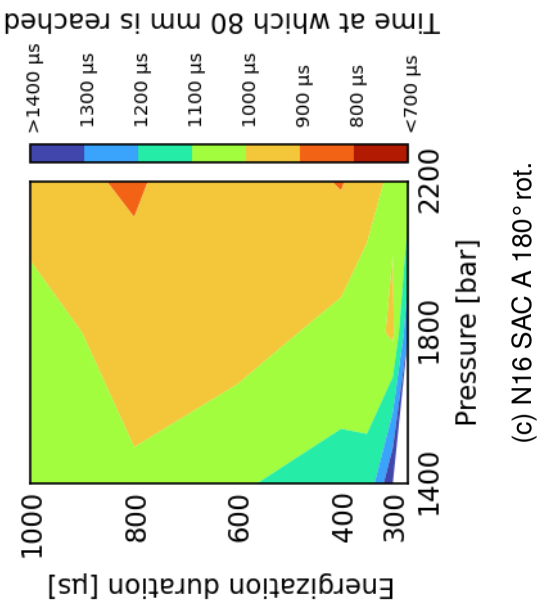
(b) N16 SAC B stand. orientation



(d) N16 SAC B 180° rot.



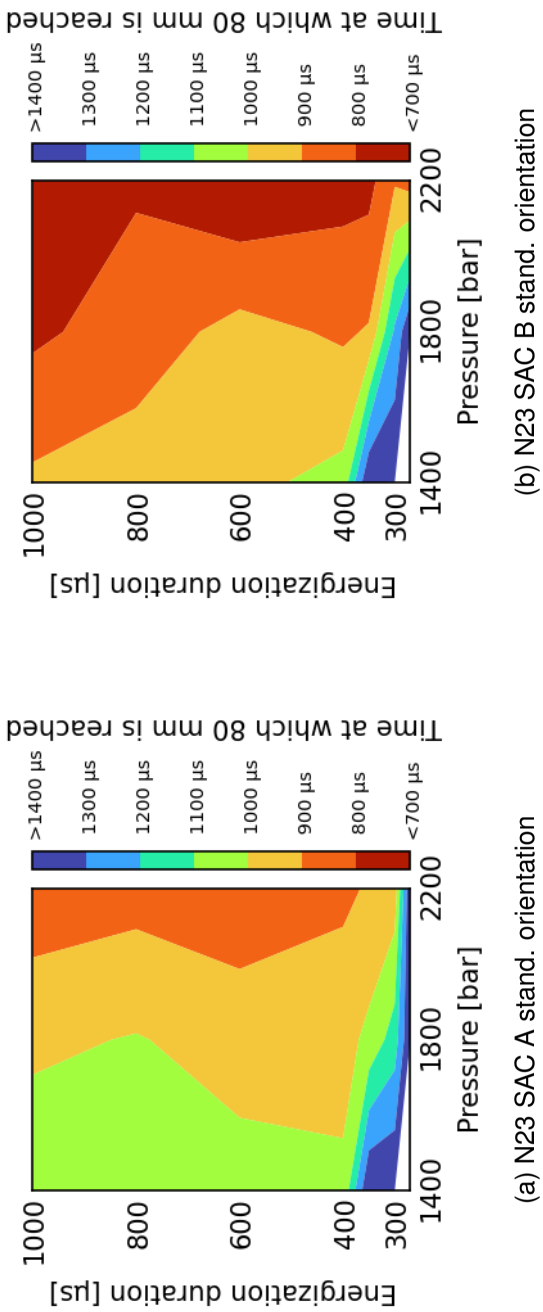
(a) N16 SAC A stand. orientation



(c) N16 SAC A 180° rot.

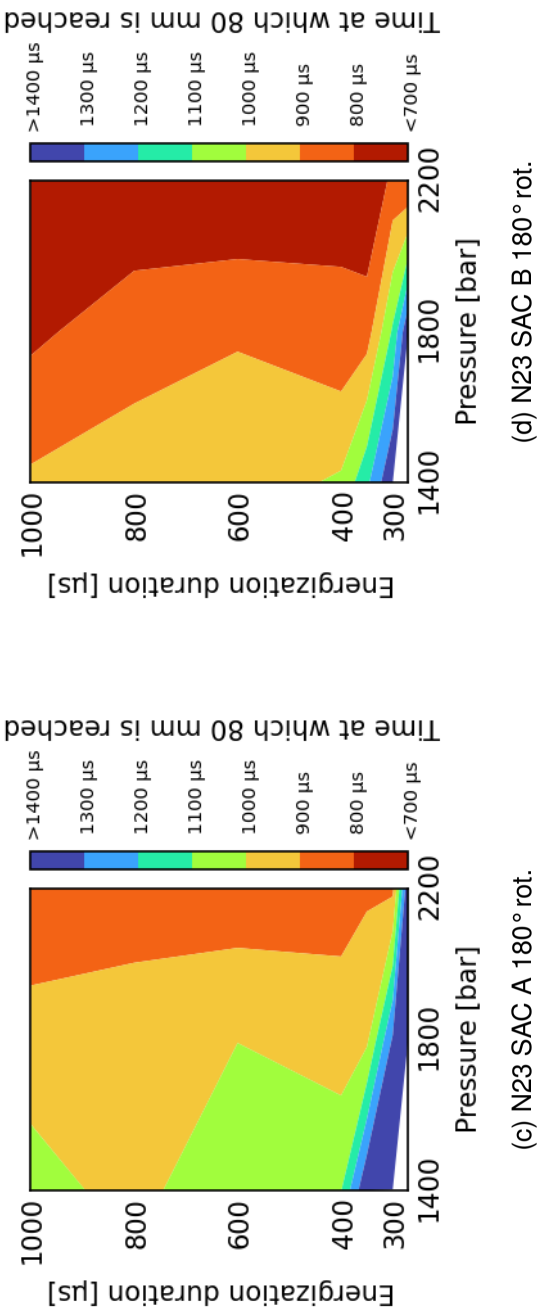
Figure 4.44: N16 contour diagram for 80 mm penetration timing

This project has received funding from the European Union Horizon 2020 Research and Innovation programme. Grant Agreement No 861002



(a) N23 SAC A stand. orientation

(b) N23 SAC B stand. orientation



(c) N23 SAC A 180° rot.

(d) N23 SAC B 180° rot.

Figure 4.45: N23 contour diagram for 80 mm penetration timing

This project has received funding from the European Union Horizon 2020 Research and Innovation programme. Grant Agreement No 861002

4.4 Summary

This study showed the potential of the TWIN nozzles to achieve spray characteristics comparable to those of single hole nozzles. However, the investigation of the influence of the geometric parameters on the TWIN nozzle spray characteristics is a key research gap addressed in this work. Achieving a stratified spray with increased penetration at minimum and maximum injection amounts is of high interest as higher spray momentum can promote air entrainment and therefore support improved mixture formation. After all the different injection cases and nozzles were analysed and the influence of the geometric values on the spray characteristics were observed, the following results were obtained:

- For 1400 bar injection pressure and nozzles with spray hole diameter d_{min} the injections from SAC hole A reach a better penetration for low energization durations and for SAC hole B with higher energization durations
- For bigger spray hole diameters, the injections from SAC hole B tend to penetrate faster than from SAC hole A
- In most of the injections, the TWIN nozzle penetrate faster than the comparison nozzles, especially with low energization durations
- For 2200 bar the spray angle of many TWIN injections is above 30° in the beginning of the injection and towards the end it is between 20 – 25°
- The influence of the relative spray angles between the two spray hole pairs was only observable with injections from d_{min} nozzles at 1400 bar injections and mostly influenced the spray angle
- In most cases, the spray area expanded similar to the penetration graphs, with the main influence from the spray hole diameter
- The spray hole distance seemed to mostly influence injections from nozzles with SAC hole B, where the peak penetration and area expansion was from h_{min}+ 0.1 mm, indicating, that a too close and too far distance between the two spray holes results in a negative impact on the injection
- The SAC geometry influences the pressure build-up inside the nozzle and the resulting spray characteristics. SAC A exhibited a slower pressure build-up and generally resulted in lower spray penetration. In contrast, SAC B enabled a faster pressure build-up and therefore higher penetration, but also showed less stable spray behaviour at short energization durations.

This project has received funding from the European Union Horizon 2020 Research and Innovation programme. Grant Agreement No 861002

Chapter 5

Adjustment of the spray penetration calculations for TWIN Nozzles

In order to predict the spray penetration of TWIN nozzles based on their geometric values, different currently in the transportation industry used spray penetration formulas were evaluated and compared to the performance of the three single hole nozzles. Afterwards, the calculations were adjusted using a Linear regression calculation based on a second degree formula derived from the injection conditions and geometric parameters, which were varied in the TWIN nozzle study. The adjustment of the spray penetration calculations was carried out because current spray penetration models, such as the formulas by Hiroyasu and by Naber and Siebers, do not accurately predict the penetration of the novel TWIN nozzles. While the spray penetration models from Hiroysau and Naber and Siebers are widely used for conventional injectors, their prediction accuracy for the investigated injector concept was unknown. Therefore, the experimental spray data were used to evaluate the performance of the existing models and to identify systematic deviations. Based on these observations the models were modified through the incorporation of a second order regression approach that accounts for the TWIN geometric parameters.

5.1 Single hole comparison and TWIN adjustment based on the Spray penetration formula from Hiroyasu and Arai

First the spray penetration from the test cases will be compared to the investigations from Hiroyasu and Arai [94]. The formula created by them is one of the most commonly

This project has received funding from the European Union Horizon 2020 Research and Innovation programme. Grant Agreement No 861002

used for predicting the spray characteristics of new nozzles but still falls short in many cases to accurately calculate the spray penetration. In order check how accurately the spray penetration of the Hiroyasu and Arai formula is predicting the single nozzles tested for comparison, the following section shows their accuracy and how to adjust the calculations to fit the TWIN nozzle measurements.

5.1.1 Single hole nozzle adjustment

The spray penetration according to Hiroyasu and Arai can be calculated as shown in Equations 5.1 - 5.3. Where

t is the time after the injection start

t_b is the breakup time

ΔP is the Pressure difference between ambient and injection

ρ_l is the liquid density

ρ_a is the ambient density

D is the spray hole diameter

$0 < t < t_b$

$$S = 0.39(\frac{2\Delta P}{\rho_l})^{0.5} t \tag{5.1}$$

$t > t_b$

$$S = 2.95(\frac{\Delta P}{\rho_a})^{0.25} (Dt)^{0.5} \tag{5.2}$$

$$t_b = 28.65 \frac{\rho_l D}{(\rho_a \Delta P)^{0.5}} \tag{5.3}$$

As this was calculated, it was observed, that the penetrations according to Hiroyasu and Arai [94] were underperforming compared to the observed penetrations of the single hole nozzles. This is due to the fact, that the tested nozzled were only manufactured with two spray holes respectively spray hole pairs. An example for this is shown in Figure 5.1, which compares the calculated penetration for the single hole nozzle with SAC hole B and a spray hole diameter of d_{min}. It is visible from this image that the discrepancy between the predicted and measured penetration is too high and therefore an adjustment of the calculation is necessary for this case.

This project has received funding from the European Union Horizon 2020 Research and Innovation programme. Grant Agreement No 861002

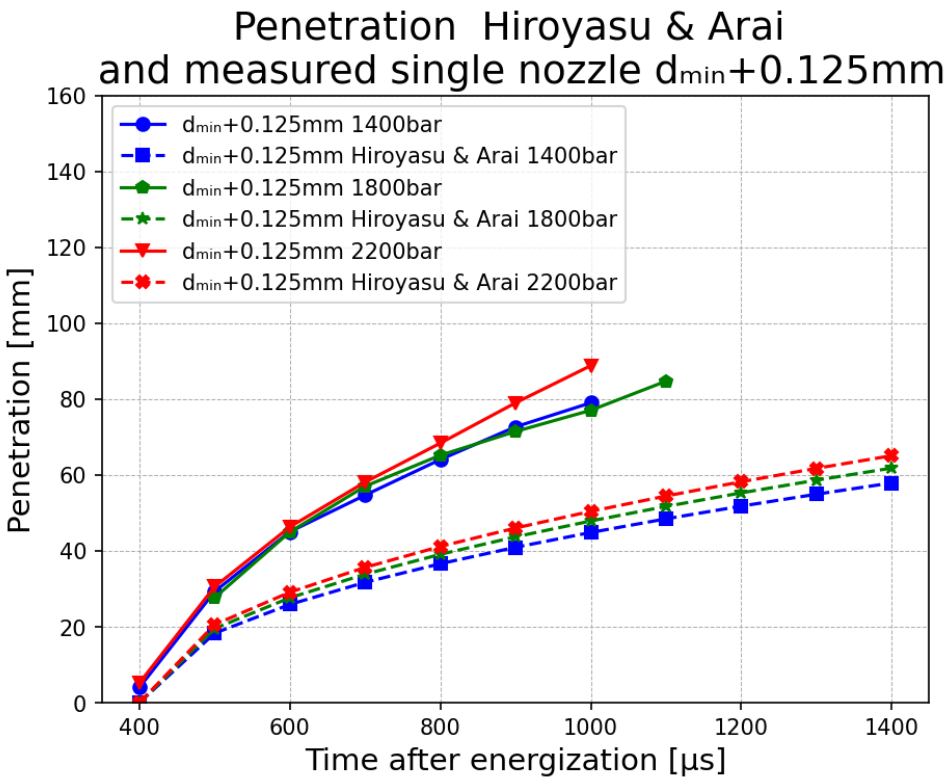


Figure 5.1: Comparison of the measured single hole nozzle penetration with the calculation after Hiroyasu and Arai

It was therefore tested, whether the coefficient value of 2.95 from Equation 5.2 could be adjusted to fit the measured penetrations. Unfortunately, this lead to a high deviation since the behaviour of each nozzle is differing too strongly depending on the pressure and energization duration. Therefore it was decided to calculate a new penetration based on the Hiroyasu and Arai [94] formula with adding a linear regression based on a second degree polynom derived from the input values injection pressureΔP, spray hole diameter D and time after the injection start t.

The adjustment for the single spray hole nozzles is shown in Equation 5.4.

$$S_{adjusted} = S + c_0 + c_1\Delta P + c_2 D + c_3 t + c_4\Delta P^2 + c_5\Delta P D + c_6\Delta P t + c_7 D^2 + c_8 D t + c_9 t^2 \quad (5.4)$$

Unlike conventional single phase fits, which mainly provide case specific correlations, the term reduction approach identifies and quantifies the underlying geometric effects and their interactions, resulting in a predictive and physically interpretable extension of the Hiroyasu model. Since the different energization durations lead to different needle opening behaviours, it was decided to calculate the coefficients for each energization separately in order to improve the efficiency. The coefficients for each energization duration from the linear regression model with usage of Equation 5.4 are

This project has received funding from the European Union Horizon 2020 Research and Innovation programme. Grant Agreement No 861002

Table 5.1: Coefficients for the single hole nozzles manufactured with SAC hole A

coeff.	270 µs	300 µs	350 µs	400 µs	600 µs	800 µs	1000 µs
c_0	-307.1	-51.5	-21.1	-11.2	-8.1	-3.7	74
c_1	2.7	0.32	0.09	-0.04	-0.13	-0.008	-0.66
c_2	$5.87*10^5$	$1.17*10^5$	-9960	$1.04*10^5$	72409.3	59680.3	$-1.5*10^5$
c_3	4150	34206	44996	17288	26784	6732	10655
c_4	-0.008	-0.002	-0.001	-0.0001	0.001	-0.0005	0.001
c_5	-478.3	626.5	351.1	54.3	-296.7	468.4	564.5
c_6	497.6	435.8	181.7	141.5	75.7	110	255.2
c_7	$-1.0*10^9$	$-5.0*10^8$	$-2.0*10^8$	$-4.2*10^8$	$-2.8*10^8$	$-4.7*10^8$	$-1.2*10^8$
c_8	$-9.6*10^7$	$-3.8*10^7$	$5.09*10^7$	$1.18*10^8$	$1.33*10^8$	$1.37*10^8$	$1.17*10^8$
c_9	$-3.5*10^7$	$-4.3*10^7$	$-3.1*10^7$	$-1.7*10^7$	$-1.6*10^7$	$-1.0*10^7$	$-2.2*10^7$

Table 5.2: Coefficients for the single hole nozzles manufactured with SAC hole B

coeff.	270 µs	300 µs	350 µs	400 µs	600 µs	800 µs	1000 µs
c_0	33376	-2.4	2.3	-63.9	-79.7	-25.7	-46.6
c_1	-347.5	-0.26	-0.28	0.079	0.43	0.13	0.39
c_2	3021.1	$1.32*10^5$	-24744	97238	$1.57*10^5$	$-1.5*10^5$	-8735
c_3	-40367	51365	71770	$1.08*10^5$	53276	58090	32273
c_4	0.89	-0.0003	0.00004	-0.0002	-0.001	-0.0001	-0.001
c_5	1545.6	1159	1032	223.7	153.9	304.2	276.2
c_6	676.1	198.5	136.6	37.7	-25.6	-38.4	73.8
c_7	$-5.0*10^8$	$-5.9*10^8$	$-3.4*10^8$	$-4.0*10^8$	$-3.8*10^8$	$7.6*10^7$	$-2.2*10^8$
c_8	$-1.3*10^8$	$-6.9*10^7$	$-2.7*10^6$	$3.6*10^7$	$4.2*10^7$	$9.5*10^7$	$1.1*10^8$
c_9	$-2.5*10^7$	$-2.8*10^7$	$-3.6*10^7$	$-4.9*10^8$	$-1.3*10^7$	$-2.0*10^7$	$-1.8*10^7$

shown in Table 5.1 for SAC hole A. Here it can be observed that the coefficients for the energization durations 300 - 1000 µs are in the same order of magnitude and only 270 µs differs, mostly caused by the different spray behaviour since this is the minimum needle opening time.

Similar to Table 5.1 the coefficients for the nozzles with SAC hole B are shown in Table 5.2. Here the same phenomena as in Table 5.1 and it can be observed and only the coefficients from 270 µs energization duration seems to have a different order of magnitude compared to the other durations.

In order to judge the quality of each adjustment calculation, the Root Mean Squared Error for all injections compared to the adjusted Hiroyasu single hole equations was calculated. The average Root Mean Squared Error for each of these formulas compared to the measured spray penetrations of the single hole nozzles is shown in Table 5.3. It can be observed that the smallest error for SAC hole A is from 600 µs energization

This project has received funding from the European Union Horizon 2020 Research and Innovation programme. Grant Agreement No 861002

Table 5.3: Root Mean Squared Error for the adjusted Hiroyasu calculations for single hole nozzles

energization duration	SAC A RMSE	SAC B RMSE
270 µs	3.944	2.760
300 µs	3.110	3.094
350 µs	3.425	3.003
400 µs	2.645	3.354
600 µs	2.131	2.097
800 µs	2.229	2.217
1000 µs	2.593	1.978

duration and for SAC hole B from 1000 µs duration. The highest error for SAC hole A is from 270 µs and for SAC hole B from 400 µs. This is caused by the high shot-to-shot variations of the spray during the needle opening times.

An example of how the adjusted penetration calculated from Equation 5.4 fits the measured penetration can be seen in Figure 5.2. The comparison was done with Nozzle N26 at 1000 µs energization duration, therefore the following coefficients were used:

$$c_0 = 74$$

$$c_1 = -0.66$$

$$c_2 = -1.5 \times 10^5$$

$$c_3 = 10655$$

$$c_4 = 0.001$$

$$c_5 = 564.5$$

$$c_6 = 255.2$$

$$c_7 = -1.2 \times 10^8$$

$$c_8 = 1.17 \times 10^8$$

$$c_9 = -2.2 \times 10^7$$

It can be seen that the predicted spray penetration is fitting the measured penetrations very closely.

This project has received funding from the European Union Horizon 2020 Research and Innovation programme. Grant Agreement No 861002

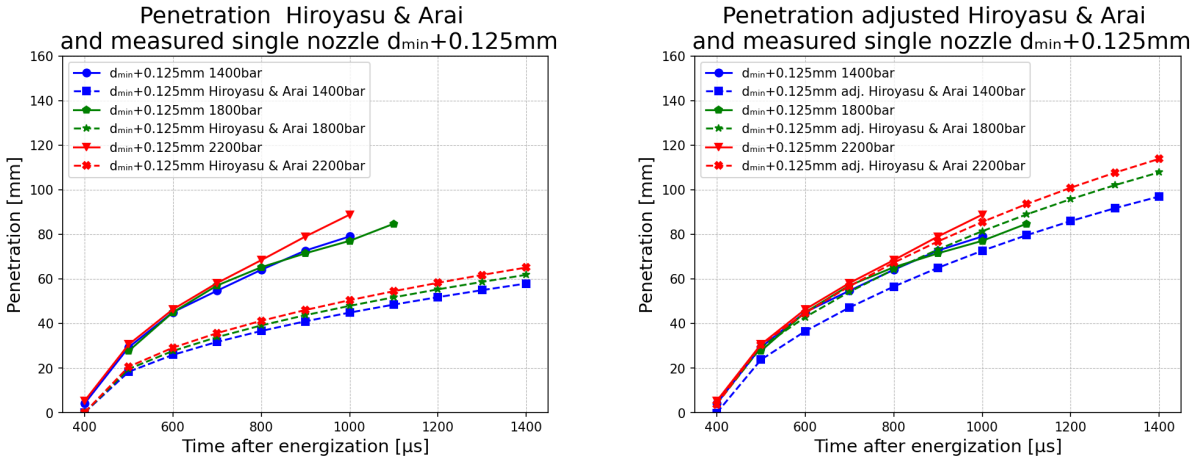


Figure 5.2: Comparison of the measured single hole nozzle (SAC A, N26, 1000 µs energization penetration with the calculation after Hiroyasu and Arai, not adjusted (a) and adjusted (b)

5.1.2 TWIN nozzle adjustments

Similar to the single hole adjustment for the spray penetration formula, the predicted penetration for the TWIN nozzles was calculated with the equations 5.1 - 5.3 and also underperformed. It was therefore decided to calculate the adjustment for the TWIN nozzles as a linear regression model based on the second degree polynomial of the input values, with adding the terms for the spray hole distance h and relative spray hole angle $\Delta\beta$. The adjustment for the TWIN nozzles is shown in Equation 5.5.

$$\begin{aligned} S_{adjustedTWIN} = S &+ c_0 + c_1\Delta P + c_2 D + c_3 h + c_4\Delta\beta + c_5 t + c_6\Delta P^2 + c_7\Delta P D + c_8\Delta P h \\ &+ c_9\Delta P\Delta\beta + c_{10}\Delta P t + c_{11}D^2 + c_{12}Dh + c_{13}D\Delta\beta + c_{14}Dt + c_{15}h^2 \\ &+ c_{16}h\Delta\beta + c_{17}ht + c_{18}\Delta\beta^2 + c_{19}\Delta\beta t + c_{20}t^2 \end{aligned} \tag{5.5}$$

The coefficients from Equation 5.5 for the nozzles with SAC hole A are shown in Table 5.4. Similar to the coefficients from the single nozzle, it can be observed that the energization duration 270 µs produces a different order of magnitude compared to the other energization durations.

The coefficients from Equation 5.5 for the nozzles with SAC hole B are shown in Table 5.5. While all energization durations require different regression coefficients, the coefficients for 270 µs and 300 µs show the largest deviations from those obtained for the longer energization durations. This is likely related to the injector operating in

This project has received funding from the European Union Horizon 2020 Research and Innovation programme. Grant Agreement No 861002

Table 5.4: Coefficients for the TWIN nozzles manufactured with SAC hole A

coeff.	270 µs	300 µs	350 µs	400 µs	600 µs	800 µs	1000 µs
c_0	293	46.4	-45.5	-3.5	-0.6	95	-67.2
c_1	-0.6	1.3	-0.02	-0.03	-0.2	-0.1	-0.2
c_2	$-1.1*10^6$	$-1.6*10^6$	$1.67*10^5$	$-2.8*10^5$	-13656	$-5.3*10^5$	$2.84*10^5$
c_3	$-8.7*10^5$	-90094	9126	27388	350.1	$-2.4*10^5$	$2.56*10^5$
c_4	-6.3	0.5	0.8	-1.1	2	2.8	-1.4
c_5	27236	23786	59418	44198	22183	4994	10845
c_6	-0.0004	-0.01	-0.001	0.0002	0.0004	-0.0002	0.0004
c_7	3026	3387	872.4	618.6	397.8	672.4	541.7
c_8	815.8	-193.3	242.2	-298.3	-226.7	112.5	-218.8
c_9	0.02	-0.01	-0.005	-0.003	-0.003	-0.002	-0.003
c_{10}	135.3	413.9	87	44.3	130.8	92.6	97.2
c_{11}	$6.42*10^8$	$1.96*10^9$	$-9.3*10^8$	$-1.2*10^8$	$-4.3*10^8$	$1.68*10^8$	$-1.1*10^9$
c_{12}	$8.69*10^8$	$6.67*10^8$	$-5.9*10^7$	$2.41*10^8$	$-6.4*10^6$	$5.78*10^8$	$-3.4*10^8$
c_{13}	18865	11186	3187	2899	518.9	-1795	3945
c_{14}	$-1.5*10^7$	$-6.6*10^7$	$1.49*10^8$	$2.68*10^8$	$2.51*10^8$	$2.92*10^8$	$2.91*10^8$
c_{15}	$7.22*10^8$	$-4.7*10^6$	$-2.6*10^7$	$2.83*10^6$	$8.04*10^7$	$1.84*10^8$	$-2.1*10^8$
c_{16}	-2437	-1399	-2249	2581	-3752	-4320	2786
c_{17}	$6.59*10^7$	$1.24*10^7$	$-2.1*10^7$	$-2.3*10^7$	$-1.2*10^7$	$-8.5*10^6$	$-5.5*10^6$
c_{18}	-0.1	-0.02	-0.02	-0.01	-0.04	-0.02	-0.02
c_{19}	388	319.5	-31.8	-365.9	-705.7	-890	-534.2
c_{20}	$-3.5*10^7$	$-3.4*10^7$	$-2.9*10^7$	$-2.6*10^7$	$-2.2*10^7$	$-1.5*10^7$	$-1.8*10^7$

the opening phase, where the hydraulic conditions differ from those of fully developed injection. This is in accordance with the spray observations from the previous chapter, since the injections with SAC hole B tend to penetrate less with low energization durations.

The average Root Mean Squared Error for each of these formulas compared to the measured spray penetrations of the TWIN nozzles is shown in Table 5.6. The lowest error for SAC hole A is from 400 µs and for SAC hole B from 1000 µs. For both SAC holes the highest error is from 270 µs.

An example of how the adjusted penetration calculated from Equation 5.5 fits the measured penetration of the TWIN nozzles N8, N18, N21 and N24 with SAC hole B and 1000 µs energization duration can be seen in Figure 5.3. It can be observed that for these injection conditions the adjusted penetration fits well for smaller spray hole diameters and differs more for bigger ones.

Afterwards it was analysed which Equation terms could be eliminated without increasing the Root Mean Squared Error exceedingly. After analysing the influence of

This project has received funding from the European Union Horizon 2020 Research and Innovation programme. Grant Agreement No 861002

Table 5.5: Coefficients for the TWIN nozzles manufactured with SAC hole B

coeff.	270 µs	300 µs	350 µs	400 µs	600 µs	800 µs	1000 µs
c_0	-319.2	-242.3	-27.5	-15	-50	-38.6	-79.1
c_1	-1.2	0.5	-0.4	-0.2	-0.004	-0.2	-0.03
c_2	$2.4*10^6$	$9.9*10^5$	53682	33628	$1.8*10^5$	$2.2*10^5$	$3.5*10^5$
c_3	$9.3*10^5$	$3.5*10^5$	84937	56421	62242	60443	$1.5*10^5$
c_4	-13.9	-0.9	0.8	0.5	2.2	1	1.2
c_5	-2189	81250	76085	23241	22790	26320	22174
c_6	0.005	-0.001	0.001	0.0002	0.0001	0.0003	0.00002
c_7	-52.5	972.7	802.5	1120	418.9	608.9	225.2
c_8	-1416	-367.4	30.6	114.5	7	318.2	219
c_9	0.03	0.004	0.001	0.003	-0.01	-0.002	0.005
c_{10}	285.4	66	53.6	-15.3	-28.6	-40.3	-11
c_{11}	$-3.*10^9$	$-2.*10^9$	$-4.*10^8$	$-8.*10^8$	$-8.*10^8$	$-6.*10^8$	$-9.*10^8$
c_{12}	$-2.*10^9$	$-7.*10^8$	$-6.*10^7$	$-1.*10^8$	$-3.*10^8$	$-6.*10^8$	$-6.*10^8$
c_{13}	14184	894.1	-3466	-2348	95.7	-164	-7261
c_{14}	$-5.*10^7$	$7.0*10^7$	$1.1*10^8$	$3.4*10^8$	$3.7*10^8$	$3.7*10^8$	$3.8*10^8$
c_{15}	$-3.*10^8$	$-1.*10^8$	$-5.*10^7$	$-5.*10^7$	$3.3*10^7$	$4.0*10^7$	$-6.*10^7$
c_{16}	12948	-202.2	-1207	-1329	-2859	-1718	-1616
c_{17}	$1.0*10^8$	$-9.*10^6$	$-2.*10^7$	$-1.*10^5$	$-2.*10^7$	$-2.*10^7$	$-4.*10^7$
c_{18}	0.01	-0.003	0.002	-0.03	-0.005	-0.002	-0.02
c_{19}	-178.9	-461.8	-318.8	-528.2	-634.6	-590.9	-484
c_{20}	$-3.*10^7$	$-4.*10^7$	$-3.*10^7$	$-2.*10^7$	$-1.*10^7$	$-1.*10^7$	$-1.*10^7$

each term on the result, it was first tested to drop $c_1\Delta P$, $c_4\Delta\beta$, $c_6\Delta P^2$, $c_7\Delta PD$, $c_{10}\Delta Pt$, $c_{12}Dh$, $c_{15}h^2$, $c_{16}h\Delta\beta$, $c_{17}ht$, $c_{18}\Delta\beta^2$ and $c_{19}\Delta\beta t$ from the calculations. The removed terms were empirically selected based on their influence on the RMSE, where all terms with little to no change in the RSME were dropped. This results in the Equation 5.6.

$$S_{adjustedTWIN} = S + c_0 + c_2D + c_3h + c_5t + c_8\Delta Ph + c_9\Delta P\Delta\beta + c_{11}D^2 + c_{13}D\Delta\beta + c_{14}Dt + c_{20}t^2 \tag{5.6}$$

With the Equation 5.6 the coefficients for the input values were newly calculated for this first term reduction. For the nozzles with SAC hole A, these are shown in Table 5.7. Compared to the previous coefficient tables, there is no difference in order of magnitude observable anymore.

Similar to Table 5.7, the coefficients for SAC hole B are shown in Table 5.8. Again, there is no difference in the order of magnitude between the coefficients of the different energization durations visible.

This project has received funding from the European Union Horizon 2020 Research and Innovation programme. Grant Agreement No 861002

Table 5.6: Root Mean Squared Error for the adjusted Hiroyasu calculations for TWIN nozzles

energization duration	SAC A RMSE	SAC B RMSE
270 µs	11.917	7.513
300 µs	7.167	4.444
350 µs	3.397	3.826
400 µs	3.039	3.342
600 µs	3.23	3.529
800 µs	3.262	3.215
1000 µs	3.177	3.201

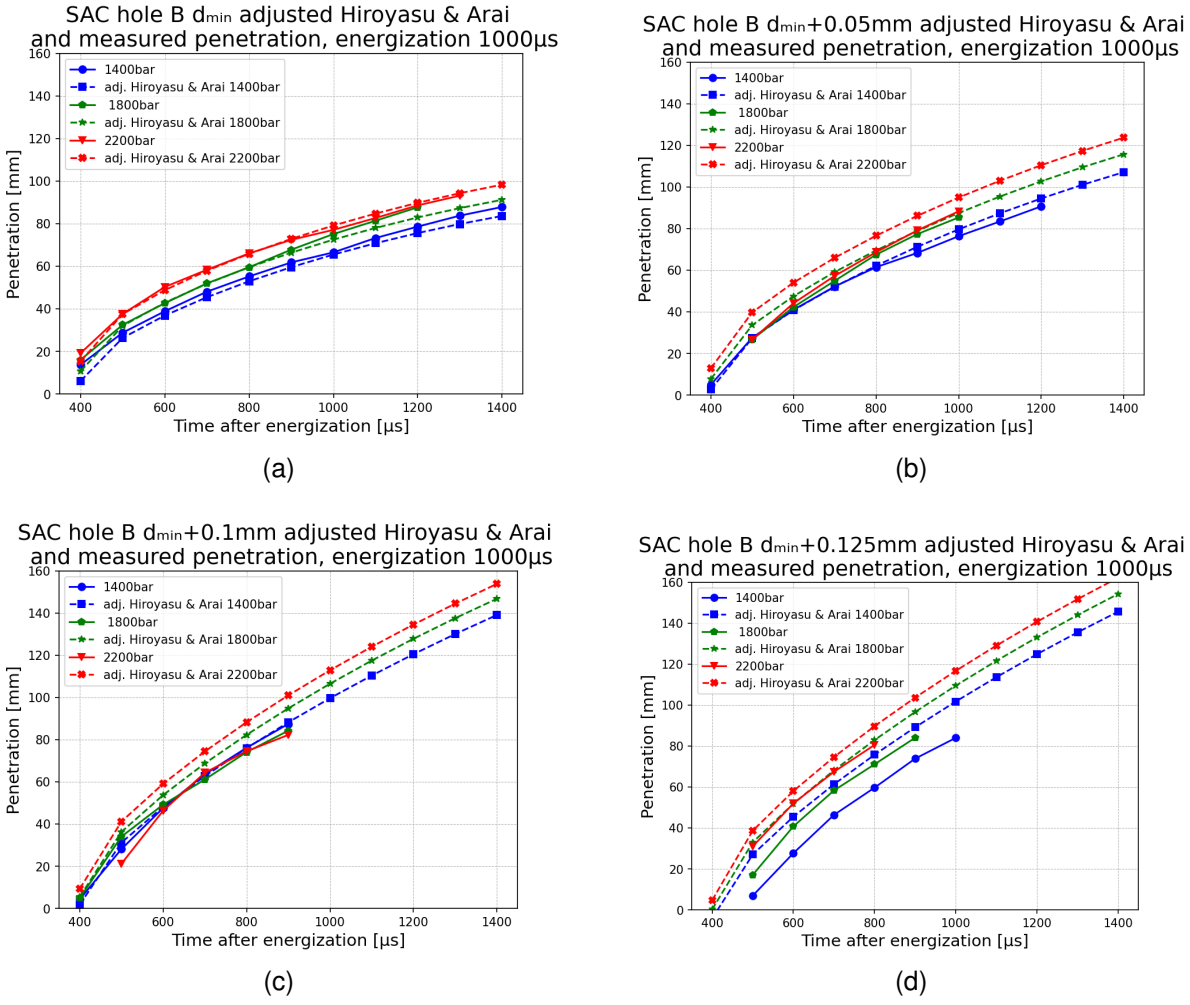


Figure 5.3: TWIN nozzle adjustment for Hiroyasu and Arai, Nozzle N8 (a), N18 (b), N21 (c) and N24 (d) for SAC hole B with 1000 µs energization

The average Root Mean Squared Error for each of these formulas compared to the measured spray penetrations of the TWIN nozzles is shown in Table 5.9. It can be

This project has received funding from the European Union Horizon 2020 Research and Innovation programme. Grant Agreement No 861002

Table 5.7: Coefficients for the TWIN nozzles manufactured with SAC hole A, with first term reduction

coeff.	270 µs	300 µs	350 µs	400 µs	600 µs	800 µs	1000 µs
c_0	-5.4	0.1	-57.9	-22.2	-29.9	-7.8	-32.8
c_2	-3.$*10^5$	-4.$*10^5$	3.0$*10^5$	-720.7	41277	-49715	2.2$*10^5$
c_3	-74222	-1.$*10^5$	-39678	-28016	-11314	-17014	-35420
c_5	83447	1.5$*10^5$	77832	48308	50524	27197	37541
c_8	594	647.5	232.5	183.7	116	130.6	143.1
c_9	0.0001	-0.01	-0.01	-0.002	-0.004	-0.002	-0.004
c_{11}	8.8$*10^8$	1.4$*10^9$	-9.$*10^8$	-3.$*10^8$	-3.$*10^8$	-2.$*10^8$	-9.$*10^8$
c_{13}	1589	8857	3409	-17.7	1755	677.7	498.1
c_{14}	-4.$*10^7$	-2.$*10^8$	1.2$*10^8$	2.5$*10^8$	2.2$*10^8$	2.6$*10^8$	2.5$*10^8$
c_{20}	-3.$*10^7$	-5.$*10^7$	-3.$*10^7$	-2.$*10^7$	-2.$*10^7$	-1.$*10^7$	-2.$*10^7$

Table 5.8: Coefficients for the TWIN nozzles manufactured with SAC hole B, with first term reduction

coeff.	270 µs	300 µs	350 µs	400 µs	600 µs	800 µs	1000 µs
c_0	-5.4	0.1	-57.9	-22.2	-29.9	-7.8	-32.8
c_2	-3.$*10^5$	-4.$*10^5$	3.0$*10^5$	-720.7	41277	-49715	2.2$*10^5$
c_3	-74222	-1.$*10^5$	-39678	-28016	-11314	-17014	-35420
c_5	83447	1.5$*10^5$	77832	48308	50524	27197	37541
c_8	594	647.5	232.5	183.7	116	130.6	143.1
c_9	0.0001	-0.01	-0.01	-0.002	-0.004	-0.002	-0.004
c_{11}	8.8$*10^8$	1.4$*10^9$	-9.$*10^8$	-3.$*10^8$	-3.$*10^8$	-2.$*10^8$	-9.$*10^8$
c_{13}	1589	8857	3409	-17.7	1755	677.7	498.1
c_{14}	-4.$*10^7$	-2.$*10^8$	1.2$*10^8$	2.5$*10^8$	2.2$*10^8$	2.6$*10^8$	2.5$*10^8$
c_{20}	-3.$*10^7$	-5.$*10^7$	-3.$*10^7$	-2.$*10^7$	-2.$*10^7$	-1.$*10^7$	-2.$*10^7$

observed that the lowest error for SAC hole A is from 400 µs energization duration and for SAC hole B from 1000 µs. The highest error is from 270 µs for both SAC holes, which is higher than from the calculations without the first term reduction and has lead to the change in the orders of magnitude.

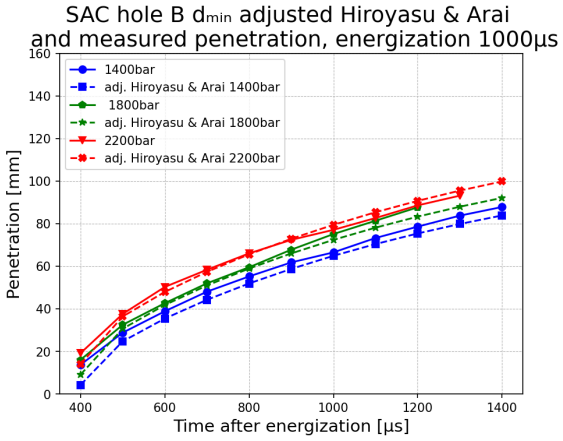
An example of how the adjusted penetration calculated from Equation 5.5 fits the measured penetration after the first iteration of dropping terms of the TWIN nozzles N8, N18, N21 and N24 with SAC hole B and 1000 µs energization duration can be seen in Figure 5.4. Again, for this case it can be observed, that the predicted penetrations fits better for smaller spray hole diameters.

A second iteration was taken to drop slightly different terms, this time the terms, $c_4\Delta\beta$, $c_9\Delta P\Delta\beta$, $c_{10}\Delta Pt$, $c_{13}D\Delta\beta$, $c_{16}h\Delta\beta$, $c_{17}ht$, $c_{18}\Delta\beta^2$, $c_{19}\Delta\beta t$ and $c_{20}t^2$ were dropped from the calculations. The selection was based on an iterative RMSE based term re-

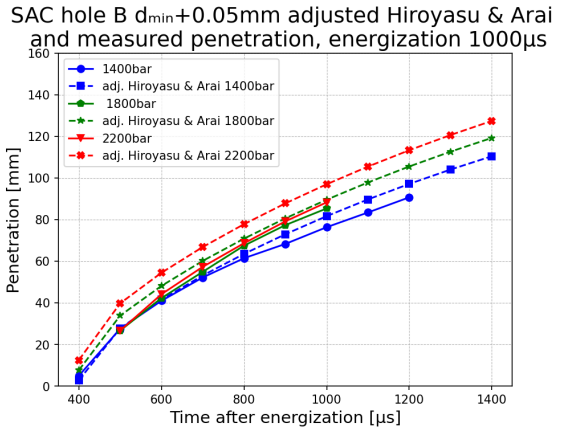
This project has received funding from the European Union Horizon 2020 Research and Innovation programme. Grant Agreement No 861002

Table 5.9: Root Mean Squared Error for the adjusted Hiroyasu calculations for TWIN nozzles, with first term reduction

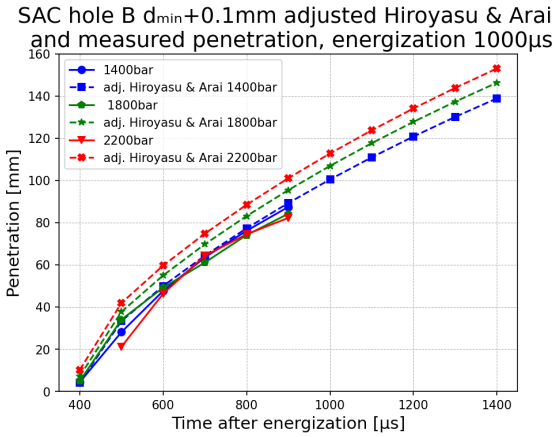
energization duration	SAC A RMSE	SAC B RMSE
270 µs	12.67	9.496
300 µs	9.404	4.974
350 µs	3.545	4.012
400 µs	3.278	3.561
600 µs	3.438	3.603
800 µs	3.511	3.397
1000 µs	3.456	3.318



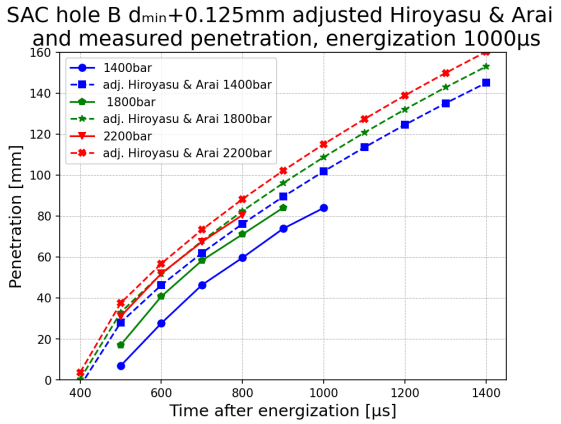
(a)



(b)



(c)



(d)

Figure 5.4: TWIN nozzle adjustment after the first iteration of dropping terms for Hiroyasu and Arai, Nozzle N8 (a), N18 (b), N21 (c) and N24 (d) for SAC hole B with 1000 µs energization

This project has received funding from the European Union Horizon 2020 Research and Innovation programme. Grant Agreement No 861002

Table 5.10: Coefficients for the TWIN nozzles manufactured with SAC hole A, with second term reduction

coeff.	270 µs	300 µs	350 µs	400 µs	600 µs	800 µs	1000 µs
c_0	266.8	-17.3	-20.8	31.7	0.8	94.2	-65.3
c_1	-0.6	1.8	0.1	0.04	0.1	0.05	-0.01
c_2	-1.$*10^6$	-1.$*10^6$	1.5$*10^5$	-3.$*10^5$	-66131	-5.$*10^5$	2.1$*10^5$
c_3	-7.$*10^5$	-81513	-62132	-21460	-32946	-2.$*10^5$	2.5$*10^5$
c_5	16572	40881	6162	-18002	-9635	-14442	-14296
c_6	-0.000004	-0.01	-0.001	0.0001	0.0002	-0.0004	0.0002
c_7	3152	3277	879.7	553.3	191.4	550.1	437.9
c_8	663	-52.1	307.8	-242.5	-284.3	65	-210
c_{11}	6.9$*10^8$	1.9$*10^9$	-9.$*10^8$	-4.$*10^7$	-3.$*10^8$	1.5$*10^8$	-9.$*10^8$
c_{12}	7.5$*10^8$	5.8$*10^8$	-4.$*10^7$	2.7$*10^8$	2.3$*10^7$	5.7$*10^8$	-3.$*10^8$
c_{14}	-3.$*10^7$	-9.$*10^7$	1.9$*10^8$	3.4$*10^8$	3.0$*10^8$	3.2$*10^8$	3.2$*10^8$
c_{15}	7.0$*10^8$	-1.$*10^7$	2.1$*10^7$	2.3$*10^7$	1.1$*10^8$	2.2$*10^8$	-2.$*10^8$

duction procedure, where terms with the smallest contribution to the model accuracy were removed first. The resulting increase in RMSE was minor and therefore considered acceptable in exchange for a more compact and robust regression model. This results in the Equation 5.7.

$$S_{adjustedTWIN} = S + c_0 + c_1\Delta P + c_2 D + c_3 h + c_5 t + c_6\Delta P^2 + c_7\Delta P D + c_8\Delta P h + c_{11} D^2 + c_{12} D h + c_{14} D t + c_{15} h^2 \tag{5.7}$$

With the Equation 5.7 the coefficients for the input values were newly calculated. For the nozzles with SAC hole A, these are shown in Table 5.10. Here the difference in the oders of magnitude is visible again, with 270 µs energization duration differing from the other durations.

Similar to Table 5.10, the coefficients for SAC hole B are shown in Table 5.11. Here no difference in the orders of magnitude is visible.

The average Root Mean Squared Error for each of these formulas compared to the measured spray penetrations of the TWIN nozzles is shown in Table 5.12. The lowest error for SAC hole A is from 400 µs and for SAC hole B from 800 µs while the highest error is from 270 µs for both SAC holes again.

An example of how the adjusted penetration calculated from Equation 5.5 fits the measured penetration after the second iteration of dropping terms of the TWIN nozzles N8, N18, N21 and N24 with SAC hole B and 1000 µs energization duration can be seen in Figure 5.5. The behaviour is in accordance with the previous comparisons.

This project has received funding from the European Union Horizon 2020 Research and Innovation programme. Grant Agreement No 861002

Table 5.11: Coefficients for the TWIN nozzles manufactured with SAC hole B, with second term reduction

coeff.	270 µs	300 µs	350 µs	400 µs	600 µs	800 µs	1000 µs
c_0	-5.4	0.1	-57.9	-22.2	-29.9	-7.8	-32.8
c_2	-3.$*10^5$	-4.$*10^5$	3.0$*10^5$	-720.7	41277	-49715	2.2$*10^5$
c_3	-74222	-1.$*10^5$	-39678	-28016	-11314	-17014	-35420
c_5	83447	1.5$*10^5$	77832	48308	50524	27197	37541
c_8	594	647.5	232.5	183.7	116	130.6	143.1
c_9	0.0001	-0.01	-0.01	-0.002	-0.004	-0.002	-0.004
c_{11}	8.8$*10^8$	1.4$*10^9$	-9.$*10^8$	-3.$*10^8$	-3.$*10^8$	-2.$*10^8$	-9.$*10^8$
c_{13}	1589	8857	3409	-17.7	1755	677.7	498.1
c_{14}	-4.$*10^7$	-2.$*10^8$	1.2$*10^8$	2.5$*10^8$	2.2$*10^8$	2.6$*10^8$	2.5$*10^8$
c_{20}	-3.$*10^7$	-5.$*10^7$	-3.$*10^7$	-2.$*10^7$	-2.$*10^7$	-1.$*10^7$	-2.$*10^7$

Table 5.12: Root Mean Squared Error for the adjusted Hiroyasu calculations for TWIN nozzles, with second term reduction

energization duration	SAC A RMSE	SAC B RMSE
270 µs	12.664	8.667
300 µs	8.143	5.124
350 µs	3.852	4.42
400 µs	3.446	3.593
600 µs	3.601	3.67
800 µs	3.555	3.434
1000 µs	3.59	3.399

A third and final iteration was undertaken to reduce all terms that were dropped in the first and second iteration, leading to the Equation 5.8.

$$S_{adjustedTWIN} = S + c_0 + c_2 D + c_3 h + c_5 t + c_7 \Delta P D + c_8 \Delta P h + c_{11} D^2 + c_{14} D t \quad (5.8)$$

With the Equation 5.8 the coefficients for the input values were calculated a third time. For the nozzles with SAC hole A, these are shown in Table 5.13. Again, there is no difference in the orders of magnitude of the coefficients visible.

Similar to Table 5.13, the coefficients for SAC hole B are shown in Table 5.14. The coefficients are in the same order of magnitude for all energization durations.

The average Root Mean Squared Error for each of these formulas compared to the measured spray penetrations of the TWIN nozzles is shown in Table 5.16. For SAC hole A the smallest error is from 400 µs and for SAC hole B from 1000 µs. The highest

This project has received funding from the European Union Horizon 2020 Research and Innovation programme. Grant Agreement No 861002

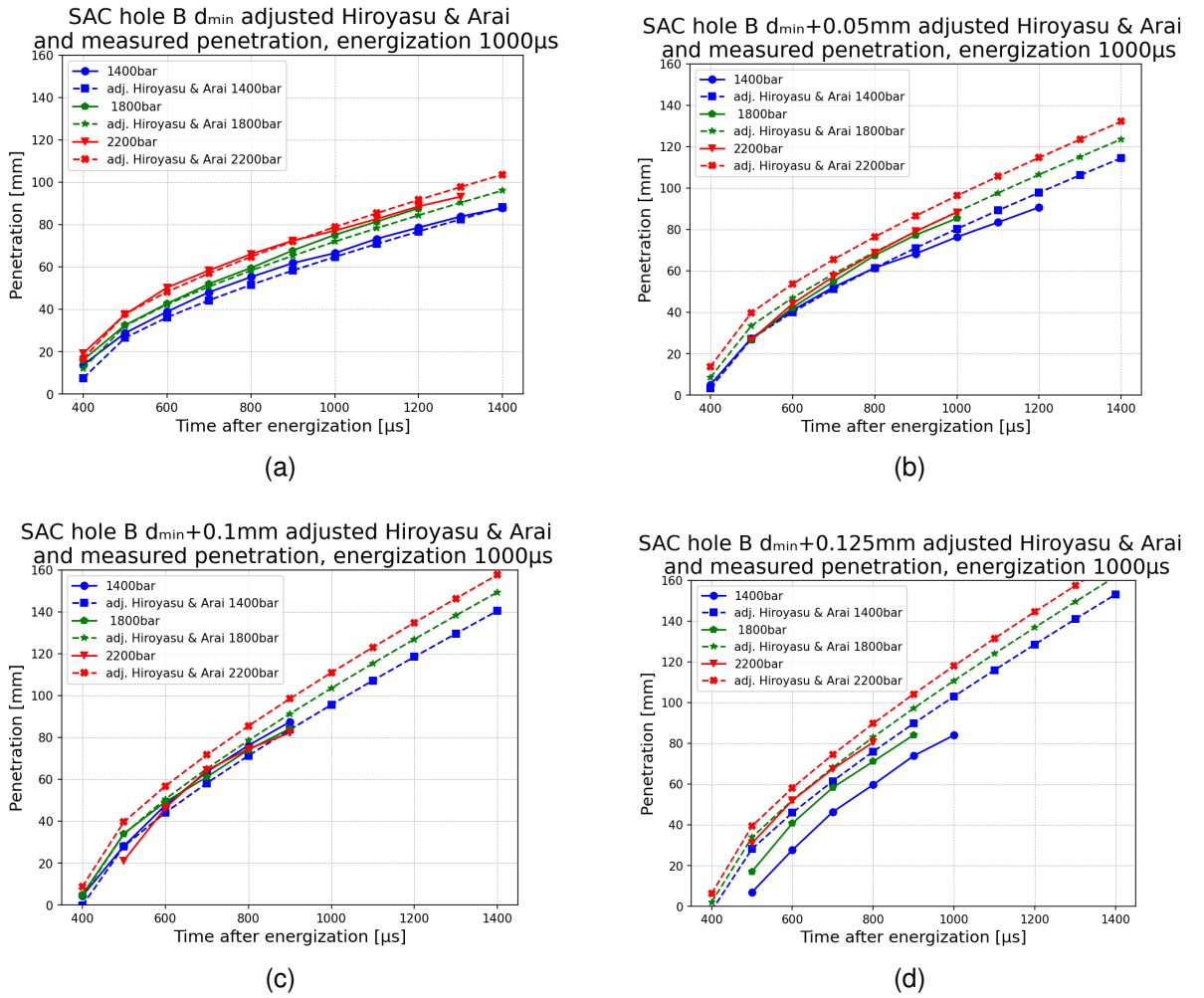


Figure 5.5: TWIN nozzle adjustment after the second iteration of dropping terms for Hiroyasu and Arai, Nozzle N8 (a), N18 (b), N21 (c) and N24 (d) for SAC hole B with 1000 µs energization

errors are from 270 µs for both SAC holes.

An example of how the adjusted penetration calculated from Equation 5.5 fits the measured penetration after the third iteration of dropping terms of the TWIN nozzles N8, N18, N21 and N24 with SAC hole B and 1000 µs energization duration can be seen in Figure 5.6. These behave in accordance with the previous penetration predictions.

For easier comparison, the difference between the Root Mean Squared Error calculated from Equation 5.5 , where no terms were dropped, to the three Root Mean Squared Errors from the term reduction Equations 5.6 - 5.8 were calculated and are shown in Table 5.16. It can be observed the highest rise in Root Mean Squared Error difference is from 270 & 300 µs for all reductions while the lowest rises are from 600 & 800 µs.

From the results in Table 5.16 it can be deducted, that all reductions have a small

This project has received funding from the European Union Horizon 2020 Research and Innovation programme. Grant Agreement No 861002

Table 5.13: Coefficients for the TWIN nozzles manufactured with SAC hole A, with third term reduction

coeff.	270 µs	300 µs	350 µs	400 µs	600 µs	800 µs	1000 µs
c_0	18.6	32.7	-32.4	8.2	-1.6	9.5	-9.1
c_2	-3.$*10^5$	-4.$*10^5$	3.0$*10^5$	-73103	-30106	-80736	1.6$*10^5$
c_3	-75670	-1.$*10^5$	-43015	-30972	-11921	-18214	-35243
c_5	17535	61982	11408	-13306	-8394	-12589	-11844
c_8	602	678.1	248.9	199.5	123.6	138.7	144.8
c_{11}	8.2$*10^8$	1.3$*10^9$	-9.$*10^8$	-2.$*10^8$	-3.$*10^8$	-2.$*10^8$	-8.$*10^8$
c_{14}	-4.$*10^7$	-2.$*10^8$	1.6$*10^8$	3.1$*10^8$	2.9$*10^8$	3.1$*10^8$	3.1$*10^8$

Table 5.14: Coefficients for the TWIN nozzles manufactured with SAC hole B, with third term reduction

coeff.	270 µs	300 µs	350 µs	400 µs	600 µs	800 µs	1000 µs
c_0	-79.1	-76.4	-24.5	-6.6	7.2	24.9	14.9
c_2	4.2$*10^5$	7.2$*10^5$	2.2$*10^5$	1.4$*10^5$	-18873	-2.$*10^5$	-71868
c_3	-28959	-64631	-43109	-52611	-33620	-45378	-37474
c_5	51184	24951	14352	-20793	-34179	-33458	-37015
c_8	580.3	440.8	294.4	301	257.4	308.3	272.2
c_{11}	-5.$*10^8$	-1.$*10^9$	-6.$*10^8$	-7.$*10^8$	-5.$*10^8$	3.6$*10^6$	-3.$*10^8$
c_{14}	-2.$*10^8$	2.3$*10^7$	1.0$*10^8$	3.4$*10^8$	4.3$*10^8$	4.3$*10^8$	4.4$*10^8$

influence on the Root Mean Squared Error, and therefore the Equation 5.8 with reduction of the single hole difference, calculated with Equation 5.4, is recommended to further calculate TWIN Nozzles in the future with Hiroyasu as base formula. Only for 270 µs and 300 µs energization duration it can be observed that there are high Root Mean Squared Errors which rise significantly with reducing the terms, showing that the variables like relative spray angle and spray hole distance have a higher influence on these. Also, due to high shot-to-shot variations with these energization durations, the Root Mean Squared Error is on a overall higher level compared to other energization durations.

This project has received funding from the European Union Horizon 2020 Research and Innovation programme. Grant Agreement No 861002

Table 5.15: Root Mean Squared Error for the adjusted Hiroyasu calculations for TWIN nozzles, with third term reduction

energization duration	SAC A RMSE	SAC B RMSE
270 µs	13.275	10.103
300 µs	10.098	5.568
350 µs	3.941	4.57
400 µs	3.655	3.819
600 µs	3.666	3.715
800 µs	3.678	3.606
1000 µs	3.776	3.445

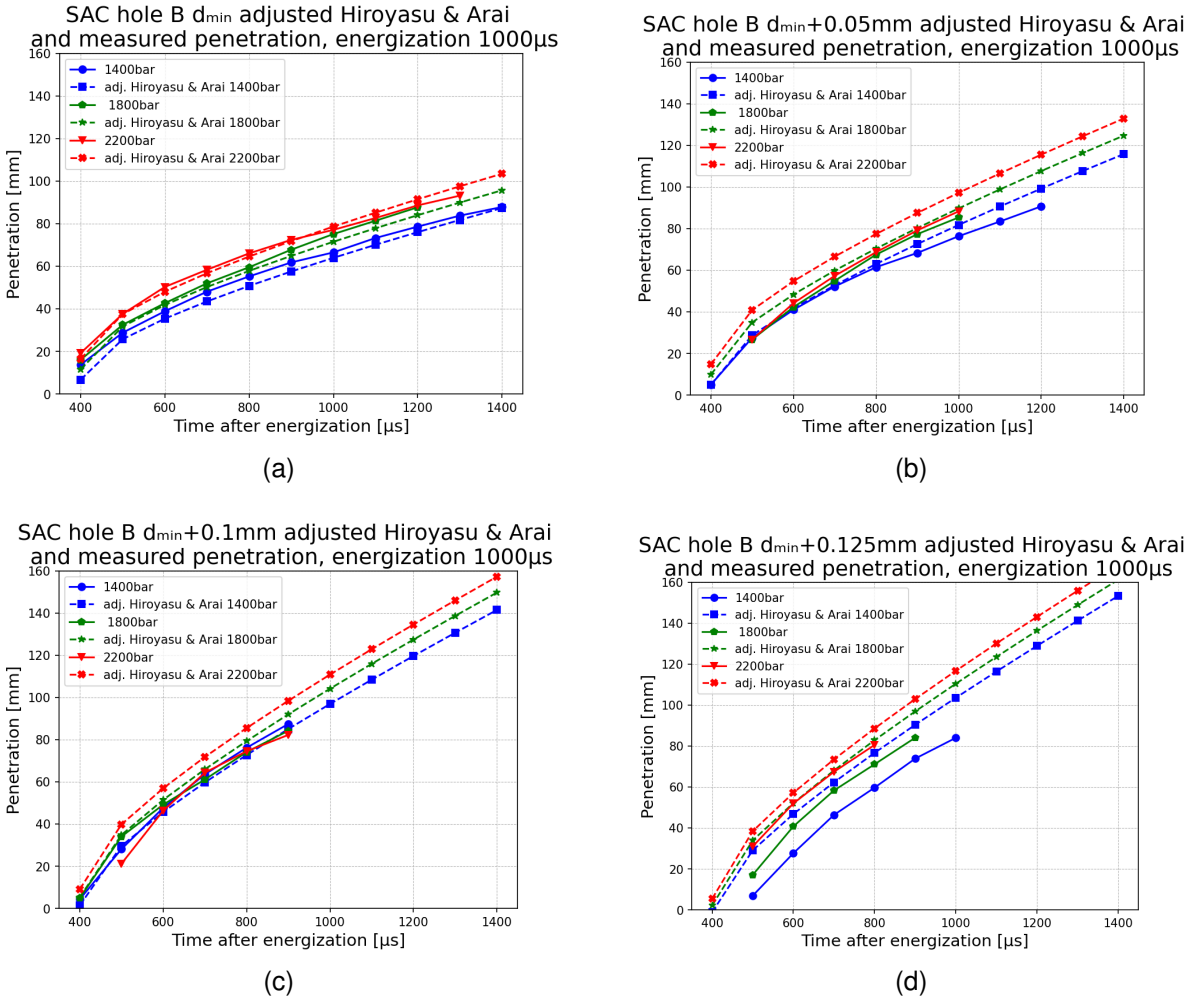


Figure 5.6: TWIN nozzle adjustment after the third iteration of dropping terms for Hiroyasu and Arai, Nozzle N8 (a), N18 (b), N21 (c) and N24 (d) for SAC hole B with 1000 µs energization

This project has received funding from the European Union Horizon 2020 Research and Innovation programme. Grant Agreement No 861002

Table 5.16: Difference between the Root Mean Squared Error without term reduction to reduced terms

energization duration	SAC A RMSE difference first reduction	SAC B RMSE difference first reduction	SAC A RMSE difference second reduction	SAC B RMSE difference second reduction	SAC A RMSE difference third reduction	SAC B RMSE difference third reduction
270 µs	0.754	1.983	0.747	1.154	1.358	2.59
300 µs	2.237	0.53	0.976	0.68	2.931	1.124
350 µs	0.148	0.186	0.455	0.594	0.545	0.744
400 µs	0.239	0.219	0.407	0.251	0.615	0.477
600 µs	0.208	0.074	0.372	0.141	0.436	0.186
800 µs	0.249	0.182	0.294	0.219	0.417	0.391
1000 µs	0.278	0.117	0.413	0.198	0.599	0.244

5.2 Single hole comparison and TWIN adjustment based on the Spray penetration formula from Naber and Siebers

For the marine transportation sector, Naber and Siebers [95] showed that the calculations from Hiroyasu and Arai [94] could be improved. Similar to the calculations from Hiroyasu and Arai [94], the calculations from Naber and Siebers [95] have been compared to the single nozzle results too. Again, these underperformed due to the presence of only two spray holes and the high pressures, therefore another formula adjustment was determined based on a second degree linear regression model using the TWIN nozzle geometric variables. The spray penetration according to Naber and Siebers can be calculated as shown in Equations 5.9 - 5.11. where

t is the time after the injection start

t_r is the transition time

ΔP is the Pressure difference between ambient and injection

ρ_l is the liquid density

ρ_a is the ambient density

D is the spray hole diameter

θ is the spray cone angle

This project has received funding from the European Union Horizon 2020 Research and Innovation programme. Grant Agreement No 861002

Table 5.17: Coefficients for the single hole nozzles manufactured with SAC hole A

coeff.	270 µs	300 µs	350 µs	400 µs	600 µs	800 µs	1000 µs
c_0	-313.2	-47.9	-22.6	-13.7	-8.8	-6.8	70.8
c_1	2.8	0.3	0.1	-0.05	-0.2	-0.01	-0.7
c_2	$5.84*10^5$	23260	-46699	72944	40868	24910	$-1.7*10^5$
c_3	15492	66714	81472	50486	64696	40266	43753
c_4	-0.01	-0.002	-0.001	-0.0002	0.001	-0.001	0.001
c_5	-257.4	958.6	445.7	161.3	-188.7	584.5	663.1
c_6	461.6	363.3	164.9	133.8	64.8	102.5	246.6
c_7	$-1.0*10^9$	$-4.0*10^8$	$-1.6*10^8$	$-3.9*10^8$	$-2.5*10^8$	$-4.4*10^8$	$-1.0*10^8$
c_8	$-1.0*10^8$	$-6.6*10^7$	$4.05*10^7$	$1.11*10^8$	$1.23*10^8$	$1.32*10^8$	$1.10*10^8$
c_9	$-3.1*10^7$	$-4.0*10^7$	$-4.0*10^7$	$-2.5*10^7$	$-2.6*10^7$	$-1.8*10^7$	$-3.0*10^7$

C_a is the area coefficient

C_v is the velocity coefficient

$0 < t < t_r$

$$S = C_v(\frac{2\Delta P}{\rho_l})^{0.5} t \tag{5.9}$$

$t > t_r$

$$S = \sqrt{\frac{C_v\sqrt{2C_a}}{0.66\tan\theta/2}}\sqrt{\sqrt{\frac{\Delta P}{\rho_a}}Dt} \tag{5.10}$$

$$t_r = \frac{\sqrt{\frac{C_a}{2}}}{C_v 0.66\tan\theta/2}\frac{D\widetilde{\rho_l}^{0.5}}{\sqrt{\frac{\Delta P}{\rho_l}}} \tag{5.11}$$

5.2.1 Single hole nozzle adjustment

The adjustment for the single spray hole nozzles is shown in Equation 5.4. The coefficients for the nozzles with SAC hole A are shown in Table 5.17. Similar to the adjustments in the previous section, it can be observed that the coefficients from 270 µs differ from the coefficients from the other energization durations.

Similar to Table 5.17 the coefficients for the nozzles with SAC hole B are shown in Table 5.18. Here, also the coefficients from 270 µs differ.

The average Root Mean Squared Error for each of these formulas compared to the measured spray penetrations of the single hole nozzles is shown in Table 5.19. It can be observed that the highest error is from 270 µs for SAC hole A and from 300 µs for SAC hole B.

This project has received funding from the European Union Horizon 2020 Research and Innovation programme. Grant Agreement No 861002

Table 5.18: Coefficients for the single hole nozzles manufactured with SAC hole B

coeff.	270 µs	300 µs	350 µs	400 µs	600 µs	800 µs	1000 µs
c_0	1.82$*10^5$	-25.3	-21.6	-69.8	-102.5	-44.6	-68.9
c_1	-1892	-0.2	-0.2	0.2	0.6	0.3	0.6
c_2	-41396	1.06$*10^5$	-41080	87075	1.02$*10^5$	-1.7$*10^5$	-55700
c_3	14282	97783	1.19$*10^5$	1.16$*10^5$	91872	90945	69639
c_4	4.9	-0.001	-0.0005	-0.001	-0.002	-0.001	-0.002
c_5	2079	1593	1391	667.6	529.2	685.3	641.3
c_6	658.4	224.9	167.2	95.6	-21.6	17.9	81.7
c_7	-6.1$*10^8$	-6.7$*10^8$	-3.9$*10^8$	-4.7$*10^8$	-4.2$*10^8$	4.28$*10^6$	-2.6$*10^8$
c_8	-1.1$*10^8$	-7.4$*10^7$	-1.7$*10^7$	2.40$*10^7$	5.70$*10^7$	9.33$*10^7$	1.16$*10^8$
c_9	-4.5$*10^7$	-4.6$*10^7$	-5.4$*10^7$	-5.1$*10^7$	-2.8$*10^7$	-3.5$*10^7$	-3.2$*10^7$

Table 5.19: Root Mean Squared Error for the adjusted Naber calculations for single hole nozzles

energization duration	SAC A RMSE	SAC B RMSE
270 µs	4.092	2.998
300 µs	2.986	3.271
350 µs	3.645	3.164
400 µs	2.917	3.18
600 µs	2.42	2.284
800 µs	2.164	2.201
1000 µs	2.92	2.222

An example of how the adjusted penetration calculated from Equation 5.4 fits the measured penetration based on the calculations form Naber and Siebers can be seen in Figure 5.7. Again, the adjusted penetrations predict the spray more accurate and will therefore be used as reference.

This project has received funding from the European Union Horizon 2020 Research and Innovation programme. Grant Agreement No 861002

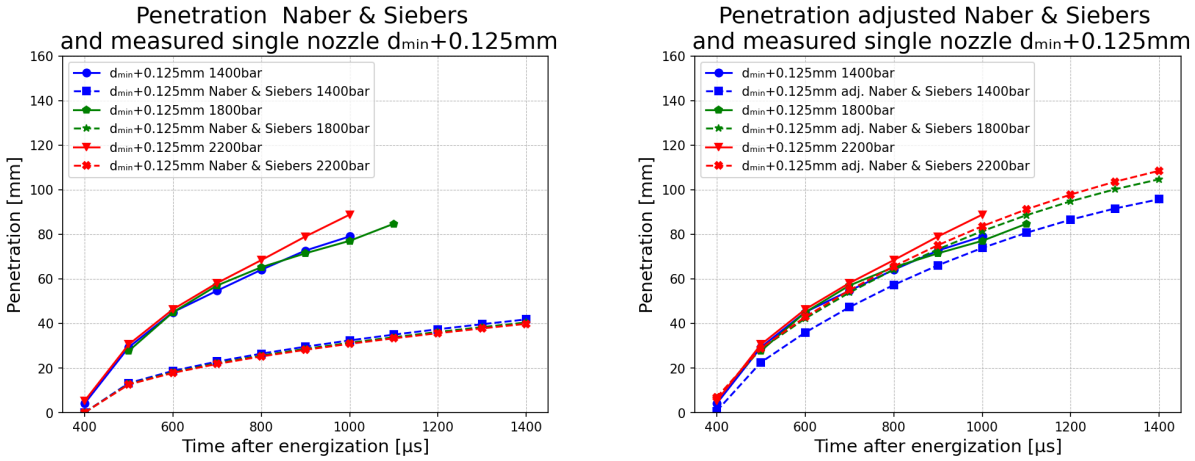


Figure 5.7: Comparison of the measured single hole nozzle penetration with the calculation after Naber and Siebers, not adjusted (a) and adjusted (b)

5.2.2 TWIN nozzle adjustments

Similar to the previous section, the Naber and Siebers Equation was adjusted for the TWIN nozzle in three iterations, starting with the usage of all coefficients from Equation 5.5. For SAC hole A, these are shown in Table 5.20. Again, the coefficients from 270 µs differ from the other coefficients du to the instability during the needle opening time.

The coefficients from Equation 5.5 for the nozzles with SAC hole B are shown in Table 5.21. Here, the coefficients for 270 and 300 µs differ, which is in accordance with the observations from the previous section.

The average Root Mean Squared Error for each of these formulas compared to the measured spray penetrations of the TWIN nozzles is shown in Table 5.22. Again, the highest error is from 270 µs for both SAC holes. The lowest error for SAC hole A is from 400 µs and for SAC hole B from 1000 µs.

An example of how the adjusted Naber and Siebers penetration calculated from Equation 5.5 fits the measured penetration of the TWIN nozzles N8, N18, N21 and N24 with SAC hole B and 1000 µs energization duration can be seen in Figure 5.8. The behaviour is similar to the adjustments from the previous section.

In accordance to Equation 5.6 the coefficients for the input values after the first drop of terms were newly calculated. For the nozzles with SAC hole A, these are shown in Table 5.23. There is no difference in the order of magnitude visible.

Similar to Table 5.23, the coefficients for SAC hole B are shown in Table 5.24. Again, no difference can be observed.

This project has received funding from the European Union Horizon 2020 Research and Innovation programme. Grant Agreement No 861002

Table 5.20: Coefficients for the TWIN nozzles manufactured with SAC hole A

coeff.	270 µs	300 µs	350 µs	400 µs	600 µs	800 µs	1000 µs
c_0	284.7	32.7	-54.1	-13	-13.8	77.5	-75.2
c_1	-0.7	1.2	-0.1	-0.1	-0.2	-0.2	-0.2
c_2	$-1.1*10^6$	$-1.5*10^6$	$1.62*10^5$	$-2.7*10^5$	-25186	$-5.2*10^5$	$2.70*10^5$
c_3	$-8.7*10^5$	-78495	5477	20896	3794	$-2.3*10^5$	$2.39*10^5$
c_4	-6.2	0.4	0.8	-1.1	1.9	2.6	-1.3
c_5	70083	70894	$1.06*10^5$	90255	73750	59088	62167
c_6	-0.0003	-0.01	-0.001	0.0003	0.001	-0.0001	0.0005
c_7	3008	3379	880.7	617.2	411.8	670.8	543.2
c_8	810.9	-199.2	233.5	-287.8	-224.8	104.7	-208.1
c_9	0.02	-0.01	-0.005	-0.003	-0.003	-0.001	-0.003
c_{10}	134	400.8	74.3	35.3	109.9	72.4	84.2
c_{11}	$6.54*10^8$	$1.94*10^9$	$-9.2*10^8$	$-1.2*10^8$	$-4.0*10^8$	$1.63*10^8$	$-1.0*10^9$
c_{12}	$8.73*10^8$	$6.37*10^8$	$-6.1*10^7$	$2.34*10^8$	$-2.4*10^6$	$5.65*10^8$	$-3.1*10^8$
c_{13}	18837	11207	2966	2676	344.9	-1694	3708
c_{14}	$-1.3*10^7$	$-7.0*10^7$	$1.48*10^8$	$2.59*10^8$	$2.42*10^8$	$2.80*10^8$	$2.79*10^8$
c_{15}	$7.24*10^8$	$-9.6*10^6$	$-2.1*10^7$	$7.93*10^6$	$7.30*10^7$	$1.73*10^8$	$-2.0*10^8$
c_{16}	-2414	-1238	-2147	2512	-3530	-4189	2637
c_{17}	$6.45*10^7$	$1.05*10^7$	$-1.9*10^7$	$-2.1*10^7$	$-1.1*10^7$	$-7.5*10^6$	$-6.6*10^6$
c_{18}	-0.1	-0.02	-0.02	-0.01	-0.04	-0.02	-0.02
c_{19}	378.2	325.1	-8.6	-299	-629.2	-789.4	-477.6
c_{20}	$-4.9*10^7$	$-4.9*10^7$	$-4.5*10^7$	$-4.2*10^7$	$-3.9*10^7$	$-3.3*10^7$	$-3.5*10^7$

The average Root Mean Squared Error for each of these formulas compared to the measured spray penetrations of the TWIN nozzles is shown in Table 5.25. The highest error is from 270 µs for both SAC holes and the lowest error for SAC hole A is from 400 µs and for SAC hole B from 1000 µs energization duration.

An example of how the adjusted Naber and Siebers penetration calculated from Equation 5.5 fits the measured penetration after the first iteration of dropping terms of the TWIN nozzles N8, N18, N21 and N24 with SAC hole B and 1000 µs energization duration can be seen in Figure 5.9.

In accordance to Equation 5.7 the coefficients for the input values were newly calculated after the second term dropping. For the nozzles with SAC hole A, these are shown in Table 5.26. The coefficients from 270 µs show a different behaviour again.

Similar to Table 5.10, the coefficients for SAC hole B are shown in Table 5.27. Here the coefficients from 270 and 300 µs differ.

The average Root Mean Squared Error for each of these formulas compared to the measured spray penetrations of the TWIN nozzles is shown in Table 5.28. The highest

This project has received funding from the European Union Horizon 2020 Research and Innovation programme. Grant Agreement No 861002

Table 5.21: Coefficients for the TWIN nozzles manufactured with SAC hole B

coeff.	270 µs	300 µs	350 µs	400 µs	600 µs	800 µs	1000 µs
c_0	-340.2	-265.5	-53.5	-39.8	-78.2	-63.9	-104.8
c_1	-1	0.7	-0.2	-0.04	0.2	-0.02	0.1
c_2	$2.3*10^6$	$9.7*10^5$	45076	19254	$1.7*10^5$	$2.0*10^5$	$3.3*10^5$
c_3	$9.1*10^5$	$3.4*10^5$	79341	47798	62145	52306	$1.4*10^5$
c_4	-13.9	-0.9	0.8	0.4	2.1	1.1	1.2
c_5	32578	$1.1*10^5$	$1.1*10^5$	63541	66515	68374	67239
c_6	0.004	-0.002	0.0001	-0.0003	-0.0004	-0.0002	-0.0005
c_7	45.5	996.9	845.1	1144	460.8	652.7	278.1
c_8	-1408	-363.5	38.7	112.4	8.5	309	219.7
c_9	0.03	0.004	0.001	0.003	-0.01	-0.002	0.004
c_{10}	325.2	117.6	100.3	40.2	18	9.7	31.7
c_{11}	$-3.*10^9$	$-2.*10^9$	$-4.*10^8$	$-8.*10^8$	$-7.*10^8$	$-6.*10^8$	$-8.*10^8$
c_{12}	$-2.*10^9$	$-7.*10^8$	$-6.*10^7$	$-1.*10^8$	$-3.*10^8$	$-6.*10^8$	$-5.*10^8$
c_{13}	14141	905.2	-3553	-2339	-50.4	-377.2	-7329
c_{14}	$-4.*10^7$	$6.8*10^7$	$1.0*10^8$	$3.2*10^8$	$3.6*10^8$	$3.6*10^8$	$3.6*10^8$
c_{15}	$-3.*10^8$	$-1.*10^8$	$-5.*10^7$	$-5.*10^7$	$3.1*10^7$	$4.4*10^7$	$-5.*10^7$
c_{16}	12909	-234.1	-1228	-1232	-2780	-1762	-1631
c_{17}	$1.0*10^8$	$-9.*10^6$	$-2.*10^7$	$1.9*10^6$	$-2.*10^7$	$-2.*10^7$	$-4.*10^7$
c_{18}	0.01	-0.003	0.003	-0.03	-0.004	-0.003	-0.02
c_{19}	-162.3	-466.4	-249	-463.5	-548.7	-591.3	-443
c_{20}	$-5.*10^7$	$-5.*10^7$	$-5.*10^7$	$-4.*10^7$	$-3.*10^7$	$-3.*10^7$	$-3.*10^7$

error for both SAC holes is from 270 µs and the lowest for SAC hole A is from 800 µs and for SAC hole B from 1000 µs.

An example of how the adjusted Naber and Siebers penetration calculated from Equation 5.5 fits the measured penetration after the second iteration of dropping terms of the TWIN nozzles N8, N18, N21 and N24 with SAC hole B and 1000 µs energization duration can be seen in Figure 5.10. The behaviour is similar to previous observations.

In accordance to the Equation 5.8 the coefficients for the input values were calculated a third time. For the nozzles with SAC hole A, these are shown in Table 5.29. There is no difference in the orders of magnitude visible.

Similar to Table 5.29, the coefficients for SAC hole B are shown in Table 5.30. Also, here there is no difference in the orders of magnitude visible.

The average Root Mean Squared Error for each of these formulas compared to the measured spray penetrations of the TWIN nozzles is shown in Table 5.32. The highest error for both SAC holes is from 270 µs and the lowest for SAC hole A is from 800 µs and for SAC hole B from 1000 µs.

This project has received funding from the European Union Horizon 2020 Research and Innovation programme. Grant Agreement No 861002

Table 5.22: Root Mean Squared Error for the adjusted Naber and Siebers calculations for TWIN nozzles

energization duration	SAC A RMSE	SAC B RMSE
270 µs	11.849	7.481
300 µs	7.104	4.372
350 µs	3.304	3.813
400 µs	2.933	3.334
600 µs	3.148	3.492
800 µs	3.152	3.195
1000 µs	3.083	3.15

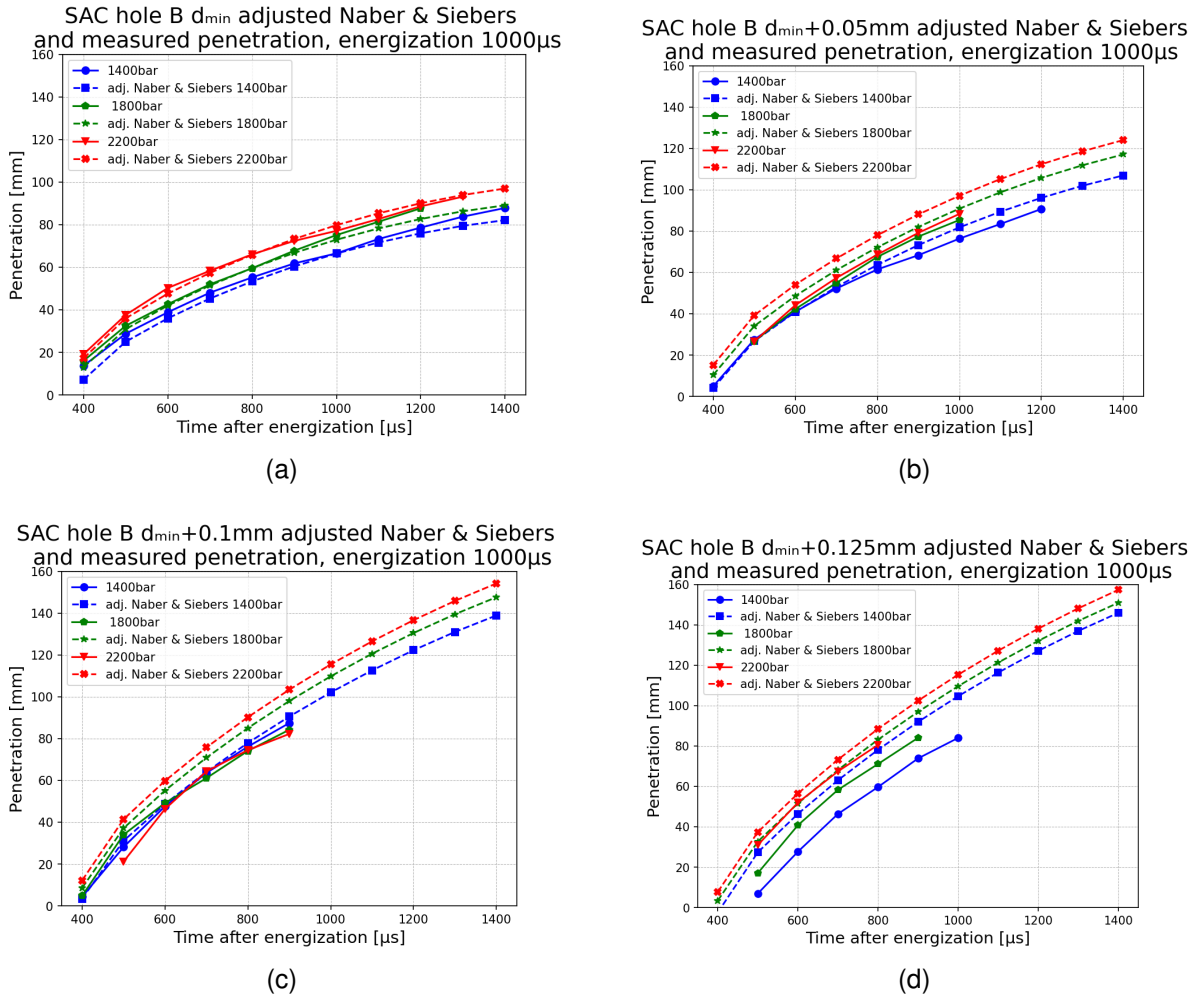


Figure 5.8: TWIN nozzle adjustment for Naber and Siebers, Nozzle N8 (a), N18 (b), N21 (c) and N24 (d) for SAC hole B with 1000 µs energization

An example of how the adjusted Naber and Siebers penetration calculated from Equation 5.5 fits the measured penetration after the third iteration of dropping terms of

This project has received funding from the European Union Horizon 2020 Research and Innovation programme. Grant Agreement No 861002

Table 5.23: Coefficients for the TWIN nozzles manufactured with SAC hole A, with first term reduction

coeff.	270 µs	300 µs	350 µs	400 µs	600 µs	800 µs	1000 µs
c_0	-16.9	-12.9	-70	-35.1	-42.8	-23	-46.4
c_2	-3.$*10^5$	-4.$*10^5$	3.0$*10^5$	3811	37626	-41595	2.2$*10^5$
c_3	-72297	-1.$*10^5$	-37612	-26113	-10095	-15545	-33266
c_5	1.2$*10^5$	1.9$*10^5$	1.2$*10^5$	92940	97270	76599	84726
c_8	584.5	635.2	219.8	171	106.8	120.6	131.7
c_9	-0.00004	-0.01	-0.01	-0.002	-0.004	-0.002	-0.003
c_{11}	8.9$*10^8$	1.3$*10^9$	-9.$*10^8$	-3.$*10^8$	-3.$*10^8$	-2.$*10^8$	-9.$*10^8$
c_{13}	1719	8815	3272	-111	1618	663.1	364.6
c_{14}	-4.$*10^7$	-2.$*10^8$	1.2$*10^8$	2.4$*10^8$	2.2$*10^8$	2.5$*10^8$	2.5$*10^8$
c_{20}	-5.$*10^7$	-6.$*10^7$	-5.$*10^7$	-4.$*10^7$	-4.$*10^7$	-3.$*10^7$	-3.$*10^7$

Table 5.24: Coefficients for the TWIN nozzles manufactured with SAC hole B, with first term reduction

coeff.	270 µs	300 µs	350 µs	400 µs	600 µs	800 µs	1000 µs
c_0	-124.5	-115.2	-63.6	-47.1	-27.8	-12.1	-19.9
c_2	4.1$*10^5$	6.6$*10^5$	2.0$*10^5$	1.9$*10^5$	30896	-1.$*10^5$	-27967
c_3	-33680	-75428	-50823	-62806	-47810	-58572	-45688
c_5	1.7$*10^5$	1.5$*10^5$	1.3$*10^5$	86589	61442	62861	55727
c_8	601.8	489.7	337.7	357.7	333.9	381.3	322.6
c_9	0.01	0.001	0.001	0.001	-0.004	-0.003	0.004
c_{11}	-5.$*10^8$	-1.$*10^9$	-5.$*10^8$	-7.$*10^8$	-4.$*10^8$	-2.$*10^7$	-3.$*10^8$
c_{13}	-8465	-2720	-2953	-2925	2252	286.1	-6093
c_{14}	-2.$*10^8$	8.3$*10^6$	7.4$*10^7$	2.6$*10^8$	3.4$*10^8$	3.5$*10^8$	3.7$*10^8$
c_{20}	-6.$*10^7$	-6.$*10^7$	-5.$*10^7$	-4.$*10^7$	-3.$*10^7$	-3.$*10^7$	-3.$*10^7$

the TWIN nozzles N8, N18, N21 and N24 with SAC hole B and 1000 µs energization duration can be seen in Figure 5.11.

For easier comparison, the difference between the Root Mean Squared Error calculated from Equation 5.5 , where no terms were dropped, to the three Root Mean Squared Errors from the term reduction Equations 5.6 - 5.8 were also calculated based on the adjustment to Naber and Siebers and are shown in Table 5.32. It can be observed the highest rise in Root Mean Squared Error difference is from 270 & 300 µs for all reductions while the lowest rises are from 600 & 800 µs. This is in accordance with the observations from the previous section.

From the results in Table 5.16 it can be deducted, that all reductions have a small influence on the Root Mean Squared Error, and therefore the Equation 5.8 with re-

This project has received funding from the European Union Horizon 2020 Research and Innovation programme. Grant Agreement No 861002

Table 5.25: Root Mean Squared Error for the adjusted Hiroyasu calculations for TWIN nozzles, with first term reduction

energization duration	SAC A RMSE	SAC B RMSE
270 µs	12.604	9.445
300 µs	9.288	5.093
350 µs	3.437	4.006
400 µs	3.176	3.564
600 µs	3.347	3.599
800 µs	3.39	3.395
1000 µs	3.363	3.3

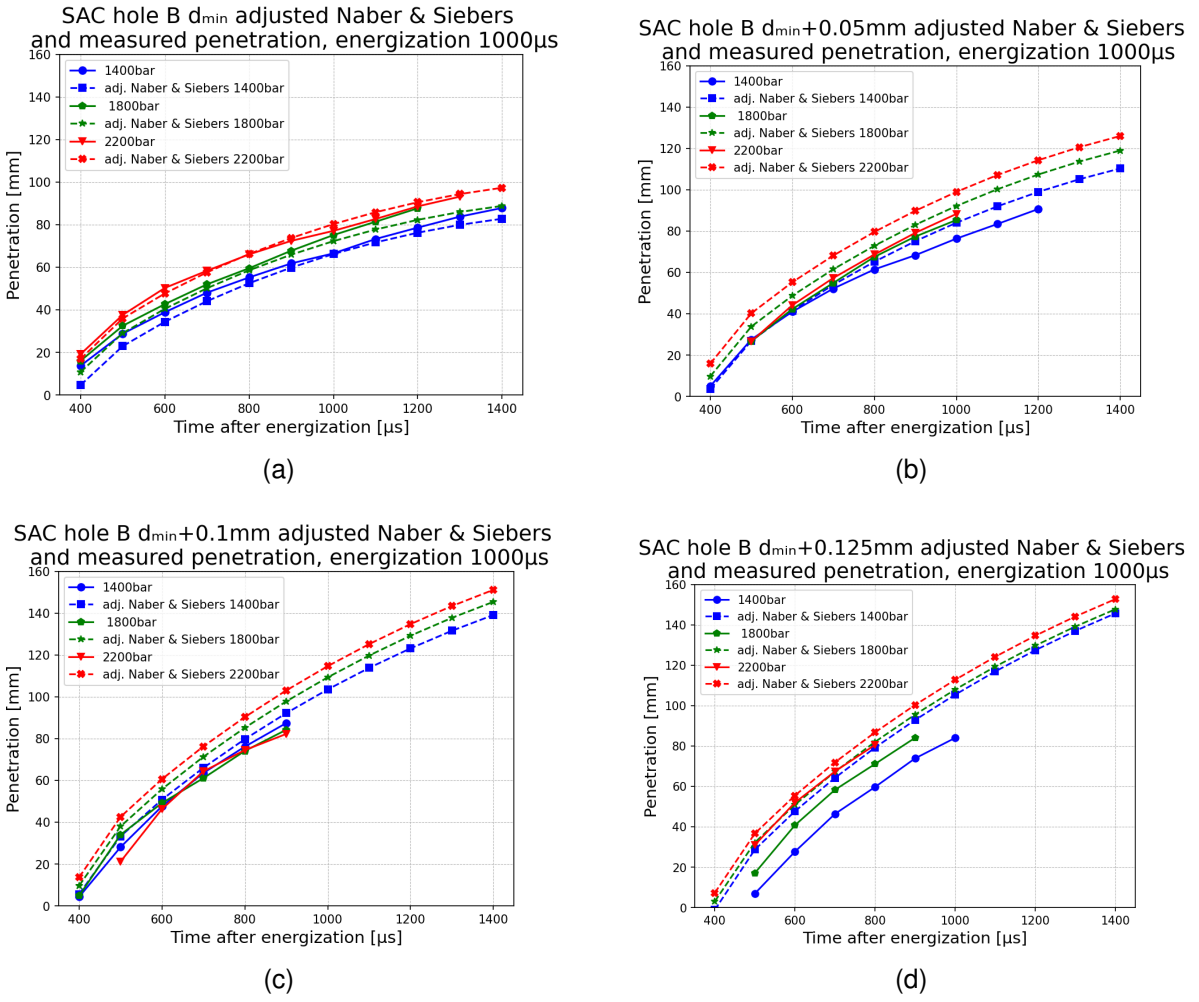


Figure 5.9: TWIN nozzle adjustment after the first iteration of dropping terms for Naber and Siebers, Nozzle N8 (a), N18 (b), N21 (c) and N24 (d) for SAC hole B with 1000 µs energization

This project has received funding from the European Union Horizon 2020 Research and Innovation programme. Grant Agreement No 861002

Table 5.26: Coefficients for the TWIN nozzles manufactured with SAC hole A, with second term reduction

coeff.	270 µs	300 µs	350 µs	400 µs	600 µs	800 µs	1000 µs
c_0	274.2	-21.1	-15.8	37.2	6.3	93.1	-55.1
c_1	-0.6	1.8	0.1	0.01	0.03	0.03	-0.04
c_2	-1.$*10^6$	-1.$*10^6$	1.4$*10^5$	-3.$*10^5$	-1.$*10^5$	-5.$*10^5$	1.6$*10^5$
c_3	-7.$*10^5$	-68040	-71932	-35786	-27749	-2.$*10^5$	2.3$*10^5$
c_5	33106	58259	20876	-5056	2425	-1537	-1533
c_6	0.0001	-0.01	-0.001	0.0002	0.0002	-0.0003	0.0003
c_7	3098	3287	935.3	541.6	224.2	553.2	457.5
c_8	659.5	-60.8	289.4	-232.2	-280.2	52.2	-197.1
c_{11}	7.2$*10^8$	1.8$*10^9$	-1.$*10^9$	-5.$*10^7$	-2.$*10^8$	1.3$*10^8$	-9.$*10^8$
c_{12}	7.9$*10^8$	5.4$*10^8$	-3.$*10^7$	2.5$*10^8$	4.2$*10^7$	5.6$*10^8$	-2.$*10^8$
c_{14}	-3.$*10^7$	-9.$*10^7$	2.0$*10^8$	3.6$*10^8$	3.3$*10^8$	3.5$*10^8$	3.5$*10^8$
c_{15}	7.2$*10^8$	-1.$*10^7$	3.6$*10^7$	4.2$*10^7$	1.0$*10^8$	2.1$*10^8$	-2.$*10^8$

duction of the single hole difference, calculated with Equation 5.4, is recommended to further calculate TWIN Nozzles in the future with Naber and Siebers as base formula.

This project has received funding from the European Union Horizon 2020 Research and Innovation programme. Grant Agreement No 861002

Table 5.27: Coefficients for the TWIN nozzles manufactured with SAC hole B, with second term reduction

coeff.	270 µs	300 µs	350 µs	400 µs	600 µs	800 µs	1000 µs
c_0	-518.3	-269.5	-38.5	-14.2	-27.5	-9.2	-45.6
c_1	-0.3	1	0.1	0.1	0.2	0.01	0.2
c_2	$2.8*10^6$	$1.0*10^6$	67981	-39826	54760	64157	$1.9*10^5$
c_3	$1.1*10^6$	$3.4*10^5$	37012	47774	13222	3577	78083
c_5	57606	34100	26549	-17764	-27098	-26433	-26110
c_6	0.004	-0.002	-0.0004	-0.0004	-0.001	-0.0003	-0.001
c_7	-695.6	816.4	806	1056	425.9	614.3	267
c_8	-1699	-366.3	34.6	106.3	58.6	340	317.9
c_{11}	$-3.*10^9$	$-2.*10^9$	$-5.*10^8$	$-8.*10^8$	$-7.*10^8$	$-5.*10^8$	$-8.*10^8$
c_{12}	$-2.*10^9$	$-7.*10^8$	$-3.*10^7$	$-1.*10^8$	$-2.*10^8$	$-5.*10^8$	$-4.*10^8$
c_{14}	$-1.*10^8$	$7.3*10^7$	$1.4*10^8$	$4.3*10^8$	$5.0*10^8$	$5.0*10^8$	$4.9*10^8$
c_{15}	$-3.*10^8$	$-1.*10^8$	$-3.*10^7$	$-5.*10^7$	$4.1*10^7$	$5.5*10^7$	$-5.*10^7$

Table 5.28: Root Mean Squared Error for the adjusted Naber and Siebers calculations for TWIN nozzles, with second term reduction

energization duration	SAC A RMSE	SAC B RMSE
270 µs	12.923	9.076
300 µs	8.464	5.722
350 µs	4.19	4.987
400 µs	3.767	4.076
600 µs	3.88	3.969
800 µs	3.755	3.815
1000 µs	3.874	3.746

Table 5.29: Coefficients for the TWIN nozzles manufactured with SAC hole A, with third term reduction

coeff.	270 µs	300 µs	350 µs	400 µs	600 µs	800 µs	1000 µs
c_0	17.1	28.9	-33.9	10	1.1	9.4	-7.6
c_2	$-3.*10^5$	$-4.*10^5$	$3.0*10^5$	-95923	-63730	-91529	$1.4*10^5$
c_3	-73841	$-1.*10^5$	-43613	-31133	-12920	-19193	-35026
c_5	33973	79448	26446	-440.2	3864	448.6	1013
c_8	594.7	679.5	248.9	197.6	127.3	142.1	145.3
c_{11}	$8.3*10^8$	$1.3*10^9$	$-1.*10^9$	$-2.*10^8$	$-2.*10^8$	$-2.*10^8$	$-8.*10^8$
c_{14}	$-4.*10^7$	$-2.*10^8$	$1.7*10^8$	$3.4*10^8$	$3.2*10^8$	$3.4*10^8$	$3.4*10^8$

This project has received funding from the European Union Horizon 2020 Research and Innovation programme. Grant Agreement No 861002

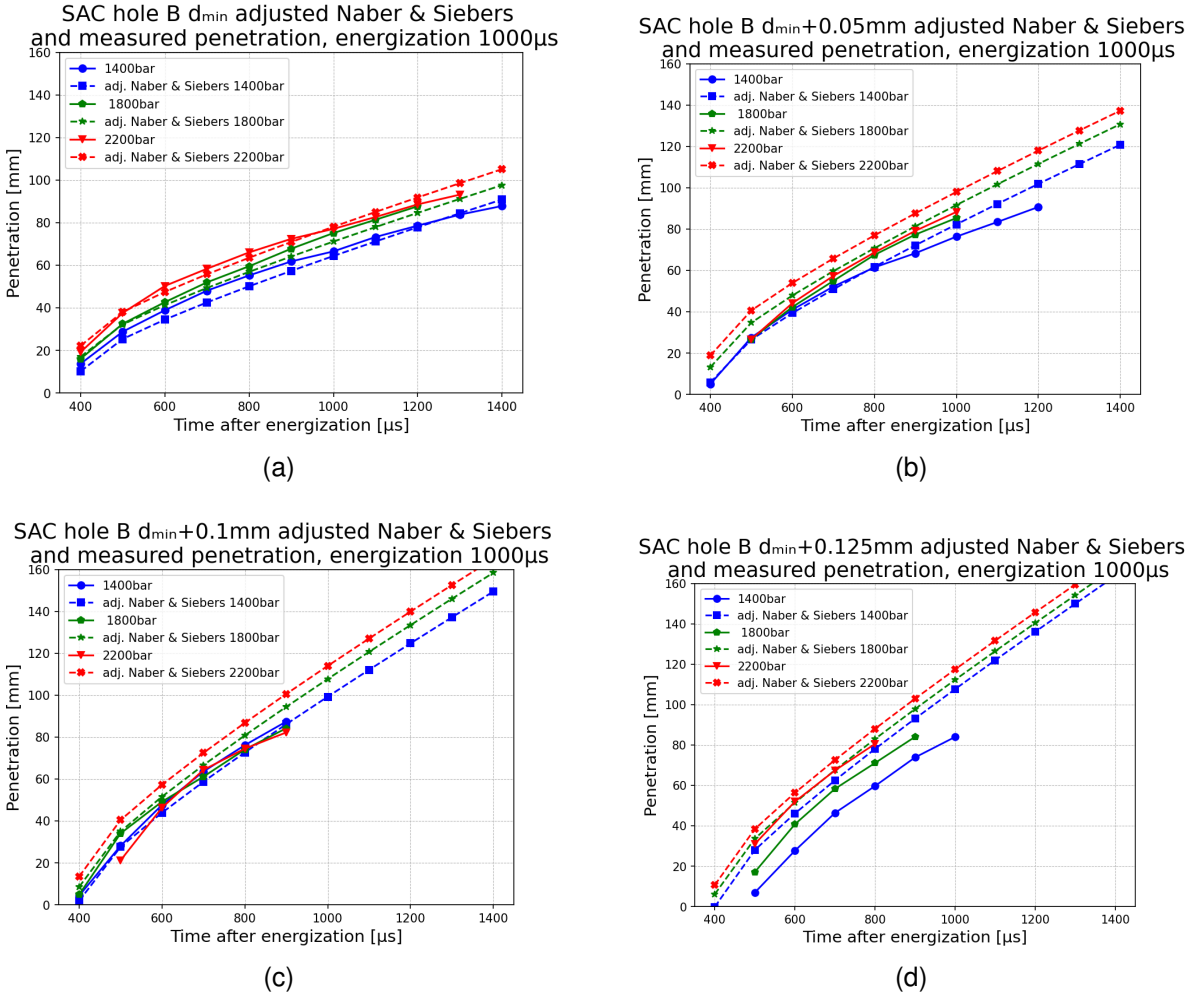


Figure 5.10: TWIN nozzle adjustment after the second iteration of dropping terms for Naber and Siebers, Nozzle N8 (a), N18 (b), N21 (c) and N24 (d) for SAC hole B with 1000 µs energization

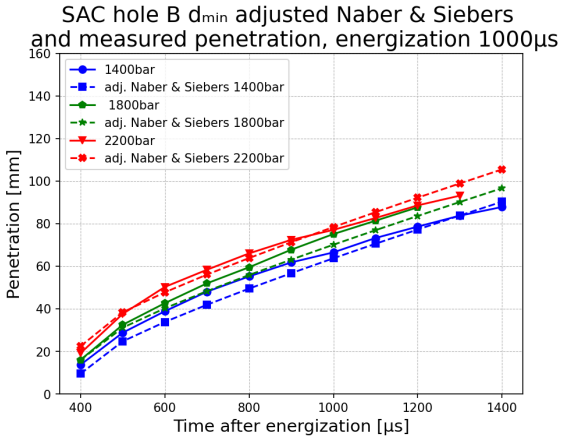
Table 5.30: Coefficients for the TWIN nozzles manufactured with SAC hole B, with third term reduction

coeff.	270 µs	300 µs	350 µs	400 µs	600 µs	800 µs	1000 µs
c_0	-80.8	-80.2	-30.2	-6.2	9.2	26.4	15.6
c_2	$4.2*10^5$	$7.3*10^5$	$2.5*10^5$	$1.2*10^5$	-49853	$-2.*10^5$	-89643
c_3	-42984	-79557	-59134	-67004	-48277	-60443	-53638
c_5	66964	43603	33466	-7839	-23267	-22357	-24735
c_8	656.3	527.8	383.2	381.6	342.4	391.6	359.1
c_{11}	$-5.*10^8$	$-1.*10^9$	$-6.*10^8$	$-7.*10^8$	$-4.*10^8$	$-9.*10^6$	$-4.*10^8$
c_{14}	$-2.*10^8$	$1.7*10^7$	$9.8*10^7$	$3.8*10^8$	$4.7*10^8$	$4.7*10^8$	$4.8*10^8$

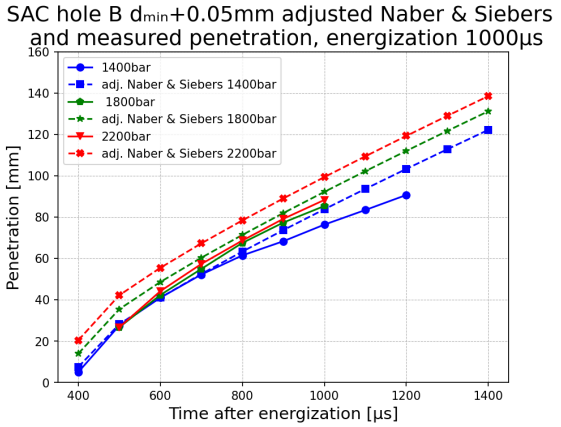
This project has received funding from the European Union Horizon 2020 Research and Innovation programme. Grant Agreement No 861002

Table 5.31: Root Mean Squared Error for the adjusted Naber and Siebers calculations for TWIN nozzles, with third term reduction

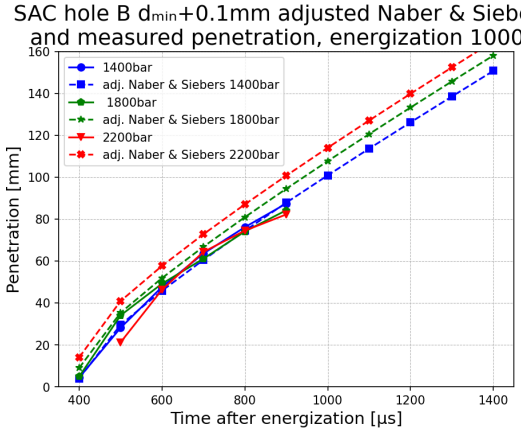
energization duration	SAC A RMSE	SAC B RMSE
270 µs	13.557	10.459
300 µs	10.354	6.252
350 µs	4.29	5.165
400 µs	3.932	4.279
600 µs	3.954	4.032
800 µs	3.857	3.973
1000 µs	4.041	3.825



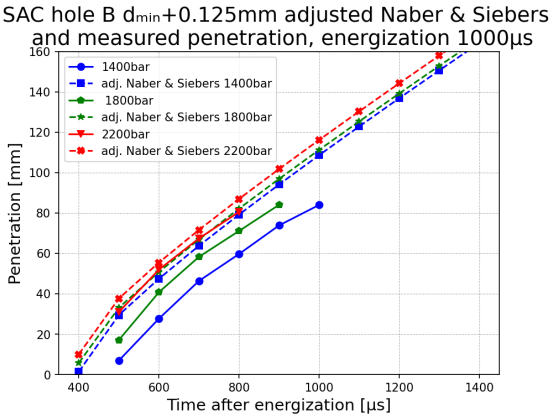
(a)



(b)



(c)



(d)

Figure 5.11: TWIN nozzle adjustment after the third iteration of dropping terms for Naber and Siebers, Nozzle N8 (a), N18 (b), N21 (c) and N24 (d) for SAC hole B with 1000 µs energization

This project has received funding from the European Union Horizon 2020 Research and Innovation programme. Grant Agreement No 861002

Table 5.32: Difference between the Root Mean Squared Error without term reduction to reduced terms

energization duration	SAC A RMSE difference first reduction	SAC B RMSE difference first reduction	SAC A RMSE difference second reduction	SAC B RMSE difference second reduction	SAC A RMSE difference third reduction	SAC B RMSE difference third reduction
270 µs	0.755	1.964	1.074	1.595	1.708	2.978
300 µs	2.185	0.722	1.36	1.35	3.25	1.881
350 µs	0.134	0.192	0.887	1.173	0.986	1.352
400 µs	0.242	0.229	0.834	0.741	0.999	0.945
600 µs	0.2	0.107	0.732	0.477	0.806	0.54
800 µs	0.238	0.2	0.603	0.62	0.705	0.778
1000 µs	0.28	0.15	0.791	0.597	0.958	0.676

This project has received funding from the European Union Horizon 2020 Research and Innovation programme. Grant Agreement No 861002

5.3 Summary

In this chapter it was shown that the most commonly used spray models for the penetrations of marine injectors by either Hiroyasu and Arai and by Naber and Siebers need to be adjusted in order to fit the penetrations measured in the TWIN nozzle experiments. Both spray penetration equations were used because they represent, at the moment this thesis is written, the best prediction models for the conventional heavy-duty injector used in this study. The Hiroyasu spray penetration model was chosen since it is often used during the injector design phase due to its easy applicability. The Naber and Siebers model further improves the Hiroyasu formula by incorporating additional physically based parameters and relationships. However, this increased accuracy comes at the cost of requiring more input variables, some of which may not be available during the early design phase. Firstly, the single hole nozzle penetrations were adjusted to the measurements of the comparison nozzles, due to the fact the the nozzles were only manufactured with two spray holes. Afterwards equations based on the second degree polynomial of the geometric parameters are used to determine the reduction in the energization duration to obtain consistent results. It is shown that the reduction are sufficient for calculation the penetrations for the energization durations 350 - 1000 µs. For the durations of 270 and 300 µs it can be observed that there is a high deviation, since the penetrations of each injection have high shot-to-shot variation due to the short needle opening times. This causes a high noise in the data and therefore complicates correctly calculating the penetrations. It is therefore this authors recommendation to calculate injections with energizations that are long enough to form stable sprays with the terms from the third term reduction. For the shorter energization durations (270 and 300 µs), the unreduced models provide higher predictive accuracy and should therefore be used without applying the term reductions. Furthermore, more research into stabilizing short energization durations is necessary to develop reliable penetration calculations.

This project has received funding from the European Union Horizon 2020 Research and Innovation programme. Grant Agreement No 861002

Chapter 6

Summary and recommendation for future studies

6.1 Summary

This thesis addressed four research gaps related to heavy duty dual-fuel combustion, optical flame development analysis, TWIN nozzle design investigation and the adaptation of established spray penetration models to the novel TWIN geometries. By combining optical combustion diagnostics, pressure based combustion analysis, spray visualization and regression based model development, the interaction between pilot fuel inluence, flame kernel development, combustion stability and spray behaviour was investigated.

These findings contribute to addressing the first research gap identified in this thesis which is the limited understanding of how pilot Diesel injection timing and duration influence low-load dual-fuel combustion. The results demonstrated that split pilot injection strategies enabled stable dual-fuel combustion with minimum Diesel quantity. However, sufficient separation between the injections is necessary for ignition kernel development.

These findings also contribute to addressing the second research gap in this thesis which is the evaluation of cycle-to-cycle variation via flame pixel analysis. The optical flame analysis demonstrated that relatively small changes in pilot injection strategy significantly affected flame kernel formation, flame propagation, and combustion stability. The pixel count based flame analysis provided a detailed assessment of spatial combustion behaviour beyond conventional global combustion parameters and showed that the development of the initial ignition kernel was governed by fuel properties, fuel quantity, and oxygen availability. While cycle-to-cycle variation remained low for pure Diesel combustion, increased variations were observed during dual-fuel operation as

This project has received funding from the European Union Horizon 2020 Research and Innovation programme. Grant Agreement No 861002

combustion became increasingly dependent on the Natural Gas-air mixture.

The main objective of this dual-fuel combustion investigation was to improve the understanding of low-load dual-fuel combustion by linking pilot injection strategy, ignition kernel development, and combustion stability. The novelty of this work lies in the combined use of optical flame imaging and pressure based combustion analysis to identify the role of early flame kernel formation in achieving stable dual-fuel combustion with minimal Diesel pilot quantities. Furthermore, these results are paving a way towards increased Natural Gas substitution rates and therefore lower CO2 emissions in heavy-duty dual-fuel engines.

The findings of the TWIN nozzle investigation contribute to addressing the third research gap identified in this thesis which is how the TWIN nozzle geometry influences the spray development. The results showed that spray hole diameter was the dominant parameter influencing the spray penetration and spray area. Furthermore, the TWIN nozzles generally achieved higher penetration than the comparison nozzles, particularly at short energization durations. This highlights the potential of these nozzles to replace the conventional Diesel nozzles for dual-fuel operation.

The influence of spray hole spacing and relative spray hole angle was comparatively limited. The relative spray hole angle mainly affected the spray angle, while a spray hole distance of h_{min}+ 0.1 mm produced the highest penetration and spray area for SAC B nozzles.

The SAC geometry influenced spray characteristics of the TWIN nozzle sprays. SAC A generally produced lower penetration but stable spray development whereas SAC B achieved higher penetration but reduced stability at short energization durations. These findings provide guidance for future injector design and can potentially improve the spray penetration modelling.

The fourth research gap concerned the applicability of established spray penetration correlations to TWIN row nozzle geometries. Both the Hiroyasu Arai and Naber and Siebers models were selected because they have been shown to predict the spray characteristics of conventional heavy-duty injectors with high accuracy. While the Hiroyasu model provides a simple and practical design tool requiring only a limited number of input parameters, the Naber and Siebers model offers a more physically based prediction at the expense of additional input requirements.

It was shown that both conventional models require modification to accurately predict the penetration of the investigated TWIN nozzles. To address this limitation a second order regression model based on the investigated geometric parameters was developed and systematically reduced using an RMSE based term reduction approach. The resulting models improved the prediction accuracy while maintaining a compact

This project has received funding from the European Union Horizon 2020 Research and Innovation programme. Grant Agreement No 861002

and physically interpretable structure. The regression analysis demonstrated that the dominant geometric influences on spray penetration are the spray hole diameter, spray hole spacing, injection pressure and energization duration.

The novelty of this thesis lies in the combined use of optical flame imaging, pressure based combustion analysis, spray visualization, and spray penetration modelling to link ignition kernel development, dual-fuel combustion stability, and TWIN nozzle spray behaviour. The results provide new insights into both low-load dual-fuel combustion and TWIN nozzle specific spray development.

6.2 Recommendations for future work

Finally, it is recommended for future work on the dual-fuel engines and TWIN nozzles to further investigate the geometric influences as well as new parameter, for example conical spray holes. Especially for the TWIN nozzles it is recommended to not only observe the single injections but to also research the influence of the pressure and energization duration on the spray characteristics further, in order to achieve a full understanding of the influence of all conditions to be able to improve the designs and adjusted calculations even further. Potential design modifications for future investigations include further optimization of the spray hole geometry to redirect the spray towards the lower spray hole during short opening times. In addition, the influence of a horizontal offset between the spray holes and the use of eccentrically positioned spray holes should be investigated, as these features may affect the internal flow behavior and spray development. It is this authors believe that a nozzle capable of injecting stable minimum amount pilot injections while also being able to run engines efficiently in pure pilot fuel combustion is achievable with further analysis and variation of the TWIN nozzle design.

This project has received funding from the European Union Horizon 2020 Research and Innovation programme. Grant Agreement No 861002

EDEM

Bibliography

[1] L. Kistner, A. Bensmann, and R. Hanke-Rauschenbach, "Potentials and limitations of battery-electric container ship propulsion systems", *Energy Conversion and Management: X*, vol. 21, p. 100 507, 2024, ISSN: 2590-1745. DOI: https://doi.org/10.1016/j.ecmx.2023.100507. [Online]. Available: https://www.sciencedirect.com/science/article/pii/S2590174523001630.

[2] P. Ni, X. Wang, and H. Li, "A review on regulations, current status, effects and reduction strategies of emissions for marine diesel engines", *Fuel*, vol. 279, p. 118 477, 2020, ISSN: 0016-2361. DOI: https://doi.org/10.1016/j.fuel.2020.118477. [Online]. Available: https://www.sciencedirect.com/science/article/pii/S0016236120314733.

[3] European Commission. "Reducing emissions from the shipping sector". Accessed: 2025-01-22. (2025), [Online]. Available: https://climate.ec.europa.eu/eu-action/transport/reducing-emissions-shipping-sector_en.

[4] Accessed: 02-01-2021. (2021), [Online]. Available: https://edem-itn.eu.

[5] Accessed: 02-01-2021. (2021), [Online]. Available: https://ec.europa.eu/programmes/horizon2020/en/what-horizon-2020.

[6] U. Spicher, A. Velji, N. Huynh, and F. Kruse, "An experimental study of combustion and fluid flow in diesel engines", *SAE Technical Paper*, no. 872060, 1987. DOI: 10.4271/872060. [Online]. Available: https://doi.org/10.4271/872060.

[7] L. Bravo, S. Ripplinger, and O. Samimi, "Influence of oxygen concentration on the auto-ignition and flame propagation characteristics of diesel jets with experimental comparison", *SAE Technical Paper*, 2017. DOI: 10.4271/2017-01-0842. [Online]. Available: https://doi.org/10.4271/2017-01-0842.

[8] H. Li, L. Wang, K. Wang, W. Zhu, *et al.*, "Study of swirl ratio on mixture preparation with a swirl control valve in a diesel engine", *SAE Technical Paper*, 2018. DOI: 10.4271/2018-01-1790. [Online]. Available: https://doi.org/10.4271/2018-01-1790.

This project has received funding from the European Union Horizon 2020 Research and Innovation programme. Grant Agreement No 861002

[9] D. Lim, J. Lee, H. Shin, *et al.*, "Effect of swirl motion on combustion and emissions characteristics with dual-fuel combustion in compression ignition engine", *International Journal of Automotive Technology*, vol. 23, pp. 379–388, 2022. DOI: 10.1007/s12239-022-0035-9.

[10] Accessed: 02-01-2021. (2021), [Online]. Available: https://dictionary.cambridge.org/de/worterbuch/englisch/internal-combustion-engine.

[11] E. Çabukoglu, G. Georges, L. Küng, G. Pareschi, and K. Boulouchos, "Battery electric propulsion: An option for heavy-duty vehicles? results from a swiss case-study", *Transportation Research Part C: Emerging Technologies*, vol. 88, pp. 107–123, 2018, ISSN: 0968-090X. DOI: https://doi.org/10.1016/j.trc.2018.01.013. [Online]. Available: https://www.sciencedirect.com/science/article/pii/S0968090X18300470.

[12] D. Thombare and S. Verma, "Technological development in the stirling cycle engines", *Renewable and Sustainable Energy Reviews*, vol. 12, no. 1, pp. 1–38, 2008, ISSN: 1364-0321. DOI: https://doi.org/10.1016/j.rser.2006.07.001. [Online]. Available: https://www.sciencedirect.com/science/article/pii/S1364032106000906.

[13] A. M. Taylor, "Science review of internal combustion engines", *Energy Policy*, vol. 36, no. 12, pp. 4657–4667, 2008, Foresight Sustainable Energy Management and the Built Environment Project, ISSN: 0301-4215. DOI: https://doi.org/10.1016/j.enpol.2008.09.001. [Online]. Available: https://www.sciencedirect.com/science/article/pii/S0301421508005016.

[14] A. Mukhopadhyay and S. Sen, *Fundamentals of Combustion Engineering*, 1st. CRC Press, 2019. DOI: 10.1201/9780429158216. [Online]. Available: https://doi.org/10.1201/9780429158216.

[15] S. Gleis, S. Frankl, D. Waligorski, D.-I. M. Prager, and P. D.-I. G. Wachtmeister, "Investigation of the high-pressure-dual-fuel (hpdf) combustion process of natural gas on a fully optically accessible research engine", SAE International, Technical Paper 2019-01-2172, 2019. DOI: 10.4271/2019-01-2172. [Online]. Available: https://doi.org/10.4271/2019-01-2172.

[16] İ. A. Reşitoğlu, K. Altinişik, and A. Keskin, "The pollutant emissions from diesel-engine vehicles and exhaust aftertreatment systems", *Clean Technologies and Environmental Policy*, vol. 17, pp. 15–27, 2015. DOI: 10.1007/s10098-014-0793-9. [Online]. Available: https://doi.org/10.1007/s10098-014-0793-9.

This project has received funding from the European Union Horizon 2020 Research and Innovation programme. Grant Agreement No 861002

[17] Accessed: 02-01-2021. (2021), [Online]. Available: https://www.beyondtoxics.org/wp-content/uploads/2011/11/OTA_Report-BiomassContributors_to_ClimateChange7-28-09.pdf.

[18] Accessed: 02-01-2021. (2021), [Online]. Available: https://www.epa.gov/sites/production/files/2015-07/documents/emission-factors_2014.pdf.

[19] G. Protocol. "Global warming potential values". Accessed: 2025-03-08. (2016), [Online]. Available: https://ghgprotocol.org/sites/default/files/ghgp/Global-Warming-Potential-Values%20%28Feb%2016%202016%29_1.pdf.

[20] U. E. P. Agency. "Greenhouse gas emission factors hub". Accessed: 2025-03-08. (2023), [Online]. Available: https://www.epa.gov/system/files/documents/2023-03/ghg_emission_factors_hub.pdf.

[21] F. Ahmad, S. R. Shah, and M. Siddiqui, "Optimization of an internal combustion engine's efficiency for fuel conservation & green environment", *2014 International Conference on Energy Systems and Policies (ICESP)*, pp. 1–9, 2014. [Online]. Available: https://api.semanticscholar.org/CorpusID:26909575.

[22] C. L. Dumitrache, B. Hnatiuc, and D. Deleanu, "Exhaust gas recirculation (egr) valve, design and computational fluid dynamic analysis", *IOP Conference Series: Materials Science and Engineering*, vol. 1182, 2021. [Online]. Available: https://api.semanticscholar.org/CorpusID:239816154.

[23] H. Pong, J. Wallace, and P. Sullivan, "Modeling of exhaust gas treatment for stationary applications", *SAE Technical Paper*, no. 2012-01-1300, 2012. DOI: 10.4271/2012-01-1300. [Online]. Available: https://doi.org/10.4271/2012-01-1300.

[24] U. Dohle and D. Eimers-Klose, "Clean diesels - future development trends for fuel injection and exhaust gas treatment systems", *SAE Technical Paper*, no. 2006-21-0025, 2006.

[25] X. Xiaoguang, G. Xiyan, W. Xiancheng, and L. Chengbin, "After-treatment for reduction of diesel exhaust particulate", *SAE Technical Paper*, no. 2001-01-3204, 2001. DOI: 10.4271/2001-01-3204. [Online]. Available: https://doi.org/10.4271/2001-01-3204.

[26] Y. Shu, M. Romzek, and L. Meda, "Thermal analysis of diesel after-treatment system", *SAE Technical Paper*, no. 2010-01-1215, 2010. DOI: 10.4271/2010-01-1215. [Online]. Available: https://doi.org/10.4271/2010-01-1215.

This project has received funding from the European Union Horizon 2020 Research and Innovation programme. Grant Agreement No 861002

[27] V. Rossi, L. Brocchi, M. Medda, S. Paltrinieri, *et al.*, "Design and assessment of an exhaust after-treatment system equipped with a fuel", *SAE Technical Paper*, no. 2023-01-0355, 2023. DOI: 10.4271/2023-01-0355. [Online]. Available: https://doi.org/10.4271/2023-01-0355.

[28] A. Joshi, "Review of vehicle engine efficiency and emissions", *SAE Int. J. Adv. & Curr. Prac. in Mobility*, vol. 4, no. 5, pp. 1704–1733, 2022. DOI: 10.4271/2022-01-0540. [Online]. Available: https://doi.org/10.4271/2022-01-0540.

[29] M. Selim and H. Saleh, "Performance and noise of dual fuel engine running on cottonseed, soybean raw oils and their methyl esters as pilot fuels", SAE International, Technical Paper 2020-01-0811, 2020. DOI: 10.4271/2020-01-0811. [Online]. Available: https://doi.org/10.4271/2020-01-0811.

[30] B. Sahoo, N. Sahoo, and U. Saha, *Effect of engine parameters and type of gaseous fuel on the performance of dual-fuel gas diesel engines-A critical review*. 2009, vol. 13, pp. 1151–1184. DOI: https://doi.org/10.1016/j.rser.2008.08.003. [Online]. Available: https://www.sciencedirect.com/science/article/pii/S1364032108001020.

[31] E. Mancaruso, M. Todino, and B. Vaglieco, "Analysis of dual fuel combustion in single cylinder research engine fueled with methane and diesel by ir diagnostics", SAE International, Technical Paper 2019-01-1165, 2019. DOI: 10.4271/2019-01-1165. [Online]. Available: https://doi.org/10.4271/2019-01-1165.

[32] R. Papagiannakis, D. Hountalas, C. Rakopoulos, and D. Rakopoulos, "Combustion and performance characteristics of a di diesel engine operating from low to high natural gas supplement ratios at various operating conditions", SAE International, Technical Paper 2008-01-1392, 2008. DOI: 10.4271/2008-01-1392. [Online]. Available: https://doi.org/10.4271/2008-01-1392.

[33] A. Wagemakers and C. Leermakers, "Review on the effects of dual-fuel operation, using diesel and gaseous fuels, on emissions and performance", SAE International, Technical Paper 2012-01-0869, 2012. DOI: 10.4271/2012-01-0869. [Online]. Available: https://doi.org/10.4271/2012-01-0869.

[34] N. Mustafi and R. Raine, "A study of the emissions of a dual fuel engine operating with alternative gaseous fuels", *SAE Technical Paper*, no. 2008-01-1394, 2008. DOI: 10.4271/2008-01-1394. [Online]. Available: https://doi.org/10.4271/2008-01-1394.

This project has received funding from the European Union Horizon 2020 Research and Innovation programme. Grant Agreement No 861002

[35] N. Dronniou, J. Kashdan, B. Lecointe, K. Sauve, *et al.*, "Optical investigation of dual-fuel cng/diesel combustion strategies to reduce co2 emissions", Tech. Rep. 2, 2014, pp. 873–887. DOI: 10.4271/2014-01-1313. [Online]. Available: https://doi.org/10.4271/2014-01-1313.

[36] J. Rochussen, G. McTaggart-Cowan, and P. Kirchen, "Parametric study of pilot-ignited direct-injection natural gas combustion in an optically accessible heavy-duty engine", *International Journal of Engine Research*, vol. 21, no. 3, pp. 497–513, 2020. DOI: 10.1177/1468087419836877. [Online]. Available: https://doi.org/10.1177/1468087419836877.

[37] M. Karimi, X. Wang, J. Hamilton, M. Negnevitsky, and S. Lyden, "Status, challenges and opportunities of dual fuel hybrid approaches-a review", *International Journal of Hydrogen Energy*, vol. 46, no. 70, pp. 34 924–34 957, 2021, ISSN: 0360-3199. DOI: https://doi.org/10.1016/j.ijhydene.2021.08.008. [Online]. Available: https://www.sciencedirect.com/science/article/pii/S0360319921030639.

[38] X. Liu, Q. Wang, W. Zhong, P. Jiang, M. Xu, and B. Guo, "An optical investigation of the effects of diesel injection pressure and intake air temperature in an ammonia-diesel dual-fuel engine under low-load conditions", *Applied Thermal Engineering*, vol. 261, p. 125 174, 2025, ISSN: 1359-4311. DOI: https://doi.org/10.1016/j.applthermaleng.2024.125174. [Online]. Available: https://www.sciencedirect.com/science/article/pii/S1359431124028424.

[39] C. J. Ulishney and C. E. Dumitrescu, "Effect of gas composition on the performance and emissions of a dual-fuel diesel-natural gas engine at low load conditions", *Fuel*, vol. 324, p. 124 531, 2022, ISSN: 0016-2361. DOI: https://doi.org/10.1016/j.fuel.2022.124531. [Online]. Available: https://www.sciencedirect.com/science/article/pii/S0016236122013801.

[40] G. Abd Alla, H. Soliman, O. Badr, and M. Abd Rabbo, "Effect of injection timing on the performance of a dual fuel engine", *Energy Conversion and Management*, vol. 43, no. 2, pp. 269–277, 2002, ISSN: 0196-8904. DOI: https://doi.org/10.1016/S0196-8904(00)00168-0. [Online]. Available: https://www.sciencedirect.com/science/article/pii/S0196890400001680.

[41] X. Zhang, J. Gao, D. Fan, *et al.*, "Impact of pilot diesel injection timing on performance and emission characteristics of marine natural gas/diesel dual-fuel engine", *Scientific Reports*, vol. 14, p. 10 713, 2024. DOI: 10.1038/s41598-024-61672-5. [Online]. Available: https://doi.org/10.1038/s41598-024-61672-5.

This project has received funding from the European Union Horizon 2020 Research and Innovation programme. Grant Agreement No 861002

[42] H. Yu, J. Gao, P. Zhang, *et al.*, "The impact of scavenging air state on the combustion and emission performance of marine two-stroke dual-fuel engine", *Scientific Reports*, vol. 14, p. 15 776, 2024. DOI: 10.1038/s41598-024-66826-z.

[43] F. M. Felayati *et al.*, *IOP Conference Series: Earth and Environmental Science*, vol. 698, p. 012 036, 2021. DOI: 10.1088/1755-1315/698/1/012036.

[44] G. Karim, *Dual-Fuel Diesel Engines*, 1st. CRC Press, 2015. DOI: 10.1201/b18163. [Online]. Available: https://doi.org/10.1201/b18163.

[45] A. Nemati, J. C. Ong, M. Zhang, and J. H. Walther, "Large eddy simulation of a premixed dual-fuel combustion: Effects of inhomogeneity level on auto-ignition of micro-pilot fuel", *Fuel*, vol. 349, p. 128 593, 2023, ISSN: 0016-2361. DOI: https://doi.org/10.1016/j.fuel.2023.128593. [Online]. Available: https://www.sciencedirect.com/science/article/pii/S0016236123012061.

[46] H. Park, E. Shim, and C. Bae, "Injection strategy in natural gas-diesel dual-fuel premixed charge compression ignition combustion under low load conditions", *Engineering*, vol. 5, no. 3, pp. 548–557, 2019, ISSN: 2095-8099. DOI: https://doi.org/10.1016/j.eng.2019.03.005. [Online]. Available: https://www.sciencedirect.com/science/article/pii/S2095809918303515.

[47] M. Choi and S. Park, "Effects of pre-mixed gas composition on combustion characteristics of micro pilot dual fuel (mpdf) in a heavy-duty dual fuel engine", *Scientific Reports*, vol. 12, p. 7871, 2022. DOI: 10.1038/s41598-022-11958-3. [Online]. Available: https://doi.org/10.1038/s41598-022-11958-3.

[48] H. Ogawa, N. Miyamoto, C. Li, and S. Nakazawa, "Low emission and knock-free combustion with rich and lean biform mixture in a dual-fuel ci engine with induced lpg as the main fuel", SAE International, Tech. Rep. 2001-01-3502, 2001. DOI: 10.4271/2001-01-3502. [Online]. Available: https://doi.org/10.4271/2001-01-3502.

[49] A. Bilcan, O. Le Corre, M. Tazerout, and A. Ramesh, "Characterization of the lpg - diesel dual fuel combustion", SAE International, Tech. Rep. 2001-28-0036, 2001. DOI: 10.4271/2001-28-0036. [Online]. Available: https://doi.org/10.4271/2001-28-0036.

[50] T. Le and T. Nguyen, "Experimental study on performance, emissions and combustion characteristics of a single cylinder dual fuel lpg/diesel engine", SAE International, Tech. Rep. 2011-32-0562, 2011. DOI: 10.4271/2011-32-0562. [Online]. Available: https://doi.org/10.4271/2011-32-0562.

This project has received funding from the European Union Horizon 2020 Research and Innovation programme. Grant Agreement No 861002

[51] A. Hegab, W. Bowling, A. Cairns, and A. Harrington, "Development of an ultra-low carbon flex dual-fuel ammonia engine for heavy-duty applications", SAE International, Tech. Rep. 2024-01-2368, 2024. DOI: 10.4271/2024-01-2368. [Online]. Available: https://doi.org/10.4271/2024-01-2368.

[52] D. Krnac, B. Manickam, P. Holand, and U. Pathak, "Comparison of tabulated and complex chemistry approaches for ammonia - diesel dual-fuel combustion simulation", *SAE International Journal of Engines*, vol. 17, no. 7, pp. 945–960, 2024. DOI: 10.4271/03-17-07-0055. [Online]. Available: https://doi.org/10.4271/03-17-07-0055.

[53] J. Vavra, I. Bortel, and M. Takats, "A dual fuel hydrogen - diesel compression ignition engine and its potential application in road transport", SAE International, Tech. Rep. 2019-01-0564, 2019. DOI: 10.4271/2019-01-0564. [Online]. Available: https://doi.org/10.4271/2019-01-0564.

[54] E. Mancaruso, S. Rossetti, and B. Vaglieco, "Analysis of dual fuel hydrogen/diesel combustion varying diesel and hydrogen injection parameters in a single cylinder research engine", SAE International, Tech. Rep. 2024-01-2363, 2024. DOI: 10.4271/2024-01-2363. [Online]. Available: https://doi.org/10.4271/2024-01-2363.

[55] N. Saravanan, G. Nagarajan, C. Dhanasekaran, and K. Kalaiselvan, "Experimental investigation of hydrogen fuel injection in di dual fuel diesel engine", SAE International, Tech. Rep. 2007-01-1465, 2007. DOI: 10.4271/2007-01-1465. [Online]. Available: https://doi.org/10.4271/2007-01-1465.

[56] R. Florea, K. Zha, X. Yu, M. Jansons, *et al.*, "Ethanol/n-heptane dual-fuel partially premixed combustion analysis through formaldehyde plif", Tech. Rep. 2, 2012, pp. 483–492. DOI: 10.4271/2012-01-0685. [Online]. Available: https://doi.org/10.4271/2012-01-0685.

[57] H. Jiang, J. Wang, and S. Shuai, "Visualization and performance analysis of gasoline homogeneous charge induced ignition by diesel", SAE International, Technical Paper 2005-01-0136, 2005. DOI: 10.4271/2005-01-0136. [Online]. Available: https://doi.org/10.4271/2005-01-0136.

[58] B. S. Chauhan, R. K. Singh, H. Cho, and H. Lim, "Practice of diesel fuel blends using alternative fuels: A review", *Renewable and Sustainable Energy Reviews*, vol. 59, pp. 1358–1368, 2016, ISSN: 1364-0321. DOI: https://doi.org/10.1016/j.rser.2016.01.062. [Online]. Available: https://www.sciencedirect.com/science/article/pii/S1364032116000927.

This project has received funding from the European Union Horizon 2020 Research and Innovation programme. Grant Agreement No 861002

[59] H. Zhao, *Laser Diagnostics and Optical Measurement Techniques in Internal Combustion Engines*. SAE International, 2012, ISBN: 978-0-7680-5782-9. DOI: 10.4271/R-406.

[60] S. Merola, B. Vaglieco, F. Corcione, and E. Mancaruso, "In-cylinder combustion analysis by flame emission spectroscopy of transparent cr diesel engine", *SAE Technical Paper*, vol. 2003, no. 01-1112, 2003. DOI: 10.4271/2003-01-1112. [Online]. Available: https://doi.org/10.4271/2003-01-1112.

[61] J. Hult, S. Matlok, and S. Mayer, "Particle image velocimetry measurements of swirl and scavenging in a large marine two-stroke diesel engine", *SAE Technical Paper*, vol. 2014, no. 01-1173, 2014. DOI: 10.4271/2014-01-1173. [Online]. Available: https://doi.org/10.4271/2014-01-1173.

[62] R. Velugula, B. Thiruvallur loganathan, L. Varadhaiyengar, R. Asvathanarayanan, and M. Mittal, "An analysis of mechanical and thermal stresses, temperature and displacement within the transparent cylinder and piston top of a small direct-injection spark-ignition optical engine", *Energies*, vol. 16, no. 21, 2023, ISSN: 1996-1073. [Online]. Available: https://www.mdpi.com/1996-1073/16/21/7400.

[63] J. Liu and C. E. Dumitrescu, "Optical analysis of flame inception and propagation in a lean-burn natural-gas spark-ignition engine with a bowl-in-piston geometry", *International Journal of Engine Research*, vol. 21, no. 9, pp. 1584–1596, 2020. DOI: 10.1177/1468087418822852.

[64] K. Zha, S. Busch, P. Miles, S. Wijeyakulasuriya, *et al.*, "Characterization of flow asymmetry during the compression stroke using swirl-plane piv in a light-duty optical diesel engine with the re-entrant piston bowl geometry", *SAE International Journal of Engines*, vol. 8, no. 4, pp. 1837–1855, 2015. DOI: 10.4271/2015-01-1699. [Online]. Available: https://doi.org/10.4271/2015-01-1699.

[65] T. Fuyuto, T. Matsumoto, Y. Hattori, K. Kugimoto, *et al.*, "A new generation of optically accessible single-cylinder engines for high-speed and high-load combustion analysis", *SAE International Journal of Fuels and Lubricants*, vol. 5, no. 1, pp. 307–315, 2012. DOI: 10.4271/2011-01-2050. [Online]. Available: https://doi.org/10.4271/2011-01-2050.

[66] E. Mancaruso, B. Vaglieco, and L. Sequino, "Using 2d infrared imaging for the analysis of non-conventional fuels combustion in a diesel engine", *SAE International Journal of Engines*, vol. 8, no. 4, pp. 1701–1715, 2015. DOI: 10.4271/2015-01-1646. [Online]. Available: https://doi.org/10.4271/2015-01-1646.

This project has received funding from the European Union Horizon 2020 Research and Innovation programme. Grant Agreement No 861002

[67] A. Larsson, "Optical studies in a di diesel engine", *SAE Technical Paper*, vol. 1999, no. 01-3650, 1999. DOI: 10.4271/1999-01-3650. [Online]. Available: https://doi.org/10.4271/1999-01-3650.

[68] Z. Yin, C. Yao, P. Geng, and J. Hu, "Visualization of combustion characteristic of diesel in premixed methanol - air mixture atmosphere of different ambient temperature in a constant volume chamber", *Fuel*, vol. 174, pp. 242–250, 2016, ISSN: 0016-2361. DOI: https://doi.org/10.1016/j.fuel.2016.02.030. [Online]. Available: https://www.sciencedirect.com/science/article/pii/S0016236116001514.

[69] S. Kang, D. Ko, S. Lee, Y. Cho, *et al.*, "An experimental study on combustion and emission characteristics of hcng with dual spark plug in a constant volume chamber", *SAE Technical Paper*, vol. 2011, no. 28-0019, 2011. DOI: 10.4271/2011-28-0019. [Online]. Available: https://doi.org/10.4271/2011-28-0019.

[70] K. Shimizu, T. Narushima, R. Sok, and J. Kusaka, "Experimental and 3d-cfd analysis of synthetic fuel properties on combustion and exhaust gas emission characteristics in heavy-duty diesel engines", *SAE Technical Paper*, vol. 2023, no. 24-0052, 2023. DOI: 10.4271/2023-24-0052. [Online]. Available: https://doi.org/10.4271/2023-24-0052.

[71] D. Baik, J. Lee, Y. Cho, and S. Lee, "Combustion and emission characteristics of cng fuel inside cvc chamber", *SAE International Journal of Fuels and Lubricants*, vol. 1, no. 1, pp. 155–161, 2009. DOI: 10.4271/2008-01-0322. [Online]. Available: https://doi.org/10.4271/2008-01-0322.

[72] J. Sureshkumar, R. Elayaraja, J. Mallikarjuna, and G. Venkitachalam, "Transient spray characteristics of air assisted fuel injection", *SAE Technical Paper*, vol. 2015, no. 01-0920, 2015. DOI: 10.4271/2015-01-0920. [Online]. Available: https://doi.org/10.4271/2015-01-0920.

[73] M. Zhao and S. Kaiser, "Optical diagnostics for knock in compression-ignition engines via high-speed imaging", *SAE International Journal of Engines*, vol. 11, no. 6, pp. 903–918, 2018. DOI: 10.4271/2018-01-0631. [Online]. Available: https://doi.org/10.4271/2018-01-0631.

[74] G. S. Settles, *Schlieren and Shadowgraph Techniques*. Springer Berlin, Heidelberg, 2001, ISBN: 978-3-540-66155-9. DOI: https://doi.org/10.1007/978-3-642-56640-0.

[75] T. Fujikawa, T. Ozasa, and K. Kozuka, "Development of transparent cylinder engines for schlieren observation", SAE International, Tech. Rep. 881632, 1988. DOI: 10.4271/881632. [Online]. Available: https://doi.org/10.4271/881632.

This project has received funding from the European Union Horizon 2020 Research and Innovation programme. Grant Agreement No 861002

[76] J. Lee, N. Kim, H. Lee, and K. Min, "The measurement of penetration length of diesel spray by using background oriented schlieren technique", *SAE International Journal of Engines*, vol. 4, no. 1, pp. 737–746, 2011. DOI: 10.4271/2011-01-0684. [Online]. Available: https://doi.org/10.4271/2011-01-0684.

[77] H. Ouchi, T. Chikahisa, and T. Murayama, "A quantitative analysis of schlieren photography for an internal combustion engine diagnostics", SAE International, Tech. Rep. 910730, 1991. DOI: 10.4271/910730. [Online]. Available: https://doi.org/10.4271/910730.

[78] J. Pastor, R. Payri, J. Garcia-Oliver, and F. Briceño, "Schlieren methodology for the analysis of transient diesel flame evolution", *SAE International Journal of Engines*, vol. 6, no. 3, pp. 1661–1676, 2013. DOI: 10.4271/2013-24-0041. [Online]. Available: https://doi.org/10.4271/2013-24-0041.

[79] K. Kunkulagunta, "Video imaging and analysis of common rail sprays in an optical engine using shadowgraphy technique", SAE International, Tech. Rep. 2000-01-1255, 2000. DOI: 10.4271/2000-01-1255. [Online]. Available: https://doi.org/10.4271/2000-01-1255.

[80] S. Daly, E. Cenker, L. Pickett, and S. Skeen, "The effects of injector temperature on spray characteristics in heavy-duty diesel sprays", *SAE International Journal of Engines*, vol. 11, no. 6, pp. 879–891, 2018. DOI: 10.4271/2018-01-0284. [Online]. Available: https://doi.org/10.4271/2018-01-0284.

[81] N. Guerrassi and J. Champoussin, "Experimental study and modeling of diesel spray/wall impingement", SAE International, Tech. Rep. 960864, 1996. DOI: 10.4271/960864. [Online]. Available: https://doi.org/10.4271/960864.

[82] M. Shimoda, T. Suzuki, and M. Shigemori, "Observation of the particulate formation process in the cylinder of a direct injection diesel engine", SAE International, Tech. Rep. 870268, 1987. DOI: 10.4271/870268. [Online]. Available: https://doi.org/10.4271/870268.

[83] D. Kim, S. Park, and C. Bae, "Schlieren, shadowgraph, mie-scattering visualization of diesel and gasoline sprays in high pressure/high temperature chamber under gdci engine low load condition", *International Journal of Automotive Technology*, vol. 19, pp. 1–8, 2018. DOI: 10.1007/s12239-018-0001-8. [Online]. Available: https://doi.org/10.1007/s12239-018-0001-8.

[84] H. Xu, P. Myers, and O. Uyehara, "In-cylinder measurement of particulate number density and size", SAE International, Tech. Rep. 820462, 1982. DOI: 10.4271/820462. [Online]. Available: https://doi.org/10.4271/820462.

This project has received funding from the European Union Horizon 2020 Research and Innovation programme. Grant Agreement No 861002

[85] B. Alataş, J. Pinson, T. Litzinger, and D. Santavicca, "A study of no and soot evolution in a di diesel engine via planar imaging", SAE International, Tech. Rep. 930973, 1993. DOI: 10.4271/930973. [Online]. Available: https://doi.org/10.4271/930973.

[86] A. Montanaro, M. Migliaccio, L. Allocca, and V. Fraioli, "Schlieren and mie scattering visualization for single-hole diesel injector under vaporizing conditions with numerical validation", SAE International, Tech. Rep. 2014-01-1406, 2014. DOI: 10.4271/2014-01-1406. [Online]. Available: https://doi.org/10.4271/2014-01-1406.

[87] K. Münch and A. Leipertz, "Investigation of spray penetration and fuel distribution inside the piston bowl of a 1.9 l di diesel engine using two-dimensional mie scattering", SAE International, Tech. Rep. 922204, 1992. DOI: 10.4271/922204. [Online]. Available: https://doi.org/10.4271/922204.

[88] Accessed: 02-01-2021. (2021), [Online]. Available: https://omlc.org/spectra/PhotochemCAD/html/001.html.

[89] C. Willman, R. Stone, M. Davy, and B. Williams, "Cycle-to-cycle variation analysis of two-colour plif temperature measurements calibrated with laser induced grating spectroscopy in a firing gdi engine", *SAE International Journal of Advances and Current Practices in Mobility*, vol. 1, no. 4, pp. 1404–1419, 2019. DOI: 10.4271/2019-01-0722. [Online]. Available: https://doi.org/10.4271/2019-01-0722.

[90] B. Scott, C. Willman, B. Williams, and P. Ewart, "In-cylinder temperature measurements using laser induced grating spectroscopy and two-colour plif", *SAE International Journal of Engines*, vol. 10, no. 4, pp. 2191–2201, 2017. DOI: 10.4271/2017-24-0045. [Online]. Available: https://doi.org/10.4271/2017-24-0045.

[91] T. Brands, T. Huelser, P. Hottenbach, and H. Koss, "Optical investigation of combusting split-injection diesel sprays under quiescent conditions", *SAE International Journal of Engines*, vol. 6, no. 3, pp. 1626–1641, 2013. DOI: 10.4271/2013-24-0034. [Online]. Available: https://doi.org/10.4271/2013-24-0034.

[92] D. Rothamer, J. Snyder, R. Hanson, and R. Steeper, "Two-wavelength plif diagnostic for temperature and composition", *SAE International Journal of Fuels and Lubricants*, vol. 1, no. 1, pp. 520–533, 2009. DOI: 10.4271/2008-01-1067. [Online]. Available: https://doi.org/10.4271/2008-01-1067.

This project has received funding from the European Union Horizon 2020 Research and Innovation programme. Grant Agreement No 861002

[93] R. Florea, K. Zha, X. Yu, and M. Jansons, "Ethanol/n-heptane dual-fuel partially premixed combustion analysis through formaldehyde plif", *SAE International Journal of Engines*, vol. 5, no. 2, pp. 483–492, 2012. DOI: 10.4271/2012-01-0685. [Online]. Available: https://doi.org/10.4271/2012-01-0685.

[94] H. Hiroyasu and M. Arai, "Structures of fuel sprays in diesel engines", *SAE Technical Paper*, vol. 900475, 1990. DOI: 10.4271/900475. [Online]. Available: https://doi.org/10.4271/900475.

[95] J. Naber and D. Siebers, "Effects of gas density and vaporization on penetration and dispersion of diesel sprays", *SAE Technical Paper*, vol. 960034, 1996. DOI: 10.4271/960034. [Online]. Available: https://doi.org/10.4271/960034.

[96] L. Liu, Y. Peng, D. Liu, C. Han, N. Zhao, and X. Ma, "A review of phenomenological spray penetration modeling for diesel engines with advanced injection strategy", *International Journal of Spray and Combustion Dynamics*, vol. 12, 2020. DOI: 10.1177/1756827720934067.

[97] J. Liu, F. Yang, H. Wang, M. Ouyang, and S. Hao, "Effects of pilot fuel quantity on the emissions characteristics of a cng/diesel dual fuel engine with optimized pilot injection timing", *Applied Energy*, vol. 110, pp. 201–206, 2013, ISSN: 0306-2619. DOI: https://doi.org/10.1016/j.apenergy.2013.03.024. [Online]. Available: https://www.sciencedirect.com/science/article/pii/S0306261913002201.

[98] R. Payri, F. Salvador, J. Gimeno, and L. Zapata, "Diesel nozzle geometry influence on spray liquid-phase fuel penetration in evaporative conditions", *Fuel*, vol. 87, no. 7, pp. 1165–1176, 2008, ISSN: 0016-2361. DOI: https://doi.org/10.1016/j.fuel.2007.05.058. [Online]. Available: https://www.sciencedirect.com/science/article/pii/S0016236107003080.

[99] S. Goto and K. Kontani, "A dual fuel injector for diesel engines", SAE International, Tech. Rep. 851584, 1985. DOI: 10.4271/851584. [Online]. Available: https://doi.org/10.4271/851584.

[100] I. Woodward. "Dual fuel injectors". Accessed: 2024-01-07. (2024), [Online]. Available: https://www.woodward.com/products/industrial/dual-fuel-injectors-2/.

[101] M. T. Heller and Woodward. "Woodward presentation at cimac circle 2019". Accessed: 2023-12-03. (2019), [Online]. Available: https://www.cimac.com/cms/upload/events/circles/circle_2019_SMM/1_Marc_Tran_Heller_Woodward.pdf.

This project has received funding from the European Union Horizon 2020 Research and Innovation programme. Grant Agreement No 861002

[102] B. Bose, *Auslegung und strahldiagnostische untersuchung von einspritzdüsen mit zwillingsspritzlöchern für großdieselmotoren*, Bachelor's thesis, 2013.

[103] A. M. Lauterkorn, X. Wang, and H. Zhao, "Analysis of combustion cycle-to-cycle variation in an optical single cylinder dual-fuel engine", *SAE Technical Papers*, vol. 2023-01-0279, pp. 1–10, 2023. DOI: 10.4271/2023-01-0279.

This project has received funding from the European Union Horizon 2020 Research and Innovation programme. Grant Agreement No 861002